University of Bath

PHD

Surface Scattering from Soft Matter at Interfaces

Hazell, Gavin

Award date:
2014

Awarding institution:
University of Bath

Link to publication

General rights
Copyright and moral rights for the publications made accessible in the public portal are retained by the authors and/or other copyright owners and it is a condition of accessing publications that users recognise and abide by the legal requirements associated with these rights.

- Users may download and print one copy of any publication from the public portal for the purpose of private study or research.
- You may not further distribute the material or use it for any profit-making activity or commercial gain
- You may freely distribute the URL identifying the publication in the public portal ?

Take down policy
If you believe that this document breaches copyright please contact us providing details, and we will remove access to the work immediately and investigate your claim.

Download date: 22. May. 2019

Surface Scattering from Soft Matter at Interfaces

Gavin D. A. Hazell

A thesis submitted for the degree of Doctor of Philosophy
University of Bath Chemistry Department

December 2014

COPYRIGHT

Attention is drawn to the fact that copyright of this thesis rests with the author. A copy of this thesis has been supplied on condition that anyone who consults it is understood to recognise that its copyright rests with the author and that they must not copy it or use material from it except as permitted by law or with the consent of the author.

This thesis may be made available for consultation within the University Library and may be photocopied or lent to other libraries for the purpose of consultation.

ACKNOWLEDGEMENTS

Firstly I would like to thank my two supervisors, Professor Karen Edler (University of Bath) and Dr Tom Arnold (Diamond Light Source), for their constant support throughout my project. I am extremely grateful for all of their guidance and the late nights they have spent with me on various scattering experiments. It has been a pleasure to work for both of them and I hope that we will continue to collaborate in the future.

I am indebted to all the members of the Edler group at the University of Bath for their assistance in conducting scattering experiments. However I am most grateful for the fruitful discussions had, often late into the night, on x-ray and neutron instruments. I would particularly like to thank Duygu Celebi, Ilaria Idini and Cecilia Tognlononi for their infinite reserve of happiness and ability to always cheer me up when things got tough. My most sincere gratitude is extended to Dr Amani El-Fagui. She has been a source of motivation throughout my PhD and has never failed to give me constructive advice regarding my work. From the point of her arrival in Bath it has been an honor to work with her.

Last but not least I thank my family for all of their support throughout the entirety of my studies. My mother has always listened to my worries and moans about the toils of a scientific career. I thank my sister for all of her encouragement and support. Finally I thank my father for his constant backing and advice. You guys are my rock.

Abstract

The aim of this work has been to make use of surface scattering techniques to study soft matter at interfaces. The work presented herein is composed of two distinct bodies of work.

The first comprises a fundamental study of the physical and structural properties of Langmuir monolayers composed of sulfobetaine surfactants. Physiochemical properties of the films have been investigated through the use of Langmuir trough techniques. This has been used to support x-ray and neutron reflectometry data, from which structural parameters were derived.

The second body of work involves attempts to find and/or characterize novel ways of aligning proteins at interfaces. Soluble proteins at lipid interfaces have been characterized in terms of their interactions with functionalized lipid monolayers. Specific interactions have been utilized to adsorb protein layers at the interface through interactions with His-tag chelating lipids within the monolayer. These have been characterized using neutron reflectometry and quartz crystal microbalance studies. Work has also been completed to design a suitable system for the adsorption of membrane proteins. This has involved aligning phospholipid bilayer nanodisc at the lipid interface and subsequent characterization through neutron reflectometry.

Table of Contents

Chapter 4.0 Characterising protein interactions with functionalized phospholipid monolayers

Chapter 5.0 Nanodisc interactions with phospholipid monolayers

Chapter 6.0 Future Work

7.0 Appendix

List of Abbreviations

A_c	Collapse point
ACMW	Air contrast matched water
A_{lim}	Limiting area
APM	Area per molecule
CMC	Critical micelle concentration
DCD	Double crystal deflector
DLS	Dynamic light scattering
DMPC	1,2-Dimyristoyl-*sn*-Glycero-3-Phosphocholine
DMPG	1,2-dimyristoyl-sn-glycero-3-[phospho-rac-(1-glycerol)] (sodium salt)
DOGS-NTA-Ni	1,2-dioleoyl-*sn*-glycero-3-[(N-(5-amino-1-carboxypentyl)iminodiacetic acid)succinyl] (nickel salt)
DOPC	1,2-dioleoyl-*sn*-glycero-3-phosphocholine
DPPC	Dipalmitoylphosphatidylcholine
G phase	Gaseous phase
GIXD	Grazing incidence x-ray diffraction
L2 phase	Secondary condensed phase of a phospholipid monolayer in which the tails are arranged perpendicular to the interface
LC phase	Liquid condensed phase
LE phase	Liquid expanded phase
MSP	Membrane scaffold protein
NR	Neutron reflectometry
OTS	Octadecyl trichlorosilane
PBP3	Penicillin binding protein 3
PC	Phosphocholine
PE	Phosphoethanolamine
POPC	2-Oleoyl-1-palmitoyl-*sn*-glycero-3-phosphocholine
PS	Phosphoserine
QCM	Quartz crystal microbalance
SANS	Small angle neutron scattering
SAXS	Small angle x-ray scattering
SB3-18	*3-[*N,N-*dimethyl*-N-*(H_{37})-octadecylammoniumyl]propane-1-sulfonate*
SB3-18-2	*3-[*N,N-*methyl*-N-*(H_{74})-dioctadecylammoniumyl]propane-1-sulfonate*
SB3-20	*3-[*N,N-*dimethyl*-N-*(H_{37})-eicosylammoniumyl]propane-1-sulfonate*
SB3-22	*3-[*N,N-*dimethyl*-N-*(H_{37})-docosylammoniumyl]propane-1-sulfonate*
SB4-18	*3-[*N,N-*dimethyl*-N-*(H_{37})-octadecylammoniumyl]propane-1-sulfonate*
SDS	Sodium dodecylsulfate
SMA	Styrene-maleic acid

XRR	X-ray reflectometry
π_c	Surface pressure for the onset of the phase plateau
π_{col}	Surface presure of the collapse point

Chapter 1.0- Introduction

Work presented in this thesis centers around x-ray and neutron reflection from lipid and surfactant monolayers at the air-water and solid-liquid interface. Experiments have been designed in which the fundamental interactions of surfactant monolayers have been probed, whilst the second half is dedicated to finding novel ways to align proteins at lipid interfaces. This thesis is therefore divided into two main bodies of work.

The first section of this thesis concerns a fundamental study of the physiochemical properties of sulfobetaine surfactants at the air-water interface. The second body of work is designed to finding novel ways to align proteins (both soluble and insoluble) upon lipid monolayers at the solid-liquid interface. The main tool of investigation is reflectometry, however this technique has been coupled with other surface sensitive techniques to aid in the interpretation of reflectometry data. A detailed discussion of the theoretical aspects of these techniques can be found in chapter 2.

The introduction will outline aspects of the literature relevant to the different parts of this thesis. It will begin with a general summary of surfactant and phospholipid behavior, with a particular focus on Langmuir monolayers. The second half of the introduction will give a summary of methods used to align proteins at interfaces and discuss novel ideas and experimental approaches for possible novel methods of protein alignment at the solid-liquid interface.

1.1 Surfactants and Lipids

Surfactants are polar, amphiphilic species comprising a hydrophilic head group (often charged) and a hydrophobic chain region[1]. These species can self-assemble at an interface or in solution to form a range of complex structures such as micelles and vesicles. The compounds are often classified by the nature of their head group, which can be ionic, zwitterionic or non-ionic. Examples of surfactant structures are shown in figure 1.0.

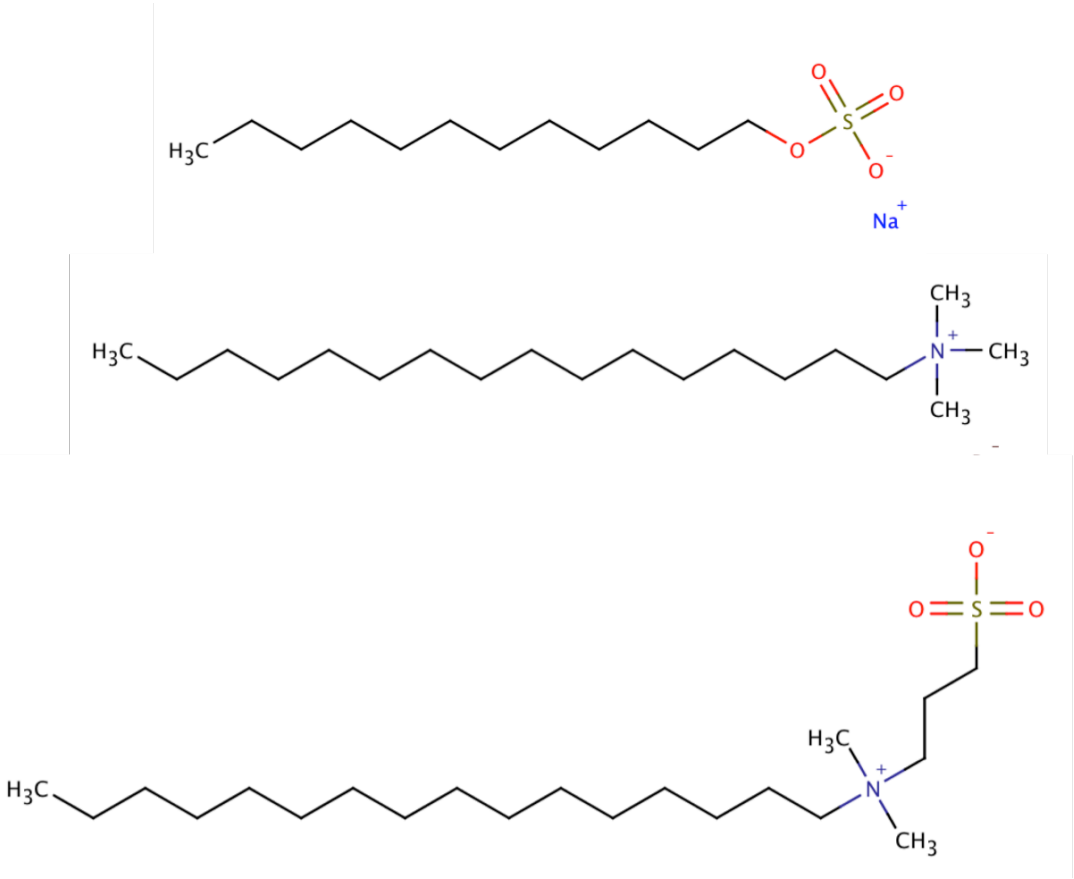

Fig 1.0- Example of surfactant structures. Top) Anionic sodium dodecyl sulphate (SDS). Middle) Cationic hexadecyltrimethylammonium bromide. Bottom) Zwitterionic 3-(N,N-Dimethylmyristylammonio) propanesulfonate (SB3-14).

Surfactant adsorption at the air-water interface will be driven by a lowering of the free energy of the system as the adsorption of these molecules lowers the surface tension, or interfacial free energy per unit area, of the interface[2-5].

A schematic plot showing the dependence of surface tension, as a function of surfactant concentration, is shown in figure 1.1.

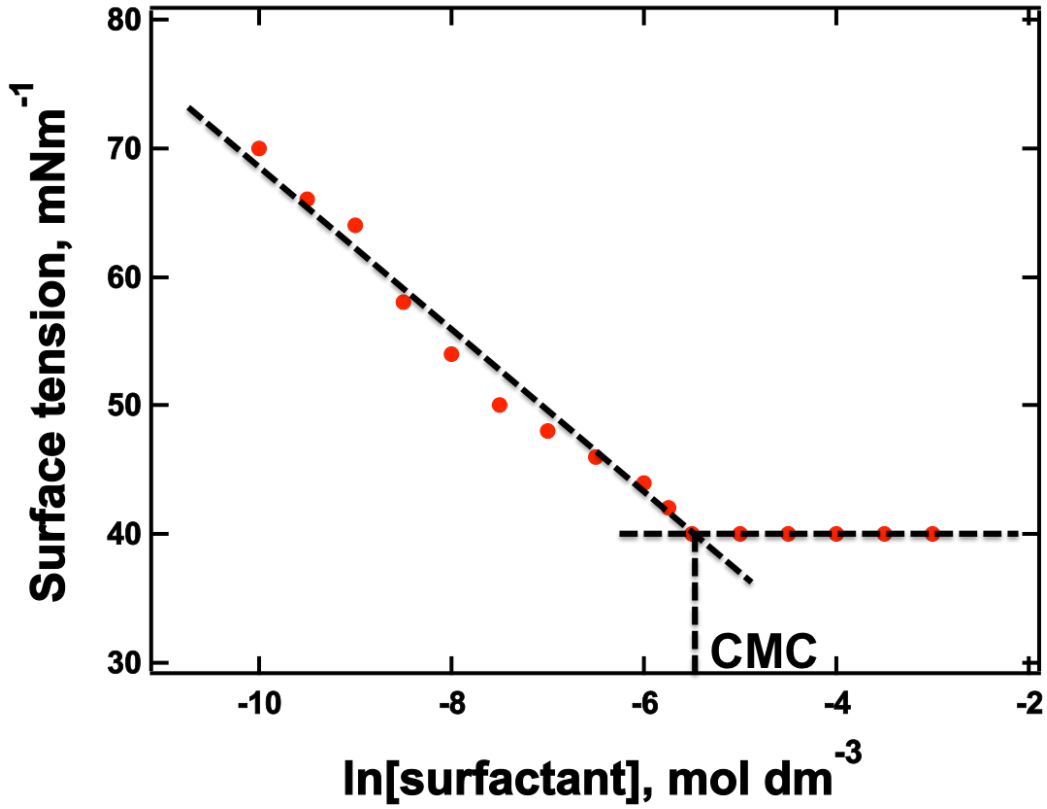

Fig 1.1- The dependence of surface tension (mNm^{-1}) as a function of surfactant concentration ($mol\ dm^{-3}$).

The relationship between the surfactant concentration and the surface tension is given by the Gibbs adsorption isotherm[6],

$$\Gamma = -\frac{1}{RT}.\frac{d\delta}{d\,(\ln C)} \qquad \text{(equation 1.0)}$$

where Γ is the surface excess concentration ($mol\ m^{-2}$), δ is the surface tension (mNm^{-1}) and C is the concentration of surfactant ($mol\ dm^{-3}$).

As shown in figure 1.1, above a given surfactant concentration, there is no longer a dependence of surface tension with regard to surfactant concentration. Here an abrupt change in the slope is observed and the surface tension remains constant with increasing surfactant concentration.

This is known as the critical micelle concentration and corresponds to the formation of aggregates in solution known as micelles[2]. The formation of micelles is driven by the entropic gain by the release of ordered water molecules associated with the surfactant hydrophobic chain[7].

When the hydrophobic moiety of the surfactant or lipid is sufficiently large, the amphiphile is rendered insoluble in water and is able to form an isolated two-dimensional monolayer upon the surface of water[8]. Films of this kind are often referred to as Langmuir monolayers. These films are a single monolayer in thickness and form with the hydrophilic head of the surfactant to lie in the water phase and the hydrophobic tail extending into the air. Due to the insoluble nature of these films, little information can be gained by assessing their relationships with a bulk phase. Attention is therefore placed on the films themselves. Molecular requirements for a Langmuir film-forming compound dictate that the surfactant or lipid must have a sufficiently large hydrophobic moiety rendering the molecule insoluble in water. The molecule must also contain a sufficiently large hydrophilic region in order to anchor the molecule at the air-water interface[2].

One such class of molecules that have been extensively studied for their Langmuir film forming properties are the phospholipids[9-12]. This class of molecules will be briefly introduced before Langmuir monolayers are discussed in more detail.

1.1.1 Phospholipids

Phospholipids are the major component of biological membranes and contain a fatty acid chain composed of an even number of carbon atoms, with 16-18 carbon long most commonly found in nature[13]. Phospholipids are usually classified by the structure and/or charge of their head group, commonly studied examples being phosphatidylcholines (PC), phosphoethanolamines (PE) and phosphatidylserines (PS)[14]. The structure of these molecules is shown in figure 1.2.

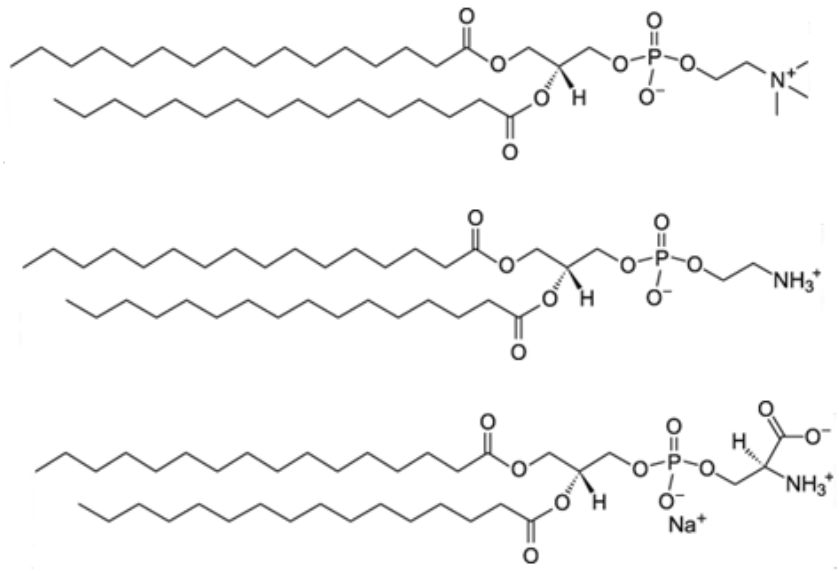

Fig. 1.2- From top to bottom: top is 1,2-dipalmitoyl-*sn*-glycero-3-phosphocholine (DPPC), middle is 1,2-dipalmitoyl-*sn*-glycero-3-phosphoethanolamine (DPPE) and bottom is 1,2-dihexadecanoyl-*sn*-glycero-3-phospho-L-serine (DPPS).

The most frequently studied phospholipids are the zwitterionic phosphocholines consisting of an inner (negatively charged) phosphate group and an outer (positively charged) ammonium group[1].

Langmuir monolayers composed of phospholipids offer an interface that mimics the biological membrane and are an ideal system to study interactions at a model cellular membrane interface[15]. Studies commonly involve assessing the interaction of proteins with monolayers[16 17] to yield information on the role of protein-phospholipid interactions. The interactions of species considered potentially toxic are also a popular area of research, with nanoparticles being particularly prominent. Assessing nanoparticle penetration into a model membrane can give an idea of the potential toxicity of these particles to cells[18]. Most relevant to the work presented here are the effects of salt on the structure and phase transitions within the monolayer[19-

[21]. Before discussing the effect of salt, Langmuir monolayers will be explained in more detail.

1.1.2 Langmuir Monolayers

The most useful tool for studying a Langmuir monolayer is a film balance or, as it is more commonly known, a Langmuir trough (shown in figure 1.3). The lipid is dissolved in a solvent, which is immiscible with the sub-phase and is highly volatile (chloroform is often used). The chloroform – lipid solution is dropped onto the surface of the liquid and once all of the solvent has evaporated a monomolecular lipid film is left[22]. A moveable barrier allows for the manipulation of the film through compression and expansion. Compressing the film leads to a decrease in the monolayer area per molecule ($Å^2$ $molecule^{-1}$) and an increase in the surface pressure (mNm^{-1}). The monolayer surface pressure, π, is defined as the difference between the surface tension of the sub-phase without a lipid, γ_0, and the surface tension of the sub-phase with a spread lipid γ [23]:

$$\pi = \gamma_0 - \gamma \qquad \text{(equation 1.1)}$$

By measuring lateral film pressure (π) as a function of molecular area it is possible to obtain a surface pressure – area isotherm. More specific details of the set-up of the Langmuir trough can be found in chapter 2 of this thesis.

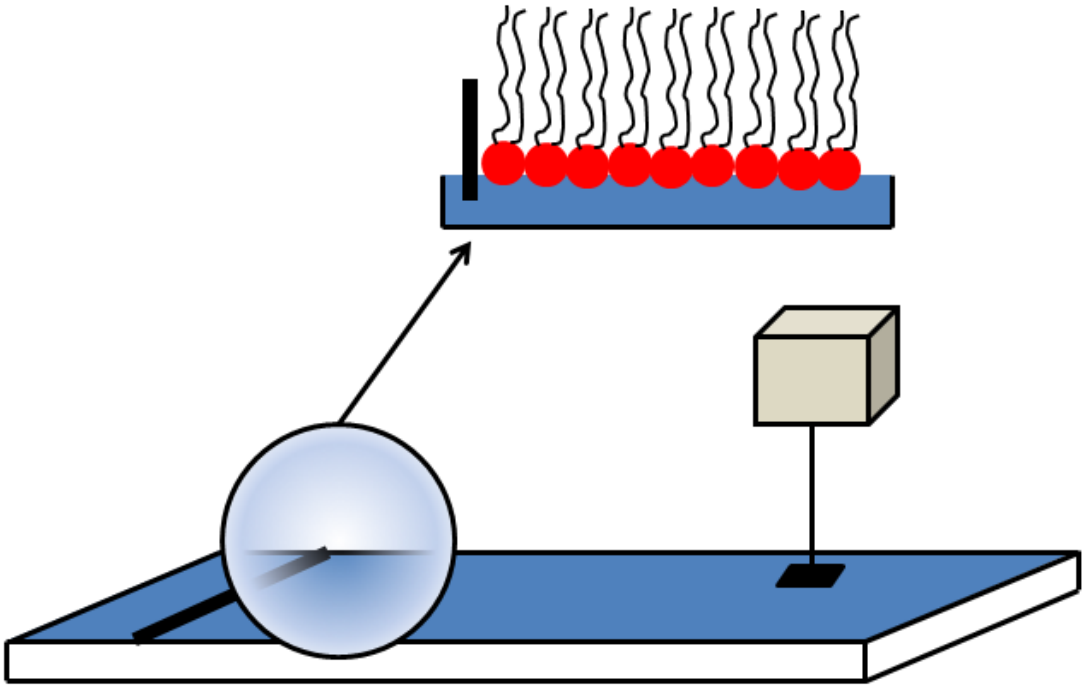

Fig 1.3- Set-up of a typical Langmuir trough experiment.

The result of a Langmuir trough experiment will yield a surface pressure-area isotherm, the shape of which, gives information on monolayer formation, phase transitions and stability. The phase transitions of a typical phospholipid monolayer are shown schematically in figure 1.4.

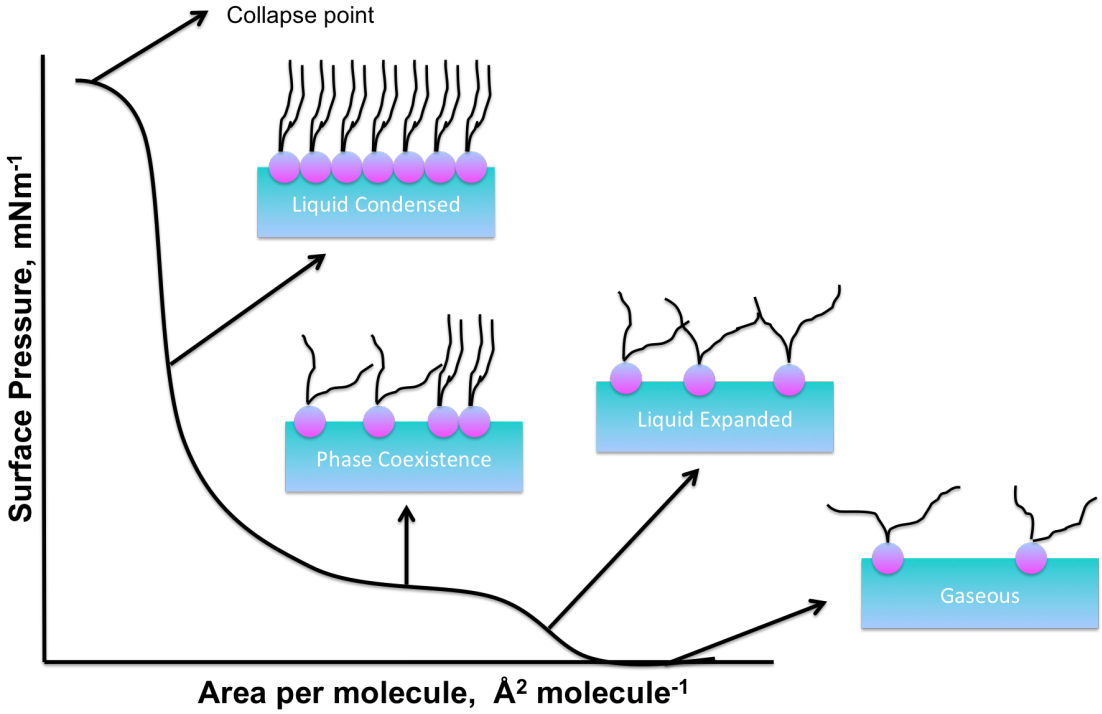

Fig 1.4- Schematic representation of phase transitions within a Langmuir monolayer.

Surface pressure-area isotherms are therefore a direct measurement of interacting components of the monolayer and the forces they exhibit on one another. As molecules approach each other these forces begin to change and a subsequent modification in the packing density of the monolayer is observed. The surface-pressure area isotherm is analogous to the 3-D pressure-volume isotherm of a gas[24].

The shape of the surface pressure-area isotherm will depend on the chemical composition of the amphiphile(s) of which the monolayer is composed. The evolving surface pressure is therefore a composite entity made up of several contributing factors:

$$\pi_{total} = \pi_{kinetic} + \pi_{dispersive} + \pi_{electrostatic} + \pi_{other} \qquad \text{(equation 1.2)}$$

Equation 1.2 shows some of the contributing interactions involved as the monolayer is compressed. The forces acting in a monolayer include kinetic

forces, dispersive Van der Waals interactions between the hydrocarbon chains, electrostatic repulsions between charged moieties on the head group and all other forces (steric, hydrogen bonding)[25].

At the start of a Langmuir trough experiment the monolayer is most commonly in the gaseous (G) phase. This phase is defined by negligible Van der Waals interactions between the hydrocarbon tail groups of the lipid, whilst electrostatic head group interactions are also insignificant[24]. Langmuir monolayers generally exhibit two liquid phases, the liquid expanded (LE) and the liquid condensed (LC) phase. Compressing the monolayer leads to the onset in the rise in surface pressure, or the LE phase. The rise in surface pressure can be attributed to increased Van der Waals interactions between hydrocarbon chains, however electrostatic interactions between the head groups remain negligible. The absence of a surface x-ray diffraction peak in this pressure regime is suggestive of translational and conformational disorder between the head and tail groups[10]. Further compression of the monolayer leads to the onset of the LC phase. Here there are significant Van der Waals interactions between the alkyl tails and they exhibit well-ordered structures, aligning themselves almost perpendicular to the interface[15 24 26].

Between the LE and the LC phase an abrupt kink in the isotherm is observed and a first order phase transition between the two phases occurs. This is known as the phase co-existence region (LE + LC). Here LC domains will begin to form in a sea of LE phase, eventually converging to form an entirely LC film. At surface pressures associated with this regime the LE and LC phases are in equilibrium with one another and a horizontal plateau in the isotherm ensues[27 28]. Throughout this phase change there is no net change in the Gibbs free energy, however there will be a change in the enthalpy and mean molecular area of the film[24]. The advent of fluorescence and Brewster angle microscopy allowed the direct visualisation of nucleating LC domains[29 30]. The shape of the LC domains will be largely dictated by the chemical structure of the lipids within the film. Figure 1.5 shows BAM images of a DPPC monolayer, along with its surface pressure-area isotherm. Table 1.0

defines important regions of the surface pressure-area isotherm. These definitions will be of particular relevance to parameters defined in chapter 3.

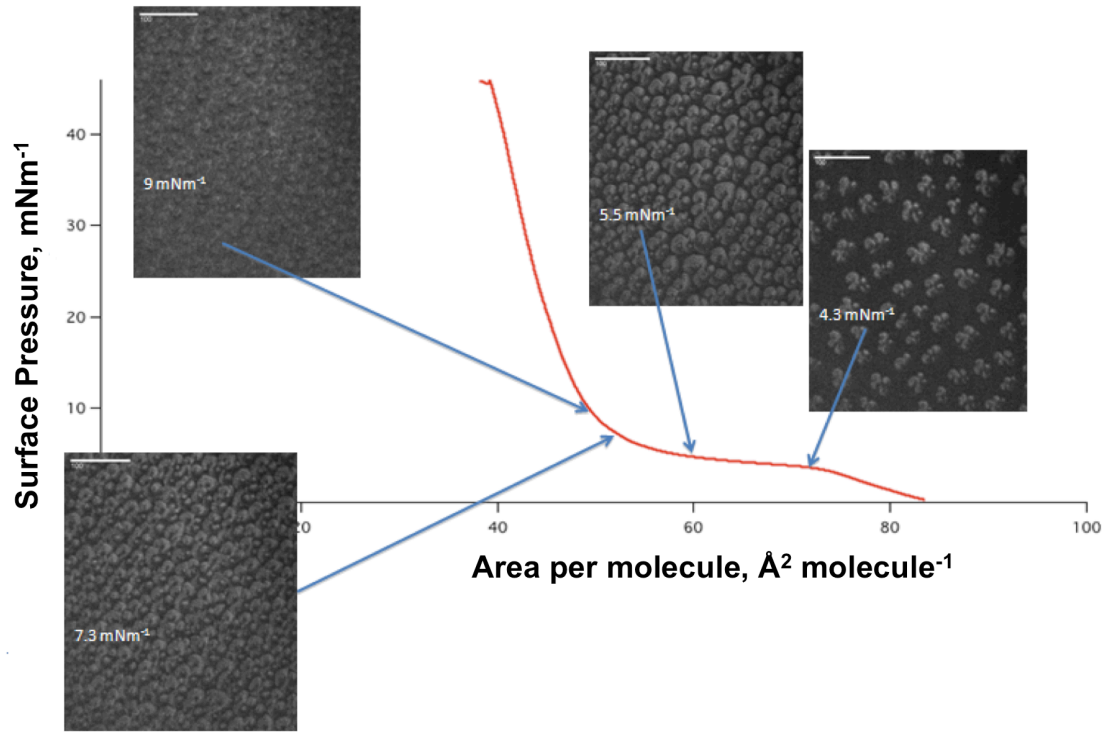

Fig 1.5- Surface pressure-area isotherm of DPPC along with corresponding BAM images. Scale bar is 100 μm.

At high surface pressures the film eventually reaches a limiting area, beyond which it can no longer be compressed. This is shown by a small drop and final plateau in surface pressure. Here the monolayer no longer maintains its two-dimensional structure and forms three-dimensional aggregates in the sub-phase such as lamellar and vesicular structures[31]. The mechanism of monolayer collapse still remains a point of debate, however it is generally agreed that the monolayer first buckles, and then folds to form a bilayer structure. This bilayer structure can then either form lamellar structures or detach as a vesicle[32].

Parameter	Definition	Units
Limiting area, A_{lim}	The minimum area at which a Langmuir monolayer can exist before the collapse point	$Å^2$ molecule^{-1}
Collapse point, π_c	The surface pressure at which the monolayer collapses	mNm^{-1}
Collapse point, A_c	The area at which the monolayer collapses	$Å^2$ molecule^{-1}
Onset of phase plateau, π_c	The surface pressure of the onset of the phase plateau	mNm^{-1}

Table 1.0- Parameters associated with the surface pressure-area isotherm of a Langmuir monolayer.

1.1.3 Interactions of phospholipid Langmuir monolayers with small ions

The effect of mono- and divalent cations upon the phase behaviour of phospholipids is important in many biophysical and biotechnological systems. Interactions between phospholipids and ions maintain the electrostatic potential across the cell membrane[33], mediate the interaction and complexation of proteins and allow for the effective two-dimensional crystallization and structural analysis of proteins[34]. Ions interact with charged phospholipids via Coulombic forces, interacting to a greater extent with negatively charged phospholipids. It has been demonstrated that cations exert a strong effect on zwitterionic phospholipids. Cations may bind to the phosphate moiety on the phospholipid head group inducing conformational order/disorder in the lipid head and tail groups[35 36].

The interaction of the phosphocholine head group and calcium ions has been probed with the use of vibrational sum frequency generation (VSFG)[36]. It has

been shown that in the presence of calcium the PO_2^- stretch is blue shifted, indicating an increase in electron density about the phosphate group. This strong interaction between cations and the phosphate group is surprising given that the cation must by-pass a positively charged ammonium group to reach the negatively charged phosphate region. Evidence of this kind raises the question as to what would happen if the charges on the head group were reversed? This is one of the key aims of this project and was the initial motivation for the sulfobetaine studies in this thesis.

Through use of surface pressure-area isotherms it has been demonstrated that sodium interacts with DPPC monolayers causing the LE and LE + LC phase to shift to higher surface pressures[37]. However the LC phase remains unaltered suggesting that sodium ions are squeezed out of the monolayer at higher surface pressures. In the same study the interaction of Ca^{2+} was also investigated. It was reported that at low surface pressures the surface pressure-area isotherm of DPPC was shifted to higher area per molecule values by 4 $Å^2$ $molecule^{-1}$, which corresponds to the cross-sectional area of a Ca^{2+} ion (calculated assuming an ionic radius for calcium of 1.14 Å[38]). However at higher surface pressures this increase in APM was reduced to 2 $Å^2$ $molecule^{-1}$. This result was explained by suggesting a 1:1 binding complex between Ca^{2+} and the lipid head group at low surface pressures, whilst at higher surface pressures, the ions are squeezed out of the monolayer, forming a 2:1 calcium/lipid complex[37]. Relationships of this kind have also been demonstrated for potassium ions[39]. This phenomenon is also well supported by molecular dynamics studies[40]. The mechanism of interaction is shown schematically in figure 1.6. Also shown in this diagram are the surface pressure-area isotherms for the DPPC monolayer on water, NaCl and $CaCl_2$ sub-phases. This was re-printed with permission from reference [37].

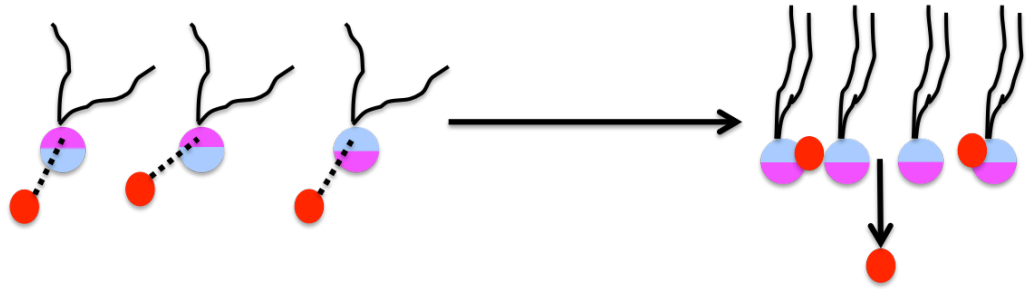

Gaseous phase

Liquid condensed phase

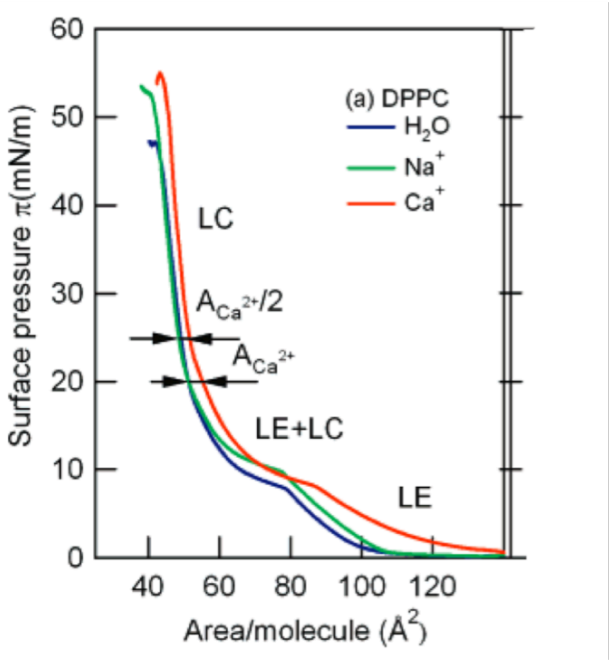

Fig 1.6- Postulated binding mechanism with lateral compression for Ca^{2+} and a zwitterionic (phosphocholine) head group. Calcium ions are represented in red. This image was re-produced with permission from reference [37].

It has also been shown that the presence of calcium can modify the domain structure and formation of DPPC monolayers. The presence of calcium can stabilise the LC phase over the LE phase. Analysis of optical microscopy images has revealed that the percentage of lipid in the LC phase when calcium is in the sub-phase is greater when compared to pure water. This indicates that calcium induces domain formation[37]. This phenomenon has also been shown for other ions including magnesium and zinc. Kewalramani

et al showed that these divalent cations lowered the surface pressure for the onset of the LE to LC phase transition for a PC type phospholipid, again supporting the notion that the presence of these species stabilises the LC phase over the LE phase[21]. In the same study it was also shown that the magnitude of the reduction in surface pressure at which the phase transition occurs was specific and followed the strength of binding constant between metal ions and simple phosphates. This is shown in figure 1.7. The data in this figure was re-printed with permission from reference [21].

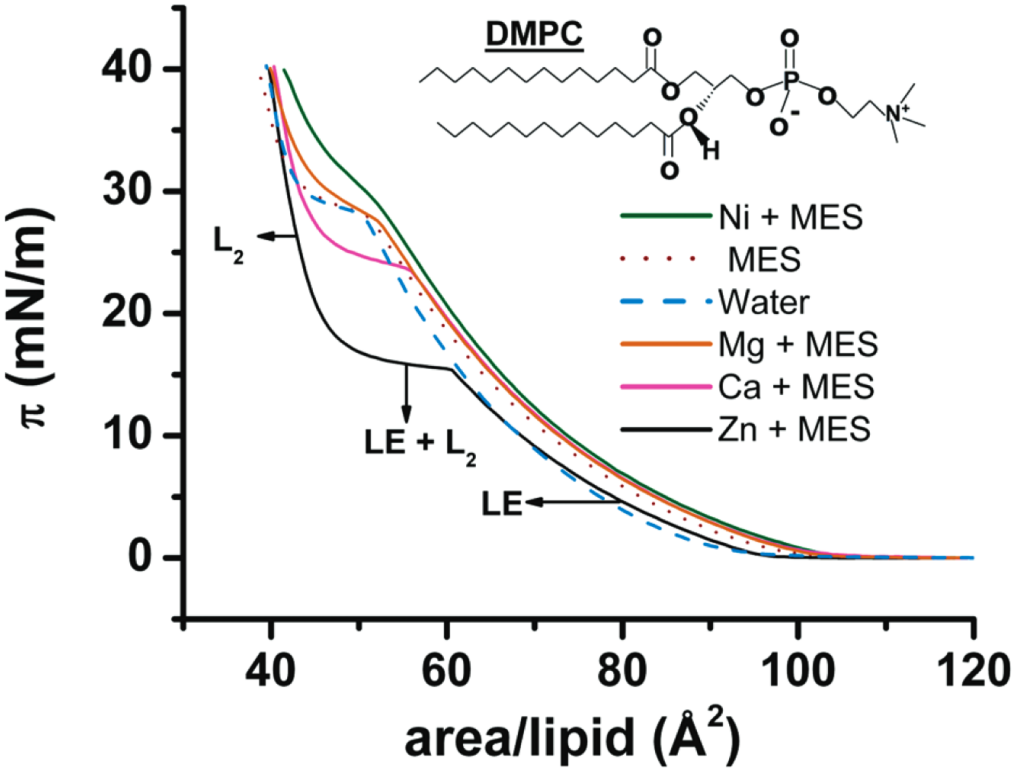

Figure 1.7- Surface pressure-area isotherm measurements for a DMPC monolayer on water and various other ion salt sub-phases (MES= 2-(N-morpholino)ethanesulfonic acid). This image was re-produced with permission from reference [21].

Grazing incidence diffraction data taken from the same monolayer on pure water and salt sub-phases indicated that although these ions had specific effects on the stability of the LC phase, there was no effect on the lipid tail packing density. The tails maintained identical conformational alignment in

the presence and absence of cationic species. X-ray reflectometry studies also exhibited no large difference between the head group electron density for all of the ions aside from Zn^{2+}. For Zn^{2+} it was possible to model an increase in electron density around the head group of the phospholipid. This implies that the interaction of some ions with the phospholipid head group is unique[21].

1.1.4 Sulfobetaine surfactants

The generic structure of a sulfobetaine surfactant is shown in figure 1.8. The head group consists of an outer (negatively charged) sulfonate group and an inner (positively charged) ammonium ion. The charge distribution at the interface is therefore reversed when compared to phospholipids (c.f. Figure 1.2).

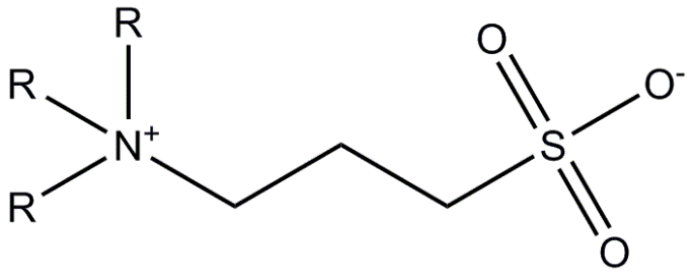

Figure 1.8- Generic sulfobetaine structure

The two charged moieties of the surfactant head can be joined by either a propyl or butyl “linker”. The positively charged ammonium region of the headgroup can be easily functionalised with long hydrophobic alkyl tails and so making them surface active.

Sulfobetaines are synthesised by a nucleophilic substitution reaction between a cyclic propane sultone compound and the appropriate alkyl amine[41]. The number of carbons within the alkane sultone will dictate the “linker” region between the ionic headgroup, whilst the level of amine functionalization will dictate the tail region of the surfactant[41]. A reaction scheme for the synthesis of single and double tailed sulfobetaines is shown in figure 1.9 with an inset showing a generalised reaction mechanism.

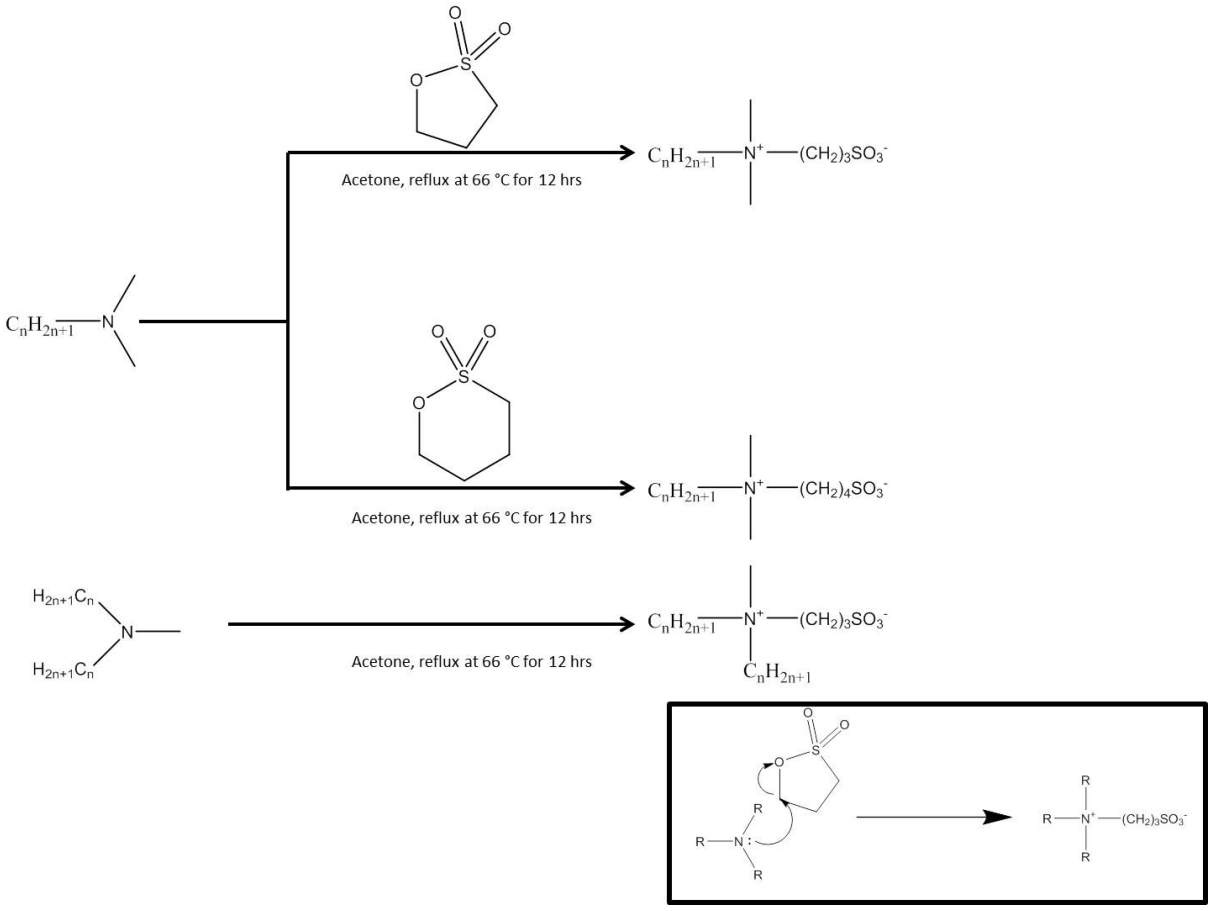

Fig. 1.9- Reaction scheme for the synthesis of a single tailed and double tailed sulfobetaine surfactant and a generic reaction mechanism for their formation (black box). Note that the R groups on the attacking amine do not have to be equivalent. The level of amine functionalization will dictate the structure of the surfactant tail group.

Sulfobetaine surfactants are widely used industrially where they function as a foam-stabilizing agent in shampoo and conditioners[42]. One of the key advantages of these surfactants is the fact that the zwitterion imparts a low toxicity on the molecule. Hence they are often used in mild formulations such as baby shampoo[41]. This class of compounds is also gaining increasing attention for their biocompatibility [43-46] as well as systems for controlled drug release [47].

Owing to their increased biocompatibility sulfobetaine functionalized polymers have been shown to act as promising coatings on medical implants, showing a high resistance to non-specific protein attachment[48-50].

The packing density of the chains was shown to play a large role in the attachment of non-specifically bound protein[48]. It has also been shown that sulfobetaines can act as coatings upon nanoparticles for temperature controlled drug release[47].

Despite a large number of potential applications of sulfobetaine surfactants in both the commercial and medical setting, their fundamental physiochemical properties are yet to have been investigated in any great detail. In particular their properties at the air-water interface have received far less attention than their phospholipid counterparts. It is vital that the behavior of sulfobetaine surfactants at the interface is understood, in order to utilize them to their full potential. This is important for their use in a commercial setting where they will be used as an interface between water and oil-droplets in detergent formulations. Salt is also regularly added to some industrial cosmetic and/or cleaning products to modify the properties of the formulation. However the effect of salt on the packing parameters and/or head group of these surfactants is unknown. Perhaps more importantly it has been shown that protein interaction with insoluble monolayers is heavily mediated by the presence of small ions, such as sodium and calcium[51-57]. If the potentially biocompatible nature of these surfactants is to be capitalized upon then it is vital that we understand how their behavior is affected in the presence of salt.

To the author's knowledge no Langmuir monolayer studies of sulfobetaine surfactants exist and the literature on the interaction of salt with sulfobetaine surfactants is limited. Most of the work completed to this effect has concentrated on organic reactions within sulfobetaine micelles, where it is generally accepted that anions preferentially bind to the micellar interface and are therefore likely to exert the largest effect on the micelle properties[58-60].

1.2 Characterising protein interactions with phospholipid monolayers

There is an increasing interest to attempt to align proteins at interfaces on layers that resemble the physiological matrix. Aligning proteins at interfaces will provide novel ways to study protein and receptor structure and function[61]. The second part of this thesis is concerned with forming ordered arrays of proteins at the phospholipid interface. The key aim of this section was to deliver protein to a phospholipid monolayer by use of a specific interaction mechanism. This will ultimately facilitate novel ways to study protein structure through use of reflectometry, grazing incidence diffraction (GID) and grazing incidence small angle scattering (GISAS) experiments. Before any discussion regarding protein interactions at phospholipid interfaces, the various types of phospholipid monolayers will be introduced.

1.2.1 Phospholipid adsorption at the solid-liquid interface

Langmuir monolayers are by far the most commonly studied kind of phospholipid interface; these have been described in detail in section 1.1.2.

Like all surfactants phospholipids are capable of adsorbing at the solid-liquid interface. There are a number of methods for immobilizing phospholipid monolayers and bilayers upon a solid support. One method uses hydrophobic self-assembled monolayers (SAMs), upon which monolayers are adsorbed. SAMs are formed by the chemisorption of the head groups of long chain, functionalised alkanes onto a solid substrate by liquid or vapor deposition[62 63]. The formation of SAMs usually takes place over several hours. Molecules are attracted to the surface as they lower the surface free energy of the interface and have a strong chemical interaction with the substrate[64]. At low molecular coverage they will begin to form disordered two-dimensional structures at the interface. As molecular coverage begins to increase head groups start to organize on the substrate surface and the tail groups organize perpendicular to the interface. The monolayer will pack

tightly as, once chemisorption has occurred, organization is largely driven by Van der Waals interactions and the associated reduction in free energy this promotes[64] [65]. This densely packed interface can provide an ideal hydrophobic support onto which phospholipids can adsorb. Two common examples are silanes on silcon[66-68] and thiols on gold[69] [70]. These hydrophobic layers are shown in figure 1.10.

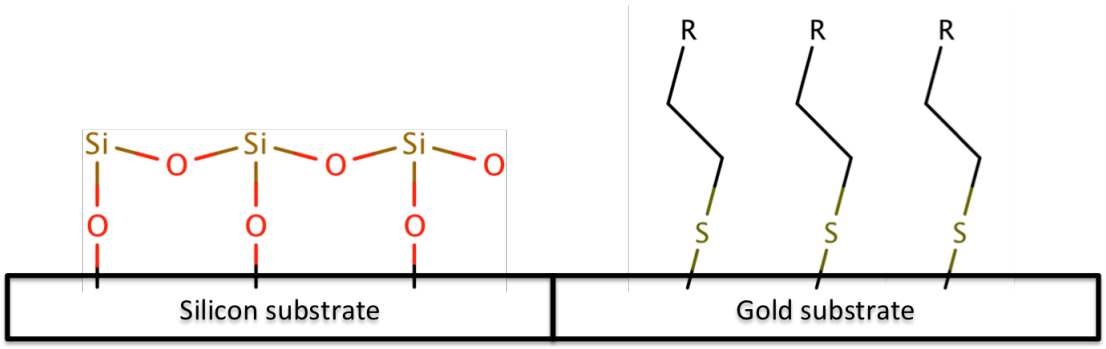

Fig. 1.10- Silane on silicon (left) and thiol on gold (right) self assembled monolayers.

Phospholipids may then be deposited upon these hydrophobic supports using two kinds of techniques. The first involves forming vesicles of the relevant phospholipid solution and injecting these upon the hydrophobic interface. Vesicles adsorb to the interface intact, where upon they rupture. Once they begin to unravel the alkyl tails of the phospholipids interact with the densely packed hydrophobic support, leaving the hydrophilic headgroups of the lipid facing solution. Their recruitment to the interface and interaction is driven by Van der Waals interactions with the underlying hydrophobic substrate and follows simple first order kinetics[71] [72]. Another way of adsorbing a lipid monolayer onto a hydrophobic support is to use the Langmuir-Blodgett technique. This method involves dipping a hydrophobic functionalized substrate through a lipid monolayer at the air-water interface in order to adsorb the interacting monolayer, and can also be used to generate multi-layers of lipids on the surface[73]. The Van der Waals interactions between lipid acyl chains and the hydrophobic layer also drive this process[73].

For comparison both of these methods are shown schematically in figure 1.11.

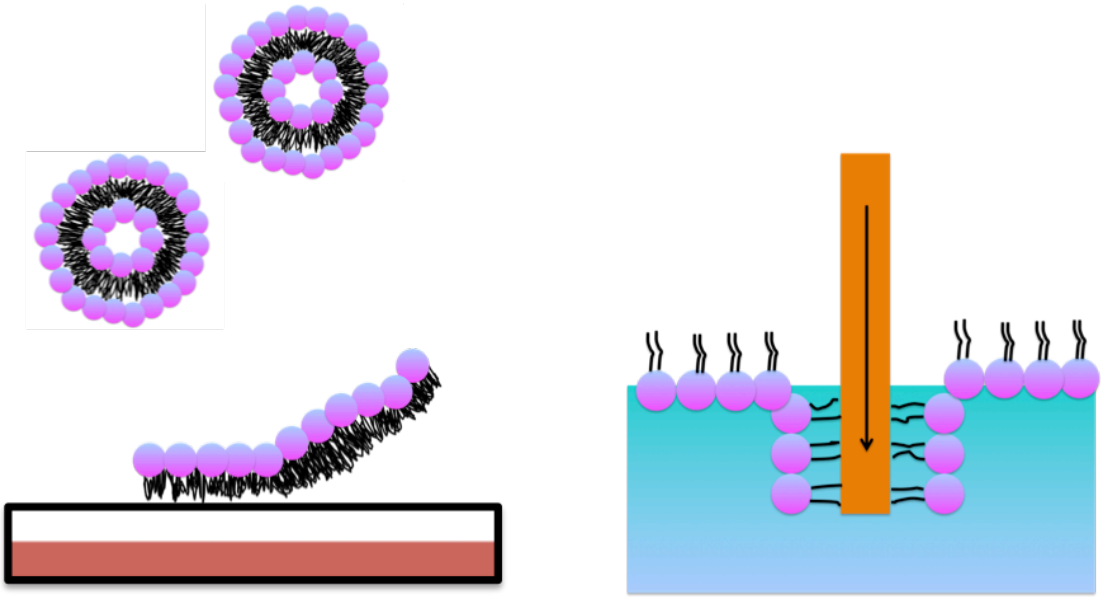

Fig. 1.11- Schematic comparison between vesicle deposition (left) and Langmuir-Blodgett (right) monolayer deposition on hydrophobic SAMs.

1.2.2 Ordered protein layers upon phospholipids at air-liquid interfaces

In 1971 it was shown by Fromherz *et al* that it was possible to obtain an ordered array of protein underneath a lipid monolayer at the air-water interface[74]. Since then many other studies have been completed demonstrating the possibility to order proteins in two dimensions at the air-water interface [75-77]. Probing protein interactions upon a lipid monolayer has many advantages including being able to work with very dilute protein solutions. These proteins can have a high lateral mobility upon the monolayer and can easily order themselves into a two dimensional array[78]. Upon protein attachment to the monolayer the surface structure of the protein at the interface can be probed by electron microscopy[79], X-ray reflectivity/grazing incidence x-ray diffraction[80-83] and Brewster angle microscopy[84]. Generally speaking adsorption of the protein to the monolayer is the first step, limiting the protein to a specific orientation with respect to the lipid plane. The protein is then able to laterally diffuse about this lipid plane,

benefitting from protein-protein interactions at the interface, promoting lateral organization of the protein monolayer. The hydrophilic head group of the lipid acts as the recognition element for the protein. The mechanism of interaction may be through electrostatic interactions or by functionalizing the lipid monolayer with a specific protein interaction element. The physical state of the monolayer is very important and must be as fluid-like as possible to facilitate the lateral mobility of proteins in the plane of the lipid. Lipid monolayers in the liquid expanded state are therefore often used for these kinds of experiments[85]. This is in order to promote the diffusion of the protein-lipid complex, whether specifically or non-specifically adsorbed, maximizing protein-protein interactions[34].

The vast majority of studies conducted involve the use of soluble proteins. Two approaches for the recruitment of the protein to the monolayer are through electrostatic interactions and the use of a specific chelating lipid. These approaches will be covered in the following sections.

1.2.3 Protein interactions mediated by electrostatics at air-liquid interfaces

Lipids that contain a positively or negatively charged head group create a charged surface that can interact with a charged protein. The charge of a protein is dependent on pH. At acidic pH values some amino acids (lysine, arginine and histidine) are protonated and can cause a protein to become cationic, whilst at basic pH values, amino acids such as aspartic and glutamic acid can give a protein a negative charge. The percentage of charged amino acids within the protein can be described by its isoelectric point (pI). If the pH of the surrounding solvent is at the pI of the protein, then the charge of the protein is zero[33]. The overall charge of both the protein and the lipid monolayer can be changed by altering the pH of the sub-phase. Furthermore the extent of the electrostatic interaction between a protein and a charged lipid monolayer can be dampened through charge screening by increasing the ionic strength of the sub-phase[85].

Darst *et al* were able to form ordered arrays of RNA polymerase II from *Escherichia coli* upon a positively charged lipid monolayer [86]. Here the binding of the protein was mediated through electrostatic interactions between the positively charged head group of the lipid and the net negatively charged protein. Two-dimensional periodic arrays of 50S ribosomal sub-units from *Bacilus stearothermorphilus* were also obtained with a similar approach. Monolayers composed of a mixture of the phospholipids DOPS and DOPC were used. DOPS is a negatively charged lipid and was used as the medium of interaction between the net positively charged protein and the lipid head group. The zwitterionic lipid, DOPC, was used to confer fluid properties upon the monolayer, ensuring that the bound protein was able to laterally diffuse about the interface[87]. By modifying the charge of the lipid monolayer it is also possible to heavily mediate the mechanism of protein interaction. Subjecting the protein chaperonin TF55 to a neutral lipid layer yields small para-crystalline regions of protein, which form filaments that group together. However, changing the lipid monolayer to a negatively charged interface results in the protein forming ordered sheets instead. The higher order of these 2 μm thick sheets was confirmed by optical diffraction [88].

Electrostatic interactions are, however, a non-specific form of protein-lipid interaction. Furthermore the non-specific nature of these interactions means that the probability of the protein interacting in a “pre-oriented” manner is limited [85].

1.2.4 Protein adsorption mediated by specific interactions at the air-liquid interface

It is possible to promote the specific interaction of protein and lipid by functionalizing the monolayer with a specific recognition element that will bind the protein of interest. This is most commonly achieved by introducing a functional derivative into the hydrophilic head group of the lipid with a ligand that has a specific interaction with a protein. These interactions may proceed through the use of a small molecule such as ATP or biotin[89]. Functionalizing

the lipid head group with metal complexes containing Ni^{2+} or Cu^{2+} also enables binding of histidine residues, which are commonly found on proteins especially through “His-tags”[90]. A His-tag is a common method used in biology and biochemistry to purify proteins expressed by genetically engineered organisms. They consist of six histidine residues attached to the N- or C- terminus of the protein. Thus such tags are conveniently present on most genetically engineered proteins and can be used to create a specific interaction within a purification column or a lipid monolayer. Some of these systems have been studied using BAM or fluorescence microscopy to study 2D crystallization at the air-liquid interface. Some key examples of these approaches are described below.

In 1989 Blankenburg *et al* showed that it was possible to crystallize streptavidin upon biotinylated lipid monolayers[89]. Streptavidin is a tetrameric protein with four binding sites for the small molecule biotin. When a biotinylated PC type phospholipid was spread over a sub-phase containing streptavidin, large protein domains were obtained with thickness values of 200 μm.

Another attractive system for the specific interaction of proteins with a monolayer is the nickel-chelating lipid, DOGS-NTA-Ni. This lipid, displayed with DPPC for comparison, is shown in figure 1.12.

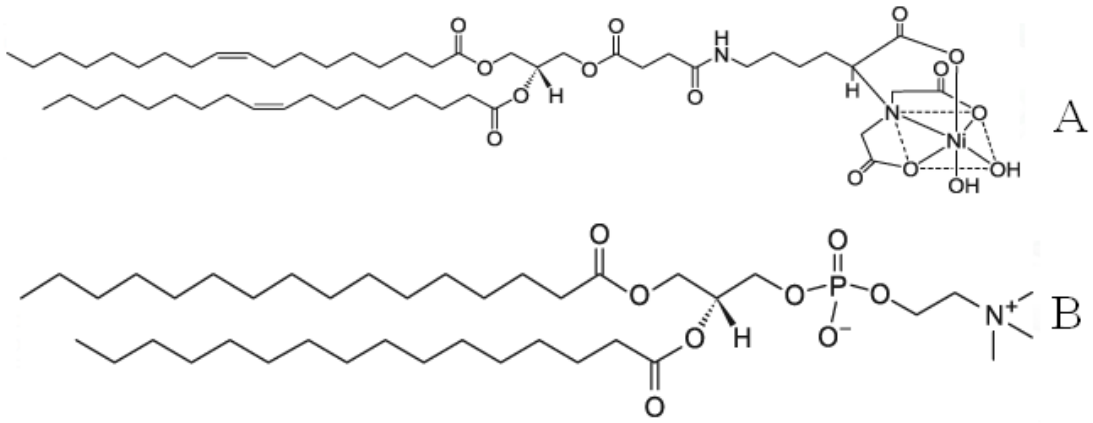

Fig. 1.12- A- 1,2-dioleoyl-*sn*-glycero-3-[(N-(5-amino-1-carboxypentyl)iminodiacetic acid) succinyl] (DOGS-NTA-Ni). B- DPPC.

Nickel chelating lipids have been used to order proteins with a genetically modified hexahistidine tag (His-tag). The nickel chelating nitriloacetic acid group (NTA) is linked to a lipid molecule that facilitates the coordination of histidine residues on the protein. Two of these histidine residues insert into the nickel coordination sphere of the NTA group and replace two water molecules. Figure 1.13 shows the interaction between two histidine residues and the nickel-chelating group.

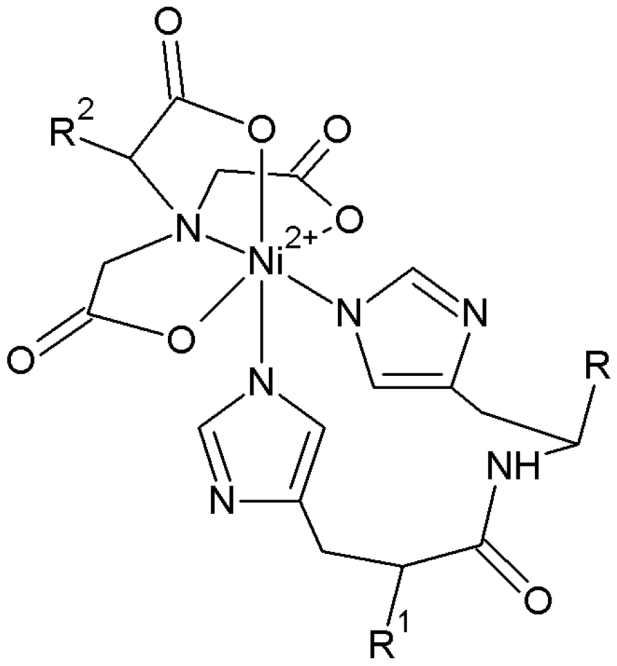

Fig 1.13- Specific interaction between two histidine residues on a protein and the nickel containing head group DOGS-NTA-Ni.

Bischler *et al* were the first to show that it was possible to order proteins upon nickel chelating lipid monolayers[90]. The group used a nickel chelating lipid spread at the air-water interface to successfully yield arrays of yeast RNA polymerase I in two-dimensions. Yeast polymerase I was His tagged on one of it's sub-units and when this His tag was altered, by attaching it to a different sub-unit, variations in protein orientation were observed.

Courty *et al* designed new amphiphilic species containing the nickel chelating head group NTA. The difference between the three synthesized lipids was the hydrophobic chain characteristics. By changing the length and

characteristics of the chains the group hoped to modify the fluidic properties of the resulting monolayers. From this they aimed to show the effect of fluidity of the monolayer upon the interaction of proteins at the air-water interface[84]. The three synthesized lipids were the previously described DOGS-NTA-Ni, Ni-NTA-BB and Ni-NTA-BF. These lipids are shown in figure 1.14. The group used several techniques to characterize the behavior of the subsequent monolayers and the attachment of His tagged HupR (His-HupR). These techniques included Langmuir trough measurements, Brewster angle microscopy and x-ray reflectivity.

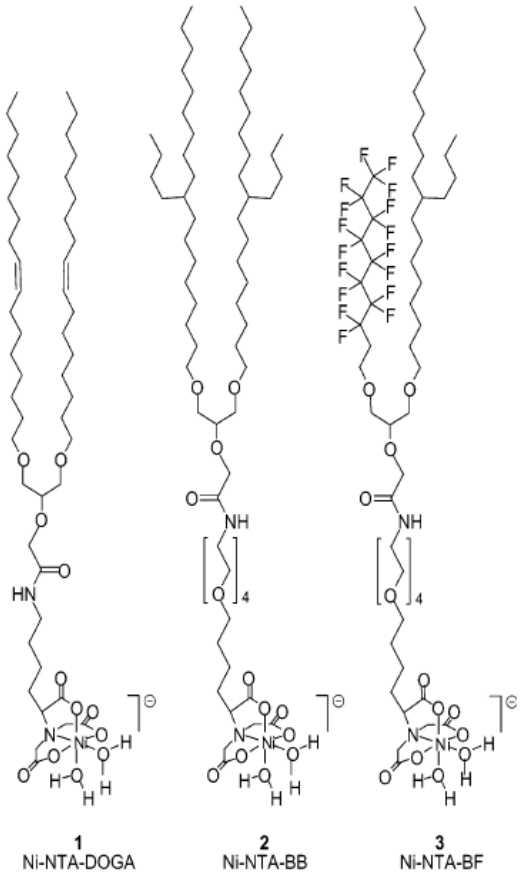

Fig. 1.14- Diagrams representing the three nickel chelating lipids used in the study by Courty *et* al (image re-produced with permission from[84]). 1= 2-(bis-carboxymethyl-amino)-6-[2-(1,3-di-*O*-oleyl-glyceroxy)-acetyl-amino]hexanoic acid nickel (II) (Ni-NTA-DOGA). 2= Ni-NTA-BB, with two alkyl chains. 3= Ni-NTA-BF, with two alkyl chains, one branched and one fluorinated. This image was re-produced with permission from reference[84].

Unsaturated nickel chelating lipids (DOGS-NTA-Ni) adopt a slightly bent conformation and this prevents the lipid alkyl chains from packing tightly within the monolayer, giving a more fluid like monolayer[91]. Ni-NTA-BB was made more fluid like by the addition of branching that will hinder liquid crystalline packing within the monolayer, whilst the addition of a fluorinated chain to Ni-NTA-BF was deigned to have a similar effect. Characterisation of these monolayers using the Langmuir trough showed that none of them had a phase plateau and all remained in the LE phase throughout lateral compression. It was shown that the rate of protein interaction was highest for DOGS-NTA-Ni, followed closely by Ni-NTA-BB. Limited protein interaction was observed for Ni-NTA-BF. The two lipids without any fluorinated chains are able to bind protein and laterally diffuse as a protein-lipid complex about the monolayer. This promoted protein-protein interaction and allows the protein layer to organize itself relative to the lipid interface, anneal and reach equilibrium with the bulk phase. The fluorinated lipid suffers from large steric repulsion between fluorine groups on one of its chains. It is therefore not able to efficiently laterally diffuse about the interface, which hampers protein adsorption and subsequent monolayer organization.

Figure 1.15 shows some examples of the kinds of ordered arrays of protein upon lipid monolayers at the air-liquid interface. The images were reproduced with permission from[84 89 90].

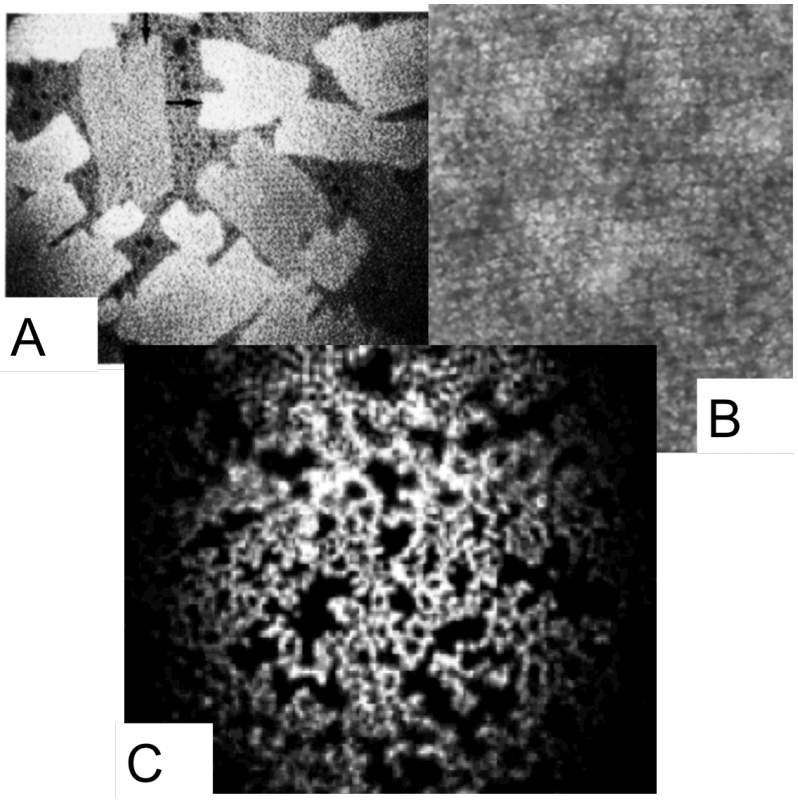

Fig 1.15- An array of ordered protein molecules upon lipid monolayers. A) Fluorescence micrograph of streptavidin[89]. B) Electron micrograph of yeast RNA polymerase I[90]. C) BAM image of HuPr[84]. These images were re-produced with permission from references [84, 89 and 90].

1.3 Studying insoluble membrane proteins

Membrane proteins represent a class of proteins within the cell membrane of the cell. The proteins are surrounded by the hydrophobic acyl tail environment of the phospholipid bilayer and are largely insoluble in water[33]. Their structure is therefore heavily dependent on their surrounding environment made up of primarily phospholipids[1]. This is in contrast to soluble proteins where their structure is, in part, dictated by amino acid residue interactions with the surrounding solvent. Membrane proteins make up a considerable percentage of the proteome (around 30 %) and account for around 70 % of therapeutic targets[92]. It is therefore of vital importance to understand the function, structure, protein-lipid and protein-protein

interactions of this important class of proteins in order to aid development of novel drug targets.

When compared to soluble proteins those found in the membrane are present in lower concentrations and their extraction involves disruption of the cell membrane. Therefore isolating these species in sufficient quantities poses a challenge. It is more common to express membrane proteins genetically, however their insoluble nature means that formation of protein aggregates is likely[93]. Given that common methods to study membrane proteins are diffraction, NMR and small angle scattering techniques they must be extracted and re-constituted into suitable environments for studies. This causes protein instability and/or structural changes compared to their native environment[94].

Given that protein solubility is vital for passing a solution of protein over the interface being studied, this presents an interesting challenge. In the past attempts have been made to solubilise membrane proteins through the use of detergents[94-96]. However this raises the question as to the effect of the detergent on the structure of the membrane protein, and whether or not this best represents the native structure and/or environment of the protein being studied[97]. Liposomes composed of naturally occurring phospholipids have been used to study membrane protein structure[98 99]. However, once again, the phospholipids surrounding the membrane protein are commonly made up of one or two types of lipid and similar questions arise as to the effect of these lipids on the membrane protein structure. Liposomes also suffer from a difficulty in preparation, in particular gaining monodisperse structures[100]. Furthermore studies have been reported where the replacement of lipids surrounding the membrane protein have lead to the deactivation of the proteins themselves[97]. One promising system to study the membrane protein in its native environment is the phospholipid bilayer nanodisc. These will be introduced in the following section.

1.3.1 Phospholipid Bilayer Nanodiscs

Nanodiscs may act as model membrane segments in which membrane proteins can be encapsulated. They therefore tackle issues associated with other membrane protein supports as the environment surrounding the protein can be precisely controlled. Furthermore membrane proteins can be isolated in a monomeric or oligomeric state, giving control on the number of encapsulated proteins in one nanodisc[101] [102]. Nanodiscs are therefore segments of phospholipid bilayer surrounded by a protein or polymer stabilising belt. The generic structure of a nanodisc is shown in figure 1.16.

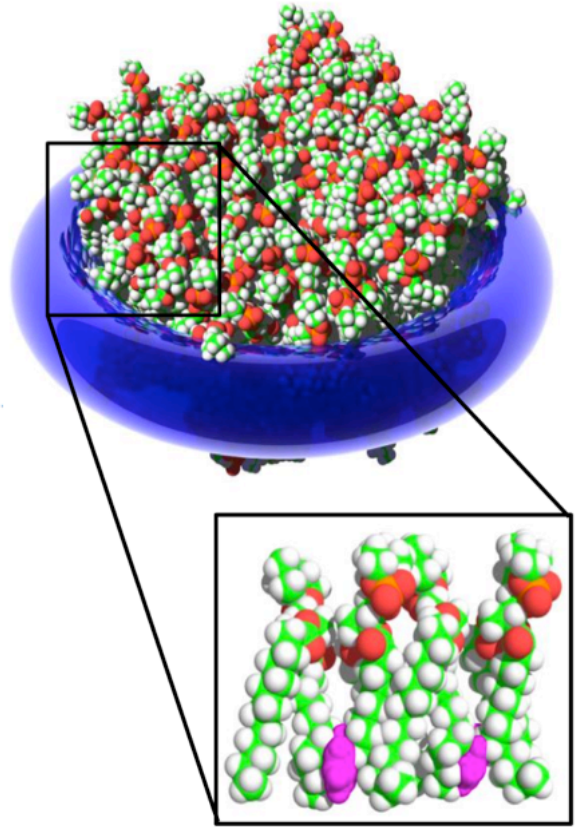

Fig 1.16- Space filling model to represent the generic structure of a nanodisc. The phospholipids are shown as space filled molecules, whilst the protein or polymer belt is shown in blue. This image has been reproduced with permission from reference[114].

Nanodiscs with an encapsulated protein were first reported in 1998 where it was shown that it was possible to incorporate cytochrome P450 reductase[103]. Nanodiscs of this kind are self-assembled disc like structures with a diameter of 8-16 nm. They are composed of a segment of phospholipid bilayer and are surrounded by a belt of membrane scaffold proteins (MSPs)[104]. By varying the length of the genetically engineered membrane scaffold protein it is possible to generate nanodiscs of differing size. However the nanodiscs within the selected size regime are all monodisperse. Their preparation involves a detergent extraction of the membrane protein from the cell membrane and subsequent reconstitution into a nanodisc by addition of phospholipids and MSPs. This is shown schematically in figure 1.17. The varying sized discs and proteins encapsulated within them have been rigorously structurally characterised[105-108].

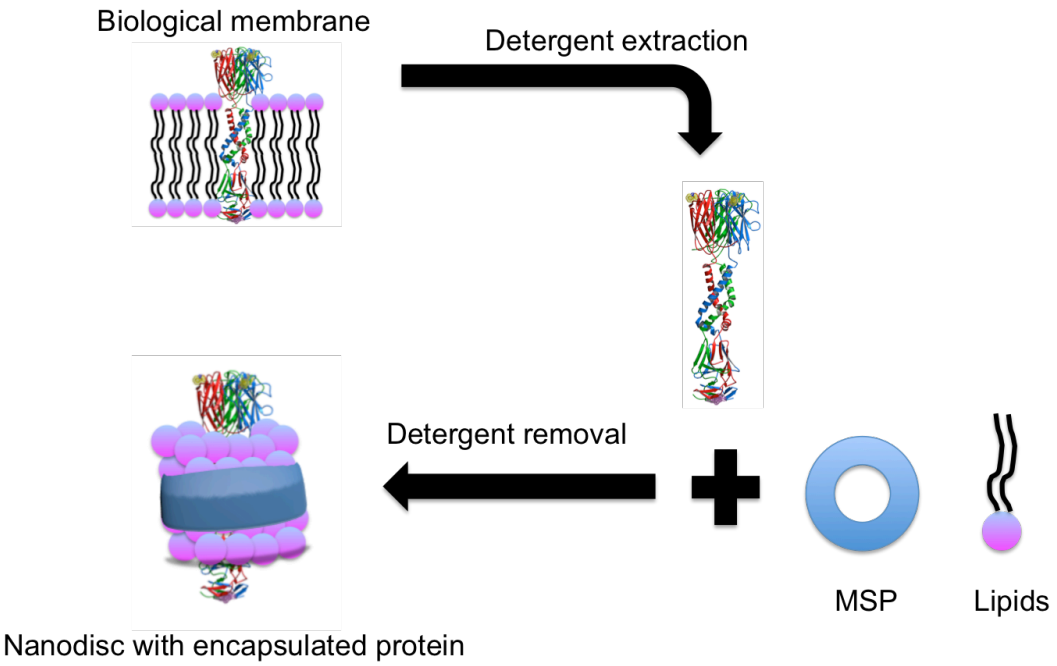

Fig 1.17- Schematic representation for the preparation and protein encapsulation for MSP stabilised nanodiscs.

Whilst membrane scaffold protein stabilised nanodiscs have been an extremely valuable tool in characterising membrane proteins, they do suffer from a few key drawbacks. The first step in their preparation involves the

purification and solubilisation of the membrane protein through use of a detergent. The detergent-protein complex is then added to the MSP/phospholipid mixture and the self-assembly process begins. Finally the detergent is removed via the use of dialysis. The unknown effect of detergent on protein structure and the fact that the protein may aggregate under dialysing conditions are key issues. Genetically engineering the MSP is also expensive and has been found to interfere with x-ray/neutron scattering signals, whilst also disrupting other characterisation techniques such as circular dichroism.

1.3.2 Styrene-maleic acid lipid particles

In 2001 Tonge *et al* showed that a styrene-maleic acid (SMA) co-polymer, when in the presence of phospholipids, was able to self-assemble into nanometre sized discs[109]. This was later patented as Lipodisq®. Daffron and Overduin developed this idea further by using the SMA co-polymer to stabilise discoidal phospholipid bilayer structures with an encapsulated protein. These structures were named styrene maleic acid lipid particles (SMALPs) and were shown to be thermostable systems that were capable of maintaining membrane protein functionality[110 111]. The major advantage of the SMA stabilised nanodiscs stems from the fact that the polymer spontaneously self-assembles into discoidal structures when in the presence of lipid membranes at basic pH values. This leads to the automatic encapsulation of the membrane protein directly from the cell membrane. This enables the process to be carried out in one step, negating the need to use detergent extraction and yielding the protein in its native membrane environment[111]. This offers advantages over the detergent extraction steps and non-native environment provided by the MSP stabilised nanodiscs. The structure of the SMA nanodiscs along with the method for protein encapsulation is shown schematically in figure 1.18.

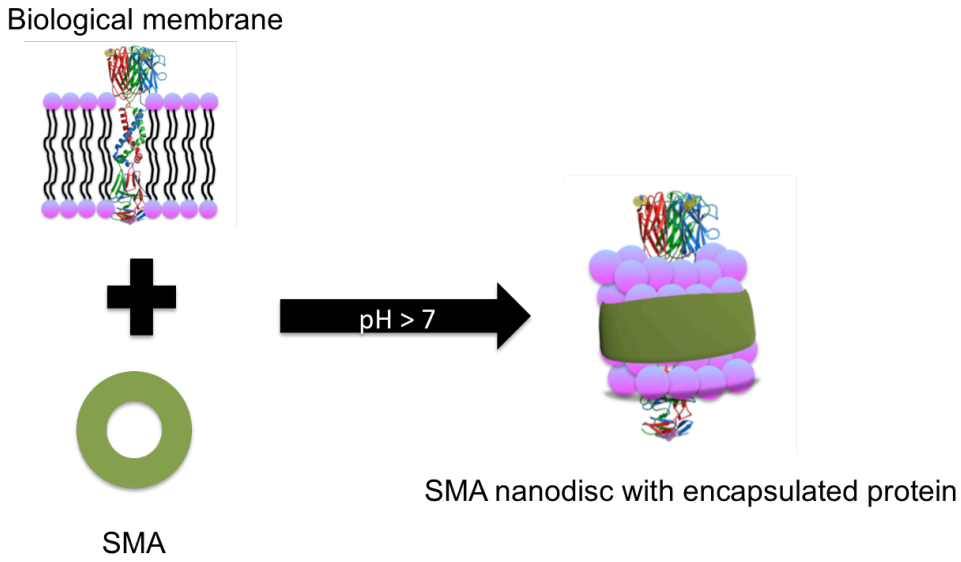

Fig 1.18- Schematic representation of SMA nanodisc preparation with encapsulated protein.

Furthermore recent experiments have shown that it is possible to encapsulate the membrane proteins PagP and bacteriorhodopsin[112 113] whilst gaining stable and monodisperse structures. Studies on encapsulation within the discs have shown the protein retains its integral structure. These systems also have the added advantage of not interfering with signals from scattering experiments, as the signal from the disc is reduced when compared to the signal from the protein[111].

1.3.3 Structural characteristics of nanodiscs

In order to understand the structure of the SMA nanodiscs SANS experiments have been conducted. Experiments were conducted on empty nanodiscs containing no membrane protein. In order to prove the dimensions of the nanodiscs varying solution contrasts (H_2O:D_2O) as well as deuterated lipids were used. This was also able to determine the position of the co-polymer and the lipids within the structure. The discs were modelled via a core shell cylinder model with a face layer on top and bottom, accounting for the presence of phospholipid head groups[114]. This model is shown schematically in figure 1.19, along with the structure of the co-polymer belt.

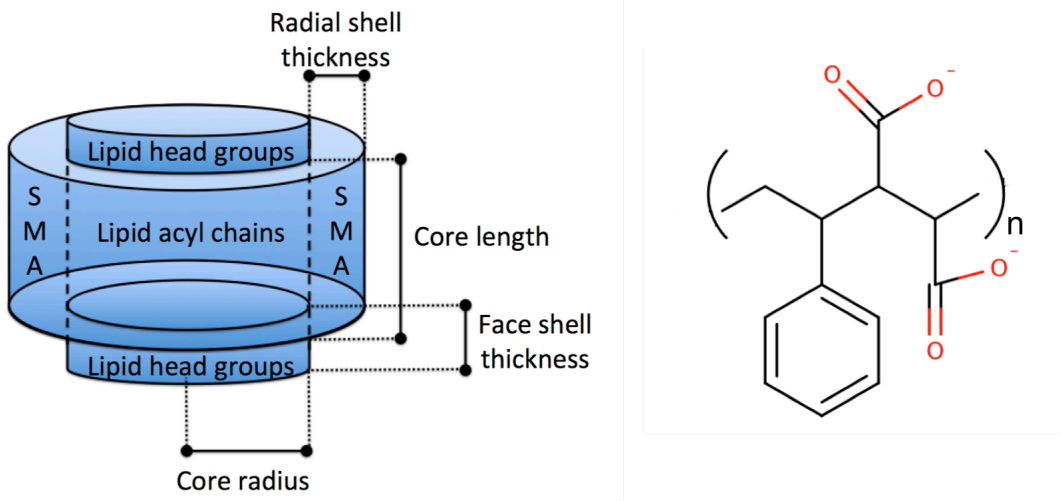

Fig 1.19- Model used for structural parameters of discs from SANS data (left) and structure of SMA co-polymer belt (right).

It was shown that the SMA polymer encapsulates a disc of lipid bilayer membrane with a radius of 38 Å. It was also shown that the discs were supported on the edges by a 7 Å thick layer of the co-polymer, indicating that a single polymer chain stabilises the nanodisc system. Polarized infrared spectroscopy and NMR was also used to give information on the orientation of chemical groups on the polymer chain with respect to the lipids. Results suggested that there was significant penetration of the styrene ring of the polymer chain into the acyl chain region of the bilayer.

1.4 Specific project aims

1.4.1 Aims of the sulfobetaine project

The specific aims of this section of the project have been to perform Langmuir isotherm studies on sulfobetaine surfactants to elucidate their behavior at the air-water interface. Sulfobetaine surfactants with varying chemical composition have been synthesized with the aim of linking differing chemical functionality to their surface pressure-area isotherms. One specific question this section of the project aims to answer is whether or not the reversal of head group charge distribution will significantly alter the

properties of the monolayer at the air-water interface, in particular, whether or not monolayer behavior will differ from that of phospholipids, which show significant interaction with cations, as discussed previously. Another question is whether or not the smaller sulfobetaine head group will alter the properties of the surfactant monolayer. The difference in size between the sulfobteaine head group and the phosphocholine head group is shown in figure 1.20 by a space-filling model.

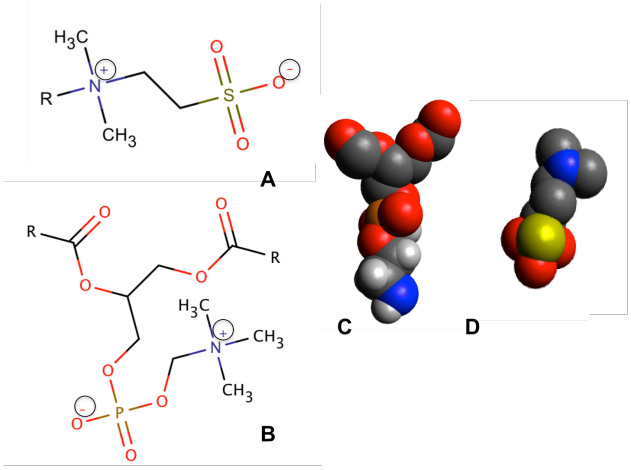

Fig 1.20- A) Sulfobetaine head group B) phosphocholine head group, C) space filling model of the phosphocholine head group and D) space filling model of the sulfobetaine head group.

To answer this question this project has combined Langmuir monolayer and Brewster angle microscopy studies (BAM) with x-ray/neutron reflectometry (XRR/NR) to obtain new structural information about sulfobetaine surfactants.

1.4.2 Aims of the protein alignment project

1.4.3 Designing a suitable system for investigation

Despite the large number of studies investigating the interaction of proteins and monolayers functionalised with DOGS-NTA-Ni at the air-water interface, to the authors knowledge, these systems are yet to have been probed at the solid-liquid interface. It was the aim of this section of the project to characterise the interaction of proteins and these monolayers using neutron reflectometry and quartz crystal microbalance studies. These techniques are described in detail in chapter two.

A rational design concept: Choice of protein and lipid interface

The chosen protein was penicillin binding protein 3. This protein was chosen as it belongs to a family of proteins with a well-defined behavior and its crystal structure has been elucidated previously[115]. The penicillin binding proteins (PBP's) are species that are involved in the end stages of cell wall synthesis in bacterium[116 117]. Antibiotics that belong to the β-lactam family are capable of binding to the active site of PBP3 and inhibiting the bacterium from forming a cell wall, leading to the death of bacterial cells[118]. A ribbon diagram of PBP3 is shown in figure 1.21.

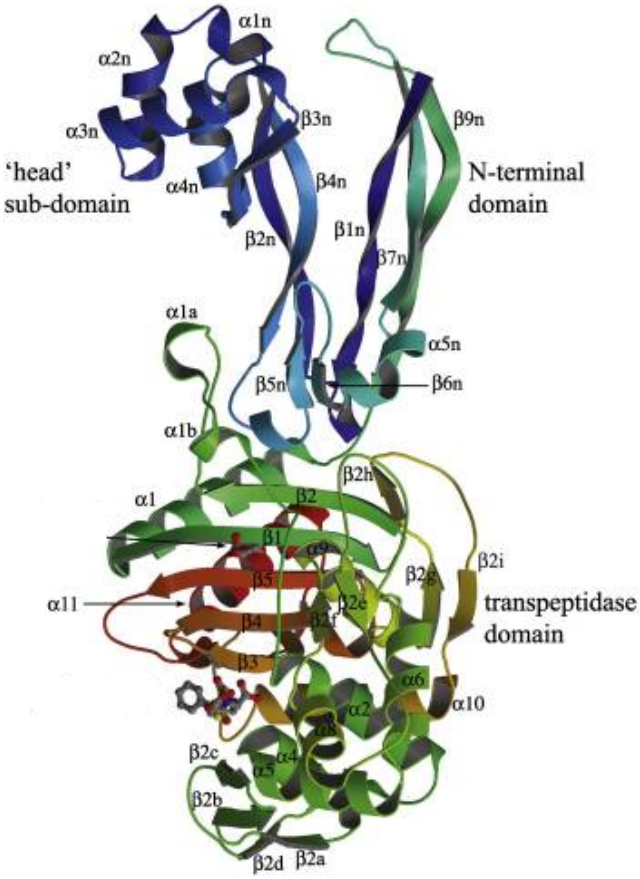

Fig. 1.21- Native structure of penicillin binding protein 3 shown in ribbon form. Image reproduced with permission from reference[115].

The lipids of choice for a suitable protein interface were the specific recognition element, DOGS-NTA-Ni, and the zwitterionic phospholipid, DOPC. DOGS-NTA-Ni was chosen, as it is able to bind the his-tag found on PBP3. DOPC was chosen as it is zwitterionic which will largely negate electrostatic interactions between the protein and the lipid monolayer. The lipid is also unsaturated conforming fluidic properties upon the formed monolayer, facilitating protein-lipid complex mobility at the interface.

Interactions were investigated at two interfaces. Initially the interaction between protein and lipid were assessed at the air-water interface. This was designed as a proof of concept experiment, allowing the conformation of protein binding before the system was assessed by neutron reflectometry. The system was then transferred to the solid-liquid interface and

characterised with reflectometry. More details of these experiments can be found in chapter 2 and chapter 4.

The final aim of these experiments was to see if it is possible to transfer the concepts of this system to form ordered arrays of insoluble membrane proteins at the solid-liquid interface.

1.4.4 Specific aims of the membrane protein alignment project

1.4.5 Nanodiscs at the interface

The final section of this thesis is concerned with the investigation of the interfacial properties of nanodiscs. This is in line with work discussed previously on forming ordered arrays of proteins at phospholipid interfaces in order to find novel ways of studying their structure. If we are able to deliver SMA nanodiscs to the interface then this will provide a novel way of delivering encapsulated membrane proteins to an interface and provide new ways to study them. This also has implications for drug delivery and biosensing.

The first aim of this section is to attempt to see if it is possible to deliver empty nanodiscs to the phospholipid interface. This will act as a proof of concept for the delivery of nanodiscs with encapsulated membrane proteins. Initially previous work completed on nanodiscs at interfaces will be discussed.

To the authors knowledge no studies involving SMA nanodiscs at interfaces have been reported. There are, however, interesting studies involving the behaviour of MSP-nanodiscs at interfaces. Wadsäter *et al* demonstrated that MSP-nanodiscs strongly adsorbed to insoluble surfactant layers at the air-water interface through the use of neutron reflectometry. By using a mixture of positively charged and negatively charged lipids within the nanodisc they formed discs with an overall net negative charge. When injected beneath a

cationic lipid monolayer the discs adsorbed to the surface forming a disc layer 40.9 Å in thickness, with coverage of 66 %. Interestingly the discs were located 15 Å beneath the lipid head groups, highlighting a long range electrostatic interaction between the head groups of the disc and the head groups of the insoluble monolayer[119]. The same group were also able to show that MSP-nanodiscs could be adsorbed at the solid-liquid interface. Here it was shown that DMPC nanodiscs formed a layer 39 Å thick on the surface of SiO_2. However, when modelled, the discs only required a 5 Å thick water layer to obtain the best fit. It was demonstrated that the best nanodisc coverage was obtained for discs where the constituent lipids were in the gel phase. These formed the most stable and irreversible nanodisc films. Once these discs had adsorbed it was possible to heat up the substrate, “melting” the membranes. This will form a more friendly and biomimetic environment for membrane proteins[120].

To conclude the protein alignment section of this thesis a schematic is provided in figure 1.22, along with explanation. This was designed to show the reader the development of the project and highlight specific aims.

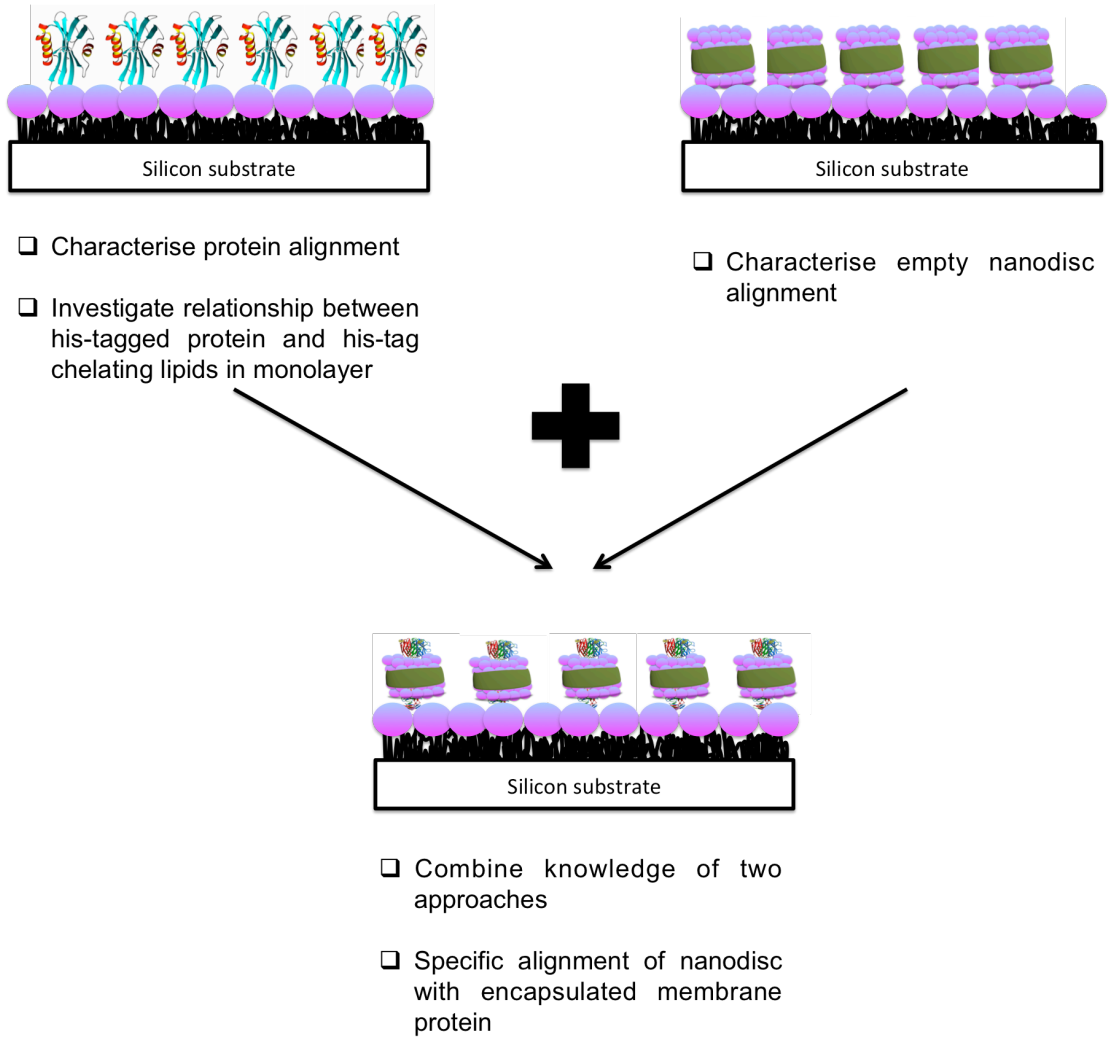

Fig 1.22- Schematic summary of specific aims of the protein section of this thesis.

This body of work will be split over two chapters of this thesis. The first protein chapter (chapter 4) will characterise soluble protein interactions (PBP3) with phospholipid monolayers containing the his-tag chelating lipid DOGS-NTA-Ni. In the final experimental chapter (chapter 5) the characterisation of empty nanodisc interaction with phospholipid monolayers is presented. Finally the interactions of membrane protein encapsulated nanodiscs with phospholipid monolayers is discussed. This is a composite section and will use the knowledge gained from the soluble protein studies and the empty nanodisc interfacial studies to specifically align a nanodisc containing a membrane protein at the phospholipid interface.

1.5 References

1. Lodish HB, D; Berk, A; Zipursky, S.L; Matsudaira, P; Darnell, J. *Molecular Cell Biology*: Scientific American Books, 1995.
2. Barnes GT, Gentle IR. *Interfacial Science: An Introduction*. New York: Oxford University Press, 2005.
3. Simister EA, Lee EM, Thomas RK, et al. Structure of a tetradecyltrimethylammonium Bromide layer at the air-water interface determined by neutron reflection. Journal of physical Chemistry 1992;**96**:1373-82.
4. Li PX, Thomas RK, Penfold J. Limitations in the use of surface tension and the gibbs equation to determine surface excess of cationic surfactants. Langmuir 2014;**30**:6739-47.
5. Li PX, Li ZX, Shen H, et al. Application of the gibbs equation to the adsorption of nonionic surfactants and polymers at the air-water interface: Comparison with surface excess determined directly using neutron reflectivity. Langmuir 2013;**29**:9324-34.
6. Alexander S, Smith GN, James C, et al. Low-surface energy surfactants with branched hydrocarbon architectures. Langmuir 2014;**30**(12):3412-21.
7. Tanford C. Hydrophobic free energy, micelle formation and the association of proteins with amphiphiles. Journal of Molecular Biology 1972;**67**(1):59-74.
8. Adamson AWG, A.P. *Physical Chemistry of Surfaces*. 6 ed: John Wiley & Sons, Inc., 1997.
9. Gomez-Serranillos IR, Minones J, Dynarowicz-Latka P, et al. Study of pi-A isotherms of miltefosine monolayers spread at the air/water interface. Physical Chemistry Chemical Physics 2004;**6**:1580-86.
10. Kaganer VMM, H; Dutta, P. Structure and phase transitions in Langmuir monolayers. Reviews of Modern Physics 1999;**71**(3):779-819.
11. Weidemann G, Volhardt D. Long-range tilt order in phospholipid monolayers: A comparitive study. Biophysical Journal 1996;**70**:2758-66.
12. Yaseen M, Lu JR, Webster JRP, et al. Adsorption of single chain Zwitterionic phosphocholine surfactants: Effects of length of alkyl chain and head group linker. Biophysical Chemistry 2005;**117**(3):263-73.
13. Stryer L. *Biochemistry*. 3 ed. New York: W.H.Freeman and Company, 1988.
14. Harrison RL, G.G. *Biological Membranes*. 2 ed: John Wiley & Sons inc., 1980.
15. Brezesinski G, Mohwald H. Langmuir monolayers to study interactions at model membrane surfaces. Advances in Colloid and Interface Science 2003;**100-102**:563-84.
16. Clifton LA, Green RJ, Hughes AV, et al. Interfacial structure of wild-type and mutant forms of puroindoline-b bound to DPPG monolayers. Journal of Physical Chemistry B 2008;**112**:15907-13.
17. Clifton LA, Sanders M, Kinane C, et al. The role of protein hydrophobicity in thionin-phospholipid interactions: a comparison of a1 and a2-purothionin adsorbed anionic phospholipid monolayers. Physical Chemistry Chemical Physics 2012;**14**:13569-79.

18. Vakurov A, Guillermo M, Drummond-Brydson R, et al. ZnO nanoparticle interactions with phospholipid monolayers. Journal of Colloid and Interface Science 2013;**404**(0):161-68.
19. Aroti A, Lenotidis E, Dubois M, et al. Monolayers, bilayers and micelles of zwitterionic lipids as model systems for the study of specific anion effects. Colloids and Surfaces A: Physiochemical Engineering Aspects 2007;**303**:144-58.
20. Aroti AL, E; Maltseva, E; Brezesinski, G. Effects of hofmeister anions on DPPC langmuir monolayers at the air-water interface. Journal of Physical Chemistry B 2004;**108**:15238-45.
21. Kewalramani K, Hlaing H, Ocko BM, et al. Effects of divalent cations on phase behaviour and structure of a zwitterionic phospholipid (DMPC) monolayer at the air-water interface. The Journal of Physical Chemistry Letters 2010;**1**:489-95.
22. Atkins PP, J. *Physical Chemistry*. 9 ed. Oxford: Oxford University Press, 2009.
23. Butt HJG, K; Kappl, M. *Physics and Chemistry of Interfaces*. 1 ed: Wiley-VCH, 2006.
24. Chattoraj DK, Birdi KS. *Adsorption and the Gibbs surface*. New York: Plenum Press, 1984.
25. Telesford DM. Langmuir trough and Brewster angle microscopy study of model lung surfactant monolayers at the air/aqueous interface. Ohio State University, 2012.
26. Duncan SL, Larson RG. Comparing experimental and simulated pressure-area isotherms for DPPC. Biophysocal Journal 2008;**94**:2965-86.
27. Mohwald H. *Handbook for Biological Physics*: Elsevier Science B.V, 1995.
28. Mohwald H. From Langmuir Monolayers to Nanocapsules. Colloids and Surfaces A: Physiochemical Engineering Aspects 2000;**171**(1-3):25-31.
29. Honig DM, D. Direct visualisation of monolayers at the air-water interface by brewster angle microscopy. Journal of Physical Chemistry 1991;**95**(12):4590-92.
30. Henon SM, J. Microscope at the Brewster angle: Direct observation of first order transitions in Langmuir monolayers. Review of Scientific Instruments 1991;**64**(4):936-39.
31. Gopal AL, K.Y.C. Morphology and collapse transitions in binary phospholipid monolayers. Journal of Physical Chemistry 2001;**105**:10348-54.
32. Baoukina SM, L; Risselada, H.J; Marrink, S.J; Tieleman, D.P. The molecular mechanism of lipid monolayer collapse. PNAS 2008;**105**(31):10803-08.
33. Alberts BJ, A; Lewis, J; Raff, M; Roberts, K; Walter, P. *Molecular Biology of the Cell*. 5 ed: Garland Science, 2008.
34. Venien-Bryan C, Lenne P, Zakri C, et al. Characterization of growth of 2D protein crystals on a lipid monolayer by ellipsometry and rigidty measurements coupled to electron microscopy. Biophysical Journal 1998;**74**:2649-57.
35. Binder H, Zschoring O. The effect of metal cations on the phase behaviour and hydration characteristics of phospholipid membranes. Chemistry and Physics of Lipids 2002;**115**:39-61.
36. Chen XH, W; Huang, Z; Allen, H.C. Interfacial water structure associated with phospholipid membranes studied by phase sensitive vibrational sum

frequence generation spectroscopy. Journal of the American Chemical Society 2010;**132**:11336-42.
37. Sovago MW, G.W.H; Smits, M; Muller, M; Bonn, M. Calcium-induced phospholipid ordering depends on surface pressure. Journal of the American Chemical Society 2007;**129**:11079-84.
38. Shannon RD. Revised effective ionic radii and systematic studies of interatomic distances in halides and chalcogenides. Acta Crystallographica 1976;**32**(5):751-67.
39. Petelska AD, Figaszewski Z. The equilibria of lipid-K+ ions in monolayers at the air-water interface. Journal of Membrane Biology 2011;**244**:61-66.
40. Pandit SAB, D; Berkowitz, M.L. Molecular dynamics simulation of a dipalmitoylphosphatidylcholine bilayer with NaCl. Biophysics 2003;**84**:3743-50.
41. Guangmiao Q, Cheng J, Wei J, et al. Synthesis, characterization and surface properties of series sulfobetaine surfactants. Journal of Surfactants and Detergents 2011;**14**(1):31-35.
42. Reich C. *Surfactants in Cosmetics*. 2 ed. New York: Marcel Dekker, 1997.
43. Lowe AB, Vamvakaki M, Wassal MA, et al. Well-defined sulfobetaine-based statistical copolymers as potential antibioadherent coatings. Journal of Biomedical Materials Research 2000;**52**(1):88-94.
44. Yuan Y, Ai F, Zang X, et al. Polyurethane vascular catheter surface grafted with zwitterionic sulfobetaine monomer activated ozone. Colloids and Surfaces B: Biointerfaces 2004;**35**(1):1-5.
45. Zhang Z, Chao T, Chen S, et al. Superlow fouling sulfobetaine and carboxybetaine polymers on glass slides. Langmuir 2006;**22**(4):10072-77.
46. Zhang Z, Chen S, Chang Y, et al. Surface grafted sulfobetaine polymers via atom transfer radical polymerisation as superlow fouling coatings. Journal of Physical Chemistry B 2006;**110**:10799-804.
47. Sun JT, Yu ZQ, Hong CY, et al. Biocompatible zwitterionic sulfobetaine copolymer-coated mesoporous silica nanoparticles for temperature-responsive drug release. Macromolecular Rapid Communications 2012;**33**(9):811-18.
48. Chang Y, Chen S, Zhang Z, et al. Highly Protein-Resistant Coatings from Well-Defined Diblock Copolymers Containing Sulfobetaines. Langmuir 2006;**22**(5):2222-26.
49. Mojtaba B, Maryam K, Larry DU. Poly(ethylene glycol) and Poly(carboxy betaine) Based Nonfouling Architectures: Review and Current Efforts. Proteins at Interfaces III State of the Art: American Chemical Society, 2012:621-43.
50. Sin MC, Chen S, Chang Y. Hemocompatibility of zwitterionic interfaces and membranes. Polymer Journal 2014;**46**:436-43.
51. Gromelski S, Brezesinski G. DNA condensation and interaction with zwitterionic phospholipids mediated by divalent cations. Langmuir 2006;**22**(14):6293-301.
52. McManus J, Radler JO, Dawson KA. Phase behaviour of DPPC in a DNA-Calcium-Zwitterionic lipid complex studied by small angle x-ray scattering. Langmuir 2003;**19**(23):9630-37.

53. Gorelov AV, Kudryashov ED, Jacquier JC, et al. Complex formation between DNA and cationic surfactant. Physica A: Statistical Mechanics and its applications 1998;**249**(1-4):216-25.
54. McLoughlin D, Dias R, Lindman B, et al. Surface complexation of DNA with insoluble monolayers. Influence of divalent counterions. Langmuir 2005;**21**:1900-07.
55. McLoughlin D, Langevin D. Surface complexation of DNA with a cationic surfactant. Colloids and Surfaces A: Physiochemical Engineering Aspects 2004;**250**:79-87.
56. Fang Y, Yang J. Two-dimensional condensation of DNA molecules on cationic lipid membranes. The journal of physical chemistry B 1997;**101**(3):441-49.
57. Matulis D, Rouzing I, Bloomfield VA. Thermodynamics of cationic lipid binding to DNA and DNA condensation: Roles of electrostatics and hydrophobicity. Journal of the American Chemical Society 2002;**124**(25):7331-42.
58. Baptista MS, Cuccovia I, Chaimovich H, et al. Electrostatic properties of zwitterionic micelles. Journal of physical Chemistry 1992;**96**:6442-49.
59. Marte L, Beber RC, Farrukh MA, et al. Specific anion binding to sulfobetaine micelles and kinetics of nucleophilic reactions. Journal of physical Chemistry B 2007;**111**:9762-69.
60. Bunton CA, Mhala MM, Moffatt JR. Nucleophilic reactions in sulfobetaine micelles of amine oxide or betaine sulfonate micelles. Journal of physical Chemistry 1989;**93**(1):854-58.
61. Wagner ML, Tamm LK. Tethered Polymer-Supported Planar Lipid Bilayers for Reconstitution of Integral Membrane Proteins: Silane-Polyethyleneglycol-Lipid as a Cushion and Covalent Linker. Biophysical Journal 2000;**79**:1400-14.
62. Schwartz DK. Mechanisms and kinetics of self-assembled monolayer formation. Annual review of physical chemistry 2001;**52**:107-37.
63. Schreiber F. Structure and growth of self-assembling monolayers. Progress in Surface Science 2000;**65**(5–8):151-257.
64. Love JC, Estroff LA, Kriebel JK, et al. Self-assembled monolayers of thiolates on metals as a form of nanotechnology. Chem Rev 2005;**105**(4):1103-69.
65. Kaifer A. *Supramolecular Electrochemistry*. Weinheim, Germany: Wiley-VCH, 2001.
66. Fragneto G, Lu JR, McDermott DC, et al. Structure of monolayers adsorbed on self-assembled monolayers on silicon: A neutron reflectivity study. Langmuir 1996;**12**:477-86.
67. Fragneto G, Thomas RK, Rennie AR, et al. Neutron reflection study of bovine B-casein adsorbed on OTS self-assembled monolayers. Science 1995;**267**:657-60.
68. Sung MM, Kluth JG, Maboudian R. Formation of alkylsiloxane self-assembled monolayers on Si3N4. Journal of Vacuum Science and Technology A 1999;**17**(2):540-44.
69. Maccarini M, Steitz R, Himmelhaus M, et al. Density Depletion at Solid−Liquid Interfaces: a Neutron Reflectivity Study. Langmuir 2006;**23**(2):598-608.

70. Unsworth LD, Tun Z, Sheardown H, et al. In situ neutron reflectometry investigation of gold-chemisorbed PEO layers of varying chain density: Relationship of layer structure to protein resistance. Journal of Colloid and Interface Science 2006;**296**(2):520-26.
71. Cho N-J, Frank CW, Kasemo B, et al. Quartz crystal microbalance with dissipation monitoring of supported lipid bilayers on various substrates. Nat Protocols 2010;**5**(6):1096-106.
72. Keller CA, Kasemo B. Surface specific kinetics of lipid vesicle adsorption measured with a quartz crystal microbalance. Biophysical Journal 1998;**75**:1397-402.
73. Petty MC. *Langmuir-Blodgett Films*. Cambridge: Cambridge University Press, 1996.
74. Fromherz P. Electron microscopic studies of lipid protein films. Nature 1971;**231**:267-68.
75. Al-kurdi.R;, Gulino-Debruc D, Martel L. A soluble VE-cadherin fragment forms 2D arrays of dimers upon binding to a lipid monolayer. Journal of Molecular Biology 2004;**337**(4):881-92.
76. Azadani ANL, J.N; Hirsa, A.H. Protein crystallisation at the air-water interface induced by shearing bulk flow. Langmuir 2007;**23**(10):5227-30.
77. Uzgiris EEK, R.D. Two-dimensional crystallisation technique for imaging macromolecules, with application to antigen-antibody complement complexes. Nature 1983;**301**(5896):125-29.
78. Dezi M, Fribourg PF, Di Cicoco A, et al. Binding, reconstitution and 2D crystallisation of membrane or soluble proteins onto functionalised lipid layers observed in situ by reflected light microscopy. Journal of Structural Biology 2011;**174**:307-14.
79. Schulz P, Crucifix C, Lebeau L. *Two-dimensional crystallisation of soluble protein complexes*. 3 ed: Humana Press Inc., 2009.
80. Kent MS, Yim H, Sasaki DY, et al. Analysis of myoglobin adsorption to Cu(II)-IDA and Ni(II)-IDA functionalised Langmuir monolayers by grazing incidence neutron and x-ray techniques. Langmuir 2004;**20**(7):2819-29.
81. Als-Nielsen J, Jacquemain D, Kjaer K, et al. Principles and applications of grazing incidence X-ray and neutron scattering from ordered molecular monolayers at the air-water interface. Physics Reports 1994;**246**(5):251-313.
82. Weygand M, Wetzer B, Pum D, et al. Bacterial S-Layer Protein Coupling to Lipids: X-Ray Reflectivity and Grazing Incidence Diffraction Studies. Biophysical Journal 1999;**76**(1):458-68.
83. Lvov Y, Ariga K, Ichinose I, et al. Assembly of Multicomponent Protein Films by Means of Electrostatic Layer-by-Layer Adsorption. Journal of the American Chemical Society 1995;**117**(22):6117-23.
84. Courty SL, L; Martel, L; Lenne, P.F; Balavonie, F; Dischert, W; Konovalov, O; Mioskowski, C; Legrand, J; Venien-Bryan, C. Two-dimensional crystallisation of a histidine-tagged protein on monolayers of fluidity-enhanced Ni2+- chelating lipids. Langmuir 2002;**18**(24):9502-12.
85. Dietrich J, Venien-Bryan C. *Strategies for two-dimensional crystallisation of proteins using lipid monolayers*. 1 ed: Imperial College Press, 2005.

86. Darst SA, Ribi HO, Pierce DW, et al. Two-dimensional crystals of Escherichia coli RNA polymerase holoenzyme on positively charged lipid layers. Journal of Molecular Biology 1988;**203**(1):269-73.
87. Avila-Sakar AJ, Guan TL, Arad T, et al. Electron cryomicroscopy of Bacillus stearothermorphilus 50 s ribosomal sub-units crystallised on phospholipid monolayers. Journal of Molecular Biology 1994;**239**:689-97.
88. Ellis MJ, Knapp S, Koeck PJB, et al. Two-dimensional crystallisation of the chaperonin TF55 from the hydrothermophilic archaeon sulfobolus solfataricus. Journal of Structural Biology 1998;**123**(1):30-36.
89. Blankenburg R, Meller P, Ringsdorf H, et al. Interaction between biotin lipids and streptavidin in monolayers: Formation of oriented two-dimensional protein domains induced by surface recognition. Biochemistry 1989;**28**:8214-21.
90. Bischler N, Balavonie F, Milkereit P, et al. Specific interaction and two-dimensional crystallisation of histidine tagged yeast RNA polymerase I on nickel chelating lipids. Biophysical Journal 1998;**74**:1522-32.
91. Venien-Bryan C, Balavonie F, Toussaint B, et al. Structural study of the response regulator HupR from Rhodobacter capsulatas. Electron microscopy study of two-dimensional crystals on a nickel chelating lipid. Journal of Molecular Biology 1997;**274**(5):687-92.
92. Arinaminpathy Y, Khurana E, Engelman DM, et al. Computational analysis of membrane proteins: the largest class of drug targets. Drug discovery today 2009;**23**(24):1130-35.
93. Drew D, Frodberg L, Baars L, et al. Assembly and overexpression of membrane proteins in Escherichia coli. Biochimica et Biophysica Acta 2003;**17**(16):3-10.
94. Seddon AM, Curnow P, Booth PJ. Membrane proteins, lipids and detergents: not just a soap opera. Biochimica et Biophysica Acta (BBA) - Biomembranes 2004;**1666**(1–2):105-17.
95. Døvling Kaspersen J, Moestrup Jessen C, Stougaard Vad B, et al. Low-Resolution Structures of OmpA·DDM Protein–Detergent Complexes. ChemBioChem 2014;**15**(14):2113-24.
96. le Maire M, Champeil P, Møller JV. Interaction of membrane proteins and lipids with solubilizing detergents. Biochimica et Biophysica Acta (BBA) - Biomembranes 2000;**1508**(1–2):86-111.
97. Garavito RM, Fergusson-Miller S. Detergents as tools in membrane biochemistry. The journal of biological chemistry 2001;**276**(25):32403-06.
98. Rigaud J-L, Pitard B, Levy D. Reconstitution of membrane proteins into liposomes: application to energy-transducing membrane proteins. Biochimica et Biophysica Acta (BBA) - Bioenergetics 1995;**1231**(3):223-46.
99. Sizer PJ, Miller A, Watts A. Functional reconstitution of the integral membrane proteins of influenze virus into phospholipid liposomes. Biochemistry 1987;**26**(16):5106-13.
100. Hutchinson FJ, Francis SE, Lyle IG, et al. The characterisation of liposomes with covalently attached proteins. Biochimica et Biophysica Acta (BBA) - Biomembranes 1989;**978**(1):17-24.

101. Boldog T, Li M, Hazelbauer GL. Using Nanodiscs to create water-soluble transmembrane chemoreceptors inserted in lipid bilayers. Methods in enzymology 2007;**423**:317-35.
102. Borch J, Hamann T. The nanodisc: a novel tool for membrane protein studies. Biological chemistry 2009;**390**(8):805-14.
103. Bayburt TH, Carlson JW, Sligar SG. Reconstitution and imaging of a membrane protein in a nanometer-size phospholipid bilayer. J Struct Biol 1998;**123**(1):37-44.
104. Denisov IG, Grinkova YV, Lazarides AA, et al. Directed self-assembly of monodisperse phospholipid bilayer nanodiscs with controlled size. Journal of the American Chemical Society 2004;**126**(11):3477-87.
105. Carlson JW, Jones AL, Sligar SG. Imaging and manipulation of high-density lipoproteins. Biophysical Journal 1997;**73**(3):1184-89.
106. Jonas A, Kezdy KE, Wald JH. Defined apolipoprotein A-I conformations in reconstituted high density lipoprotein discs. J Biol Chem 1989;**264**(9):4818-24.
107. Li Y, Kijac AZ, Sligar SG, et al. Structural analysis of nanoscale self-assembled discoidal lipid bilayers by solid-state NMR spectroscopy. Biophys J 2006;**91**(10):3819-28.
108. Bayburt TH, Sligar SG. Self-assembly of single integral membrane proteins into soluble nanoscale phospholipid bilayers. Protein Science 2003;**12**(11):2476-81.
109. Tonge SR, Tighe BJ. Responsive hydrophobically associating polymers: a review of structure and properties. Advanced drug delivery review 2001;**53**(1):109-22.
110. Knowles TJ, Finka R, Smith C, et al. Membrane Proteins Solubilized Intact in Lipid Containing Nanoparticles Bounded by Styrene Maleic Acid Copolymer. Journal of the American Chemical Society 2009;**131**(22):7484-85.
111. Jamshad M, Lin YP, Knowles TJ, et al. Surfactant-free purification of membrane proteins with intact native membrane environment. Biochem Soc Trans 2011;**39**(3):813-8.
112. Long AR, O'Brien CC, Malhorta K, et al. A detergent-free strategy for the reconstitution of active enzyme complexes from native biological membranes into nanoscale discs. BMC Biotechnology 2013;**13**(41):6750-63.
113. Bayburt TH, Grinkova YV, Sligar SG. Assembly of single bacteriorhodopsin trimers in bilayer nanodiscs. Archives of biochemistry and biophysics 2006;**450**(2):215-22.
114. Jamshad M, Grimard V, Idini I, et al. Structural analysis of a nanoparticle containing a lipid bilayer used for detergent free extraction of membrane proteins. Nano Research 2014.
115. Sainsbury S, Bird L, Rao V, et al. Crystal structures of penicillin binding protein 3 from pseudomonas aeruginosa: Comparison of native and antibiotic-bound forms. Journal of Molecular Biology 2011;**405**(1-3):173-84.
116. Spratt BG. Distinct penicillin binding proteins involved in the division, elongation and shape of Escherichia Coli K12. Proceedings of the National Academy of Sciences 1975;**72**(8):2999-3003.

117. Spratt BG, Pardee AB. Penicillin-binding proteins and cell shape in E. coli. Nature 1975;**254**:516-17.
118. Waxman DJ, Strominger JL. Penicillin-binding proteins and the mechanism of action of beta-lactam antibiotics. Annual Review of Biochemistry 1983;**52**:825-69.
119. Wadsater M, Simonsen JB, Lauridsen T, et al. Aligning nanodiscs at the air-water interface, a neutron reflectivity study. Langmuir 2011;**27**(24):15065-73.
120. Wadsater M, Barker R, Mortensen K, et al. Effect of phospholipid composition and phase on nanodisc films at the solid-liquid interface as studied by neutron reflectivity. Langmuir 2013;**13**(29):2871-80.

Chapter 2.0 Principles of Analysis and Experimental Methodology

2.1 Introduction

This chapter will first introduce the concepts of x-ray and neutron reflectometry. Initially the generation of x-rays and neutrons at large central facilities will be discussed. This will be followed by some general scattering theory and followed with a discussion of the two techniques. Details of generic x-ray and neutron reflectometry experiments will be given along with specific details of the beamlines used for data collection as part of this thesis.

The second section of this chapter will give theoretical information regarding all of the other supporting techniques used to aid the interpretation of reflectometry data. These are Brewster angle microscopy, the quartz crystal microbalance and the Langmuir trough. A very brief note on dynamic light scattering and small angle scattering is included, as these have been used to assist in some experiments. However as they do not form a large part of the work conducted here the reader will be referred to relevant literature if more information is required.

Finally the chapter will conclude by detailing the materials and methods used in sample preparation and analysis for all the experimental data found in this thesis.

2.2 X-ray Sources

In this work, the main source of x-rays used was a synchrotron source. For completeness a brief description of both laboratory and synchrotron based x-ray production follows.

2.2.1 Laboratory X-rays

Laboratory based x-ray production commonly involves bombarding a metal target with electrons. Upon bombardment a Bremsstrahlung spectrum is produced, with a sharper and more intense region observed on top[1]. The line spectrum is dependent on the metal target. Copper is the most common metal target and this produces the K alpha emission lines (Cu K_α spectrum)[2]. This spectrum is shown in figure 2.0.

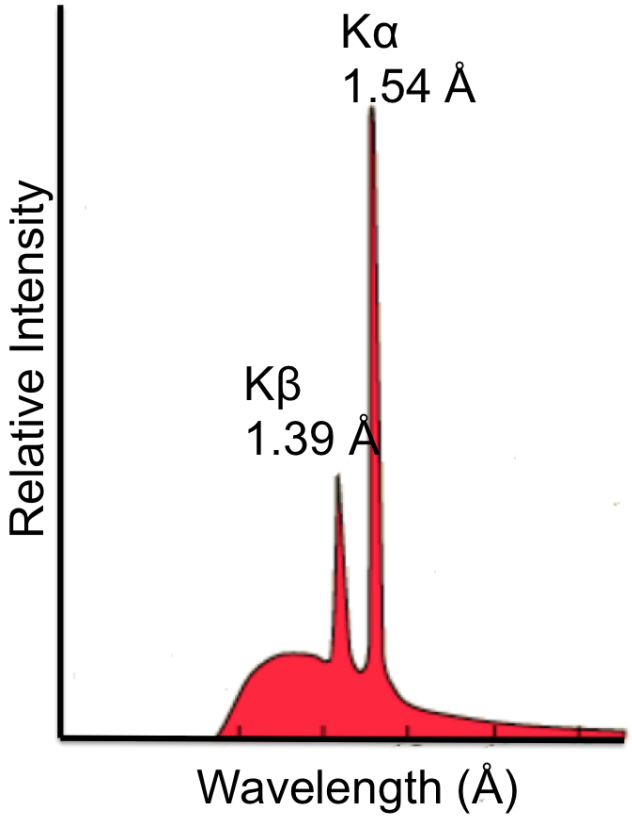

Fig 2.0- The Cu K_α spectrum for laboratory produced x-rays.

Laboratory based sources suffer from a lack of intensity and the inability for the user to tune the energy of emitted radiation. To overcome these drawbacks large-scale synchrotron sources are often used.

2.2.2 Synchrotron radiation

In the 1970s it was realized that synchrotron radiation was emitted from charged particles orbiting high-energy particle accelerators[3] [4]. This was considered a much more intense and useful source of x-rays for material science characterization.

A synchrotron ring is similar to a multi-sided polygon in which charged particles are accelerated and orbited at a constant energy. For example the energy for the Diamond Light Source ring is maintained at 3 GeV. These

charged particles, consisting of electrons, are orbited in bunches and move at relativistic speeds. The general lay out of most synchrotron sources is similar and is shown in figure 2.1. Electrons are first produced and accelerated in a linear accelerator and then transferred into a smaller booster synchrotron, whereby they undergo further acceleration. They are then injected into the main synchrotron ring[5]. Such manipulations of electrons are achieved using the Lorentz force,

$$F = eV \times B \qquad \text{(equation 2.0)}$$

where *e* is the magnitude of the electric field, V is the velocity of the charged particle and B is the magnitude of the magnetic field.

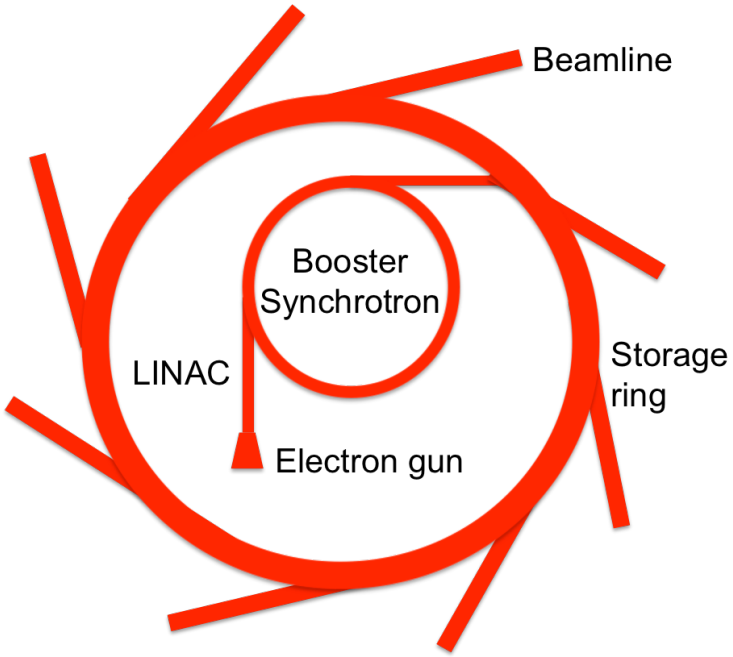

Fig 2.1- Schematic layout of a synchrotron source.

Synchrotron light is produced when the electrons change direction. This can be when the trajectory is modified by bending magnets in order to circulate electrons within the main ring. Production of synchrotron light occurs when electrons pass through a magnetic field perpendicular to their direction of motion. The associated acceleration felt by the electrons as they pass through the bending magnets causes them to radiate synchrotron light. The

emitted light then departs the bending magnet in a tangential fashion[6]. Bending magnets have been used in first generation synchrotron light sources. Currently undulators and wigglers are used (insertion devices). These consist of a periodic array of dipole magnets, which periodically laterally deflect the electron beam, leading to the production of synchrotron light[7 8].

Synchrotron sources therefore have several benefits over laboratory based x-ray production[9]. These include a large increase in the intensity of the source, low beam divergence and high coherence. The photon energy is tunable and so allows beamlines to select an energy range appropriate to the experiment of interest. This means that a large number of differing types of experiment can be conducted. Finally the produced photons can be efficiently circularly or linearly polarized.

2.3 Neutron Sources

Neutrons produced at large scale facilities are done so in one of two ways, a reactor source[10] or a spallation source[11]. Reactor sources use nuclear fission to produce neutrons, whilst spallation sources make use of a particle accelerator to accelerate protons into a heavy metal target. Both of these methods are described in the following sections.

2.3.2 Reactor Sources

The reactor source used in this work was the Institute-Laue-Langevin (ILL) in Grenoble, France. This facility uses nuclear fission of Uranium 235 to produce neutrons. When Uranium 235 absorbs a thermal neutron a fission reaction occurs, producing 2.5 fast neutrons, 180 MeV of energy and two fission fragments[12]. This is shown in equation 2.1 and in the form of a diagram in figure 2.2.

$$n_{thermal} + U^{235} \rightarrow 2\ fission\ fragments + 2.5\ n_{fast} + 180\ MeV$$

(equation 2.1)

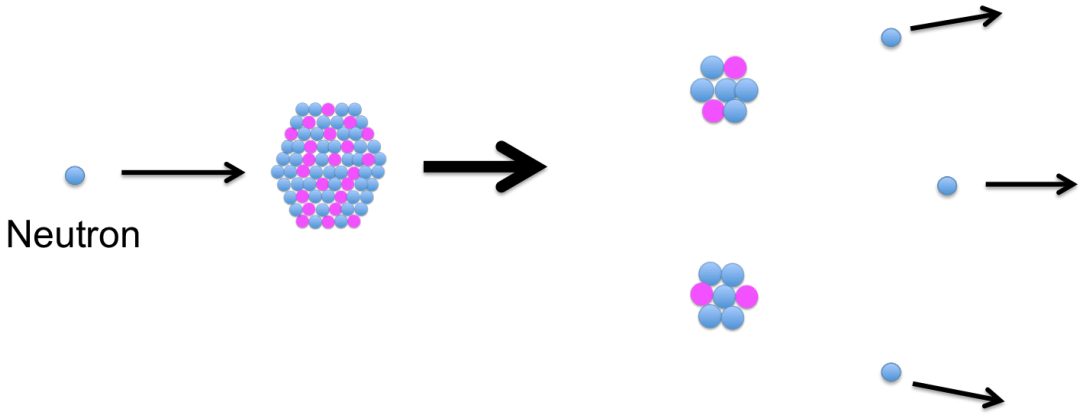

Fig 2.2- Schematic representation of the fission process

2.3.3 Spallation sources

The spallation source used in this work was the ISIS Spallation source near Oxford, U.K. This source uses a linear accelerator to accelerate protons into a Tantalum target at 800 MeV. These are absorbed by the heavy nuclei within the target and undergo an internal nucleon cascade ejecting high-energy neutrons. The nuclei then follow an internuclear cascade whereby an evaporation process occurs and the nuclei emit slow neutrons and a range of other particles[13]. This is shown in figure 2.3.

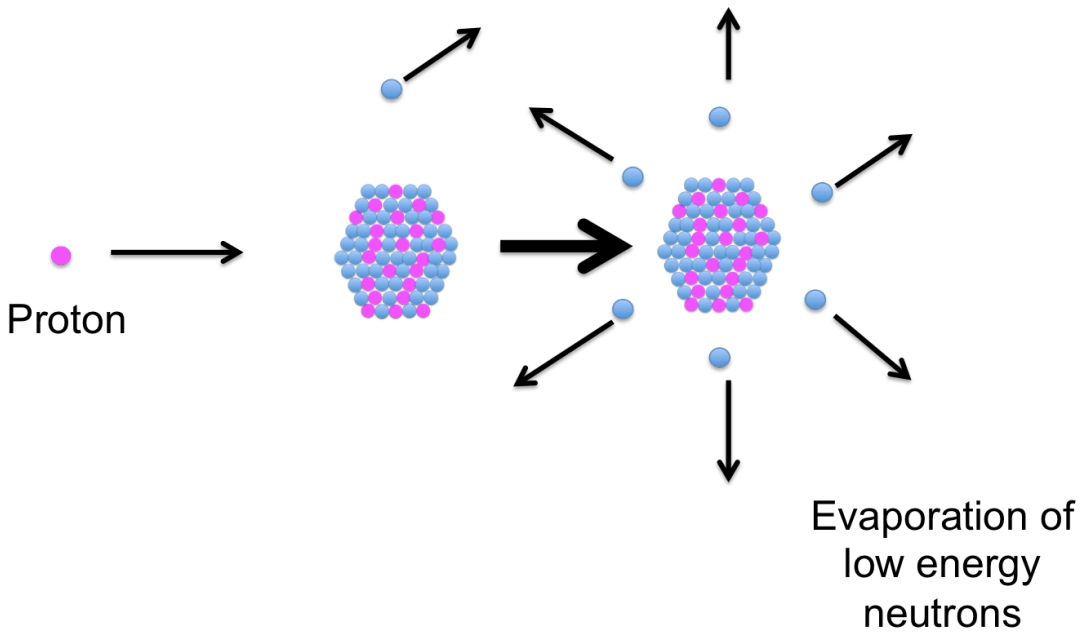

Fig 2.3- Schematic representation of the spallation process

2.3.4 Moderation

Reactor and spallation sources produce epithermal neutrons, which have a very high energy. These are not useful for scattering experiments and a moderator must be used to reduce the energy of the neutrons ~ 25 meV. A moderator slows the energy of neutrons via inelastic collisions, bringing them into thermal equilibrium with the moderator. H_2O and methane are common materials found within moderators[14].

2.4 General Scattering theory

There are three processes by which x-rays and neutrons can interact with matter. These are absorption, scattering and refraction[15 16].

2.4.1 Absorption

An atom can absorb energy, in the form of x-rays, via the photoelectric effect. This energy is then transferred to the electrons, which may then be expelled

from the atom, leaving it ionized. The gap left by the expelled electron is then filled by another electron from a higher energy level, simultaneously emitting a photon. This is known as fluorescence. Depending on the type of system the energy associated with photon emission in fluorescence may not be used for this purpose at all. Instead the energy may be used to expel another electron from the system. This is known as Auger electron emission. These processes are shown in figure 2.4 and can also be used to study the properties of materials[17].

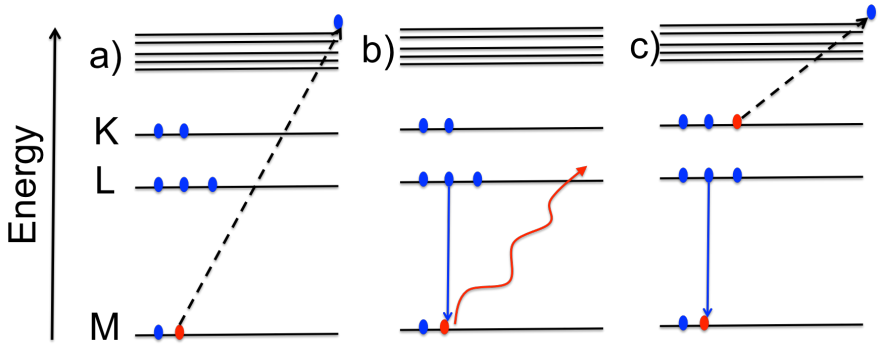

Fig 2.4- Absorption of x-rays by an atom (a) and subsequent fluorescence (b) and Auger (c) processes.

From this a linear adsorption coefficient, μ (cm^{-1}), may be defined for μdz being the attenuation of the x-ray beam through a thin sheet with a known thickness of dz at a depth from the surface, z,

$$I = I_0 \exp(-\mu t) \qquad \text{(equation 2.2)},$$

where t is the thickness and I_0 is the initial intensity of the x-ray beam. The linear adsorption coefficient can be found experimentally by measuring the intensity through a sample with a defined thickness and comparing this value to the initial intensity. This yields a proportionality factor between I and I_0, known as the absorption cross section.

For neutrons the absorption process is fundamentally different. An incident neutron must be absorbed by the nucleus of an atom which leads to a subsequent nuclear reaction within that nucleus.

2.4.2 Scattering

X-ray scattering occurs via the interaction of the electric field of the incoming beam with the electrons within a material. Therefore the interaction of x-rays with matter increases linearly across the periodic table. This is not the case for neutrons where the interaction is between the incoming neutron and the nuclei of the material. The variation of interaction varies apparently randomly across the periodic table.

Scattering processes can be divided into two categories, inelastic (incoherent) and elastic (coherent)[18]. Inelastic scattering occurs when an incident photon strikes an electron within the material and immediately bounces off, in turn loosing a small portion of its energy. Inelastic scattering of x-rays is useful for understanding the electronic structure of materials[19] but is not usually used to characterize the atomic structure of materials so will not be further developed in this chapter. For neutrons, inelastic scattering also involves exchange of energy between a neutron and an atom following a collision. In this case the resultant scattering gives information about the dynamics of motion within a material[20], but again, since this is not directly relevant to this thesis it will not be discussed further.

An elastic scattering event occurs when an incident photon strikes a material and there is no exchange of energy during the collision. Instead upon photon collision with the material, the electrons within begin to oscillate at the same frequency as the incoming radiation. Therefore neighboring atoms will oscillate in synchrony with one another and coherent waves are produced. The scattered waves produce an interference pattern that contains structural information about the material. This interference may be constructive (i.e in phase), where a bright spot on the detector is observed, or destructive (i.e out of phase), where a dark region on the detector is observed. This phenomenon produces a 2D diffraction pattern at the detector[21]. The geometry of an elastic scattering event is shown in figure 2.5.

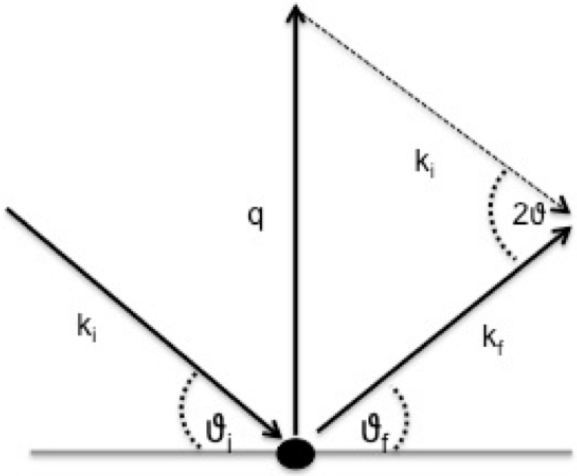

Fig 2.5- Schematic representation of an elastic scattering event.

A scattering vector can then be defined as,

$$Q = k_f - k_i \qquad \text{(equation 2.3)},$$

having units of ($Å^{-1}$), where k_f and k_i are the out going and incoming wave vectors respectively and $|k|$ is given by $2\pi/\lambda$.

2.5 X-ray and Neutron Reflectometry

When an interface is irradiated with x-rays or neutrons at grazing incidence angles the intensity of reflected waves is highly dependent on the refractive index profile normal to that interface[22-24]. Thus analysis of the observed reflectivity as a function of the angle of incidence can yield information about the interfacial density profile with resolution down to sub-Angstrom levels[25 26]. The interfacial density that is probed differs between the two techniques with x-rays interacting with the electron cloud of atoms within the sample and neutrons interacting with the constituent atomic nuclei[27 28]. Therefore neutron reflectivity stems from the scattering amplitude density profile of nuclei within the sample, which varies in an apparent random fashion across the periodic

table[29]. In the case of x-rays they interact with the electron cloud of constituent atoms[28] and therefore probe the electron density profile across an interface[30]. The two techniques therefore yield slightly different, though highly complimentary information on the structure of matter at interfaces. A reflectometry experiment therefore involves probing the structure of a material normal to the interface. The geometry of a typical reflectometry experiment is shown in figure 2.6.

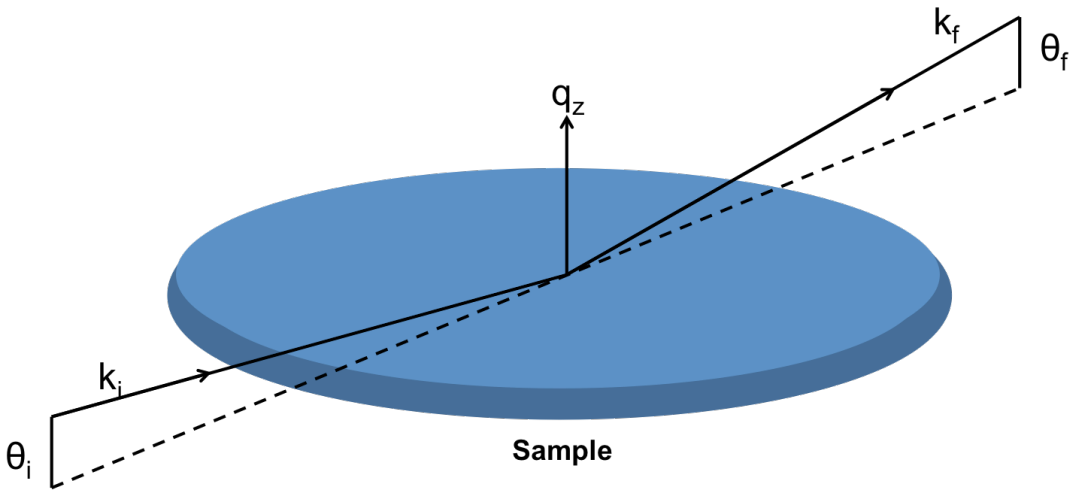

Fig 2.6- Geometry of a typical reflectivity experiment.

When an x-ray or neutron beam passes through differing transparent media, it's direction will change due to the difference in refractive index between the two media[31]. This is shown schematically in figure 2.7.

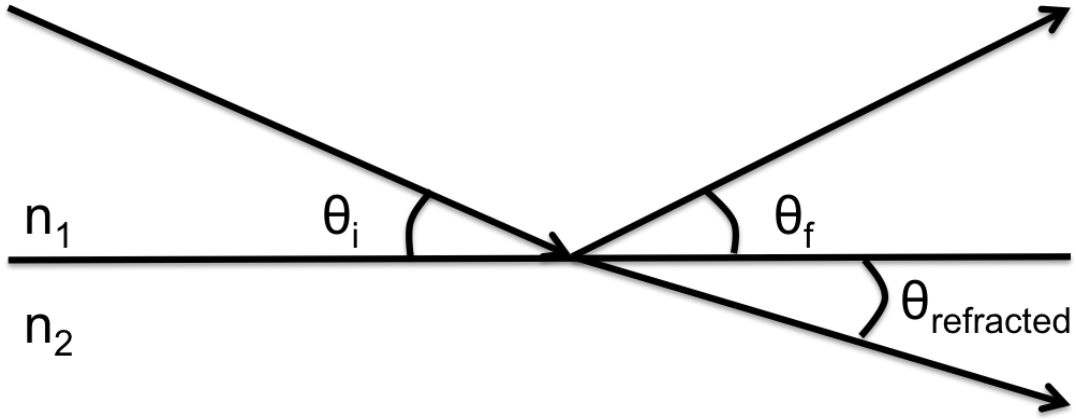

Fig 2.7- Fate of an x-ray or neutron wave incident at an interface.

For both x-rays and neutrons Snell's law relates the refractive index change across an interface ($n_1 \neq n_2$) to the angle of incidence and angle of refraction,

$$n_1\theta_i = n_2\theta_{refracted}$$ (equation 2.4),

where θ_i and $\theta_{refracted}$ are the angles of incidence and refraction respectively.

The complex refractive index, n, for x-rays and neutrons is given by,

$$n = 1 - \delta + i\beta$$ (equation 2.5),

where for x-rays,

$$\delta = \frac{r_0 \rho_e \lambda^2}{2\pi} \text{ and } \beta = \frac{\mu\lambda}{4\pi}$$ (equation 2.6),

where r_0 is the classical radius of an electron (2.82×10^{-15} m)[32], λ is the wavelength, ρ_e is the electron density and μ is the mass adsorption coefficient. In the case of neutrons, $r_0\rho_e$ is replaced by the neutron scattering length density,

$$\rho = \sum_j n_j b_j$$ (equation 2.7),

where n_j is the number density and b_j is the coherent scattering length[33]. Some scattering lengths of commonly used atoms are shown in table 2.1.

Nucleus	Coherent Scattering length, 10^{-5} Å^{-1}
^{1}H	-3.7406
^{2}H	6.671
C	6.646
N	9.36
^{16}O	5.803
Na	3.63
S	2.874

Table 2.1- Coherent scattering lengths of some common elements

It is found that weak interactions cause δ in equation 2.5 to be small, generally around 10^{-5}-10^{-6}. The adsorption term, β<δ is generally neglected in the treatment of reflectometry data[34].

If the surface of a free solid or liquid is considered then n_1=1 and because δ is slightly greater than 1, n_2<1. Hence Snell's law (equation 2.4) predicts that the angle of refraction will be less than the angle of incidence. Hence upon irradiating a surface at sufficiently low angles, a finite angle, θ_c or the critical angle, is achieved where $\theta_{refracted}$=0 and total external reflection occurs. This angle is related to the refractive index by,

$$cos\theta_c = n = 1 - \delta \text{ (equation 2.8).}$$

Here the reflectivity from the surface, $r=E_{reflected}/E_{incident}$ is unity and the reflectivity is given as $R = |r|^2$.

For angles of incidence greater than the critical angle, this rule no longer applies, and for an ideally flat surface the reflectivity is given by Fresnel's laws,

$$r = |r| = \frac{Q_0 - Q_1}{Q_0 + Q_1} \quad \text{and} \quad R_F(Q) = \left|\frac{Q_0 - Q_1}{Q_0 + Q_1}\right|^2 \quad \text{(equation 2.9),}$$

where $Q=4\pi/\lambda\sin\theta_i$, $Q_1=\sqrt{Q^2-Q_c^2}$ and the term for adsorption is neglected. For a more in depth discussion on the derivation of the Fresnel laws the reader is directed to the following references[35-38].

Of course an interface under investigation will not be abrupt and will not be perfectly flat. The surface of liquids suffer from thermally induced capillary waves[39 40], whilst on the surface of solids, structural defects or crystalline imperfections[41] cause the density profile to deviate from an ideally flat surface. This will therefore cause the reflectivity from the surface to deviate from Fresnel's law. Approaches for calculating the reflectivity in these cases will be discussed in the next section.

2.5.1 Roughness and reflectometry

All interfaces will show roughness. Roughness may come in the form of a local chemical gradient or through inter-diffusion between layers at the interface[42].

For a flat, smooth interface the dependence of reflectivity on Q can be shown by,

$$R = \frac{{Q_c}^4}{16Q^4} \quad \text{(equation 2.10).}$$

This means that after the critical edge the reflectivity will fall off at a rate of Q^{-4}. Any divergence from a flat, smooth interface will cause the reflectivity to fall off at a greater rate[43]. This is because more intensity is reflected off as diffuse scatter as opposed to being reflected in the specular direction[44]. This is shown schematically in figure 2.8.

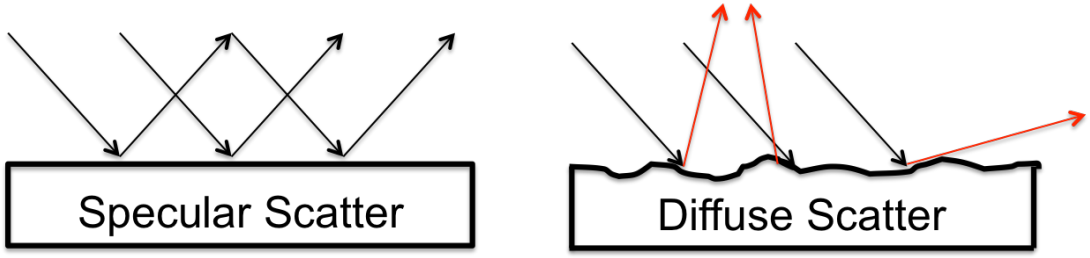

Fig 2.8- The effect of roughness on scattering from an interface.

By adding an exponential parameter to the Fresnel reflectivity coefficient it is possible to account for the effect of roughness,

$$R = \frac{Q_0 - Q_1}{Q_0 + Q_1} exp^{(-Q_0 Q_1 \sigma^2)}$$ (equation 2.11).

2.5.2 Reflection from more complicated systems: The Abeles Matrix Method

The previous methods shown for the calculation of the reflectivity are only for a single, smooth and homogenous interface. This section will highlight approaches to calculate the reflectivity from more complicated systems. These are systems containing many adsorbed layers and each layer is approximated as a smooth, homogenous slab with a characteristic scattering length density. For a more in depth discussion regarding these approaches the reader is directed to the following references [35 45-47]

Initially a phase factor, β, is defined, which is dependent on the thickness of each layer within the sample. This is defined as,

$$\beta_n = k_n d_n \qquad \text{(equation 2.12).}$$

A matrix, C_n, is then formed for each layer within the sample. The matrix is composed of the reflectivity coefficients plus the phase factor, β,

$$C_n = \begin{bmatrix} \exp\beta_n & r_n \exp(\beta_n) \\ r_n \exp(-\beta_n) & \exp(-\beta_n) \end{bmatrix} \qquad \text{(equation 2.13).}$$

The matrix for each layer within the model is then summed giving,

$$M = \prod_{n=0}^{n} C_n \qquad \text{(equation 2.14)}$$

and the reflectivity can be calculated as

$$R = \left| \frac{M_{11}}{M_{12}} \right|^2 \qquad \text{(equation 2.15).}$$

2.5.3 Background and reflectometry

The observed reflectivity in an experiment will be a composite value of the measured signal in the specular direction plus the background. Common sources of background are usually detector noise, air scattering and sample-related diffuse scattering. The largest source of background for a reflectivity experiment arises from incoherent scattering, which has been described previously. Subtracting the background is therefore important to gain information from the true specular reflectivity. It is common to assume that the major component of background scattering comes from incoherently scattered incident waves. To allow measurement of the background the reflectivity is measured in the non-specular direction. This may be achieved by measuring the reflected intensity using an off-specular scan. This is

similar to the geometry of a specular scan but involves offsetting the detector angle by a small amount to just miss the specular signal, thus measuring incoherent scattering from the sample. These processes will be described in more detail in the following sections where specific instrumentation is discussed.

2.5.4 The importance of contrast variation in neutron reflectometry

For a system containing many layers solving the reflectometry profile is often complicated, as there is usually more than one solution to the model. This is because, as with all scattering techniques, neutron reflectometry suffers from the phase problem. This issue may be negated, however, by use of several systems that are chemically identical, but differ in their scattering length density make-up. The contrast variation method relies on the large difference in bound coherent scattering length, and therefore scattering length density, between hydrogen and deuterium (-3.74 and 6.67 fm respectively). Thus by varying the H/D content of the bulk solution or by isotopic substitution of the molecules under investigation, scattering from different parts of the layered structure can be highlighted or matched out. This helps to co-refine several contrasts together in an attempt to pin down a realistic model.

Figure 2.9 shows an example set of contrast experiments for a surfactant monolayer on the surface of water. This highlights the way in which deuterium can be used instead of hydrogen (structurally analogous) to yield information about the lipid tails and head groups.

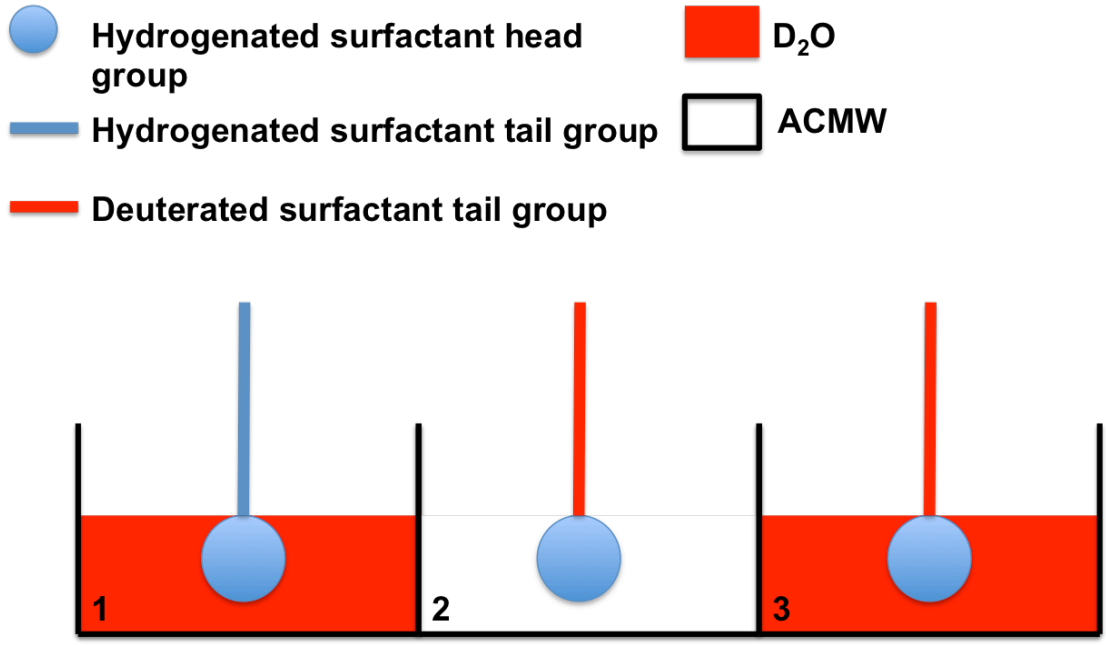

Fig 2.9- Schematic representation of a set of contrast variation experiments that may be performed on a surfactant monolayer at the air-water interface. (ACMW= air contrast matched water).

1) represents an entirely hydrogenated surfactant on the surface of D_2O which will highlight scattering from the lipid monolayer. 2) shows a surfactant with a hydrogenated head group and a deuterated tail group on a surface with a specific D_2O/H_2O ratio that matches the scattering length density of the solvent to air (0.08:0.92 volume fraction of D_2O:H_2O). In particular this highlights the scattering from the tail groups of the surfactant. 3) shows a hydrogenated surfactant head group and a deuterated tail group on D_2O. This ensures the scattering from the solvent (D_2O) and the deuterated tail groups are similar and highlights the scattering/information obtained from the head group. An additional contrast can also be obtained with x-ray reflectometry.

2.6 Instrumentation and experimental considerations

This section will describe the considerations which must be taken into account for a generic x-ray and neutron reflectometry experiment. It will also discuss specific details of the reflectometers used as part of this work.

2.6.1 X-rays

The only x-ray reflectometer used in this work was the I07 beamline at Diamond light source, Oxford, U.K. Therefore this section will primarily revolve around the set-up of this beamline.

2.6.2 Generic X-ray experiments

As described previously an x-ray reflection experiment measures the intensity of specular reflection as a function of momentum transfer, Q_z, perpendicular to the interface. X-ray reflectometers at synchrotron sources commonly use a monochromatic x-ray beam and vary the incident and detector angles in order to scan the desired Q range.

2.6.3 Data reduction and corrections

In a reflectometry experiment the background is measured separately to the true specular signal. Such background originates from detector noise, air scattering or sample-related diffuse scattering (incoherent scattering). Subtracting the background is preferable, as it can affect the roughness parameters derived from the model. Background subtraction is usually completed in one of two ways. The first is to perform an offset scan in which the signal is measured just parallel to the specular ridge (shown schematically in figure 2.10) and later subtracted from the specular signal. This type of scan has disadvantages and is not ideal for background determination as, at higher angles, the offset is not entirely perpendicular to the specular ridge, whilst the magnitude by which it is offset is also an arbitrary amount. The second type of scan is called a rocking scan (also shown in figure 2.10). This involves performing rocking scans at several points along the specular ridge. These rocking curves are then fit with a Gaussian profile to determine the true specular signal. This has advantages over the offset scan, as there is no arbitrary offset and therefore the determination of the background is more accurate as it is determined by more than one point. However, this approach significantly increases

measurement time and for soft-matter this can cause problems such as beam damage. Rocking scans, however, cannot be performed on liquid interfaces.

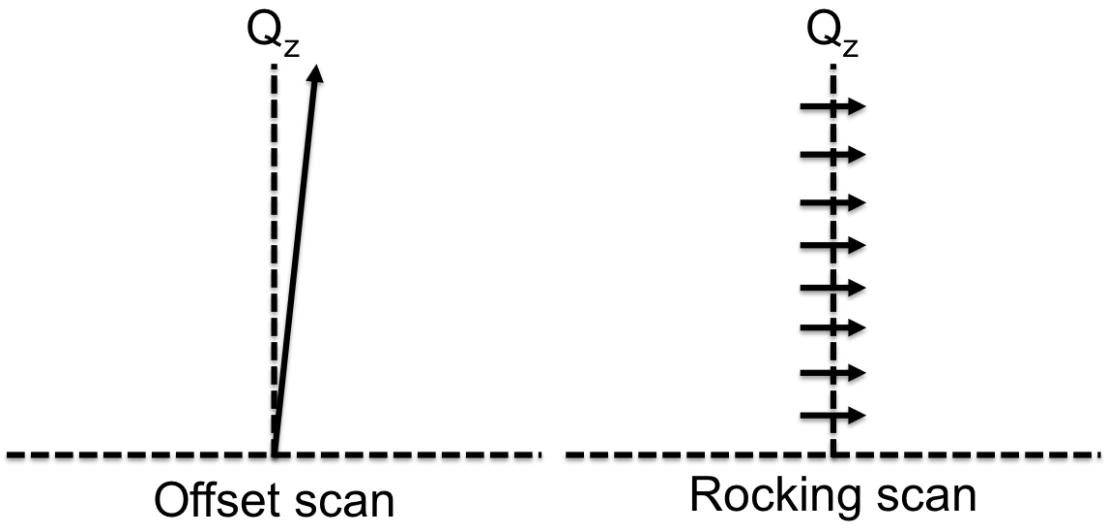

Fig 2.10- Types of scan performed to find the background in a reflectometry experiment.

The effect of beam footprint is also taken into consideration for an x-ray reflectometry experiment. For a well-collimated and uniform direct beam, the size of the footprint on the sample can be shown by,

$$F = \frac{T}{\sin\alpha} \qquad \text{(equation 2.16),}$$

where T is the thickness of the beam and α the angle of incidence of the direct beam[48]. This is shown schematically in figure 2.12.

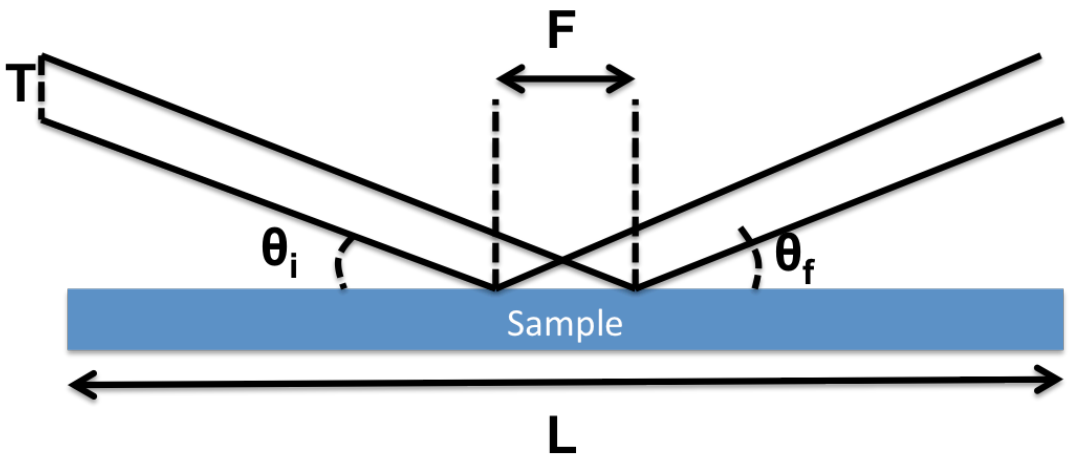

Fig 2.12- Schematic representation of beam footprint on sample surface.

For any given experiment it is important to ensure that the sample length is considerably larger than the footprint of the beam in order to gain total external reflection at values less than or equal to the critical edge[48].

Finally an x-ray reflectometry experiment will utilize three or four Q scans to generate an entire reflectometry profile. This involves measuring the reflected intensity in smaller Q ranges and later stitching these together. This kind of raw data is shown in figure 2.13.

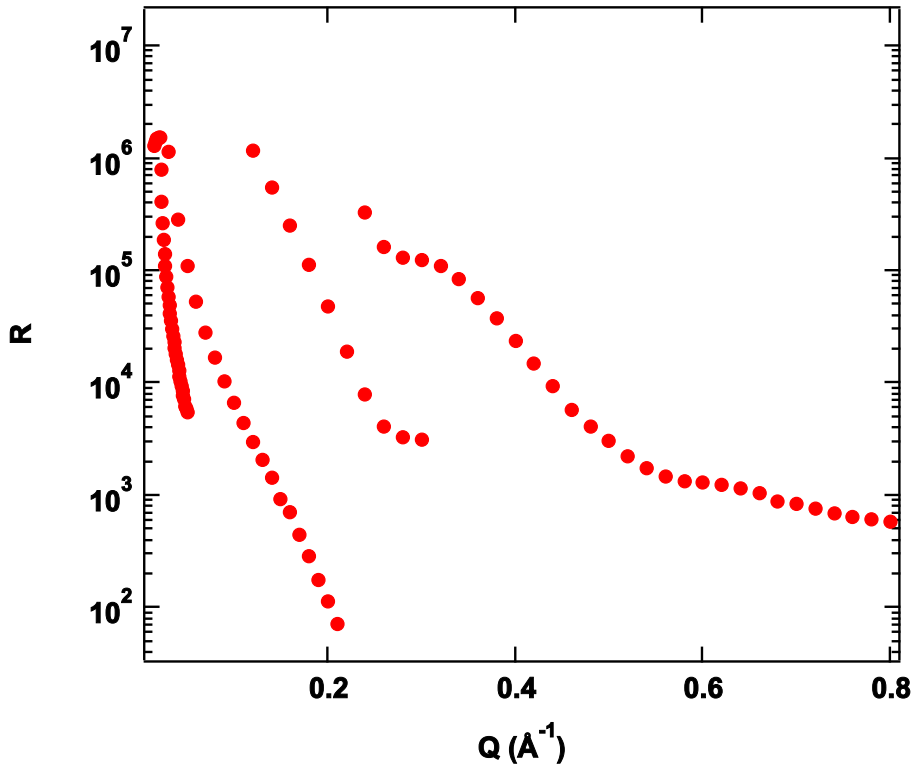

Fig 2.13- Raw reflectometry profile taken straight from the beamline. Figure highlights the smaller Q ranges chosen. Here they are 0.015-0.05, 0.03-0.21, 0.12-0.3 and 0.24-0.8.

Q ranges that measure values close to the critical edge and/or at low Q therefore require a higher attenuation (as described in figure 2.13). These are filters placed in the beam to absorb x-rays, therefore avoiding oversaturation of the detector. On I07, for example, these consist of a set of eleven aluminium and molybdenum foils with varying thicknesses. Care must be taken to ensure that sufficient overlap between these smaller Q ranges is chosen so that they can be stitched together. The reflectivity signal is then defined as the ratio of the incident and scattered photon flux. In order to effectively compare the experimental data with a theoretical model (and to allow effective stitching of measured Q regimes), the measured data must be normalized to the incident flux. This is usually achieved in one of two ways. The first involves measuring the incident flux without the sample in position and maintaining the same optical set-up as the planned experiment. The second method involves normalizing the data against values found just before the critical edge, the so-called plateau of total external reflection.

However the latter, although the choice for air-water interfaces, is not ideal if the sample is highly absorbing.

2.6.4 I07, Diamond Light Source, U.K

The I07 beamline is capable of providing experiments for several scattering geometries including XRR, grazing incidence small angle x-ray scattering (GISAXS) and grazing incidence x-ray diffraction (GIXD). All XRR measurements in this thesis were conducted using this instrument. The principal beamline optics are comprised of a cryo-cooled undulator, a double crystal monochromator Si(111) and vertical and horizontal focusing mirrors. This provides a highly collimated beam with well-defined properties. The reflected beam is then tracked with a diffractometer mounted Pilatus 100k detector or by a stationary Pilatus 2M detector positioned appropriately for small angle scattering experiments. Reflectivity experiments on water are commonly conducted at an incident beam energy of 12.5 keV and various angular $Q_z(=4\pi \sin\theta/\lambda)$ ranges. Data is collected using a region of interest to integrate the specular reflection, while a second region of interest of the same size is used to approximately subtract the background. A “footprint” correction[48] for over-illumination is applied to the data assuming a Gaussian beam profile and ignoring meniscus effects. The data is usually collected over three attenuation regimes and normalized to the critical edge. In order to minimize beam damage on the sample the sample can be horizontally translated between attenuation regimes. The beamline optics are represented schematically in figure figure 2.14.

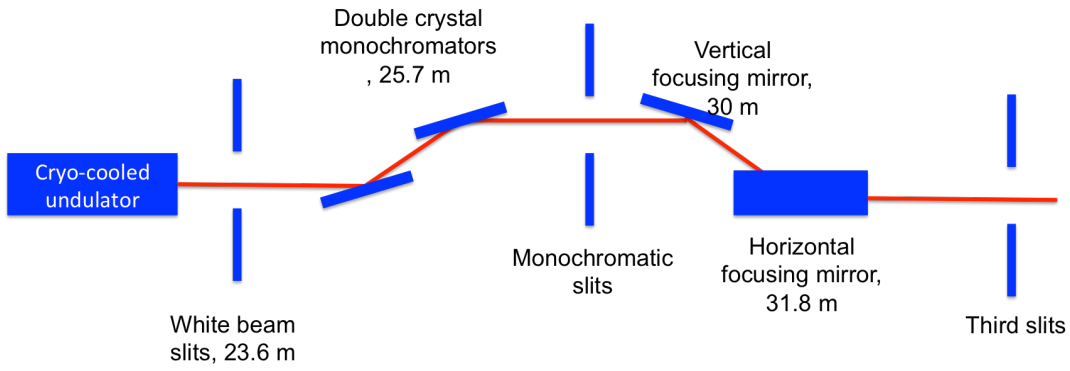

Fig 2.14 - Schematic representation of the optics on beamline I07

The beamline also contains a "double crystal deflector" (DCD) which is used for reflectivity from liquid interfaces[25]. Given that all XRR experiments in this thesis were conducted at the air-liquid interface, a slightly extended discussion will be devoted to the DCD.

Studies of liquid interfaces at synchrotron sources are a challenge as neither the liquid surface or the synchrotron can be tilted to allow measurement of varying incident angle. The DCD on I07 uses two silicon crystals, Si(111) and Si(220), and their subsequent Bragg reflections, to allow deflection of the beam onto a liquid surface, removing the need to move the sample in order to vary incident angle, as the beam now pivots at a fixed sample position. The geometry of the DCD is shown in figure 2.15.

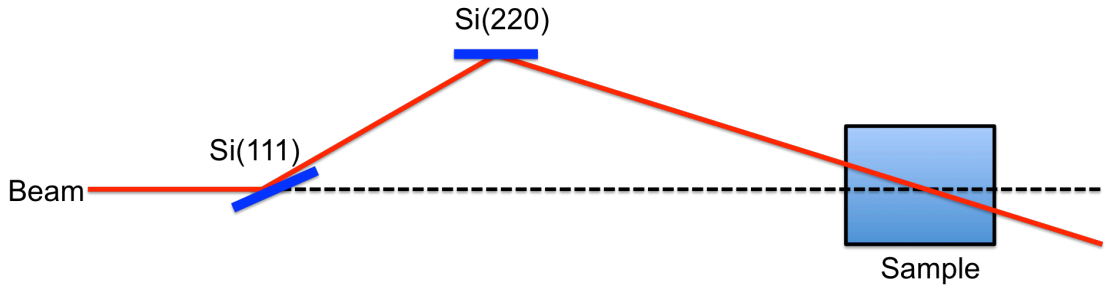

Fig 2.15- Schematic representation of the DCD set-up on I07.

The beam is deflected initially by Si(111) and then back in the opposite direction by Si(220). A beam deflection is therefore produced, $2\Delta\theta$, where $\Delta\theta$ is equal to the difference in the Bragg angles of the two crystals. The pair of

crystals are mounted on one rotation stage that has an axis well aligned to the incoming beam. The pair of crystals can then be rotated around this axis so that the path of the beam is moved, leading to a variation in the angle of incidence at a constant sample position. The vertical incidence angle, α, is given by,

$$\sin\alpha = \sin\varphi \sin 2\Delta\theta \qquad \text{(equation 2.17)},$$

where φ is the angle of rotation about the incoming beam axis. A change in φ will also result in a change in the horizontal deflection, β, which will therefore define the angles that the detector must follow in order to track the reflected beam,

$$\sin\beta = \cos\varphi \sin 2\Delta\theta \qquad \text{(equation 2.18)}.$$

There are other beamlines containing similar optical set-ups for the deflection of a beam onto a liquid surface. However the DCD on I07 has the advantage that it has been built within an already existing x-ray reflectometer and fits well with the existing equipment. Therefore users can take advantage of the fact that there is a diffractometer and P2M detector. This allows rapid switching between XRR, GIXD and GISAXS geometries, making the beamline extremely diverse in the types of experiments it is able to offer.

2.6.5 Neutrons

2.6.6 Generic neutron experiments

As with x-ray reflectometry, a neutron reflection experiment measures the intensity of specular reflection as a function of the momentum transfer, Q_z, perpendicular to the interface ($Q_z = 4\pi\sin\theta/\lambda$). The data reduction and correction is conceptually analogous to those performed on x-ray data.

Neutron reflection measurements can be carried out in two ways. The first is to use a monochromatic beam of neutrons and vary the incident and detector angles to scan the desired Q range. Much more common, however, is the time of flight mode. These experiments utilize a fixed incident angle and measure a polychromatic neutron beam as it arrives at the detector. The range of wavelengths found in the neutron beam therefore correspond to a range of momentum transfer values, which can be deduced from the time at which they arrive at the detector, relative to the time of each pulse. On most TOF beamlines a pair of mechanical choppers are used, with the separation and length of each pulse being defined by the speed and relative phase of the choppers. The main advantage of this technique is that an entire Q range can be measured simultaneously (or at most with only two discrete angles).

2.6.7 Data reduction and corrections

For a neutron reflectivity experiment there are several requirements that need to be fulfilled before the data can be analyzed. A transmission beam spectrum must be recorded for each incident angle to allow the calibration of the reflectivity onto an absolute scale. The reflectivity must also be corrected for the background arising from incoherent scattering. Neutron reflectometry suffers from a higher background as opposed to x-rays owing to the large number of incoherently scattered neutrons arising from collisions with hydrogen. Background subtraction is effected via subtracting the background scattering for each point along the specular ridge. To gain an entire Q range in TOF mode, two or three incident angles are usually measured. These must be stitched together to yield the final, complete reflectivity profile. However, to facilitate this, care must be taken when designing the experiment to ensure that there is sufficient overlap in Q between incident angles. Finally the reflectivity is divided by the incident neutron spectrum (I_0) to give the relative intensity (I/I_0).

2.6.8 INTER- ISIS, Oxford, U.K

INTER is a neutron reflectometer located on Target Station 2 at the ISIS pulsed neutron source (Oxford, U.K)[26]. The instrument benefits from high flux and high resolution. It is therefore possible to perform reflectometry experiments at the air-water, solid-liquid and liquid-liquid interfaces. The instrument does however have a particular focus on adsorption at the air-water interface[49]. The set-up of the instrument is shown in figure 2.16.

INTER has two choppers for sorting the neutron pulse which arrives at the guide entrance of the instrument. The first chopper is functional at 20 Hz and is responsible for separating the unmoderated spectrum of neutrons from the pulsed source. The second chopper is a counter-rotating disk and is ultimately responsible for defining the bandwidth of neutrons that the instrument uses. The beam then enters the fine collimation slits followed by a supermirror allowing the adjustment of angle appropriate for a liquid interface. The sample position is of horizontal geometry and two ^{3}He gas detectors detect the reflected beam. The first detector detects the reflected beam, whilst the second is responsible for detecting the incoherent background.

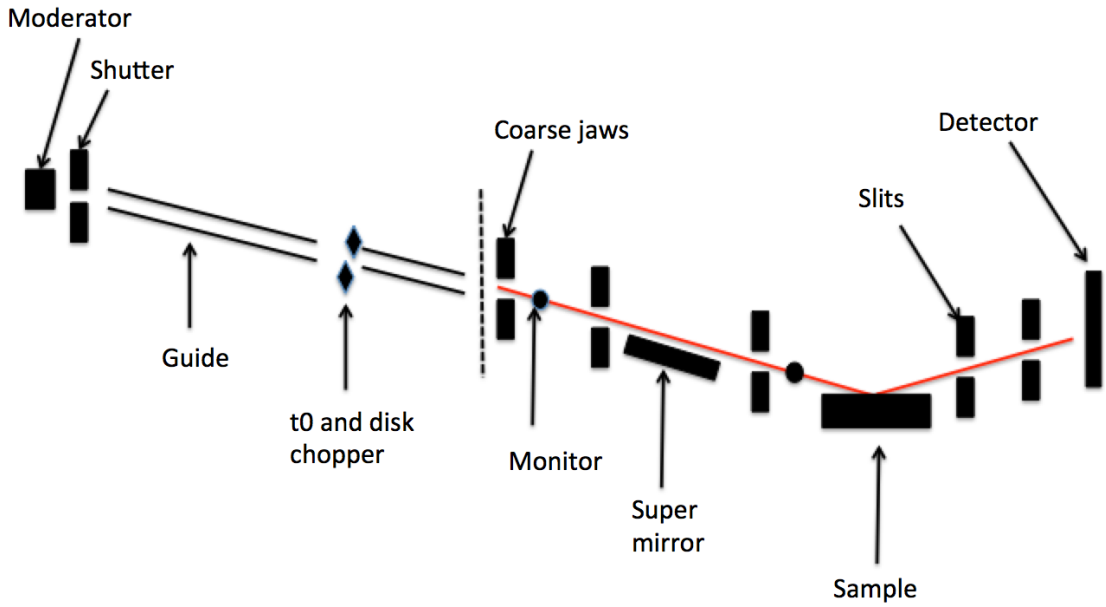

Fig 2.16- Scehmatic showing the instrument set-up of the INTER beamline at ISIS[26].

INTER has particular strengths and benefits when compared to other reflectometers at ISIS. Firstly the lower repetition rate of the pulse on Target Station 2 (10 Hz as opposed to 50 Hz on TS1) means that a wider range of neutron wavelengths is available within each pulse. This means that it is possible to measure a wider Q range on INTER within a short period of time. This is not possible on instruments such as SURF and CRISP found on Target Station 1. INTER also benefits from an increased flux (around 10 times that of SURF at 10^7 n/s/cm^2). This means that a larger range of substrates and experimental conditions can be employed.

2.6.9 OFFSPEC- ISIS, Oxford, U.K

OFFSPEC is a neutron reflectometer also positioned on Target Station 2 at the ISIS spallation source. The instrument is principally designed for off-specular (in-plane) measurements using spin-echo techniques, but can also measure routine specular neutron reflectometry. The instrument can also

make use of a neutron polarizer making polarized neutron reflection experiments possible[50]. As with INTER, OFFSPEC also benefits from a high resolution and a high flux. The instrument has a similar chopper set-up to INTER and uses ^{3}He gas detectors to detect reflected neutrons.

2.6.10 SURF- ISIS, Oxford, U.K

The SURF beamline is located on Target Station 1 at the ISIS spallation source. It is a reflectometer optimized for the surface chemistry of soft condensed matter research[51]. The instrument comprises a focusing supermirror, which focuses the beam at the sample position and a 2D area detector which detects reflected neutrons from the sample surface.

2.6.11 D17- ILL, Grenoble, France

D17 is a neutron reflectometer found at the ILL reactor source. One particular benefit of this instrument is that it has two modes of operation, allowing both time of flight and monochromatic experiments[52]. The latter enables the user to conduct polarized neutron reflectometry. The instrument utilizes a 2D area detector to detect reflected neutrons from the sample surface.

2.7 Reflectometry Data Modeling

The most common way of analyzing reflectivity data is through the comparison of reflectivity simulations with measured reflectivity profiles. Data in this thesis was modeled using MOTOFIT, which was written for IGOR Pro, by Dr Andrew Nelson (ANSTO). This program utilizes the Abeles matrix method, described in section 2.4.7, to sum contributions from layered samples in terms of reflectivity, surface roughness, scattering length density and film thickness[45]. The method splits the system up into slab models and iterates the roughness, thickness and scattering length density of each individual layer along with solvent penetration (volume fraction of water). If the user wishes then there are a number of algorithms which can be

performed iterating these values via a non-linear least squares regression on the experimental data until it finds the best fit[46].

For a layer which is made up of two components, a chemical species and solvent, the scattering length density is calculated by,

$$\rho_{layer} = \phi\rho_s + (1-\phi)p_w \qquad \text{(equation 2.19),}$$

where ρ_s and ρ_w are the scattering length density of the chemical species and the solvent. ϕ is the volume fraction of species s within the layer. If more than one chemical species is present within the adsorbed layer then ρ_s is found by considering the volume fraction of each species within the layer. In practice MOTOFIT allows fitting of each variable within the layer separately, giving the user much more control over the theoretical model, but also requiring more contrasts to pin down a unique fit.

The program also allows an estimation of the errors associated with each parameter,

$$\chi^2 = \sum_{n=1}^{L} \frac{1}{L-p}\left(\frac{y_{n,obs}-y_{n,calc}}{y_{n,error}}\right)^2 \qquad \text{(equation 2.20),}$$

where L is the number of measured data points, p is the number of variables in the fitting procedure, y_{obs} corresponds to the experimental data, y_{error} is the error associated with that experimental data (an instrument specific artifact) and y_{calc} is the theoretical mode. The calculated value of χ^2 is therefore a measure of the "closeness" of the theoretical model to the experimental reflectivity profile, with the lower the χ^2 value indicating a better model fit.

2.8 Other scattering techniques

Two other scattering techniques have been used to a small extent as part of this work. Here a brief outline is given. If the reader wishes to learn more about these techniques, they are directed towards the references within this section.

2.8.1 Dynamic Light Scattering

Dynamic light scattering or photon correlation spectroscopy is a technique used to determine the size of sub-micron particles in liquid suspensions[53 54]. When light interacts with these particles the electric component of the incident wave causes the electrons within the sample to oscillate and produce a scattered wave. It is therefore possible to determine structural and dimensional information of the scattering objects in solution. A typical experimental set-up involves irradiating a sample with a monochromatic laser. The signal from the scattered light at a fixed angle is detected by a photon counting device. This is then converted to a correlation function represented by an exponential decay in scattering, which will vary depending on the size of particles in solution, and their Brownian motion. From this information the particles diffusion coefficient can be found, and by application of the Stokes-Einstein equation[55], their hydrodynamic radius and/or diameter[56]. This value will be larger than the physical size of the object as the bound water and charge cloud around them will contribute to the apparent size.

2.8.2 Small angle scattering

Small angle x-ray/neutron scattering (SAXS/SANS) is a technique that utilizes the elastic scattering of atoms to yield information about the shape and size of macromolecules or other partially ordered materials such as colloids in solutions or emulsions[57 58]. The technique relies on scattering

from a relatively densely packed ensemble of particles where the relative distance between particles is on the same scale as the size of the particles themselves. The interference pattern at the detector therefore contains information about the size and structure of the particles as well as information about inter-particle distances and assembly. This information is denoted as the form factor (F(Q)) and the structure factor (P(Q)) respectively[59]. Therefore for a number of particles (N) with an electron density ρ_1, embedded in a matrix of electron density ρ_2 the scattered intensity is defined by,

$$I_1 = I_o \times (\Delta_\rho)^2 \times {V_1}^2 \times F(Q) \times P(Q) \qquad \text{(equation 2.21).}$$

As with neutron reflectometry, this is a model dependent technique so some information about the sample is required to interpret the data. The use of neutrons again benefits from multiple contrast experiments. This can be a valuable tool in pinning down a unique fit to the data. X-ray and neutron data can also be highly complimentary, allowing combined data to be modeled together.

2.9 Brewster Angle Microscopy

Brewster angle microscopy was developed in 1991, completely independently, by the groups of Honig and Mobius (Germany) and Henon and Meunier (France)[60 61]. The technique can be used to visualize changes in a monolayer at the air-water interface, phase separation and domain formation[62] as well as the direct observation of monolayers at the solid-liquid interface[63].

If the air-water interface is illuminated with p-polarised light at an incident angle equal to the Brewster angle then no light will be reflected from the surface[61]. The Brewster angle is defined by,

$$tan\alpha = \frac{n_2}{n_1} \qquad \text{(equation 2.22)}$$

where α is the Brewster angle and n_1 and n_2 are the refractive indices of media 1 and 2. The Brewster angle for the air-water interface is 53.1 ° [64].

If a layer of amphiphilic molecules is spread over the air-water interface, then a new n_1/n_{film} system has been created, i.e. the refractive index of the water layer has been modified. This means that α no longer equals the Brewster angle and it can be said that the Brewster condition is no longer satisfied and light will reflect from the interface[64]. This is shown schematically in figure 2.17.

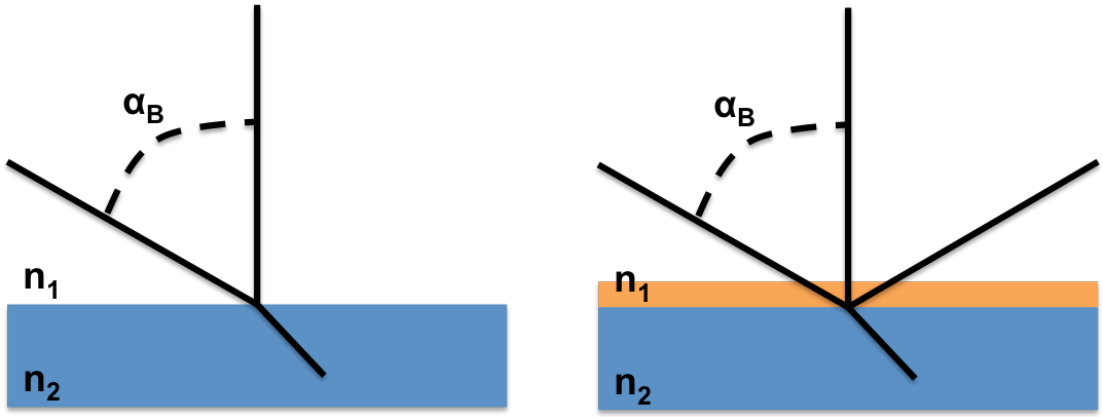

Fig. 2.17 - Schematic representation of Brewster angle microscopy at the air-water interface. left) The Brewster condition is satisfied and no reflection from the surface is observed, right) an amphiphilic monolayer is spread at the air-water interface causing the Brewster condition to no longer be satisfied and reflection to occur. This allows the direct visualization of the lateral monolayer.

If a microscope coupled to a charge coupled device camera is positioned at the Brewster angle then direct visualization of the lateral layer becomes possible.

2.10 Quartz Crystal Microbalance

The QCM is a technique in which nanograms of material adsorbing to the surface of a material can be investigated[65]. The technique became widely applicable after the demonstration of the relationship between the change in frequency associated with the adsorption of mass onto an oscillating quartz crystal[66]. Today the technique is commonly used to interrogate the adsorption of lipid monolayers onto solid-supported surfaces[67 68], to probe protein interactions with biomaterial surfaces[65 69 70], to follow the formation of polymeric films on surfaces[71 72] and to monitor cell adhesion in attempts to improve biocompatibility[73].

The key principle of the QCM technique is to apply a sufficient alternating electrical field across a quartz crystal, which will induce an oscillating expansion and contraction of the crystal at or close to its resonant frequency[65 72]. The experimental set-up of a typical QCM is shown in figure 2.18.

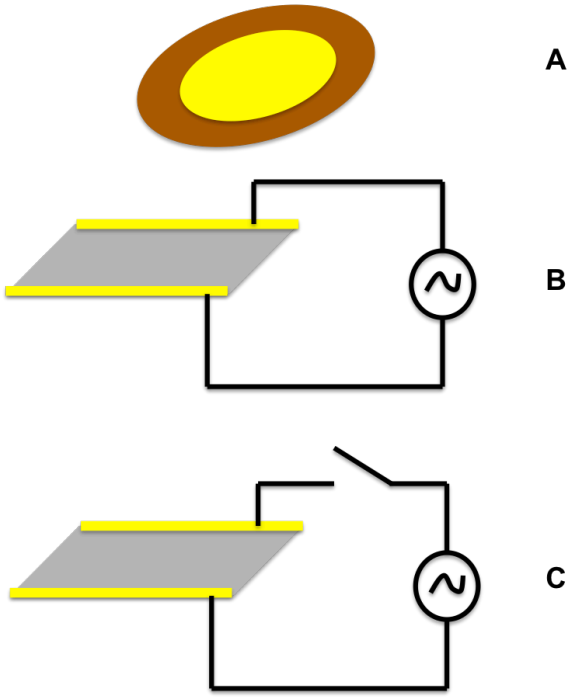

Fig 2.18 – Schematic representation of a) QCM quartz electrode with surrounding electrodes b) the QCM in frequency-mass detection mode c) the QCM in dissipation mode.

The adsorption of any mass to the surface of the oscillating quartz crystal will act to dampen, or reduce, the frequency at which it oscillates. This yields a frequency-time plot and allows the investigator to track mass adsorption with time. A schematic frequency-time plot can be seen in figure 2.19. This characteristic frequency change is directly proportional to the adsorbed mass on the surface and can be shown by the Saurbrey equation[66 72],

$$\Delta f = \left[\frac{-2 f_{ro}^2}{A\sqrt{\rho_q G_q}} \right] \qquad \text{(equation 2.23),}$$

where Δf is the change in frequency upon mass loading, f_{ro} is the resonance frequency of the quartz crystal without mass adsorbed, ρ_q and G_q are the density and shear modulus of the quartz crystal and A is the surface area of the resonating crystal. Most of the parameters within this equation are constants and it is much more common to write the equation in its simpler form,

$$\Delta m = -C.\frac{1}{n}.\Delta f \qquad \text{(equation 2.24)},$$

where n is the harmonic number and C is a constant given by,

$$C = \frac{t_q.\rho_q}{f_{ro}} \qquad \text{(equation 2.25)},$$

where t_q is the thickness of the quartz crystal.

For the Saurbrey model to be valid and accurately represent the mass loaded on the surface of the crystal, three assumptions must be made. The adsorbed mass must be much smaller than the mass of the quartz crystal, the adsorbed mass must be rigidly coupled to the surface of interest and therefore behave elastically similar to that of the quartz crystal itself and the adsorbed species must be evenly distributed over the active area of the crystal[65 66 72].

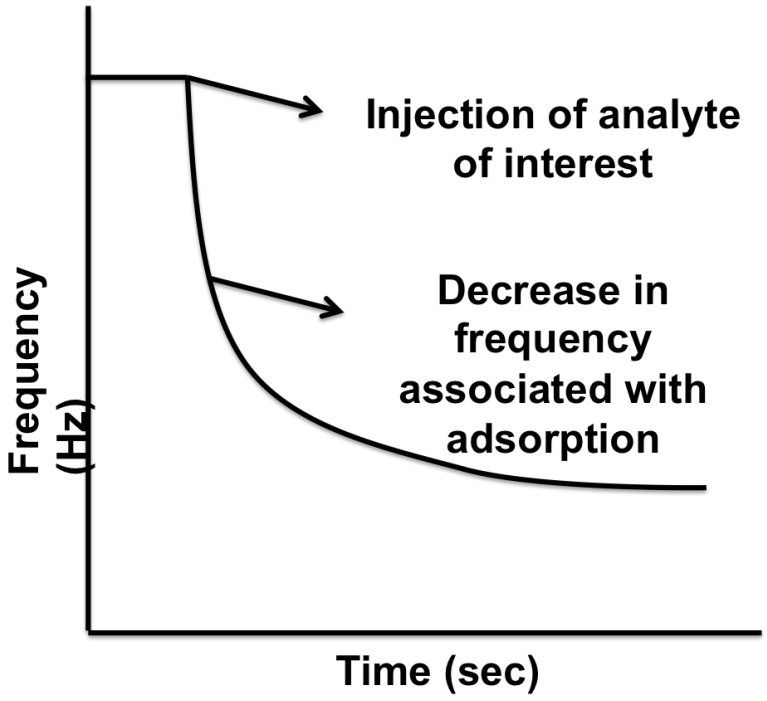

Fig 2.19- Schematic example of a frequency-time plot

Usually for a given QCM experiment the adsorbed mass is sufficiently lower than the mass of the crystal (given that this is a nanogram sensitive technique). It is also common for the adsorbed mass to be evenly distributed over the active surface area of the crystal. There is, however, difficulty in establishing how well coupled the adsorbed layer is to the quartz crystal itself. There is much controversy within the literature about the validity of the Saurbrey equation under highly visco-elastic conditions. Indeed it is generally believed that a highly visco-elastic layer will not elastically behave in a similar manner to the quartz crystal and therefore oscillate out-of-phase with the crystal, thus the Saurbrey model will under-estimate the adsorbed mass on the surface[72]. Under such circumstances the QCM with dissipation monitoring can be used to assess the visco-elastic nature of the adsorbed mass and predict whether or not the Saurbrey model is valid.

QCM with dissipation (also shown schematically in figure 2.16) monitoring allows the assessment of the decay in oscillation (energy loss throughout the system) after the applied AC voltage has been switched off[74]. The amplitude of oscillation will gradually decay and will be dependent solely on the properties of the adsorbed mass (as the quartz crystal remains constant)[75 76]. This decay in frequency (or amplitude of oscillation), f_0 can be compared with a reference frequency f_R and the difference fit to an exponentially damped sinusoidal function[65],

$$A(t) = A_0 e^{\frac{\tau}{\mathrm{T}}} \sin(2\pi f t + \alpha) \qquad \text{(equation 2.26),}$$

where $f=f_0-f_R$, the dissipation factor can then be shown by,

$$D = \frac{1}{\pi f \mathrm{T}} \qquad \text{(equation 2.27).}$$

The dissipation factor is dimensionless and can be defined by the following,

$$D = \frac{E_{dissipated}}{2\pi E_{stored}} \qquad \text{(equation 2.28),}$$

where $E_{dissipated}$ is the energy lost during a single oscillatory cycle, E_{stored} the energy retained during one oscillatory cycle[65].

2.10 Langmuir Trough

Molecular asymmetry associated with amphiphilic species dictates that these molecules will have a natural tendency to seek the surface of water and if the hydrophobic chain is sufficiently long, the amphiphile becomes insoluble in water and forms an isolated two-dimensional monolayer upon the surface of water[77]. This is known as a Langmuir monolayer and can be seen in figure 2.20.

The most useful tool for studying a Langmuir monolayer is a film balance or, as it is more commonly known, a Langmuir trough. A Langmuir trough consists of a trough made from polytetrafluoroethylene (PTFE, Teflon ®) which houses a liquid sub-phase (usually water). A lipid or surfactant is then dissolved in a solvent, which is immiscible with the sub-phase and is highly volatile (chloroform is often used). The chloroform – lipid solution is then dropped onto the surface of the liquid and once all of the solvent has evaporated a monomolecular lipid film is left[32]. A moveable barrier allows for the manipulation of the film through compression and expansion. Compressing the film leads to a decrease in the monolayer area per molecule ($Å^2$ mol^{-1}) and an increase in the surface pressure (mNm^{-1}). The monolayer surface pressure, π, is defined as the difference between the surface tension of the sub-phase without a film γ_0 and the surface tension of the film covered by a film γ [78]:

$$\pi = \gamma_0 - \gamma \qquad \text{(equation 2.29).}$$

By measuring lateral film pressure as a function of molecular area it is possible to obtain a surface pressure – area isotherm.

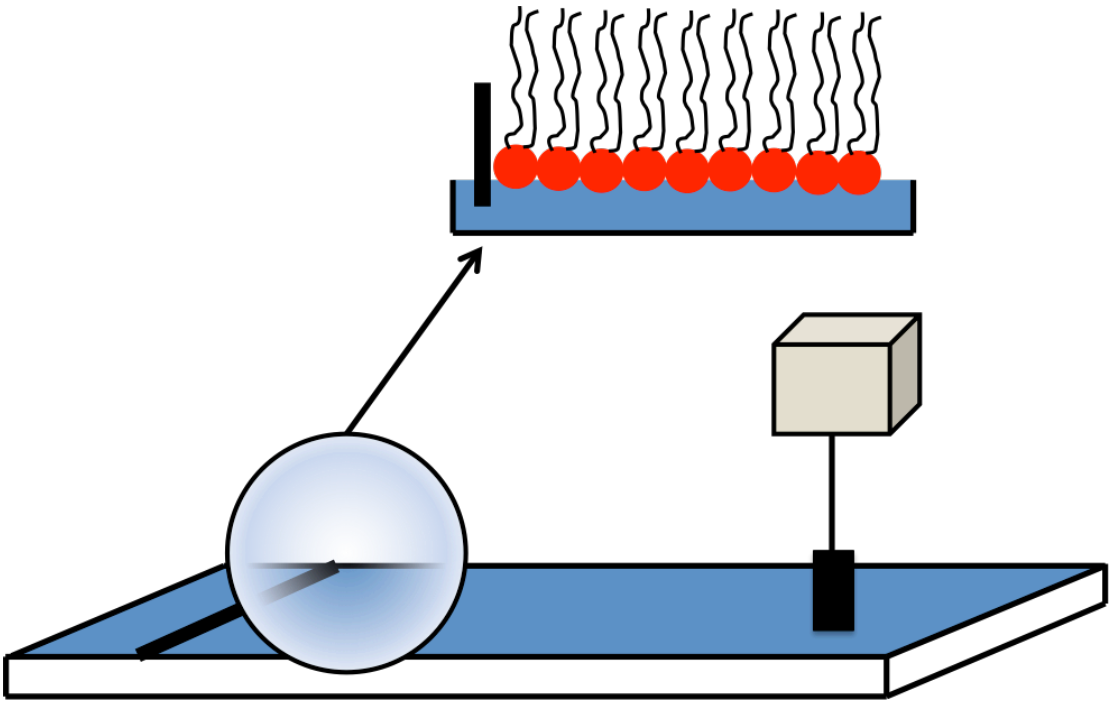

Fig. 2.20- Diagram to show set-up of a Langmuir trough; highlighting the moveable barrier and the Wilhelmy plate.

The Langmuir trough is designed in such a way as to allow the movement of the barriers to allow water molecules to flow freely underneath them but still maintain the overall composition of the insoluble monomolecular film whilst increasing or decreasing the lateral surface pressure.

The Langmuir trough can therefore be used to study the two dimensional phase behaviour of a surfactant or lipid throughout lateral compression up until the collapse point of the monolayer where three-dimensional structures are formed. The theory behind these phase changes is explained in the introduction (chapter 1.0).

2.11.1 The Wilhelmy plate

Figure 2.21 shows a schematic representation of the Wilhemy plate set-up along with parameters used to calculate the surface tension and therefore the surface pressure.

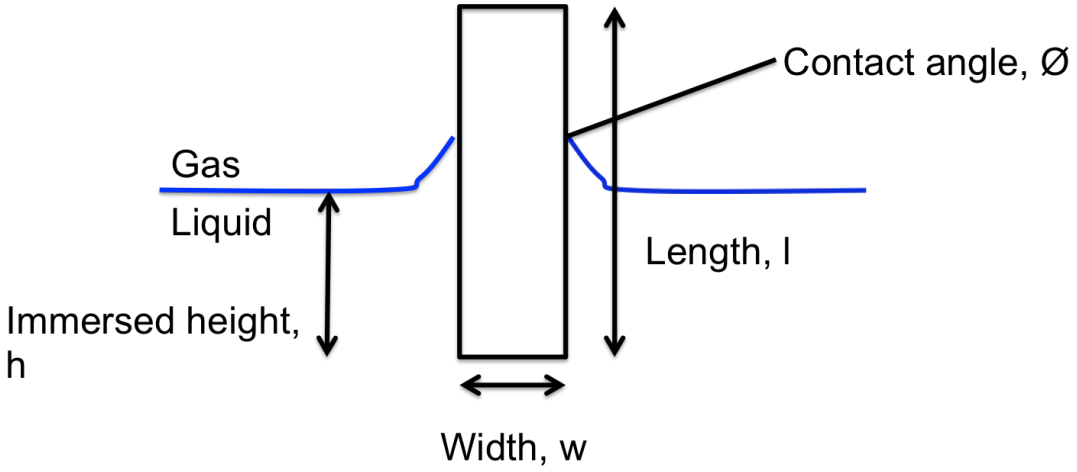

Fig 2.21- Schematic representation of the Wilhelmy plate set-up.

When the plate is immersed into the water sub-phase, there are a number of forces acting upon it. These consist of the weight of the plate itself, the upthrust on the immersed part of the plate and the surface tension of the liquid acting on the plate[79]. The dimensions of the plate can be defined from its length, width and thickness (l x w x t), along with the height at which it is submerged in the water. A summation of the forces acting on the plate can be defined as,

$$Force = (\rho_P lwt).g - (\rho_L hwt).g + 2.(w+t).ST.\cos\theta \quad \text{(equation 2.30)},$$

where ρ_P is the density of the plate, ρ_L is the density of the liquid, ST is the surface tension of the liquid sub-phase, θ is the contact angle the liquid makes with the plate and g is a correction factor due to the acceleration of gravity[80].

At the start of a Langmuir trough experiment, the surface balance is always zeroed. This negates the effect of the weight of the plate itself and reduces equation 2.30 to just the upthrust the immersed part of the plate experiences and the surface tension[80],

$$Force = -(\rho_L hwt).g + 2.(w+t).ST.\cos\theta \quad \text{(equation 2.31).}$$

The Wilhelmy plate is immersed in the water sub-phase for extended periods of time before any measurement is made, allowing it to be perfectly wetted. This ensures that the liquid meniscus will form where the plate passes through the liquid, giving a contact angle of zero. The force and upthrust acting on the plate can all be measured and hence the surface tension can be calculated[81].

2.12 Materials and Methods

The materials and methods section has been split up into each results chapter. This was designed to make it easier for the reader to follow. Specific specifications of each instrument will be given here. For more general theoretical aspects of each technique the reader is asked to refer back to sections 2.0-2.8 of this chapter.

2.12.1 Materials and methods for chapter 3 "Langmuir monolayers composed of sulfobetaine surfactants"

Materials

1-Bromoeicosane, 1-Bromodocosane, 1,3-propanesultone, 1,4-butanesultone dimethylamine (5.6 M ethanolic solution), NaCl, $CaCl_2$ and $NaClO_4$ were purchased from Sigma-Aldrich (U.K) at purity levels of 96 % or higher. N,N-dimethyloctadecylamine was purchased from Fischer Scientific (U.S.A) at a purity level of 96 %. N,N-di-n-methyloctadecylamine was purchased from ABCR Chemicals (Germany) at a purity level of 95 %.

Bromooctadecane-d_{37} was purchased from CDN Isotopes (Canada) at a purity level of 98 % and 98 atom % D. All chemicals were used without further purification. Deionized water was purified with a Milli-Q Plus system (Millipore, Germany) to achieve a resistivity of 18 MΩ cm.

Surfactant synthesis

Single tail 18 carbon chain sulfobetaines

All amines used were prepared according to Menger[82]. Under an atmosphere of N_2, to either 1-bromo-$^2H_{37}$-octadecane, 1-bromoeicosane or 1-bromodocosane (1.35 mmol, 1.00 eq.) in ethanol (2.00 mL) was added dropwise an ethanolic solution of dimethylamine (5.6M, 2.41 mL, 13.5 mmol, 10.0 eq.). The mixture was heated at 75 °C for 21 hr, and allowed to cool. The solution was concentrated under reduced pressure. To the resultant white solid was added NaOH (1.0M, 30 mL) and hexane (30 mL). The phases were separated and the aqueous layer was further extracted with hexane (3 x 30 mL). The combined organic extracts were dried over anhydrous $MgSO_4$, filtered and concentrated under reduced pressure to give N-*(($^2H_{37}$-octadecyl)*-N,N-*dimethylamine* (226 mg, 50%), as an oily white solid (m.p. 21-24 °C), N-*((eicosyl)*-N,N-*dimethylamine* (51% yield) as an oily white solid (m.p. 21-24 °C) or N-*((docosyl)*-N,N-*dimethylamine* (58% yield) as an oily white solid (m.p. 21-24 °C).

The deuterated SB3-18, hydrogenated SB3-20 and SB3-22 were then prepared according to Guangmiao *et al*[83]. Under an atmosphere of air, to a solution of *N*-(($^2H_{37}$-octadecyl)-*N,N*-dimethylamine, N-*((eicosyl)*-N,N-*dimethylamine* or N-*((docosyl)*-N,N-*dimethylamine* (0.564 mmol, 1.00 eq.) in acetone (2.0 mL) was added a solution of 1,3-propanesultone (2.82 mmol, 5.00 eq.) in acetone (3.0 mL). The mixture was heated at reflux for 18 hr, then allowed to cool. The white solid was filtered off and washed with acetone to give the crude product, which was purified by crystallisation from methanol/acetone to give *3-[*N,N-*dimethyl*-N-*($^2H_{37}$)*-

octadecylammoniumyl]propane-1-sulfonate (d-SB3-18) (68% yield) as a white solid (m.p. 280-285 °C (dec.)), *3-[*N,N-*dimethyl*-N-*(H_{37})*-*eicosylammoniumyl]propane-1-sulfonate* (SB3-20) (65% yield) as a white solid (m.p. 260-280 °C (dec.)) or *3-[*N,N-*dimethyl*-N-*(H_{37})*-*docosylammoniumyl]propane-1-sulfonate* (SB3-22) (63% yield) as a white solid (m.p. 260-280 °C (dec.)).

SB4-18

This compound was prepared according to Guangmiao *et al*[83]. Under an atmosphere of air, to a solution of N,N-dimethyloctadecylamine (0.564 mmol, 1.00 eq.) in acetone (2.0 mL) was added a solution of 1,4-butanesultone (2.82 mmol, 5.00 eq.) in acetone (3.0 mL). The mixture was heated at reflux for 18 hr, then allowed to cool. The white solid was filtered off and washed with acetone to give the crude product, which was purified by crystallisation from methanol/acetone to give *3-[*N,N-*dimethyl*-N-*($^2H_{37}$)*-*octadecylammoniumyl]propane-1-sulfonate* (40% yield) as a white solid (m.p. 260-280 °C (dec.)).

SB3-18-2

This compound was prepared according to Qu *et al*[83]. Under an atmosphere of air, to a solution of N,N-di-n-methyloctadecylamine (0.564 mmol, 1.00 eq.) in acetone (2.0 mL) was added a solution of 1,4-butanesultone (2.82 mmol, 5.00 eq.) in acetone (3.0 mL). The mixture was heated at reflux for 18 hr, then allowed to cool. The white solid was filtered off and washed with acetone to give the crude product, which was purified by crystallisation from methanol/acetone to give *3-[*N,N-*methyl*-N-*(H_{74})*-*dioctadecylammoniumyl]propane-1-sulfonate* (77% yield) as a white solid (m.p. 260-280 °C (dec.)).

Characterisation

d-SB3-18: dH (250 MHz, $CDCl_3$) 2.21 (s, 6H, 1-CH_3); dC (75 MHz, $CDCl_3$) 45.7 (1-C); ν_{max} (film) 2941, 2813, 2763, 2668, 2626, 2193, 2089, 1465, 1260, 1086, 1017, 946, 800

SB3-20: dH (300 MHz, CH_3OD): 0.89 (3H, t, -$(CH_2)_{18}$-$C\underline{H_3}$) 1.29 (36H, m, -$(C\underline{H_2})_{18}$-) 1.78 (2H, m, N^+-CH_2-$(CH_2)_{18}$-) 2.18 (2H, tt, SO_3^--CH_2-$C\underline{H_2}$-) 2.87 (2H, t, SO_3^--$C\underline{H_2}$-) 3.08 (6H, s, N^+-$C\underline{H_3}$) 3.49 (2H, m, SO_3^--CH_2-CH_2-$C\underline{H_2}$-); ν_{max} (film): 3039, 2959, 2918, 2851, 1468, 1240, 1227, 1215, 1196, 1183, 1139, 1123, 1039, 1030, 752, 719

SB3-22*:* dH (300 MHz, CH_3OD): 0.90 (3H, t, -$(CH_2)_{20}$-$C\underline{H_3}$) 1.29 (40H, m, -$(C\underline{H_2})_{20}$-) 1.77 (2H, m, N^+-CH_2-$(CH_2)_{20}$-) 2.18 (2H, tt, SO_3^--CH_2-$C\underline{H_2}$-) 2.87 (2H, t, SO_3^--$C\underline{H_2}$-) 3.08 (6H, s, N^+-$C\underline{H_3}$) 3.50 (2H, m, SO_3^--CH_2-CH_2-$C\underline{H_2}$-); ν_{max} (film): 3039, 2959, 2918, 2851, 1468, 1412, 1317, 1229, 1197, 1182, 1169, 1139, 1123, 1038, 999, 984, 966, 753, 71

SB4-18: dH (300 MHz, CH_3OD): 0.90 (3H, t, -$(CH_2)_{16}$-$C\underline{H_3}$) 1.26 (32H, m, -$(C\underline{H_2})_{16}$-); ν_{max} (film): 3034, 2917, 2850, 1018, 1491, 1471, 1223, 1200, 1182, 1152, 1063, 1037, 720, 607

SB3-18-2: dH (300 MHz, CH_3OD): 0.89 (6H, t, -$(CH_2)_{16}$-$C\underline{H_3}$) 1.26 (64H, m, -$(C\underline{H_2})_{16}$-) 1.69 (4H, m, N^+-$C\underline{H_2}$-$(CH_2)_{16}$-) 2.26 (2H, m, O_3S^--CH_2-$C\underline{H_2}$-) 2.98 (2H, t, O_3S^--$C\underline{H_2}$-) 3.24 (3H, m, N^+-$C\underline{H_3}$) 3.76 (2H, m, SO_3^--CH_2-CH_2-$C\underline{H_2}$-); ν_{max} (film): 2954, 2916, 2872, 2850, 1655, 1483, 1471, 1249, 1204, 1189, 1178, 1038, 717, 608

Langmuir Trough Studies

Monolayers of the insoluble surfactant were prepared by the deposition of a 100 µl surfactant solution (0.5 mg ml^{-1} in chloroform) over the sub-phase. Ten minutes was allowed for chloroform evaporation. Surface pressure -

Area (π-A) isotherm measurements were carried out using a Nima Technology type 611 Langmuir trough with an area of 700 cm^2, using a 1cm wide Wilhelmy plate sensor. All metal ion sub-phases used were at a concentration of 50 mM to ensure sufficient interaction of ions with the surfactant head groups. π-A isotherm measurements were conducted using a double-barrier compression system at a compression rate of 20 cm^2 min^{-1} to ensure high resolution in the resulting isotherms. All the isotherms reported in this paper are the averages of at least three experiments.

Brewster angle microscopy studies

BAM studies were conducted using a Nanofilm EP3 imaging ellipsometer (532 nm). Monolayers were prepared as above on a purpose made Nima 712BAM trough. The BAM images were recorded periodically throughout continuous compression (at the same rate as above).

XRR Studies

All XRR measurements were conducted using beamline I07 at Diamond Light Source (Oxford, U.K) using the “double crystal deflector” (DCD) for reflectivity from liquid interfaces[25] . All reflectivity experiments in this study were conducted at an incident beam energy of 12.5 keV. Data was collected using a region of interest on a Pilatus 100k detector to integrate the specular reflection, while a second region of interest of the same size was used to approximately subtract the background. A “footprint” correction[48] for over-illumination was applied to the data assuming a Gaussian beam profile and ignoring meniscus effects. The data was collected over three attenuation regimes and normalized to the critical edge. In order to minimize beam damage the trough was enclosed under a helium atmosphere, which helps to prevent lipid oxidation, and horizontally translated by small increments between each attenuation regime.

NR Studies

NR measurements for SB3-18 were conducted using the INTER beamline[26] on Target Station 2 at the ISIS pulsed neutron source (Oxford, U.K). NR measurements for SB3-18_2 were conducted on the SURF beamline on Target Station 1 of the same neutron source. Measurements utilized a single detector and fixed grazing incidence angles of 0.8° and 2.3°. Absolute reflectivity was calibrated with respect to the direct beam and the reflectivity from a clean D_2O surface. NR experiments for SB3-18 were performed using two different contrasts. Hydrogenated SB3-18 (h-SB3-18) on D_2O and d-SB3-18 on air-contrast-matched-water (ACMW; 8mol% D_2O in H_2O). NR experiments for hydrogenated SB3-18_2 were also performed using two different contrasts 100 % D_2O and 70 % by volume D_2O.

In both XRR and NR experiments the surface pressure of the monolayer was controlled with a Nima trough (Custom model: 40x20cm). The monolayer was prepared as earlier but single barrier compression was used for XRR and double barrier for the NR experiments. Structural measurements were made at surface pressures of 15, 20 and 25 mNm^{-1}. These surface pressure measurements were chosen to track the monolayer through its compression isotherm.

2.12.2 Materials and methods for chapter 4 "Characterising protein interactions with functionalized phospholipid monolayers".

Materials

Chloro(dimethyl)octylsilane, trichloroethylene, Tris base, NaCl, H_2SO_4, H_2O_2 (30 wt. % in H_2O), hexadecane, octadecyltrichloro silane and dichloromethane were purchased from Sigma-Aldrich (U.K) at purity levels of 90 % or higher. Hellmanex was purchased from Hellma Analytics (Germany. Decon was purchased from Decon Laboratories (U.K). 1,2-dioleoyl-*sn*-glycero-3-[(N-(5-amino-1-carboxypentyl)iminodiacetic acid)succinyl] (nickel salt) (DOGS-NTA-Ni), 1,2-dioleoyl-*sn*-glycero-3-phosphocholine (DOPC) and 1,2-Dimyristoyl-*sn*-Glycero-3-Phosphocholine (DMPC) were purchased from

Avanti Polar Lipids (U.S.A) at purity levels of 99 %. All chemicals were used without purification.

Methods

Expression and purification of Penicillin binding protein 3

The protein was produced in collaboration with the Oxford Protein Production Facility, Oxford, U.K. The protein was expressed and purified using the protocol set out by Sainsbury *et al*[84]. The protein was overexpressed in *E.coli* strain Rosetta *p*LysS (DE3) using autoinduction[85]. The cells were grown in 2L cultures of Overnight Express Instant TB media (Merck) at 37 °C for 4 hours, after which the temperature was reduced to 25 °C. The cells were then left to incubate for a further 20 hours, after which they were harvested by centrifugation for 15 minutes at 6000g and lysed using a Basic-Z Cell Disruptor (Constant Systems) at 30, 000 psi in the presence of Tris-HCl (pH 7.5), 500 mM NaCl, 0.2 % Tween-20, 10 µg/ml DNase and an ethylenediaminetetraacetic acid free Protease Inhibitor Cocktail Tablet (Roche). The lysed cells were then centrifuged at 16, 000g for 30 minutes in order to remove unwanted cell debris and the soluble freaction was loaded onto a 1 ml His Trap FF column (GE Healthcare). Before the elution of the protein the column was washed with 50 mM Tris-HCl (pH 7.5), 500 mM NaCl and 500 mM imidazole. The protein was then injected onto a 16/60 HiLoad Superdex 75 column (GE Healthcare) and eluted in 20 mM Tris-HCl (pH 7.5) and 200 mM NaCl. Protein containing fractions were combined, yielding an overall protein concentration of 1.1 mg/ml. The protein was split into 50 µl aliquots, flash frozen and stored at -80 °C.

Vesicle preparation

100 mol % DMPC, 1, 5 and 10 mol % DOGS:DMPC vesicles were prepared from stock solutions of the lipids at a concentration of 0.5 mg/ml. The chloroform was then evaporated under a stream of N_2 gas until dry. The

formed lipid film was then re-hydrated, under vortexing, in buffer (20 mM NaCl, 20 mM Tris, pH 7.5). the lipid solution was then subjected to three freeze-thaw cycles using a series of liquid nitrogen and warm water. The samples were then extruded through 200 nm polycarbonate filters (Whatman) using a LipoFast LF-50 nitrogen extruder at 2.5 bar. The heating jacket controlled by a water bath was maintained at 30 °C. Samples were extruded a total of four times until the solution was clear.

Protein was added from a 1.1 mg/ml stock solutions in 50 µl aliquots in in 20mM NaCl, 20 mM Tris, pH 7.5 buffer. The protein stock solution was stored at -80 °C until needed, removed and equilibrated to room temperature. The sample was mixed and allowed to stand for 30 minutes before analysis.

Vesicle Characterisation

Extruded lipid vesicles were analysed at 25 °C using an Anton Paar SAXSess laboratory small angle x-ray scattering instrument with a Panalytical PW3830 x-ray generator (1.54 Å Cu Kα). The samples were exposed for 20 hours after which the detector image plates were read using a Perkin Elmer storage Phosphor system Cyclone ™. The image plates were always read within 10 minutes of the experiment finishing. Data was extracted using SAXSquant 3.50 software.

All lipid vesicles were analysed at 23 °C by DLS using a Zetasizer Nano ZS (Malvern instruments). A laser (623 nm) was used to illuminate the sample with scattering detected at a fixed angle of 173 °. Samples were filtered through 4 mm PVDF syringe filters of 450 nm pore size prior to analysis to prevent artefacts caused by large contaminating particles. Data was exported to IGOR Pro software and log-normal distributions were fit to the data as a function of intensity distribution.

BAM Studies

BAM studies were conducted using a Nanofilm EP3 imaging ellipsometer. 10µg/ml protein solutions in buffer (20 mM Tris, 20 mM NaCl, pH 7.5) were

placed in a custom built trough of 20 x 30 mm dimensions. 20 µl of either a 5, 10 or 20 mol % DOGS:DMPC lipid solution in chloroform (0.5 mg/ml) was then added drop-wise to the surface to form a monolayer, which was observed over around 100 minutes. Protein interaction with this monolayer was imaged periodically throughout the experiment and the time recorded.

QCM Studies

All QCM studies were conducted using a QSense E4 instrument (QSense, Sweden). This is a 4 channel system with dissipation monitioring and a HPLC pump for sample injection. Studies were conducted at 25 $^{\circ}$C maintained by a heating plate within the sample chamber. QCM quartz crystals functionalized with SiO_2 (Qsense, Sweden) were rinsed with water and ethanol and then dried under N_2 gas. The crystals were then placed onto a clean glass plate and cleaned via UV-Ozone treatment. The QCM crystals were then hydrophobised by placement into a dessicator with an attached vacuum pump. At the bottom was placed 5 ml of chloro(dimethyl)octylsilane. The vacuum pump was switched on and left over night. The QCM crystals were then removed and sonicated in trichloroethylene three times, followed by a final rinse in ethanol.

Before use the QCM sample chamber was rinsed through with a 2 % Hellmanex solution, then ethanol and copious amounts of water. The QCM crystals were then added to the sample chambers and the frequency was set to zero.

Lipid monolayers were prepared from stock solutions of DOPC and DOGS-NTA-Ni at 0.5 mg/ml. 100 mol % DOPC, 5 10 and 20 mol % DOGS-NTA-Ni were prepared and the chloroform evaporated under a stream of N_2 gas until a lipid film was present on the walls of the sample vial. The lipid films were then re-hydrated in 20 mM Tris, 20 mM NaCl, pH 7.5 buffer under vortexing. The lipid solution was then sonicated using a probe sonicator at 40 % power for 7 minutes or until the solution was clear. The lipid solution was kept on

ice throughout sonication. To remove TiO_2 obtained from the tip sonicator the resultant clear solution was then centrifuged at 1500 rpm for 6 minutes or until a black spot was visible at the bottom of the centrifuge tube. The supernatant lipid solution was then removed and transferred to a clean sample vial, leaving behind the TiO_2.

Lipid solutions were then injected into the sample cells at a rate of 0.1 ml/min and the experiment was stopped when both dissipation and frequency plateaued. The frequency was then normalized back to zero and protein was injected into the sample cells at concentrations of 5-25 μg/ml (in increments of 5 μg/ml) at a rate of 0.1 ml/min. The experiment was stopped when both the dissipation and frequency had plateaued.

NR Studies

NR measurements were conducted using the INTER beamline[26] on Target Station 2 at the ISIS Pulsed Neutron Source (Oxford, U.K). Measurements utilized a single detector and fixed grazing incidence angles of 0.7° and 2.3°. Absolute reflectivity was calibrated with respect to the direct beam and the reflectivity from a clean silicon block in the sample cell filled with D_2O.

Neutron reflectometry was completed upon silicon blocks of 8 x 5 x 1.5 cm dimensions housed in a purpose built PEEK sample cell with Teflon© inserts to hold the silicon blocks in place. The sample cells and all tubing were rinsed with a 2 % Decon solution followed by copious amounts of MiliQ water to ensure cleanliness. Prior to the experiment all silicon blocks were immersed in a Piranha solution (33 % H_2O, 50 % H_2SO_4, 17 % H_2O_2) for 15 minutes, under stirring at 80 °C. The blocks were then removed and sonicated in ethanol and then water for 3 x 15 minutes each.

To hydrophobise the silicon blocks they were placed in a solution of hexadecane containing 1 mM octadecyltrichlorosilane and left to stir for a minimum of 4 hours. Care was taken to ensure that the beakers were sealed

with parafilm to prevent large amounts of water penetration. The blocks were then removed and immediately placed in dichloromethane and sonicated for 15 minutes. This is to ensure the removal of any unpolymerised OTS from the surface. The blocks were then sonicated in ethanol for 3 x 15 minutes. OTS blocks were placed into the sample cell and measured in D_2O, 4MW and H_2O.

Lipid solutions were prepared as described in the QCM studies section and were injected into the sample cell. Thirty minutes was allowed for vesicle depositon at which point the sample cells were rinsed with buffer. They were then characterized in D_2O, 4MW and H_2O. Protein injection was as described in the QCM studies section and 30 minutes was allowed for protein adsorption. The protein layer was then characterized in D_2O, 4MW and H_2O.

2.12.3 Materials and methods for chapter 5 "Nanodisc interactions with phospholipid monolayers".

Materials

HCl, NaOH, styrene, maleic anhydride, 2-(Dodecylthiocarbonothioylthio)-2-methylpropanoic acid (DDMAT), *α,α'*-Azoisobutyronitrile (AIBN), dioxane, 2-Oleoyl-1-palmitoyl-*sn*-glycero-3-phosphocholine (POPC) and dioctadecyldimethylammonium bromide (DODAB) were all purchased from Sigma-Aldrich (U.K). All were purchased at a purity level of 96 % or higher and used without further purification. The only exceptions were AIBN, which was re-crystallised from methanol, and styrene, which was purified using a silica column to remove the inhibitor. 1,2-dimyristoyl-d54-*sn*-glycero-3-phosphocholine (d-DMPC) and 1,2-dimyristoyl-d54-*sn*-glycero-3-[phospho-*rac*-(1-glycerol)] (sodium salt) (d-DMPG) were purchased from Avanti Polar Lipids (U.S.A). They were purchased at purity levels of 99 % and 98 % atom D. They were used without further purification.

Methods

Polymer synthesis

The encapsulating polystyrene-co-maleic acid belt which stabilizes the nanodisc was synthesized according to Harrison *et al*[86]. This is a RAFT polymerization process. 500 mg of styrene, 202 mg of maleic anhydride, 3.8mg of DDMAT, 3.43 mg of AIBN and 0.7 ml of dioxane were added to a sealed single necked round bottom flask with a magnetic stirrer under an atmosphere of N_2. The content within the flask was de-gassed and re-filled with N_2 via three consecutive freeze-thaw cycles. The flask was covered with aluminium foil to avoid radical initiator (AIBN) degradation. The solution was then heated to 60 °C under stirring for 21 hours and then allowed to cool to room temperature. Once cooled the polymer was precipitated in ice-cold diethyl ether three times. The precipitate was collected using a Buchner filter and a nylon filter. This was then dried overnight at a temperature of 40 °C. This resulted in the synthesis of polystyrene-co-maleic anhydride. This process is shown schematically in figure 2.22.

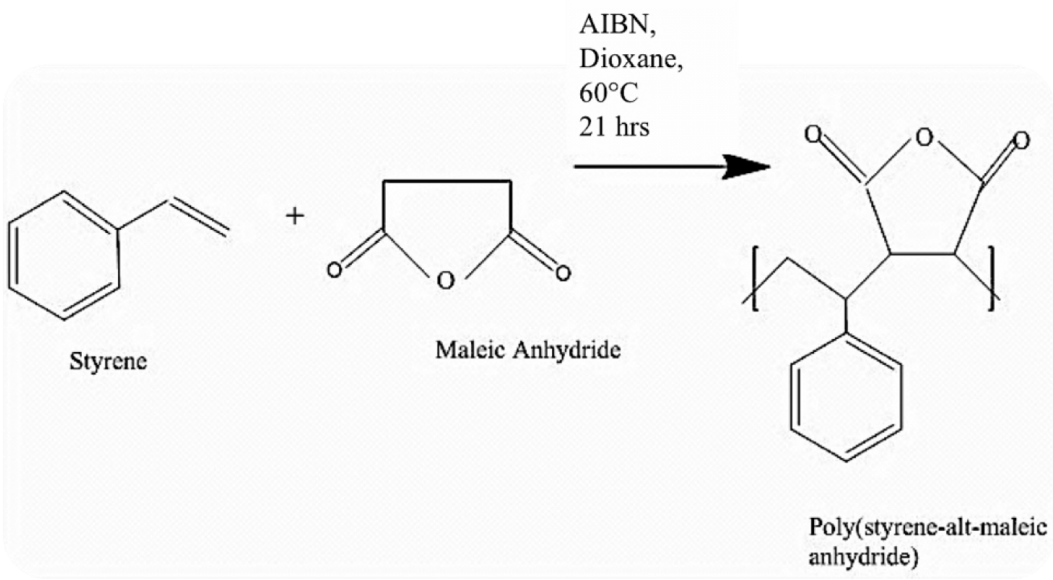

Fig 2.22- Synthesis of polystyrene-co-maleic anhydride.

The precipitate was then converted to polystyrene-co-maleic acid via reflux under basic conditions. The polystyrene-co-maleic anhydride was added to a 50 ml of a 2 M NaOH solution and refluxed for 3 hours. The solution was allowed to cool to room temperature. Added drop-wise to this was 500 ml of a 2 M HCl solution. The resulting cloudy mixture was then centrifuged at 5000 rpm for 10 minutes where a polymer pellet formed at the bottom of the centrifuge tube. The pellet was then re-dissolved in a small amount of 2 M HCl and centrifuged once more. This process was completed three times. The final polymer pellet was then dissolved in a minimum amount of 1 M NaOH and freeze dried overnight.

For a confirmation of polymer synthesis see the appendix of this thesis. Polymer synthesis was confirmed using NMR, FTIR and GPC.

Nanodisc formation

Nanodiscs were prepared according to Jamshad *et al*[87]. A 0.5 wt % lipid solution was made by adding 0.025 g of the relevant phospholipid(s) to 3.92ml of buffer (50 mM phosphate buffer, 200 mM NaCl, pH 8). This solution was sonictaed for around 10 minutes to enable lipid dispersion within the buffer. 1.08 ml of a 6.5 wt % polystyrene-co-maleic acid solution in buffer was then added to the lipid suspension, giving a final co-polymer concentration of 1.5 wt %.This solution was agitated by hand for 5 minutes in order to accelerate the self-assembly process. At the end the solution was completely clear, indicating the formation of nanodiscs.

NR at the air-water interface

Neutron reflectometry at the air-water interface was conducted using Teflon troughs of dimensions 15.2 x 4.2 x 0.3 cm. Nanodisc solutions composed of deuterated phospholipids (either 100 % d-DMPC or 25 % d-DMPG:d-DMPC) were made up in either D_2O or ACMW buffer (50 mM phosphate buffer, 200mM NaCl, pH 8) as described in the previous section. 5 ml of this solution

was then added to 25 ml of either D_2O or ACMW buffer and poured into the Teflon trough. Subsequently either a 0.5 mg/ml of h-POPC or h-DODAB was deposited over these solutions to a surface pressure of 15 mNm^{-1}. Surface pressure was recorded using a Nima technology surface pressure sensor. Measurements were also taken in an analogous way but with the nanodiscs absent in order to characterize the lipid monolayers on their own.

NR measurements at the air-water interface were conducted using the INTER beamline[26] on Target Station 2 at the ISIS Pulsed Neutron Source (Oxford, U.K). Measurements utilized a single detector and fixed grazing incidence angles of 0.8° and 2.3°. Absolute reflectivity was calibrated with respect to the direct beam and the reflectivity from a clean silicon block in the sample cell filled with D_2O.

NR at the solid-liquid interface

Two neutron reflectometry experiments were conducted at the solid-liquid interface. One for the empty nanodiscs and another for nanodiscs encapsulated with a membrane protein.

Empty nanodiscs

NR studies for the empty nanodiscs were completed on the OFFSPEC beamline on target station 2 at the ISIS spallation source. Measurements utilized a single detector and fixed grazing incidence angles of 0.5, 1.0 and 2.0°. Absolute reflectivity was calibrated with respect to the direct beam and the reflectivity from a clean silicon block in the sample cell filled with D_2O.

NR measurements were conducted on silicon blocks of 8 x 5 x 1.5 cm dimensions. The cleaning of the blocks and the formation of OTS and DOPC monolayers were as described in section 2.11.2 for the soluble protein studies. DODAB monolayers were formed in an analogous way but utilizing a 0.5 mg/ml DODAB stock solution. 5 ml of nanodisc stock solution was prepared as described previously in D_2O, H_2O or 4MW buffer (50 mM

phosphate buffer, 200 mM NaCl, pH 8). The 5 ml nanodisc solutions were then injected into the sample cell where nanodisc adsorption was characterized in D_2O, H_2O and 4MW buffer contrasts. Around 30 minutes was allowed for nanodisc adsorption before data collection.

ZipA filled nanodiscs neutron reflectometry

Neutron reflectometry for the ZipA nanodiscs at the solid-liquid interface was conducted on the D17 beamline at the ILL reactor source. The preparation of ZipA nanodiscs is described in the following section. A 1.0 mg/ml stock solution of ZipA filled nanodiscs in H_2O buffer (20 mM phosphate buffer, 50mM NaCl, pH 8) was used to generate 25 µg/ml sample aliquots. 5 ml of these sample aliquots were injected into the sample cell in H_2O buffer where around 30 minutes was allowed for nanodisc adsorption. The preparation of DOPC:DOGS monolayers, OTS monolayers and cleaning of the silicon blocks was analogous to the methods described in section 2.10.2. Measurements were conducted at two fixed incident angles of 0.8 and 2.3°. Absolute reflectivity was calibrated with respect to the direct beam and the reflectivity from a clean silicon block in the sample cell filled with D_2O. Contrast measurements were preformed in D_2O, H_2O and either silicon matched water (SMW) or four matched water (4MW).

2.13 References

1. Cullity BD, Stock SR. *Elements of x-ray diffraction*. 3 ed: Pearson, 2013.
2. Smart LE, Moore EA. *Solid state chemistry: an introduction*. 4 ed: CRC Press, 2012.
3. Elder FR, Gurewitsch AM, Langmuir RV, et al. Radiation from electrons in a synchrotron. Physical Review 1947;**71**(11):829-30.
4. Bordovitsyn VA. *Synchrotron radiation theory and its development*. Russia.
5. Duke P. *Synchrotron radiation: production and properties*. Oxford: Oxford University Press, 2008.
6. Winick H. *Synchrotron radiation sources: A primer*: World scientific publishing Co., 1995.
7. Willmott P. *An introduction to synchrotron radiation*: Wiley-Blackwell, 2011.

8. Wiedemann H. *Synchrotron Radiation*. New York: Springer, 2003.
9. Riviere JC, Myhra S. *Handbook of surface and interface analysis: Methods for probem solving*: CRC Press, 1998.
10. Heenan R, Penfold J, King SM. SANS at pulsed neutron sources: Present and future prospects. Journal of Applied Crystallography 1997;**30**:1140-47.
11. Carpenter JM. Pulsed spallation neutron sources for slow neutron scattering. Nuclear instruments and methods 1977;**145**(1):91-113.
12. Willis BTM, Carlile CJ. *Experimental neutron scattering*. 2 ed. Oxford: Oxford University Press, 2013.
13. Wilson CC. A guided tour of ISIS- the UK spallation neutron source. Neutron News 1995;**6**(2):27-34.
14. Stacey WM. *Nuclear reactor physics*. 2 ed: Wiley, 2007.
15. Newton RG. *Scattering theory of waves and particles*. New York: Springer, 2014.
16. Sivia DS. *Elementary scattering theory*. Oxford: Oxford University Press, 2011.
17. Bunker G. *Introduction to XAFS: A practical guide to x-ray absorption fine structure spectroscopy*. 1 ed. Cambridge: Cambridge University Press, 2010.
18. Christillin P. Nuclear compton scattering. Journal of physics G: Nuclear physics 1986;**12**(9):837.
19. Schulke W. Inelastic x-ray scattering. Nuclear Instruments and Methods in Physics Research Section A: Accelerators, Spectrometers, Detectors and Associated Equipment 1989;**280**(2-3):338-48.
20. Hauser W, Feshbach H. The inelastic scattering of neutrons. Physical Reviews 1952;**87**:366.
21. Xemb T, Lindner P. *Neutrons, x-rays and light: Scattering methods applied to soft condensed matter*. 1 ed. Holland: Elsevier, 2002.
22. Bosio L, Benattar JJ, Rieutord F. X-ray and neutron reflectivity of a Langmuir monolayer on water. Physical Review Applied 1987;**22**:775-78.
23. Penfold J, Richardson RM, Zarbakhsh A, et al. Recent advances in the study of chemical surfaces and interfaces by specular neutron reflection. Journal of the Chemical Society, Faraday Transactions 1997;**93**(22):3899-917.
24. Penfold J, Thomas RK. The application of the specular reflection of neutrons to the study of surfaces and interfaces. Journal of physics: condensed matter 1990;**2**:1396-412.
25. Arnold T, Nicklin C, Rawle J, et al. Implementation of a beam deflection system for studies of liquid interfaces on beamline I07 at Diamond. Journal of Synchrotron Radiation 2012;**19**:408-16.
26. Webster J, Holt S, Dalgliesh. INTER the chemical interfaces reflectometer on target station 2 at ISIS. Physica B 2006;**385**:1164-66.
27. Dunning JR, Pegram GB, Fink GA, et al. Interaction of neutrons with matter. Physical Review 1935;**48**:265.
28. Agarwal BK. *Interaction of x-rays with matter*. New York: Springer, 1991.
29. Jacrot B, Zaccai G. Determination of molecular weight by neutron scattering. Biopolymers 1981;**20**(11):2413-26.

30. Helm CAM, H; Kjaer, K; Als-Nielsen, J. Phospholipid monolayer density distribution perpendicular to the water surface. A synchrotron x-ray reflectivity study. Europhysics Letters 1987;**4**(6):697-703.
31. Born M, Wolf E. *Principles of Optics*. Oxford: Pergamon, 1970.
32. Atkins PP, J. *Physical Chemistry*. 9 ed. Oxford: Oxford University Press, 2009.
33. Sears VF. Neutron scattering lengths and cross sections. Neutron News 1992;**3**(3):26-37.
34. Zhou XL, Chen SW. Theoretical foundation of x-ray and neutron reflectometry. Physics Reports 1995;**257**(4-5):223-348.
35. Daillant J, Gibaud A. *X-ray and neutron reflectivity*. New York: Springer, 2009.
36. Als-Nielsen J, Jacquemain D, Kjaer K, et al. Principles and applications of grazing incidence X-ray and neutron scattering from ordered molecular monolayers at the air-water interface. Physics Reports 1994;**246**(5):251-313.
37. Zhou X-L, Chen S-H. Theoretical foundation of X-ray and neutron reflectometry. Physics Reports 1995;**257**(4–5):223-348.
38. Thomas RK, Penfold J. Neutron and X-ray reflectometry of interfacial systems in colloid and polymer chemistry. Current Opinion in Colloid & Interface Science 1996;**1**(1):23-33.
39. Braslau A, Pershan PS, Swislow G, et al. Capillary waves on the surface of simple liquids measured by x-ray reflectivity. Physical Review 1988;**38**:2457.
40. Braslau A, Deutsch M, Pershan PS, et al. Surface roughness of water measured by x-ray reflectivity. Physical Review Letters 1985;**54**:114.
41. Chauvineau JP. Soft x-ray reflectometry applied to the evaluation of surface roughness variation during the deposition of thin films. Physical Review Applied 1988;**23**:1645-52.
42. Steyerl A. *Effect of surface roughness on the total reflection and transmission of slow neutrons*. 1 ed. New York: Springer, 1972.
43. de Boer DKG. Influence of roughness on the specular reflectivity of x-rays and neutrons. Physical Review B 1994;**49**:5817.
44. Sinha SK, Sirota EB, Garoff S, et al. X-ray and neutron scattering from rough surfaces. Physical Review B 1988;**38**:2297.
45. Nelson A. Co-refinement of multiple-contrast neutron/x-ray reflectivity data using MOTOFIT. Journal of Applied Crystallography 2006;**39**(2):273-76.
46. Heavens O. Optical properties of thin films. London: Butterworth, 1955.
47. Penfold J. Instrumentation for neutron reflectivity. Physica B: Condensed Matter 1991;**173**(1-2):1-10.
48. Gibaud A, Vignaud G. The correction of geometrical factors in the analysis of x-ray reflectivity. Acta Crystallographica 1993;**49**:642-48.
49. Lu JR, Thomas RK, Penfold J. Surfactant layers at the air/water interface: structure and composition. Advances in colloid and interface science 2000;**84**(1-3):143-304.
50. Dagliesh RM, Langridge S, Plomp J, et al. Offspec, the ISIS spin-echo reflectometer. Physica B 2011;**406**:2346-49.
51. Bucknall DG, Penfold J, Webster J, et al. SURF- a second generation neutron reflectometer. Proceedings of the meetings ICANS- XIII and ESS-PM4 1995;**27**(18):27061020.

52. Cubbit R, Fragneto G. D17: the new reflectometer at the ILL. Applied physics A: Materials science processing 2002;**74**:329-31.
53. Schartl W. *Light scattering from polymer solutions and nanoparticle dispersions*. 1 ed. New York: Springer, 2007.
54. Pecora R. *Dynamic light scattering: applications of photon correlation spectroscopy*. 1 ed. New York: Plenum Press, 1985.
55. Day RA, Robinson BH, Clarke JHR, et al. Characterisation of water-containing reversed micelles by viscosity and dynamic light scattering methods. Journal of the Chemical Society, Faraday Transactions 1979;**75**:132-39.
56. Zwanzig R, Harrison AK. Modifications of the Stokes-Einstein formula. The journal of chemical physics 1985;**83**:5861.
57. Jamieson SA, Tong KWK, Hamilton WA, et al. Small Angle Neutron Scattering (SANS) Studies on the Structural Evolution of Pyromellitamide Self-Assembled Gels. Langmuir 2014.
58. Svergun DI, Kock MH, Timmins PA, et al. *Small angle x-ray and neutron scattering of biological macromolecules*. 1 ed. Oxford: OUP, 2013.
59. Glatter O, Kratky O. *Small angle x-ray scattering*. 1 ed. London: Academic press inc., 1982.
60. Honig D, Mobius D. Brewster Angle Microscopy of LB films on solid substrates. Chemical Physics Letters 1991;**195**:50-52.
61. Honig DM, D. Direct visualisation of monolayers at the air-water interface by brewster angle microscopy. Journal of Physical Chemistry 1991;**95**(12):4590-92.
62. Henon SM, J. Microscope at the Brewster angle: Direct observation of first order transitions in Langmuir monolayers. Review of Scientific Instruments 1991;**64**(4):936-39.
63. McLoughlin D, Langevin D. Surface complexation of DNA with a cationic surfactant. Colloids and Surfaces A: Physiochemical Engineering Aspects 2004;**250**:79-87.
64. Kaercher T, Honig D, Mobius D. Brewster angle microscopy: A news method for visualising the spreading of Meibomian lipids. International Opthamology 1993;**17**:341-48.
65. Dixon MC. Quartz crystal microbalance with dissipation monitoring: Enabling real-time characterisation of biological materials and their interaction. Journal of biomolecular techniques 2008;**19**(3):151-58.
66. Saurbrey G. Verwendung von schwingsquarzen zur waegun dunner schichten und zur mikrowaegung. Zeitschrift fur physik 1959;**155**:206.
67. Richter R, Brisson A. Following the formation of supported lipid bilayers on mica: A study combining AFM, QCM-D and ellipsometry. Biophysical Journal 2005;**88**(3422-3433).
68. Richter R, Mukhopadhyay A, Brisson A. Pathways of lipid vesicle deposition on solid surfaces: A combined QCM-D and AFM study. Biophysical Journal 2003;**85**:3035-47.
69. Ayela C, Roquet F, Valera L, et al. Antibody-antigenic peptide interactions monitored by SPR and QCM-D: A model for SPR detection of IA-2 autoantibodies in human serum. Biosensors and bioelectronics 2007;**22**:3113-19.

70. Hook F, Rodahl M, Brzezinski P, et al. Energy dissipation kinetics for protein antibody-antigen adsorption under shear oscillation on a quartz crystal microbalance. Langmuir 1998;**14**:729-34.
71. Cho N-J, Frank CW, Kasemo B, et al. Quartz crystal microbalance with dissipation monitoring of supported lipid bilayers on various substrates. Nat Protocols 2010;**5**(6):1096-106.
72. Vogt BD, Lin EK, Wu W, et al. Effect of film thickness on the validity of the saurbrey equation for hydrated polyelectrolyte films. Journal of Physical Chemistry B 2004:12685-90.
73. Rodahl M, Hook F, Fredriksson C, et al. Simultaneous frequency and dissipation factor QCM measurements of bimolecular adsorption and cell adhesion. Faraday discussions 1997;**107**:229-46.
74. Rodahl M, Hook F, Krozer A, et al. Quartz crystal microbalance setup for frequency and Q-factor measurements in gaseous and liquid environments. Review of scientific instruments 1995;**66**(7):3924-30.
75. Rodahl M, Kasemo B. A simple setup to simultaneously measure the resonant frequency and the absolute dissipation factor of a quartz crystal microbalance. Review of scientific instruments 1996;**67**(9):3238-41.
76. Arnau A. A review of interface electronic systems. Sensors 2008;**8**:370-411.
77. Adamson AWG, A.P. *Physical Chemistry of Surfaces*. 6 ed: John Wiley & Sons, Inc., 1997.
78. Butt HJG, K; Kappl, M. *Physics and Chemistry of Interfaces*. 1 ed: Wiley-VCH, 2006.
79. Wu N, Dai J, Micale FJ. Dynamic Surface Tension Measurement with a Dynamic Wilhelmy Plate Technique. Journal of Colloid and Interface Science 1999;**215**(2):258-69.
80. Martin P, Szablewski M. *Tensiometers and Langmuir-Blodgett Troughs*. 5 ed. Coventry: Nima Technology, 1999.
81. Barnes GT, Gentle IR. *Interfacial Science: An Introduction*. New York: Oxford University Press, 2005.
82. Seredyuk V, Alami E, Nyden M, et al. Micellization and adsorption properties of novel zwitterionic surfactants. Langmuir 2001;**17**:5160-65.
83. Guangmiao Q, Cheng J, Wei J, et al. Synthesis, characterization and surface properties of series sulfobetaine surfactants. Journal of Surfactants and Detergents 2011;**14**(1):31-35.
84. Sainsbury S, Bird L, Rao V, et al. Crystal structures of penicillin binding protein 3 from pseudomonas aeruginosa: Comparison of native and antibiotic-bound forms. Journal of Molecular Biology 2011;**405**(1-3):173-84.
85. Studier FW. Protein production by auto-induction in high density shaking cultures. Protein expression and purification 2006;**41**:207-34.
86. Harrison S, Wooley KL. Shell-crosslinked nanostructures from amphiphilic AB and ABA block co-polymers of styrene-alt-(maleic anhydride) and styrene: polymerisation, assembly and stabilisation in one pot. Chemical Communications 2005;**26**:3259-61.
87. Jamshad M, Grimard V, Idini I, et al. Structural analysis of a nanoparticle containing a lipid bilayer used for detergent free extraction of membrane proteins. Nano Research 2014.

Chapter 3.0 Langmuir monolayers composed of sulfobetaine surfactants

The aim of this chapter is to present experimental results characterising sulfobetaine surfactants at the air-water interface. Sulfobetaines have been introduced in chapter 1.0. The behaviour of sulfobetaine surfactant monolayers has been investigated by two key approaches. The first was to investigate the phase behaviour of the surfactant using the Langmuir trough. This technique was coupled with BAM in order to image the phase behaviour with lateral compression. Finally in order to link the two-dimensional phase behaviour of the surfactants with structural information, combined XRR and NR have been used.

Investigation started by considering the structure and behaviour of a single tailed sulfobetaine surfactant, SB3-18. This is by far the most commonly studied sulfobetaine surfactant in the literature[1-4], however their monolayer structure has not yet been studied. To gain insight into the effect of modification of tail and head group a series of novel sulfobetaine structures were synthesised. This involved assessing the effect of increasing the head group linker length (SB4-18) or tail group (SB-3-20/22). A second chain was added to the sulfobetaine head group to assess the effect of increasing the hydrophobic nature of the surfactant (SB3-18-2). The characterisation of SB3-18-2 can be found in section 3.3 of this chapter. For a table of percentage yields for any novel structures see section 3.1 of this chapter.

The effect of salt in the sub-phase (NaCl, $CaCl_2$ and $NaClO_4$) was assessed and is presented for both SB3-18 and SB3-18-2. NaCl and $CaCl_2$ sub-phases are known to significantly alter the properties of phospholipids at the air-water interface as described in section 1.1.3 of chapter 1.0, whilst $NaClO_4$ has been shown to alter the properties of sulfobetaine micelles. It was therefore a specific aim of this section of the project to see if the reversal in

head group charge distribution, compared with phospholipids, would change the monolayers affinity for salt. Results on the effect of salt in the sub-phase were also assessed by Langmuir trough/BAM and XRR/NR.

3.1 Sulfobetaine Surfactant Synthesis

The generic synthesis of sulfobetaine surfactants has been described in section 1.1.4 of this thesis. A summary of the sulfobetaine surfactants made and then used in this work is presented in table 3.0. The only surfactant that was not synthesised was hydrogenated SB3-18 which is a commercially available product. The structures of all of the sulfobetaine surfactants used in this work are presented in figure 3.0. Surfactants that have been synthesised as part of this work are also shown with a percentage yield and an estimated purity. NMR, MS and IR profiles showing the confirmation of the synthesis of all novel compounds can be found in the appendix of this thesis.

Sulfobetaine	Percentage Yield	Percentage Purity
SB3-18	Commercial product	98 %
d-SB3-18	68 %	95 %
SB3-20	65 %	95 %
SB3-22	63 %	95 %
SB4-18	40 %	95 %
SB3-18-2	77 %	95 %

Table 3.0- List of sulfobetaine compounds synthesised as part of this work along with the percentage yields obtained from the synthesis.

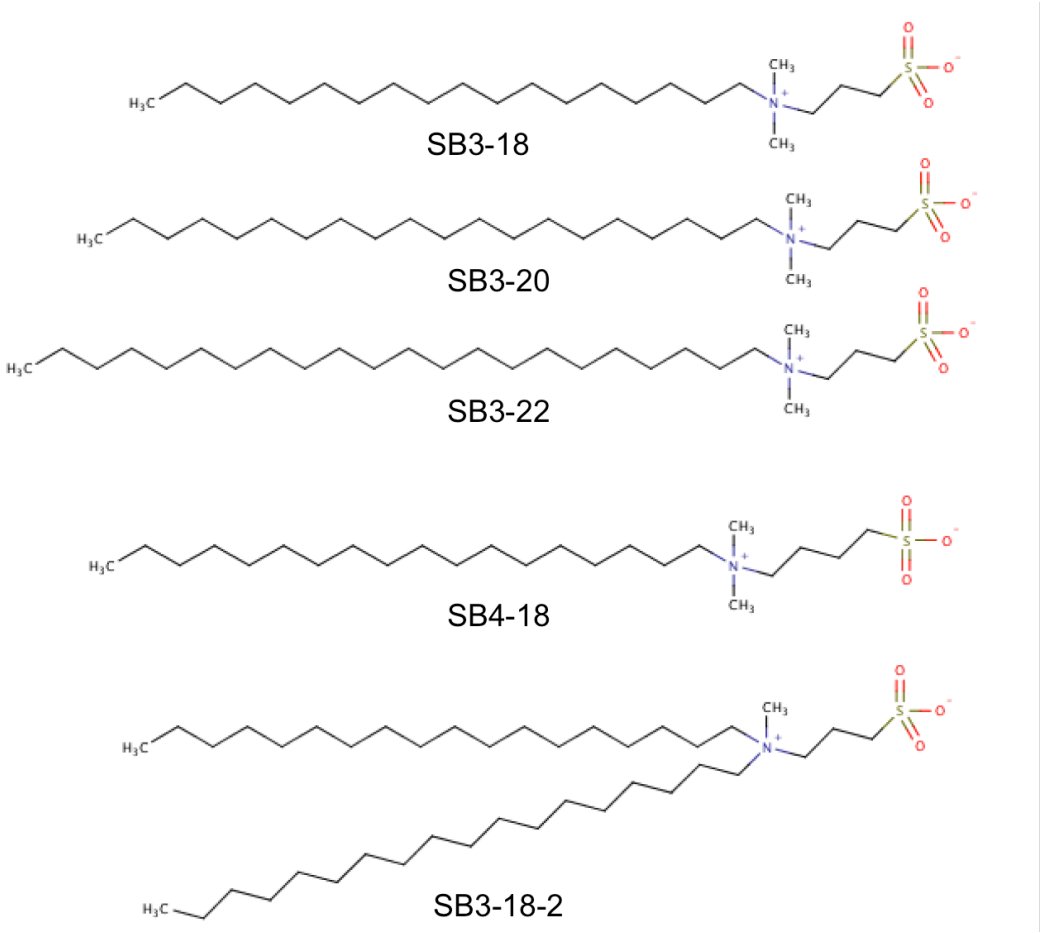

Fig 3.0- Structures of all sulfobetaine surfactants used as part of this study.

3.2 Single Tailed Sulfobataine Surfactants

3.2.1 Langmuir Trough and Brewster Angle Microscopy Studies

The surface pressure isotherm for SB3-18 on pure water is shown in figure 3.1.

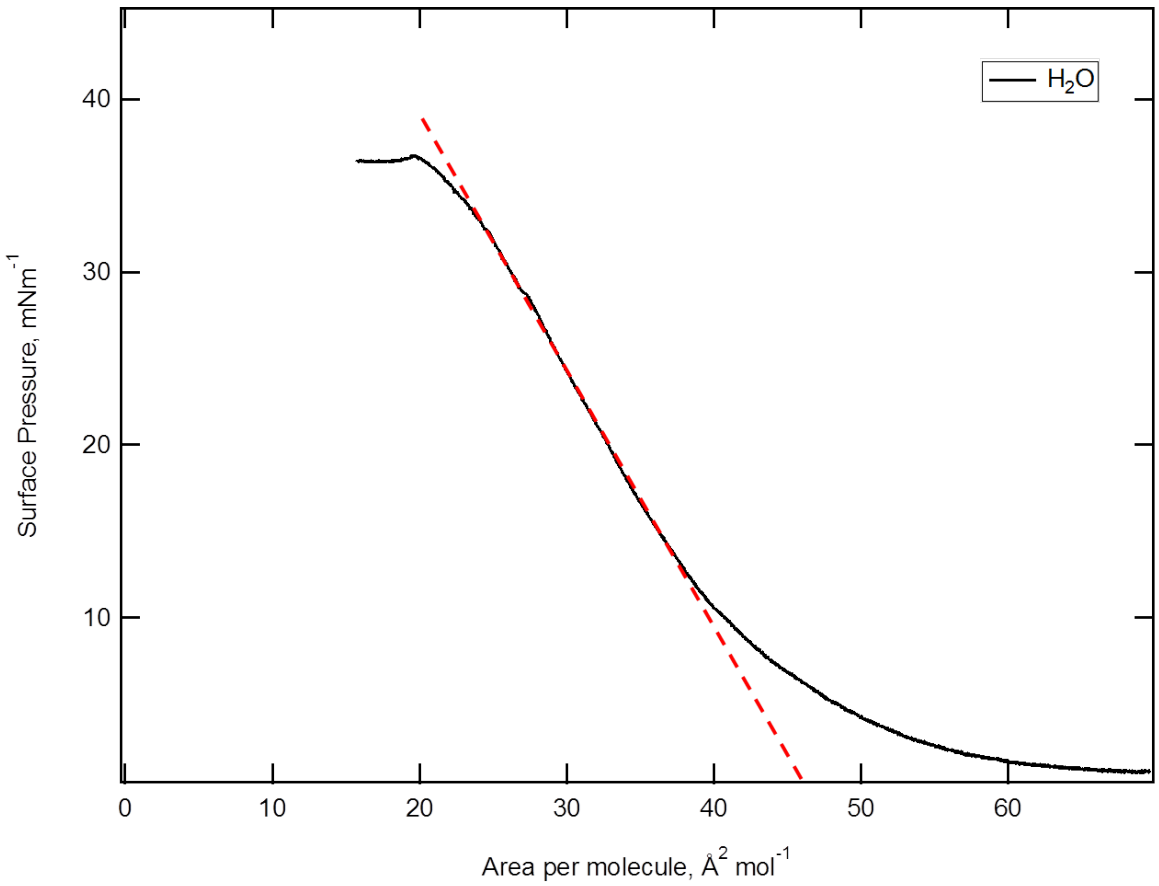

Fig. 3.1- Surface pressure-area isotherm for SB3-18 on water.

The rise in surface pressure is monotonic until the monolayer collapses at 36.7 (± 0.8) mNm^{-1} and 19.7 (± 0.8) $Å^2$ mol^{-1}. The error associated with these parameters is derived from at least three isotherm repeats. The limiting area occupied by one surfactant molecule is 46 $Å^2$ mol^{-1}. The lack of phase plateau shows that the monolayer remains in a liquid expanded state throughout lateral compression. This is confirmed by a series of BAM images shown in figure 3.2. The three images taken at 5, 15 and 25 mNm^{-1} are consistent with a single homogenous phase of liquid expanded surfactant[5]. However upon reaching the collapse point of the monolayer at 36.5 mNm^{-1} a series of white spots become visible. This shows that, post monolayer collapse, matter is buckling and forming multi-layers. This corresponds to the evolution of three-dimensional structures in the sub-phase, such as micelles and liposomes.

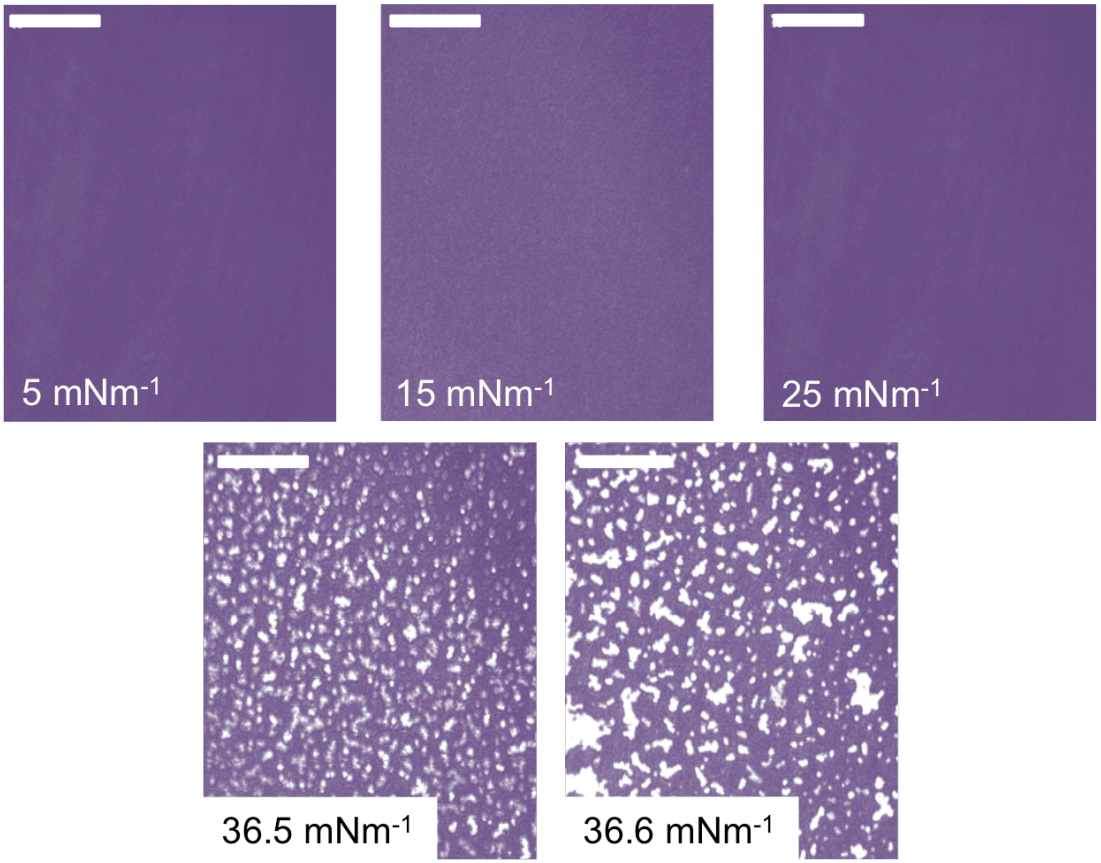

Fig. 3.2- BAM images for SB3-18 on water throughout lateral compression. Scale bar is 50 μm.

Another valuable tool for assessing the phase behaviour of a monolayer is the calculation of its two-dimensional compressibility, C_s, at a given molecular area, defined by equation 3.1,

$$C_s = -\frac{1}{A}\left(\frac{\partial A}{\partial \pi}\right)_T \qquad \text{(equation 3.1)}$$

where A is a given molecular area ($Å^2$ mol^{-1}) and π is the surface pressure of the monolayer (mNm^{-1}). However, in the case of Langmuir monolayers, it is more common to report the reciprocal of this parameter known as the surface compressional modulus, C_s^{-1}, which is highly dependent on the physical state of the film, tending towards higher values for condensed monolayers[6]. The compressional modulus is then plotted against the evolving surface pressure from isothermic data and allows quantitative interpretation. Indeed it is generally considered that if the maximum compressional modulus of a monolayer lies between 12.5 – 50 mNm^{-1} the

monolayer exists in a liquid expanded state. Values of 100 mNm^{-1} and above are considered to be liquid condensed in character[5 7-9].

The compressional modulus of the SB3-18 monolayer (from fig 3.1) was calculated and is shown in figure 3.3. The maximum compressional modulus value is 52 mNm^{-1} and is therefore further evidence supporting the entirely liquid expanded state of this monolayer throughout lateral compression.

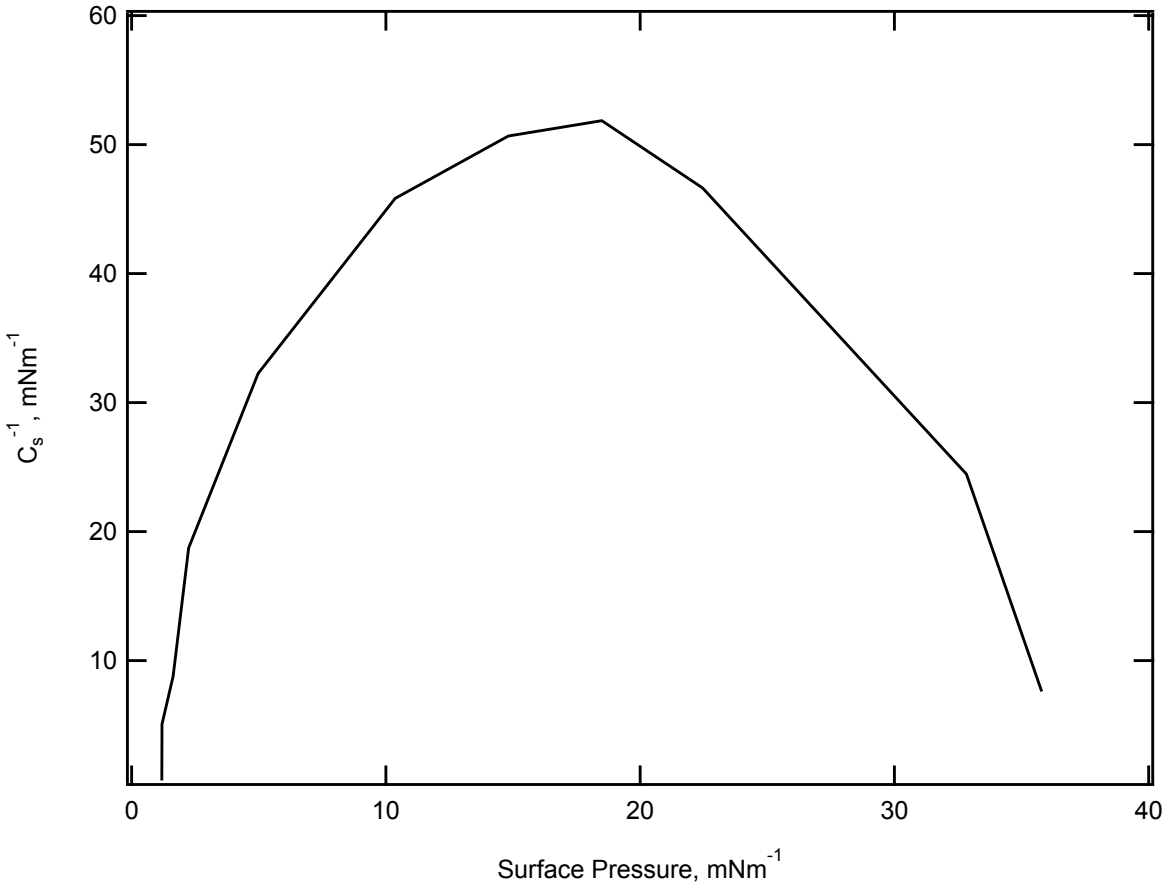

Fig. 3.3- Compressional modulus vs. surface pressure for SB3-18 on water.

To the author's knowledge there are no studies characterising the fundamental physical chemistry of sulfobetaine surfactants. Studies largely involve the lyso phospholipids (Lyso-PC's) or single tailed phospholipids. Table 3.1 shows a list of parameters taken from a number of studies assessing the behaviour of lyso-PC's at the air-water interface along with comparable values recorded for SB3-18. The definition of these parameters can be found in section 1.1.2 of chapter 1.

Lipid/Surfactant	# Carbons in tail group	Headgroup composition	Max C_s^{-1}, mNm^{-1}	A_{lim}, $Å^2$ mol^{-1}	π_{col}, mNm^{-1}	A_{col}, $Å^2$ mol^{-1}
Edelfosine[7]	18	Phosphocholine	65	80	35	50
Mitlefosine[5]	16	Phosphocholine	50	75	40	35
C_{18}Lyso-PC[9]	18	Phosphocholine	61	70	41	33
PAF*[8]	18	Phosphocholine	68	87	40	45
Lyso-PAF*[8]	18	Phosphocholine	57	80	44	31
Palmitic Acid[11]	16	Carboxylate	-	30	40	22
SB3-18	18	Sulfobetaine	52	46	37	20

Table. 3.1- Comparison of Langmuir isotherm data between SB3-18 and lyso-PC's. *PAF= platelet activating factor.

In all of the studies for lyso-PC's found in table 3.1 it was reported that the monolayers exhibited entirely liquid expanded character. This was shown by featureless BAM images indicative of single homogenous phases, which agrees with the BAM images shown for SB3-18. Furthermore this notion was supported by Langmuir isotherm data. Values of compressional modulus (C_s^{-1}) and collapse pressure (π_{col}) are comparable between the lyso-PC's and SB3-18. Compressional moduli values are centered around 50 mNm^{-1} and collapse pressures are consistently centered around 40 mNm^{-1}, again supporting the notion of the liquid expanded character of SB3-18. However there are differences for area occupied by one molecule (A_{lim}) and the area of collapse (A_{col}) between lyso-PC's and SB3-18. A_{lim} and A_{col} for SB3-18 occur at 46 $Å^2mol^{-1}$ and 20 $Å^2$ mol^{-1} respectively; values considerably lower than the corresponding lyso-PC monolayers. These values do make sense however when the difference in size between the headgroups are considered. The phosphocholine headgroup is much larger than the sulfobetaine headgroup (see introduction, section 1.1.5). The values found for the lyso-PC's are suggestive of bulky headgroups bound to a chain with a low cross sectional area[8]. The size of the bulkier PC headgroup relative to the area occupied by the tail group will impede the packing of the lipid

molecules leading to larger values in limiting area and area of collapse[10]. It is therefore more instructive to compare A_{lim} and A_{col} of SB3-18 to a monolayer with a less bulky headgroup. Palmitic acid remains in a liquid expanded state throughout compression[11]. The A_{lim} and A_{col} of palmitic acid is around 30Å^{2}mol^{-1} and 22 Å^2 mol^{-1} respectively[11]. The area of collapse of this monolayer is comparable to SB3-18 and the limiting area of palmitic acid is slightly smaller. The fact that the limiting area of palmitic acid is smaller than SB3-18 is logical as the surfactants carboxylate headgroup is less bulky than the analogous sulfobetaine moiety[5 7 11]. The limiting area and area of collapse of sulfobetaine is therefore found in between that of the lyso-PC's and the carboxylate surfactant derivatives.

3.2.2 The effect of surfactant tail length

Sulfobetaine derivatives containing 20 and 22 carbons in the tail group region were also synthesised to assess the effect of increasing tail length upon the physiochemical properties of the monolayer. The isotherms and compressional moduli for these sulfobetaines are shown in figure 3.4, along with the key parameters extracted in table 3.2.

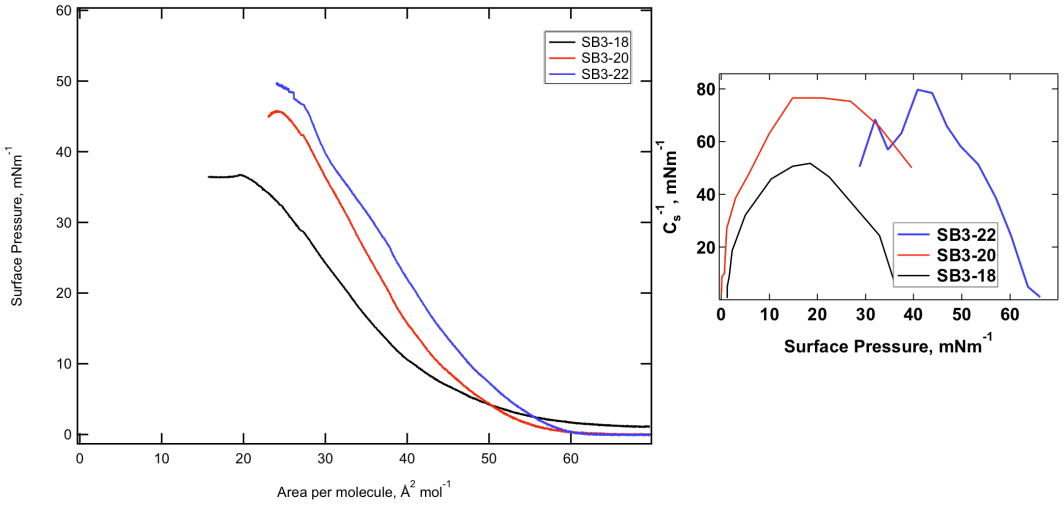

Fig. 3.4- Langmuir isotherm and compressional moduli data for SB3-20 and SB3-22.

Sulfobetaine	Max C_s^{-1}, mNm^{-1}	A_{lim}, $Å^2$ mol^{-1}	π_{col}, mNm^{-1}	A_{col}, $Å^2$ mol^{-1}
SB3-18	52	46	37	20
SB3-20	77	45	45	24
SB3-22	80	51	49	24

Table. 3.2- Key parameters from the isotherm and compression modulus data for SB3-18, SB3-20 and SB3-22.

Increasing the carbon tail length by two and four carbons increases the compressional modulus of the monolayer to 77 and 80 mNm^{-1} respectively, compared to a value of 52 mNm^{-1} for SB3-18. This indicates that with increasing tail length the monolayer is becoming more liquid condensed in comparison to SB3-18. It is important to note however that the phase of both SB3-20 and SB3-22 is still liquid expanded. The increase in the more condensed nature of the film can be rationalised by the increase in hydrophobic nature of the surfactant monolayer. An increase in chain length will promote increased hydrophobic interactions of the tails, causing a monolayer with a more condensed character.

3.2.3 The effect of head group linker length

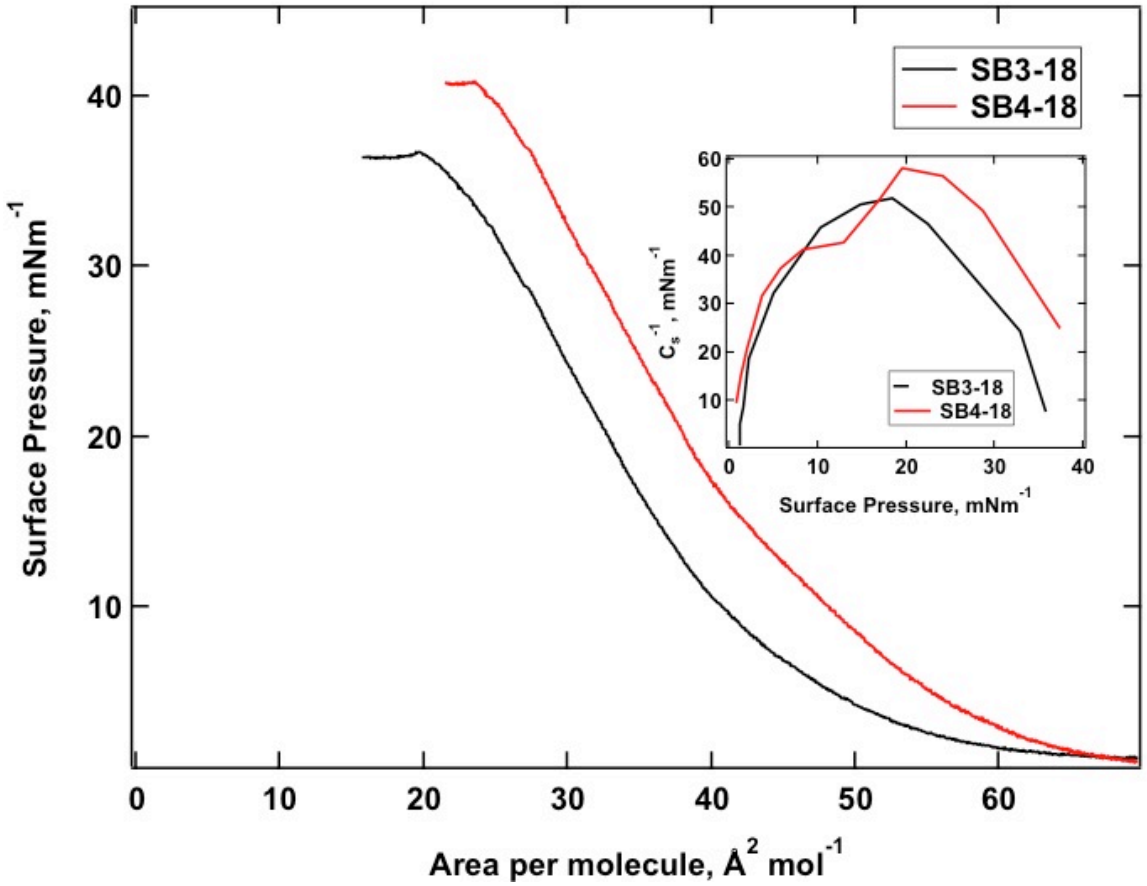

Fig 3.5- Langmuir isotherm and compressional moduli data for SB3-18 and SB4-18.

On increasing the length of the headgroup linker from 3 to 4 it is clear that film expansion occurs. This is shown by larger area per molecule values at a fixed surface pressure. At 20 mNm^{-1} the area per molecule of SB3-18 is 32$Å^2mol^{-1}$. This is compared to SB4-18 at the same surface pressure with an APM of 38 $Å^2$ mol^{-1}. This increase in APM at a fixed surface pressure is due to steric consequences since the increased linker length means the head group occupies more space within the monolayer. However these small changes in area per molecule (5 $Å^2$ mol^{-1}) are unlikely to result in any major structural change in head group conformation such as bending or curling of the linker[10 12 13].

3.2.4 The effect of salt in the sub-phase

The influence of various metal salt sub-phases on the phase behaviour of the monolayer was also characterised. As explained in section 1.1.3, this is of interest as it has been shown that salt sub-phases significantly affect the behaviour of phospholipid Langmuir monolayers. The key question here is whether or not the reversal in distribution of head group charge, relative to phospholipids, will affect the interaction of salt. Figure 3.6 displays π-A isotherms for SB3-18 on NaCl, $CaCl_2$ and $NaClO_4$ sub-phases (water also shown for comparison). Compressional moduli vs. surface pressure curves have also been calculated for these systems.

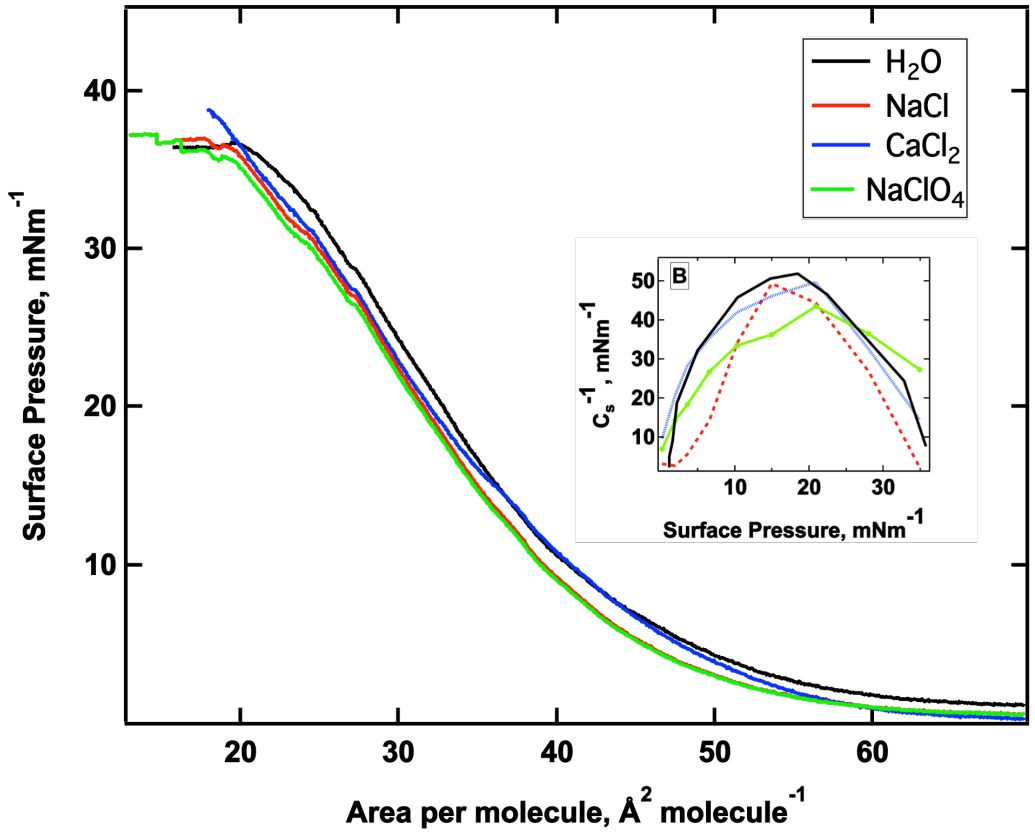

Fig. 3.6- π-A isotherms for SB3-18 on water (black line), NaCl (red line) and $CaCl_2$ (blue line) subphases, along with surface compressional modulus vs. surface pressure curves for the same systems.

There is a slight contraction and/or condensation of the monolayer in the presence of salt, which can be seen from the smaller area per molecule

values at a fixed surface pressure. At a fixed surface pressure of 20 mNm^{-1} SB3-18 is at 33.1 (± 0.6) $Å^2$ mol^{-1}, whilst when in the presence of NaCl, this value is reduced to 31.8 (± 0.5) $Å^2$ mol^{-1}. Given the small error in these values it is clear that the presence of salt does marginally contract the monolayer, however these changes are small and are not specific to any one salt. The phase behaviour of the monolayer in the presence of salt is therefore very similar to that of its behaviour on pure water. This may be because of the formation of a diffuse ion layer beneath the surfactant head group region, and does not suggest any significant penetration of ions into the head group region of the monolayer[14]. The monolayer collapses at similar surface pressures whether on salt or water sub-phases. Furthermore the maximum surface compressional moduli values do not exceed $50mNm^{-1}$, showing that the monolayer maintains its liquid expanded character regardless of the presence of salt. The surfactant was also investigated upon a range of other salt sub-phases ($MgCl_2$, $BaCl_2$, $CsCl_2$). The behaviour on these salts was very similar to that of NaCl and/or $CaCl_2$ and so the data is not shown here. This behaviour on salt is in contrast to lipid monolayers composed of PC phospholipids where significant ion penetration into the monolayer is found. This has been discussed in section 1.1.3. In some cases an increase of 5-10 $Å^2$ mol^{-1} for these systems has been observed. This is indicative of significant ion penetration into the monolayer and the changes in APM are far greater than those observed for SB3-18 [14-17].

3.3 X-ray and Neutron Reflectometry of SB3-18 Langmuir monolayers

Figure 3.7 displays co-refined XRR and NR data for the SB3-18 monolayer at 15, 20 and 25 mNm^{-1}. As this surfactant remains in the liquid expanded phase throughout compression, these values of surface pressure were chosen to track the structure of the film throughout the length of its isotherm. Table 3.3 shows a summation of the structural parameters that were used to gain the best fit for the experimental data. The scattering length density of the tail group was calculated assuming a molecular tail volume of 510 $Å^3$,

which has previously been reported for a cationic surfactant with the same tail length[18]. The SLD of the head group was calculated using a molecular volume of 181 Å^3, which has been derived from the characterisation of soluble sulfobetaine micelles[19]. The concept and calculation of the SLD has been explained in chapter 2 of this thesis.

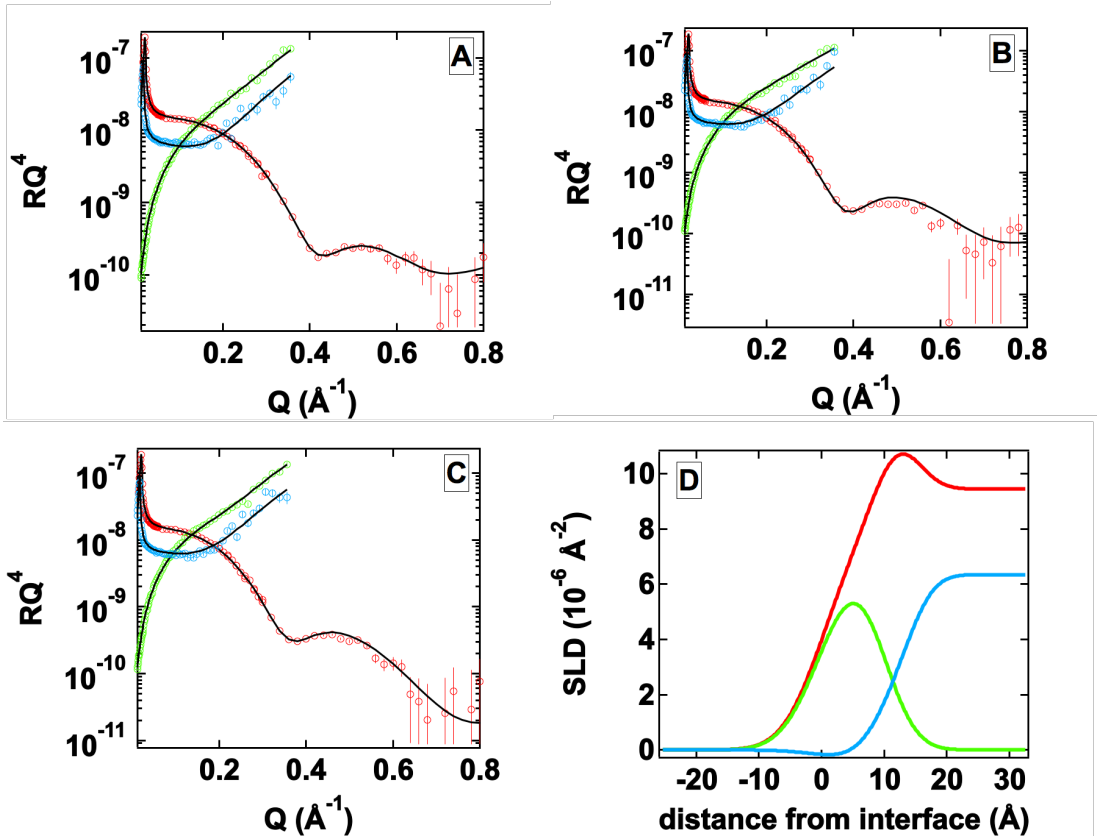

Fig 3.7- Co-refined XRR and NR data for SB3-18 at A) 15, B) 20 and C) 25 mNm^{-1}. D) shows an example scattering length density profile for the relevant model at 25 mNm^{-1}. X-ray data is shown in red, D_2O neutron contrast data in green and ACMW neutron contrast data in blue. The black line represents the modelled fit. X^2 values are 1.2, 1.8 and 1.4 x 10^{-17} for 15, 20 and 25 mNm^{-1} respectively.

	Scattering Length Density (10^{-6} Å^{-2})			Model:					
				Surface pressure /mN m^{-1}					
				15		20		25	
	d-	h-	x-ray	t/Å	σ /Å	t/Å	σ /Å	t/Å	σ /Å
Lipid Tail	7.2	-0.36	7.9	8.6 ±0.3	3.7 ±0.1	8.8 ±0.2	4.6 ±0.3	9.5 ±0.3	5 ±0.2
Lipid Head	0.99		14.4	4.9 ±0.4	3.7 ±0.2	4.9 ±0.2	3.2 ±0.2	4.9 ±0.3	3.7 ±0.2
Water	6.35	-0.56	9.45		3.2 ±0.3		3.2 ±0.2		3.8 ±0.3

Table 3.3- Summary of fitting parameters used to model the SB3-18 monolayer at surface pressures of 15, 20 and 25 mNm^{-1}. In the table t is the thickness of the layer and σ is the roughness of the layer.

The model has also been constrained using the obtained APM values shown in the Langmuir isotherm data in figure 3.1 and table 3.1. The modeled APM value can be found from the theoretical scattering length density of the relevant part of the molecule and dividing it by the product of the thickness and the SLD of the layer as a whole. Table 3.4 shows these experimental values compared with the APM value found from the best fit. The APM value found from the fits was always restricted to be within 10 % of the experimental data. This value is sensible and can be explained by a number of factors[20], including the static versus dynamic pressure variation between

the two experiments. It may also be related to the repeatability of the measurement between x-ray and neutron results, including the repeatability of the individual contrast experiments performed with neutrons.

Surface Pressure (mNm^{-1})	Experimental APM ($Å^2$ mol^{-1})	Modeled APM ($Å^2$ mol^{-1})	Percentage difference
15	36.2 ± 1	34.6 ± 1	-4.4%
20	32.0 ± 2	34.1 ± 1	+6.5%
25	29.6 ± 1	32.5 ± 1	+9.8%

Table 3.4- Comparison between experimentally observed and modelled APM values.

The modeled data shows that as the surfactant is laterally compressed (reducing the available area) the overall increase in the thickness of the monolayer is minimal. The thickness increases from 13.5 ± 0.1 Å to 14.4 ± 0.2 Å; an increase in thickness of around 1 Å. This behaviour is consistent with a surfactant that remains in the liquid expanded phase throughout lateral compression[7-9].

3.3.1 The effect of salt as investigated by XRR and NR

As with the Langmuir isotherm data presented in figure 3.6 the structure of the surfactant was also investigated on NaCl, $CaCl_2$ and $NaClO_4$ sub-phases, using XRR and NR. The same set of surface pressures was chosen as those conducted on pure water. Figure 3.8 shows the reflectometry data for the surfactant on NaCl, $CaCl_2$ and $NaClO_4$ sub-phases, whilst the structural parameters used to model the data are shown in table 3.5. Due to time constraints and availability of beam time the $NaClO_4$ data only consists of x-ray data and the D_2O neutron contrast. For clarity this has been shown

as a separate figure (3.9), however the fitting parameters can still be found in table 3.4.

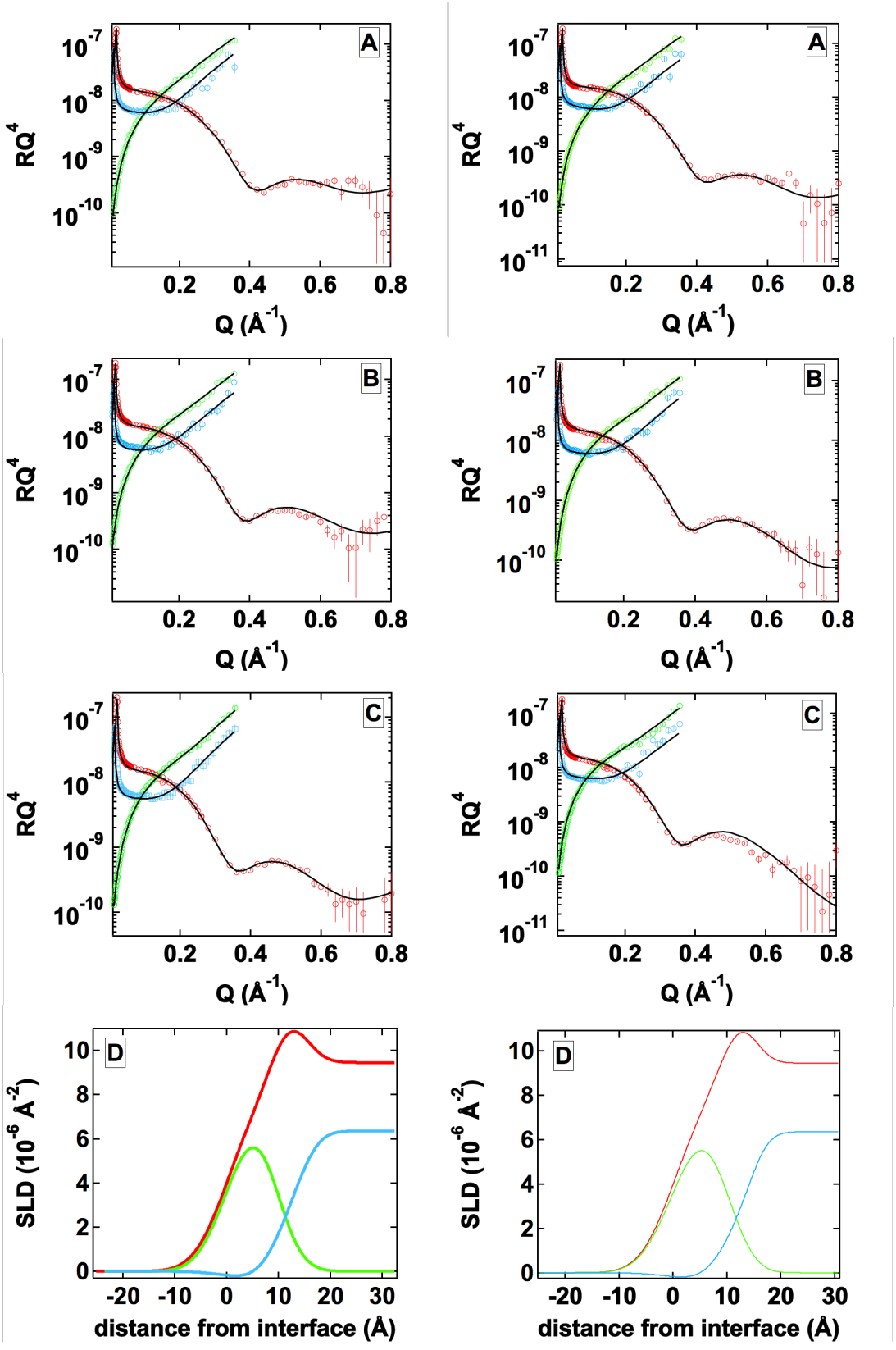

Figure 3.8- Left) Co-refined XRR and NR data for SB3-18 on NaCl at A) 15, B) 20 and C) 25 mNm^{-1} along with D) an example SLD profile for SB3-18 at 25 mNm^{-1} on a 50 mM $CaCl_2$ sub-phase. X-ray data is shown in red, D_2O neutron contrast data in green and ACMW neutron contrast data in blue. The black line represents the modeled fit. X^2 values are 1.1, 6.2 and 1.3 x 10^{-18} for 15, 20 and 25 mNm^{-1} respectively. Right) Co-refined XRR and NR data for SB3-18 at A) 15, B) 20 and C) 25 mNm^{-1} along with D) an example SLD profile for SB3-18 on $CaCl_2$ at 25 mNm^{-1} on a 50 mM $CaCl_2$ sub-phase. X-ray data is shown in red, deuterated contrast neutron data in green and hydrogenated contrast neutron data in blue. The black line represents the modeled fit. X^2 values are 9.5, 7.9 and 6.3 x 10^{-18} for 15, 20 and 25 mNm^{-1} respectively.

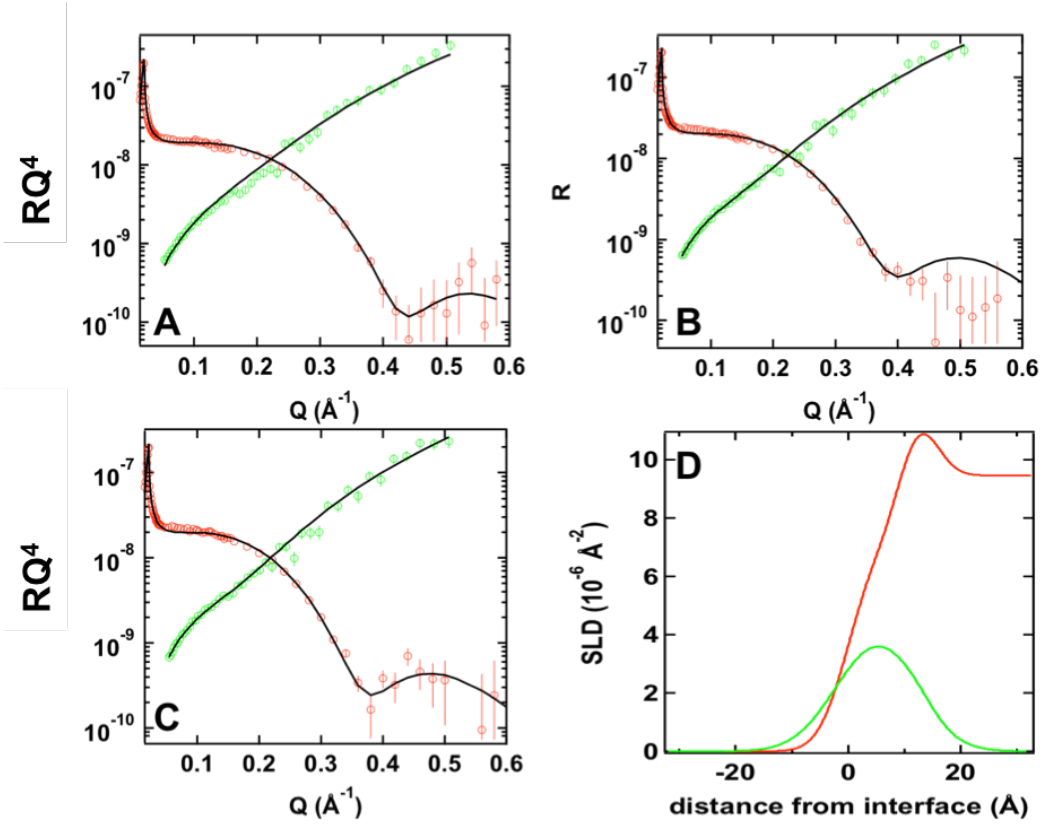

Fig 3.9- Co-refined XRR and NR data for SB3-18 on 50 mM $NaClO_4$ at 15, 20 and 25 mNm^{-1} (A, B and C respectively) along with a corresponding SLD profile at 25 mNm^{-1} (D). X-ray data is shown in red, ACMW neutron contrast data is shown in green and the model fit is shown in black. X^2 values are 1.44, 1.52 and 1.21 x 10^{-16} for 15, 20 and 25 mNm^{-1} respective

	Scattering Length Density (10^{-6} Å^{-2})			Layer and sub-phase	Model:					
					Surface pressure /mN m^{-1}					
					15		20		25	
	d-	h-	x-ray		t/Å	σ /Å	t/Å	σ /Å	t/Å	σ /Å
Lipid Tail	7.2	-0.36	7.9	NaCl	8.6 ±0.3	3.4 ±0.2	8.7 ±0.4	4.7 ±0.1	9.8 ±0.2	4.9 ±0.2
				$CaCl_2$	8.5 ±0.2	3.5 ±0.3	8.8 ±0.3	4.6 ±0.2	9.6 ±0.3	5 ±0.2
				$NaClO_4$	8.5 ±0.3	3.3 ± 0.5	8.6 ±0.4	4.4 ±0.3	9.8 ±0.4	4.2 ±0.5

Lipid Head	0.99		14.4	NaCl $CaCl_2$ $NaClO_4$	4.9 ±0.4 4.9 ±0.3 4.9 ±0.3	3.8 ±0.1 3.2 ±0.1 3.8 ±0.5	5.0 ±0.3 4.7 ±0.4 4.9 ±0.3	3.2 ±0.2 3.0 ±0.2 3.1 ±0.5	4.9 ±0.2 4.9 ±0.3 4.9 ±0.3	3.6 ±0.2 3.5 ±0.2 3.6 ±0.4
Water	6.35	-0.56	9.45			3.2 ±0.3		3.2 ±0.2		3.8 ±0.3

Table 3.5- Structural parameters used to model data on NaCl, $CaCl_2$ and $NaClO_4$ sub-phases at 15, 20 and 25 mNm^{-1}.

In all cases for the monolayer on a salt sub-phase (NaCl, $CaCl_2$ $NaClO_4$) the best fit was obtained for the same structural parameters (within error) as for the surfactant on pure water. The lack of change in structural parameters observed here, in particular thickness of the head group and head group scattering length density, is suggestive of no significant ion penetration into the film. This supports the notion that there is a diffuse ion layer formed beneath the surfactant head groups, as shown by Langmuir trough data.

Figure 3.10 shows the raw x-ray reflectometry data for SB3-18 on a $CaCl_2$ sub-phase at 15 mNm^{-1}. Also plotted on the graph are calculated reflectivity profiles for the surfactant head group with 1, 2 and 3 bound calcium ions. Only x-ray data was shown here, as it is the most sensitive towards the incorporation of relatively large ions bound to the surfactant head group. The calculated reflectivity shown in figure 3.9 were calculated from a model retaining the structural parameters shown in table 3.5, but systematically increasing the scattering length density of the head group to allow for the incorporation of an increasing number of calcium ions. The model was generated by calculating the volume of one Ca^{2+} ion based on an ionic radius of 1.14 Å[21], giving a volume of 6.21 $Å^3$. This value along with the x-ray scattering length of calcium (5.64 x 10^{-4} $Å^{-1}$)[22] was incorporated into the SLD calculation of the head group and inserted into the model. This model does not account for the incorporation of water into the head group region, which may act to dilute this effect. However if an ion was bound to the surfactant head group an increase in the SLD is still expected. It is clear that when the model accounts for the incorporation of ions into the head group region of the surfactant, the calculated reflectivity deviates by a large amount from the measured reflectivity data. If the SLD of the head group is increased and other parameters are modified to try and account for ion incorporation, no good fit is obtained that is consistent with neutron and Langmuir trough data. This supports the notion that there is no significant penetration of ions into the surfactant head group.

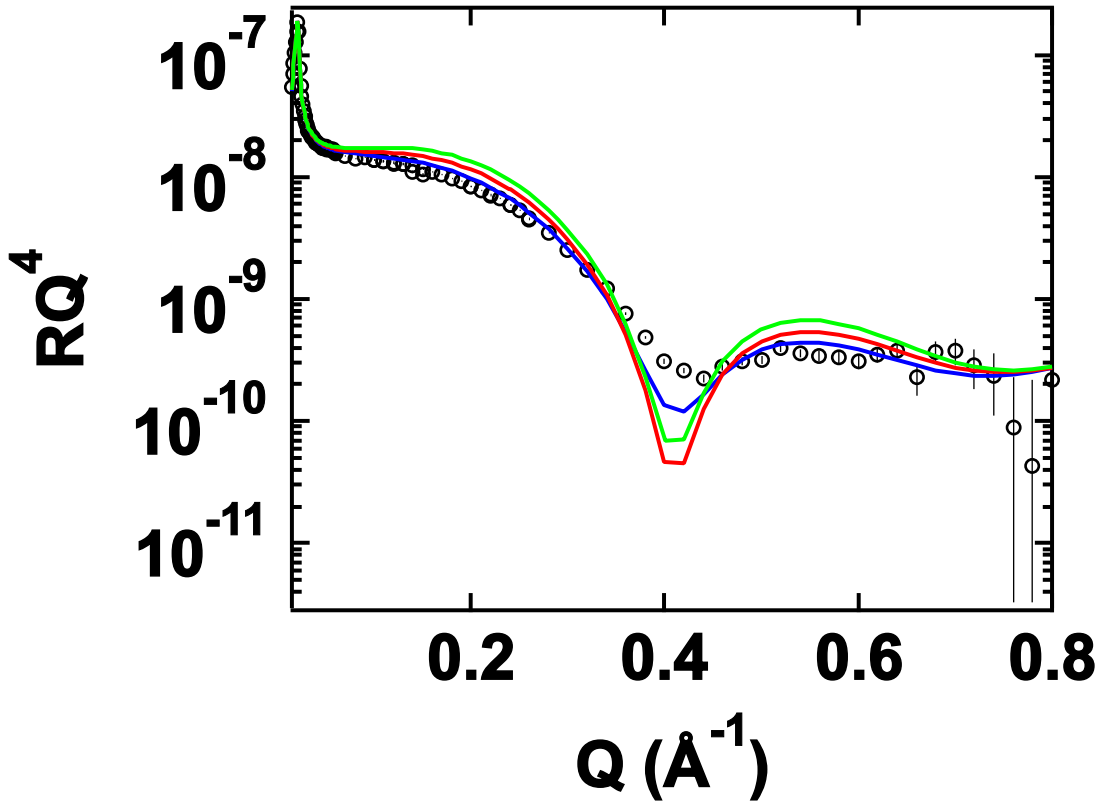

Fig 3.10- Raw reflectivity data for SB3-18 on a $CaCl_2$ sub-phase at 15 mNm^{-1}. Calculated reflectivity for the surfactant head group with incorporated 1 (blue line), 2 (green line) and 3 (red line) calcium ions.

3.3.2 Other structural considerations

The small rise in the thickness of the monolayer shown by XRR and NR, as the monolayer is compressed, implies that the tilt of the carbon-chain of the surfactant normal to the interface decreases with respect to the surface normal. A simple trigonometric calculation can be used to estimate the chain tilt of the tail group normal to the interface. This is based on using the theoretical value of an all trans 18-carbon tail and the thickness of the overall monolayer[5]. This calculation is shown schematically in figure 3.11.

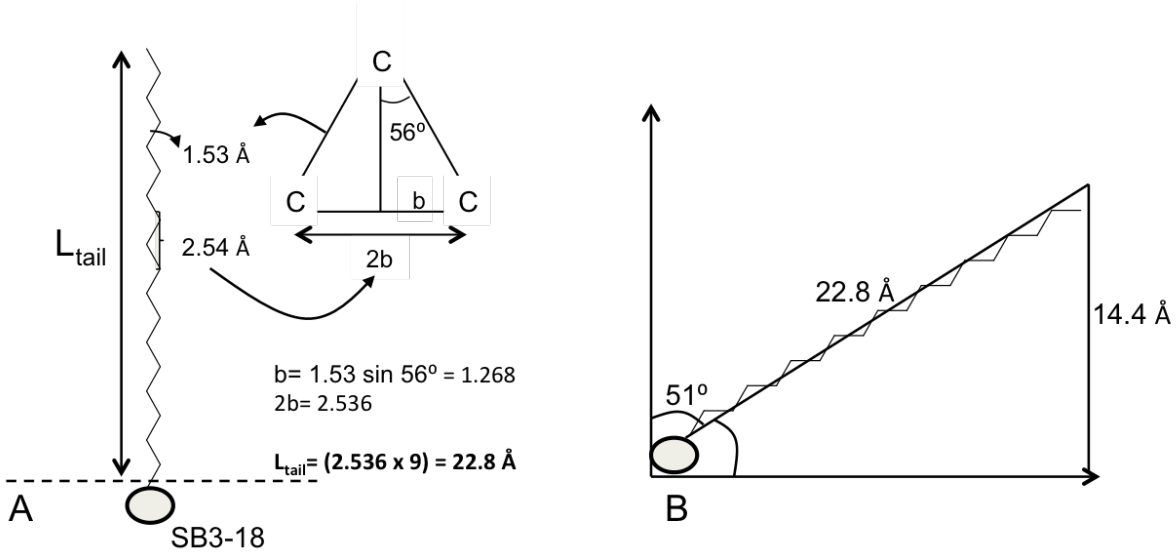

Fig 3.11- Schematic representation of the chain tilt calculation for a Langmuir monolayer

Surface Pressure (mNm^{-1})	Chain Tilt (°) with respect to the surface normal
15	53.9
20	53.3
25	51.9

Table 3.6- Change in chain tilt as a function of surface pressure for the SB3-18 monolayer.

Chain tilt values as a function of surface pressure are presented in table 3.6. The data shows that the chain tilt of the monolayer only changes by around 2 ° on going from 15 to 25 mNm^{-1}. This phenomenon is well documented for single tailed phospholipids (e.g. Lyso-PC's) analysed by reflectometry. It has been shown that the small change in chain tilt throughout compression is a function of the liquid expanded character of the film[8 9].

The chain tilt angles of SB3-18 are considerably smaller when compared to the structurally similar Lyso-PCs, which show chain tilt angles of 75° at 15 mNm^{-1}. This is due to the fact that Lyso-PC's have a much bulkier PC head group, with a larger polar region than SB3-18. This larger head

group will prevent the molecules packing closely so that the tails need to lie relatively flat in order to maximise tail-tail (Van der Waals) interactions[5]. To further this notion the chain tilt value found for SB3-18 can also be compared to a film which is more liquid condensed in character. DPPC has comparatively much smaller chain tilt values at 15 mNm^{-1} of 34.9 °. DPPC has an additional hydrophobic tail group, which facilitates an increased interaction between chains, causing tail-tail interactions to dominate at larger molecular areas. This acts to drive the alignment of the tails and cause them to stand more upright, leading to a more condensed film containing lower chain tilt values[23 24]. It is therefore found that the chain tilt value of SB3-18 lies in between the values found for the expanded Lyso-PCs and lipids of a more condensed nature such as DPPC. The size of the sulfobetaine surfactant head group is smaller than the PC analogue and does not hinder chain erection as with the bulkier phosphocholine moiety. The higher chain tilt values observed for SB3-18, when compared to monolayers, which are more condensed in nature, are a large contributor in dictating the LE characteristics of the film. Figure 3.12 shows a schematic representation of the difference in chain tilt with increasing surface pressure for SB3-18.

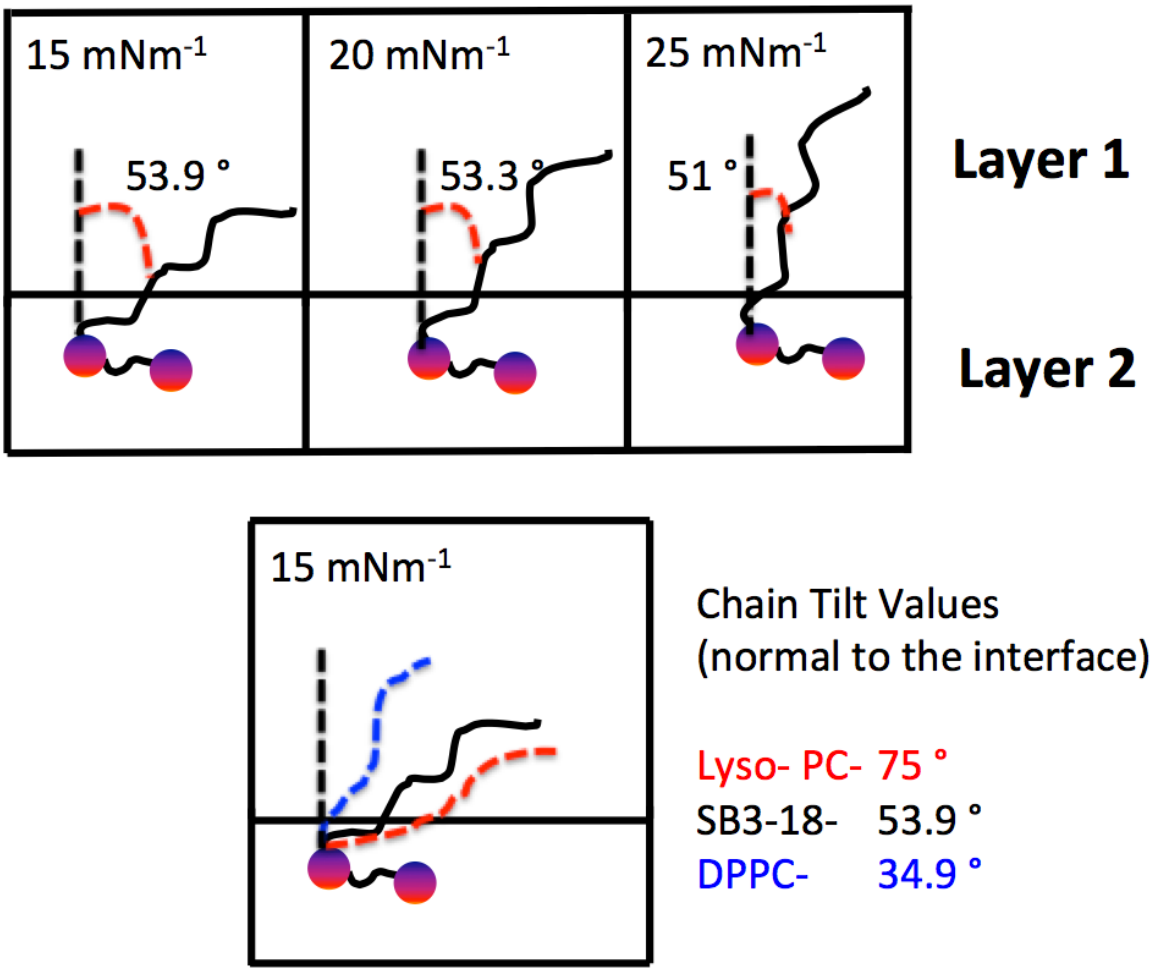

Fig 3.12- Variation in chain tilt with increasing surface pressure for SB3-18, along with comparison of chain tilt at 15 mNm^{-1} between SB3-18 and Langmuir monolayers of differing phase behaviour.

3.4 Double tailed sulfobetaine surfactants

In the previous sections it was argued that the liquid expanded character of the single tailed sulfobetaine surfactant was largely dictated by its limited ability to form Van der Waals interactions due to insufficient hydrophobicity within the tail group region of the monolayer. This in turn did not enable the surfactant to reach the LC phase. To assess the role of hydrophobicity of the tail group region of the monolayer, a novel sulfobetaine was made, comprising two hydrocarbon chains. This surfactant is given the notation SB3-18-2 and was investigated with a similar approach to that of SB3-18.

3.4.1 Langmuir Trough and Brewster Angle Microscopy Studies

The surface pressure-area isotherm for SB3-18-2 on water is shown in figure 3.13.

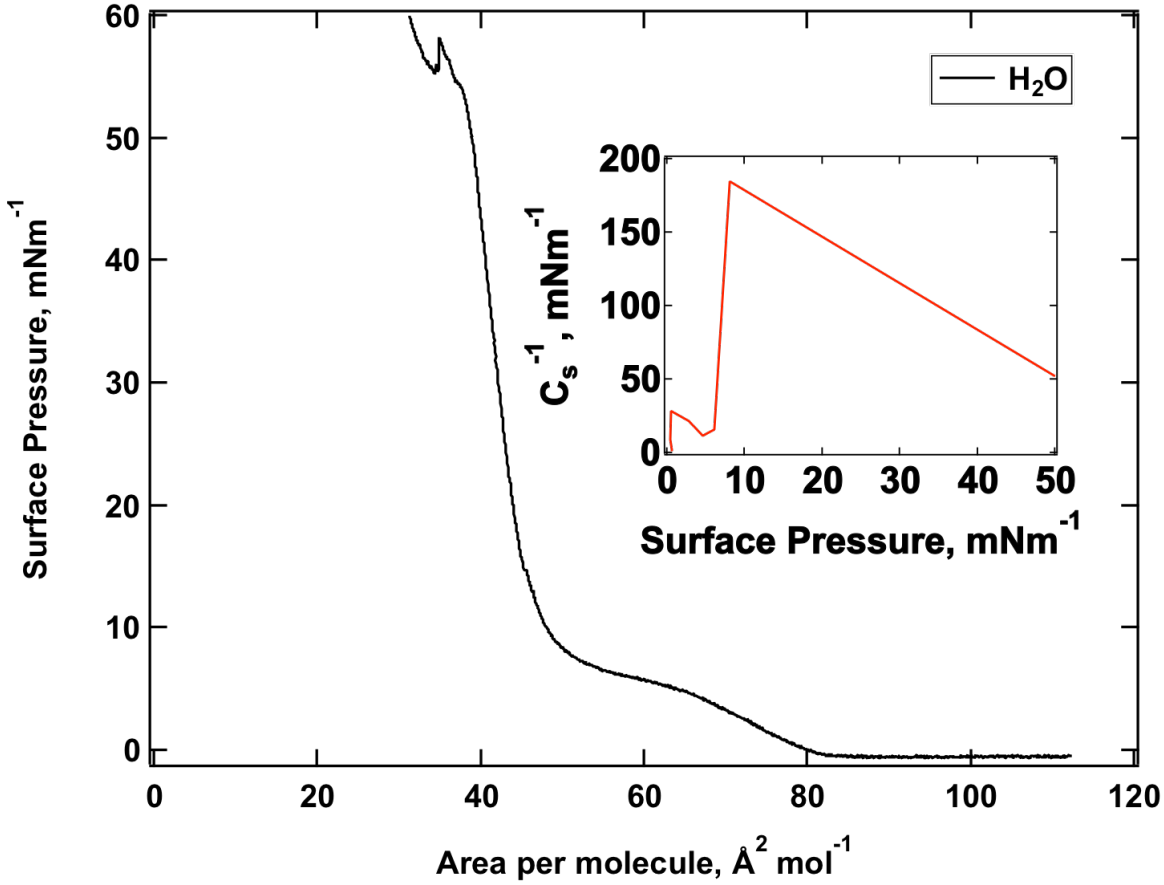

Fig. 3.13- Surface pressure-area isotherm and compressional modulus data for SB3-18-2 on water. Isotherm was conducted at room temperature.

The rise in surface pressure is no longer monotonic as with the single tailed species on water. There is now a visible phase transition occurring at 4.3 mNm^{-1} (± 0.6 mNm^{-1}) and 60.1 $Å^2$ mol^{-1} (± 0.7 $Å^2$ mol^{-1}). The end of the phase transition occurs at 6.9 mNm^{-1} (± 0.6 mNm^{-1}) and 51.6 $Å^2$ mol^{-1} (± 0.4 mNm^{-1}). This phase transition is highlighted by a pseudo plateau in the surface pressure and corresponds to the surfactant entering a phase co-existence region. Here liquid condensed domains will start to nucleate in a sea of liquid expanded phase surfactant. The presence of

liquid expanded domains has been confirmed by BAM and these are shown in figure 3.14. These images taken at 4.3, 5.2, 6.0 and 7.0 mNm^{-1} show that the liquid condensed domains begin to nucleate at the onset of the phase transition. The domains subsequently grow and become striated. At higher surface pressures the domains begin to interact with one another, converge and form a liquid condensed film. Also shown in figure 3.13 is the surface compressional moduli data for SB3-18-2. The maximum of the surface compressional modulus is now found at 184 mNm^{-1}. This is compared with the maximum found for the single tailed species at 52 mNm^{-1}. This is further evidence suggesting that the film forms a structure that is considerably more condensed than SB3-18. The value, which is above 100 mNm-1, is well into the regime for a liquid condensed species[6]. The maximum value of surface compressional modulus value found for SB3-18-2 agrees well with literature values reported for double tailed phospholipids (DPPC), which is around 200 mNm^{-1} [25 26].

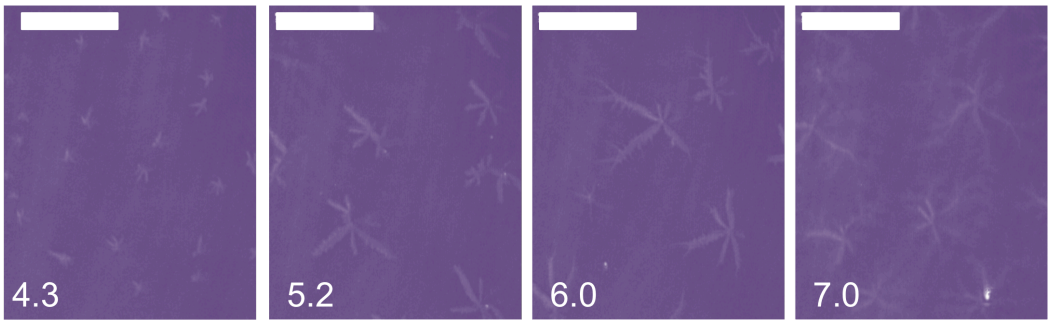

Fig 3.14- BAM images for SB3-18-2 on water throughout lateral compression. Scale bar is 50 μm. BAM measurements were conducted at room temperature.

Given that the double tailed sulfobetaine exhibits well defined phase behaviour and the evolution of liquid condensed domains upon compression the monolayer can be compared with the phospholipid analogue, DPPC. Table 3.7 shows values obtained from Langmuir isotherm data reported in the literature.

Lipid/ Surfactant	# Carbons in tail group	Headgroup composition	Max C_s^{-1}, mNm^{-1}	A_{lim}, $Å^2$ mol^{-1}	π_{col}, mNm^{-1}	A_{col}, $Å^2$ mol^{-1}
DPPC[25 27]	16	Phosphocholine	200	54	56	43
SB3-18-2	18	Sulfobetaine	184	48	54	38

Table. 3.7- Comparison of Langmuir isotherm data between SB3-18-2 and DPPC.

In all studies concerning double tailed phospholipids that exhibit well-defined phase behaviour BAM images can be found[28-32] (see figure 1.5 in the introduction). These typically consist of images taken at or around the phase co-existence region and highlight the nucleation and growth of liquid condensed domains. The monolayer is then shown to complete the phase transition into the liquid condensed phase[28 29 31]. The compressional modulus values found for SB3-18-2 are comparable to DPPC at around 200 mNm^{-1}. A_{lim}, π_{col} and A_{col} are slightly larger for DPPC when compared to SB3-18-2. This most likely reflects the size of the two head groups. The phosphocholine (PC) headgroup is larger than the sulfobetaine headgroup as discussed previously for the single tailed species. These values are suggestive of a bulky head group bound to a chain with a low cross sectional area [8].The larger PC head group relative to the area that is occupied by the tail group will lead to larger values in A_{lim}, π_{col} and A_{col}[10].

3.4.2 The effect of salt

Figure 3.15 shows surface pressure-area isotherms and compressional moduli data for SB3-18-2 on water, NaCl and $CaCl_2$ sub-phases.

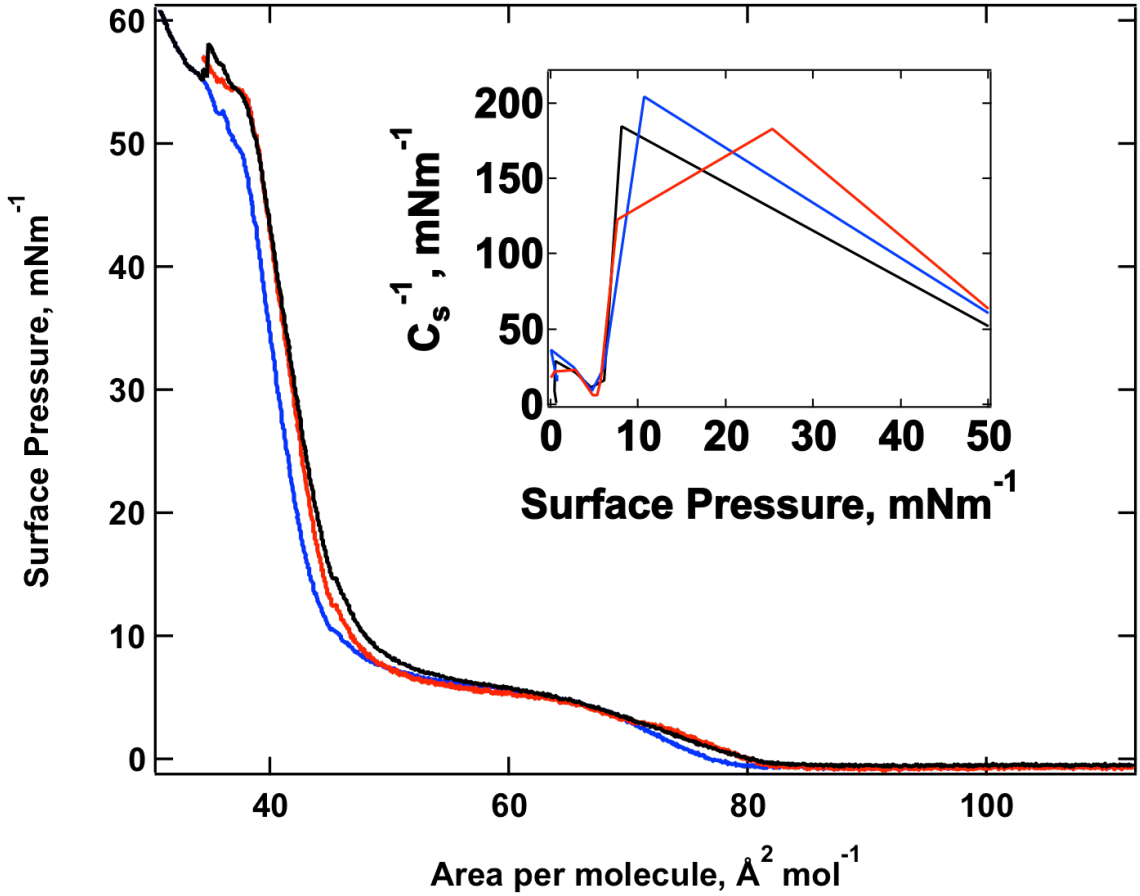

Fig 3.15- Surface pressure-area isotherms and surface compressional moduli data (inset) for SB3-18-2 on water (black line), NaCl (red line) and $CaCl_2$ (blue line).

As with SB3-18 there is a slight contraction and/or condensation of the monolayer when salt is present in the sub-phase. This is evident by a small decrease in area per molecule at a fixed surface pressure. Taking a fixed value of surface pressure at 20 mNm^{-1} on water the APM value is found to be 43.8 (±0.6) $Å^2$ mol^{-1}. Whilst on a $CaCl_2$ sub-phase this value is found to be 42.2 (± 0.7) $Å^2$ mol^{-1}. Again as with the single tailed species in the presence of salt the formation of a diffuse ion layer beneath the monolayer is postulated but no significant penetration of ions into the head group region is observed. The presence of the salts presented here does not affect the surface compressional moduli of the monolayer with all sub-phases showing maximum C_s^{-1} values at around 200 mNm^{-1}. This can also be shown qualitatively by BAM. Figure 3.16 shows BAM images for the monolayer on NaCl and $CaCl_2$ sub-phases. The shape of the liquid

domains is unaffected by the presence of these salts in the sub-phase and is reminiscent of domain formation on pure water.

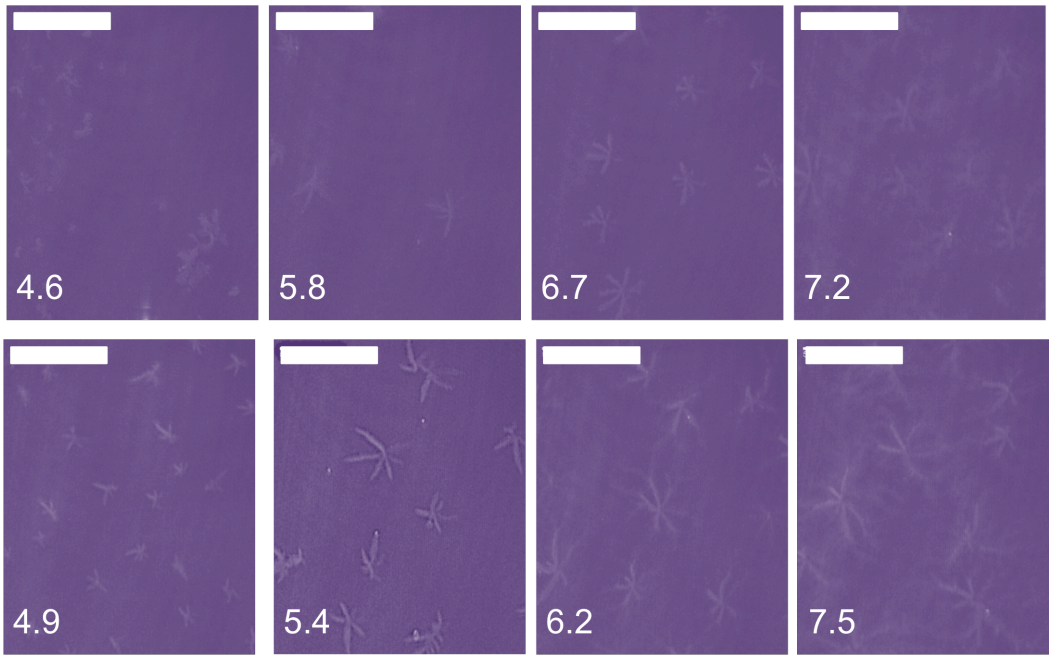

Fig 3.16- BAM images for SB3-18-2 on water throughout lateral compression on NaCl (above) and $CaCl_2$ (below). The images have a colour filter applied to them to high light the contrast between the liquid condensed domains and the sea of liquid expanded surfactant. Scale bar is 50 μm.

Unlike the SB3-18 monolayer there is a significant change observed in the isotherm when sodium perchlorate is present in the sub-phase. Figure 3.17 shows the surface pressure-area isotherm, along with compressional modulus data for SB3-18-2 on a 50 mM $NaClO_4$ sub-phase.

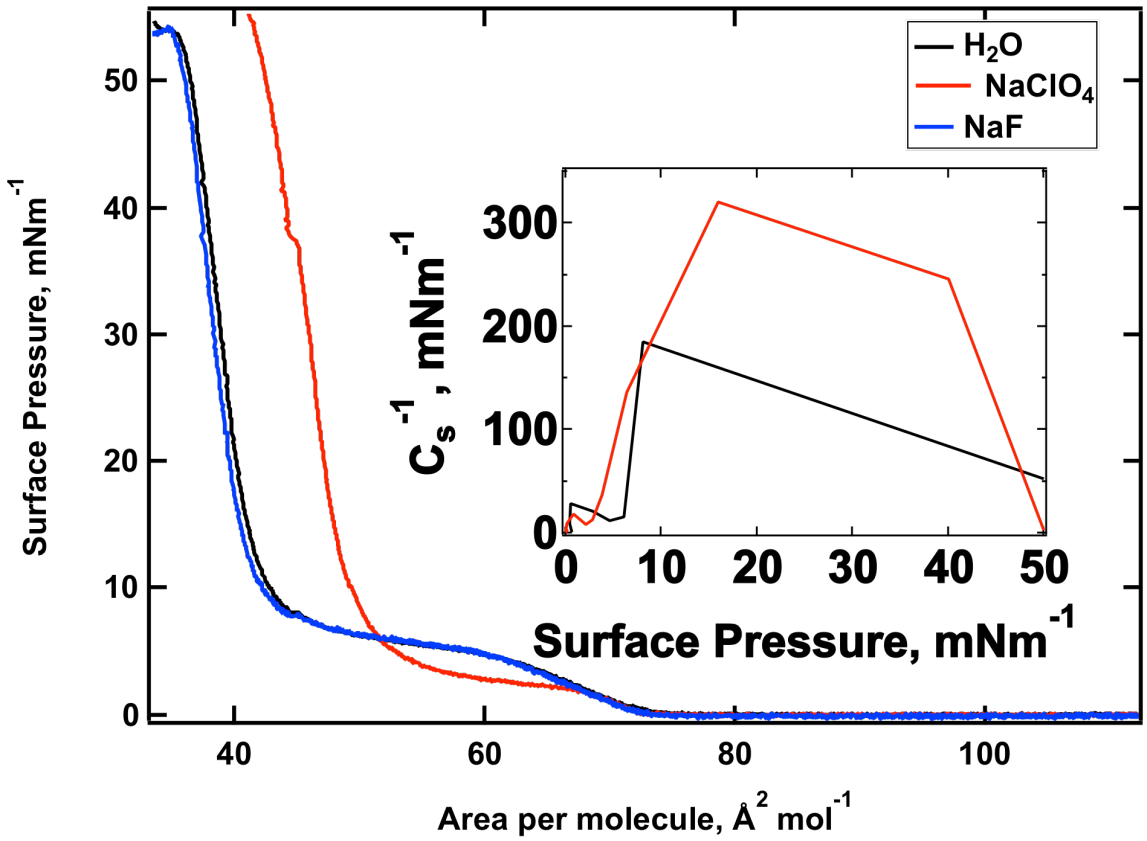

Fig 3.17- Surface pressure-area isotherm and compressional modulus data (inset) for SB3-18-2 on water and $NaClO_4$. NaF data is shown in blue for reference.

The onset and surface pressure of the phase plateau associated with the liquid expanded to liquid condensed phase transition is shifted to higher area per molecule values when in the presence of $NaClO_4$. The onset occurs at 66.8 $Å^2$ mol^{-1} (± 0.3 mNm^{-1}) and 1.8 mNm^{-1} (± 0.3 mNm^{-1}) compared to 60.1 $Å^2$ mol^{-1} and 4.3 mNm^{-1} when on pure water. This corresponds to an increase in area per molecule of 5.3 $Å^2$ mol^{-1}. Given that the monolayer exhibits little physical change in the presence of NaCl it is most likely that the effects observed on $NaClO_4$ are specific to the perchlorate anion. To ensure that this effect was truly a function of the presence of the perchlorate anion, isotherm data is also presented for NaF (also shown in figure 3.17). Isotherms were also conducted on NaBr, however these were also similar to the isotherms presented in figure 3.18 and are not shown here. Therefore the change in the phase behaviour of the monolayer on $NaClO_4$ suggests that the perchlorate anion is

interacting with the head group of the surfactant. Any interaction is likely to be an electrostatic one between the negatively charged anion and the positively charged ammonium group on the surfactant head. The anion interacts with this moiety on the surfactant throughout lateral compression, as there is still an increase in area per molecule in the liquid condensed phase. At a fixed surface pressure of 35 mNm^{-1} the area per molecule of the monolayer is increased by 7.1 (± 0.8) $Å^2$ mol^{-1}. The reduction in the surface pressure of the phase plateau and the subsequent area per molecule at which it occurs implies that the perchlorate anion stabilises the liquid condensed phase over the liquid expanded phase. This stabilisation of the liquid condensed phase can also be shown by large differences in the surface compressional modulus of the monolayer. When in the presence of perchlorate C_s is increased by around 100 $mNm^{-1.}$ This interaction can be shown with BAM. Figure 3.18 shows BAM images of the SB3-18-2 monolayer throughout compression on the $NaClO_4$ sub-phase.

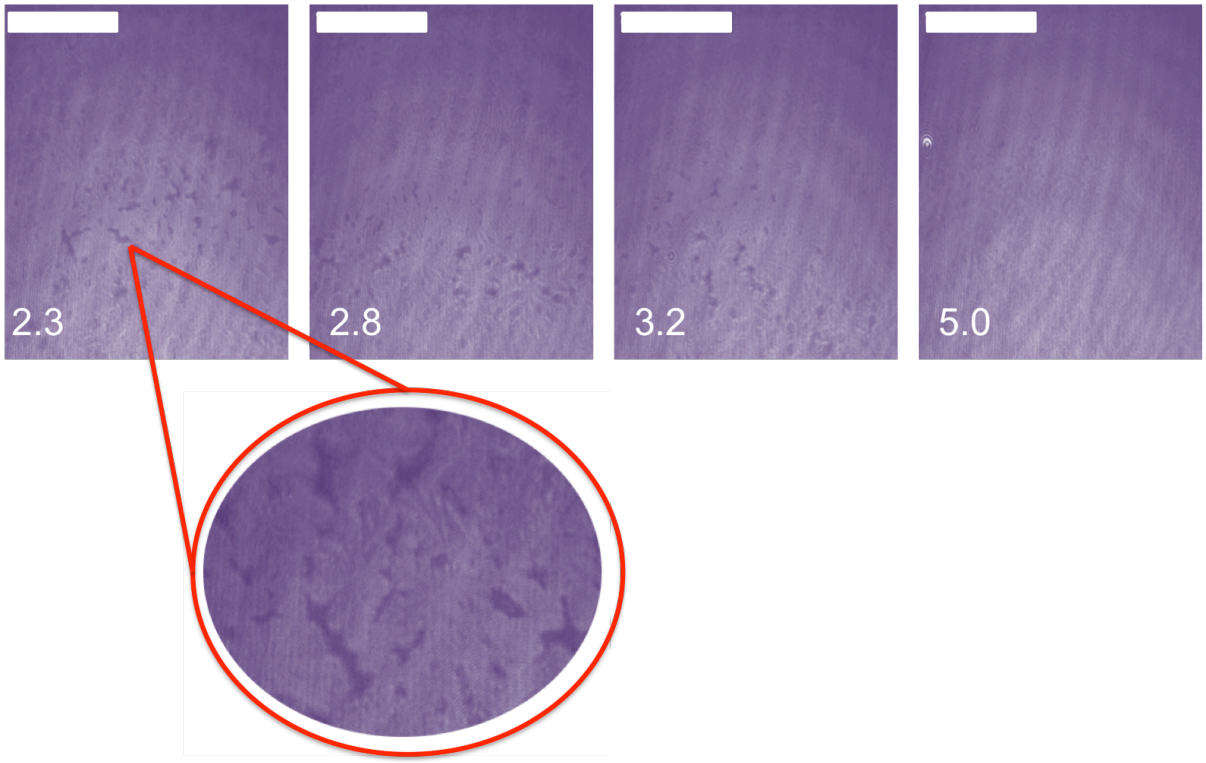

Fig 3.18- BAM images of SB3-18-2 throughout lateral compression on $NaClO_4$ sub-phase. The images have an applied colour filter to enhance the contrast between the two-surfactant phases. The scale bar represents 50 μm.

Analysis of the BAM images clearly shows that the presence of the perchlorate anion modifies the onset of the phase co-existence region. At 2.3 mNm^{-1} the BAM images consists largely of liquid condensed domains and a homogenous condensed film is obtained by 5 mNm^{-1}. The domain shape of the nucleating liquid condensed phase is also changed in the presence of perchlorate. The domains now take on a much more round-lobed structure as opposed to the sharp-striated structures observed on water and the previous salt sub-phases. Comparison between the sulfobetaine-perchlorate interaction and the phospholipid-perchlorate interaction is difficult as no literature exists for the phospholipid system.

3.5 X-ray and neutron reflectometry of SB3-18-2 Langmuir monolayers

Figure 3.19 displays co-refined XRR and NR data for the SB3-18-2 monolayer at 6 and 35 mNm^{-1}. The approach of structural investigation was slightly different for this monolayer compared with SB3-18. Instead of tracking the monolayer throughout lateral compression, two surface pressures were chosen for reflectometry studies. The first was chosen at, 6 mNm^{-1}, as this lies within the phase co-existence region. The second, at 35 mNm^{-1}, as this lies roughly in the middle of the liquid condensed phase of the surfactant. Table 3.8 shows a summation of the structural parameters that were used to gain the best fit for the experimental data. The scattering length density of the head group was used as calculated in section 3.2 of this thesis. The scattering length density of the tail group was calculated assuming a molecular volume of 799 $Å^3$, which has previously been reported for a cationic surfactant with the same tail structure[38]. Due to the nature of the synthesis it was not possible to yield SB3-18-2 with deuterated tail groups. This was due to the time constraints associated with surfactant synthesis before the allocated beamtime. The hydrogenated surfactant was therefore measured using two neutron contrasts. These were pure D_2O and 70 % D_2O.

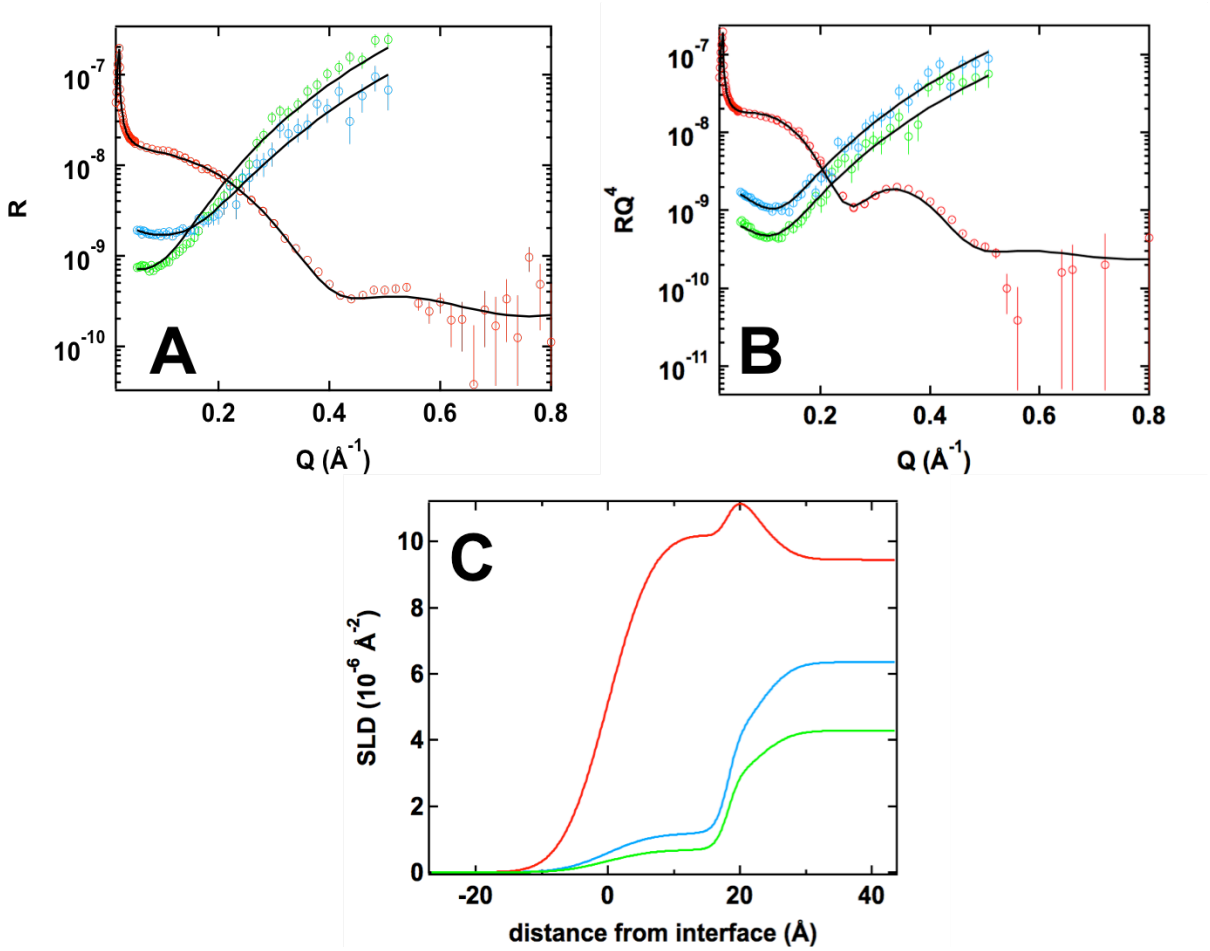

Fig 3.19- Co-refined XRR and NR data for SB3-18-2 on a pure water sub-phase at A) 6 and B) 35 mNm^{-1}. C) shows an example scattering length density profile for the relevant model at 35 mNm^{-1}. X-ray data is shown in red, D_2O contrast shown in blue and 70 % D_2O contrast is shown in green.X^2 values are 8.4, and 3.4 x 10^{-17} for 6 and 35 mNm^{-1} respectively.

	Scattering Length Density (10^{-6} Å^{-2})			Model:			
				Surface pressure /mN m^{-1}			
				6		35	
	D_2O	70 % D_2O	x-ray	t/Å	σ /Å	t/Å	σ /Å
Lipid Tail	-0.46		10.5	7.1 ±0.2	5.6 ±0.2	18.1 ±0.4	5.4 ±0.2
Lipid Head	0.99		14.4	4.5 ±0.3	2.4 ±0.3	4.5 ±0.3	2.4 ±0.2
Water	6.35	4.28	9.45		2.2 ±0.4		4.0 ±0.4

Table 3.8- Summary of fitting parameters used to model the SB3-18-2 monolayer at surface pressures of 6 and 35 mNm^{-1}.

As with the single tailed surfactant reflectometry data in section 3.2 the model has been constrained using the experimental APM values shown in figure 3.12 and table 3.7. Table 3.9 shows the experimental values compared with the APM value found from the best fit. The APM value found from the fits was always restricted to be within 10 % of the experimental data. Reasons for this have been explained in section 3.2 of this thesis.

Surface Pressure (mNm^{-1})	Experimental APM ($Å^2$ mol^{-1})	Modeled APM ($Å^2$ mol^{-1})	Percentage difference
6	63.9 ± 0.7	69.4 ± 1	+8.6%
35	38.3 ± 0.6	35.2 ± 1	-8.1%

Table 3.9- Comparison between experimentally observed and modeled APM values.

At 6 mNm^{-1} the surfactant monolayer has a thickness of 11.6 ± 0.5 Å. At this surface pressure the surfactant remains in the co-existence region and the tail group is therefore expected to exhibit a high chain tilt normal to the surface (see figure 3.22). However at the higher surface pressure of 35 mNm^{-1} the surfactant is now well into the liquid condensed phase. At this surface pressure the monolayer has a thickness of 22.6 ± 0.7 Å. The increased thickness of the monolayer shows that the addition of the extra hydrocarbon tail now promotes Van der Waals interactions between the chains and allows for the alignment of the surfactant tail groups normal to the surface, which ultimately drives the phase transition from the liquid expanded phase through to the liquid condensed phase. This behaviour is characteristic of a lipid/surfactant in the liquid condensed phase [10 39 40].

3.5.1 The effect of salt as investigated by XRR and NR

As with the Langmuir isotherm data presented in figure 3.15 the structure of the surfactant was also investigated on NaCl and $CaCl_2$ sub-phases, using XRR and NR. The same set of surface pressures was chosen as those conducted on pure water. Figure 3.20 shows the reflectometry data for the surfactant on NaCl and $CaCl_2$ sub-phases, whilst the structural parameters used to model the data are shown in table 3.10.

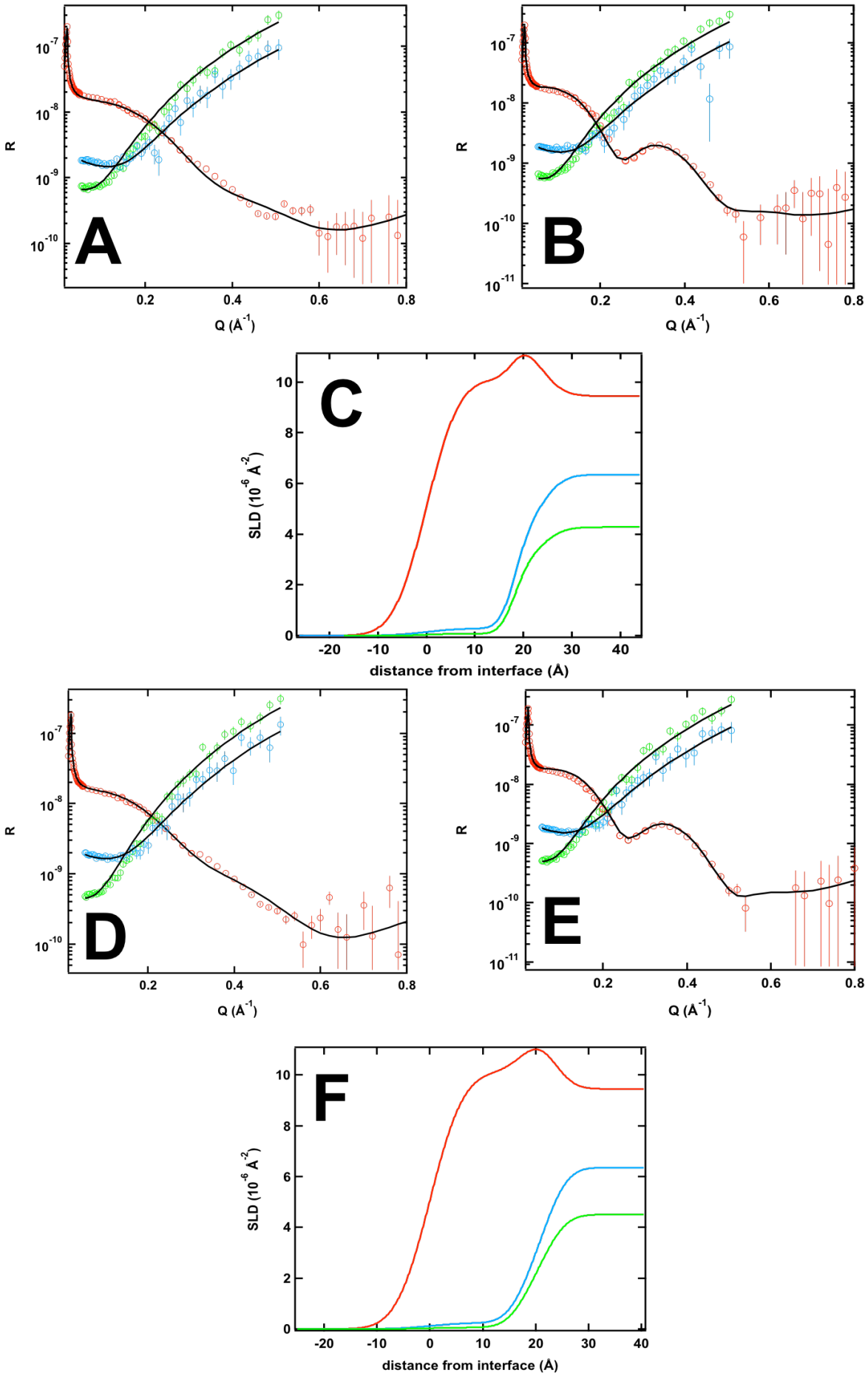
A
B
C
D
E
F
R
Q (Å^{-1})
SLD (10^{-6} Å^{-2})
distance from interface (Å)

Fig 3.20- A andB) SB3-18-2 monolayer on 50 mM NaCl at 6 and 35 mNm^{-1} respectively. X^2 values are 6.16 $x10^{-17}$ and 1.15 $x10^{-16}$ for 6 and 35 mNm^{-1} respectively. C) Scattering length density profile for SB3-18-2 on 50 mM NaCl at 35mNm^{-1}. D and E) SB3-18-2 monolayer on 50 mM $CaCl_2$ at 6 and 35 mNm^{-1} respectively. X^2 values are 9.69 $x10^{-16}$ and 5.5 $x10^{-17}$ for 6 and 35 mNm^{-1} respectively. F) Scattering length density profile for SB3-18-2 on 50 mM $CaCl_2$ at 35 mNm^{-1}.

	Scattering Length Density (10^{-6} Å^{-2})			Layer and sub-phase	Model:			
					Surface pressure /mN m^{-1}			
					6		35	
	D_2O	70% D_2O	x-ray		t/Å	σ /Å	t/Å	σ /Å
Lipid Tail	-0.46		10.5	NaCl	8.0 ±0.4	5.5 ±0.3	18 ±0.3	5.3 ±0.2
				$CaCl_2$	7.3 ±0.4	5.2 ±0.5	18.4 ±0.2	5.0 ±0.2
Lipid Head	0.99		14.4	NaCl	4.9 ±0.3	2.8 ±0.2	4.8 ±0.3	3.3 ±0.2
				$CaCl_2$	4.9 ±0.4	2.9 ±0.4	4.7 ±0.4	3.0 ±0.2
Water	6.35	4.28	9.45			4.0 ±0.4		3.1 ±0.3

Table 3.10- Summary of fitting parameters used to model the SB3-18-2 monolayer on NaCl and $CaCl_2$ sub-phases at surface pressures of 6 and 35 mNm^{-1}.

The behaviour of the surfactant on sub-phases containing NaCl and $CaCl_2$, in terms of salt interaction, is similar to that of the single tailed species. The best fit was obtained for analogous structural parameters as for the fit on pure water. This again supports the notion that a diffuse ion

layer is present beneath the monolayer, owing to the small contraction of the film on salt sub-phases. Scattering data is suggestive of no significant penetration of Na^+, Ca^{2+} or Cl^- into the surfactant head group region.

3.5.2 Other structural considerations

The large difference in the SB3-18-2 monolayer thickness values between 6 and 35 mNm^{-1} implies that the tilt of the carbon-chain of the surfactant normal to the interface decreases by a large amount with lateral compression. Calculated chain tilt values as a function of surface pressure are presented in table 3.11.

Surface Pressure (mNm^{-1})	**Chain Tilt (°) with respect to the surface normal**
6	59.1
35	8.1

Table 3.11- Change in chain tilt as a function of surface pressure for the SB3-18 monolayer.

In comparison to the single tailed species the chain tilt changes dramatically with increasing surface pressure. Changes of 51 ° are observed on going from 6 to 35 mNm^{-1}. The chain tilt of 59.1 ° found for 6 mNm^{-1} is similar to the value found for SB3-18 and is consistent with the surfactant still remaining in a largely liquid expanded phase at this surface pressure. The large change found on increasing the surface pressure to 35 mNm^{-1} is consistent with data reported for double tailed phospholipids where a large change in chain tilt is observed on going from the liquid expanded to the liquid condensed phase[39].

As with the single tailed species it is important to compare these values to known chain tilts of structurally similar phospholipids. It has been reported that, in the liquid condensed phase, DPPC has an average chain tilt of 33 °, a value far greater than that of SB3-18-2. However this difference is consistent with that observed between SB3-18 and the lyso

phospholipids. The larger phosphocholine head group has an increased polar region and will inhibit the erection of tails to their full extent. The smaller sulfobetaine will allow for more efficient packing of the surfactant at the interface and promote the alignment of tail groups relative to the surface normal. This is shown schematically in figure 3.21.

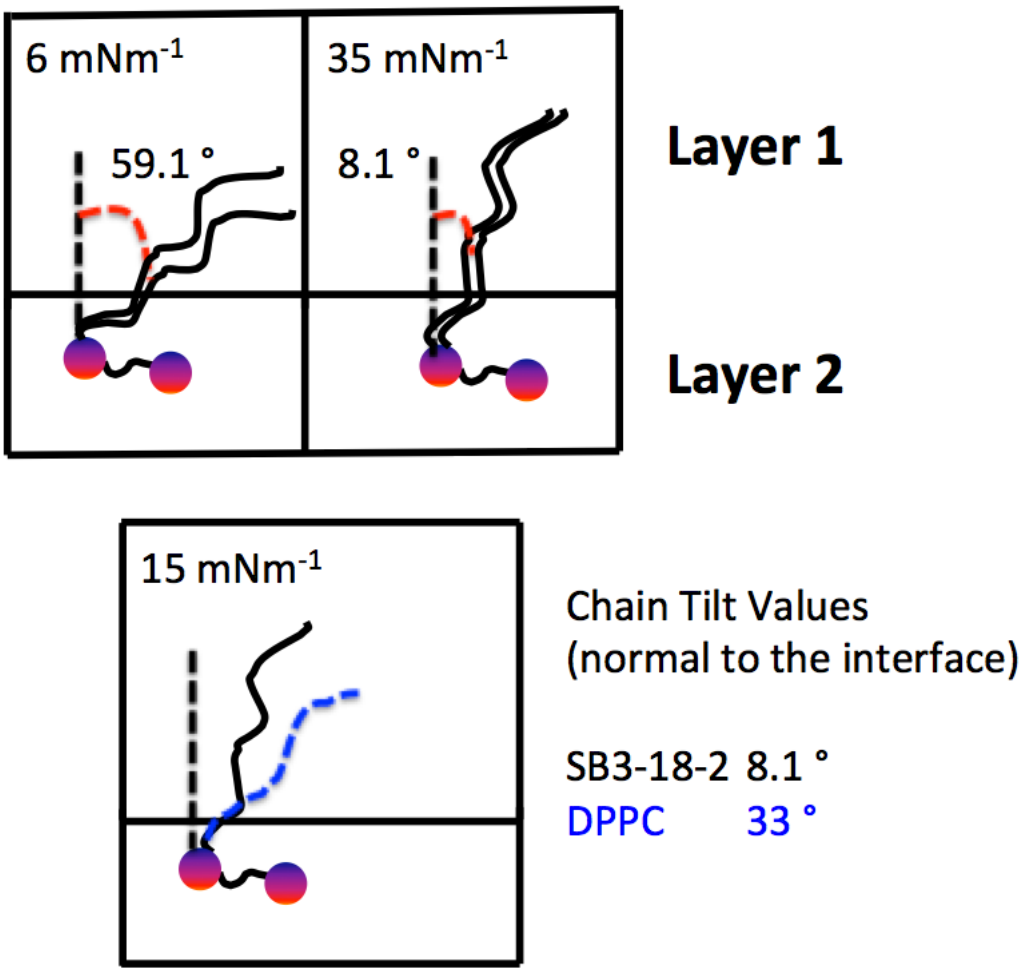

Fig 3.21- Variation in chain tilt with increasing surface pressure for SB3-18-2, along with comparison of chain tilt of the liquid condensed phase between SB3-18-2 and DPPC.

3.5.3 Probing the nature of perchlorate interaction

Figure 3.22 shows raw x-ray reflectometry data for SB3-18-2 at 35 mNm^{-1} on a pure water, NaCl, $CaCl_2$ and $NaClO_4$ sub-phases. The scattering on the water and previously described salt sub-phases is indistinguishable. However when the monolayer is spread over the sub-phase containing

the perchlorate anion there is a distinct difference in the reflectometry data. The minimum at ca. Q= 0.3 $Å^{-1}$ is more pronounced and this is most likely due to the strong interaction between the sulfobetaine head group and the perchlorate anion.

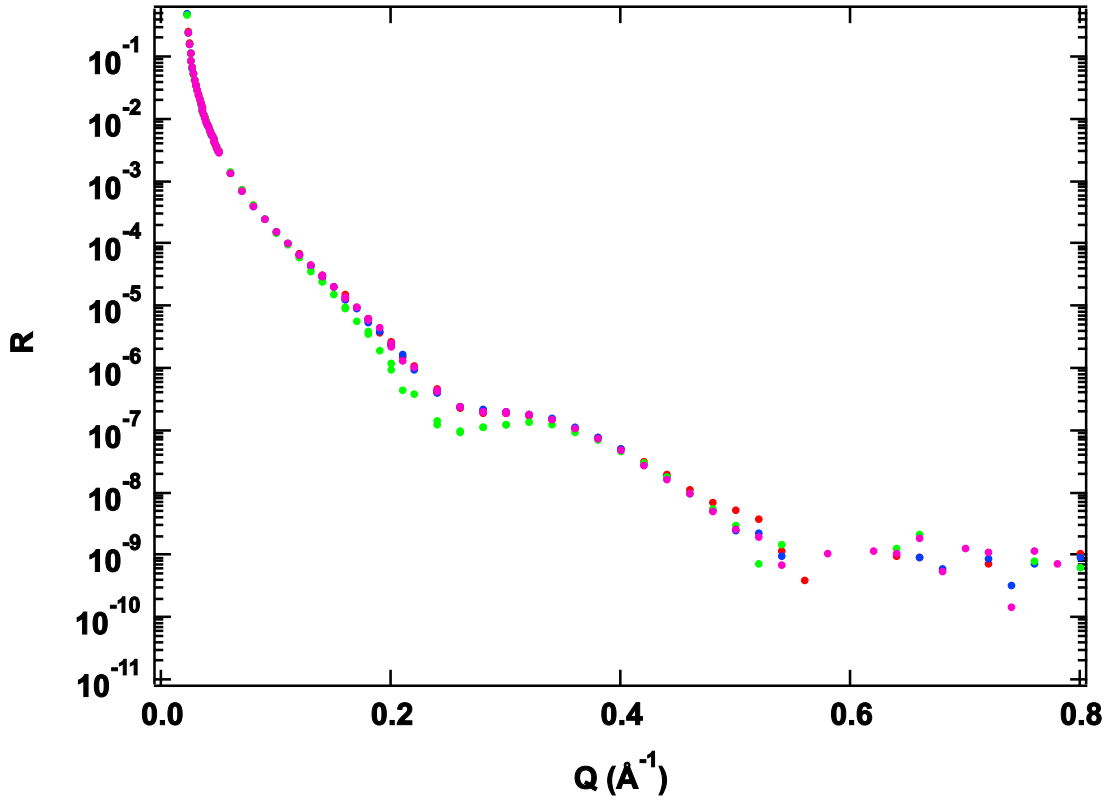

Fig 3.22- Raw x-ray reflectometry data for SB3-18-2 on water (red), NaCl (pink), $CaCl_2$ (blue) and $NaClO_4$ (green) sub-phases at 35 mNm^{-1}.

Three possible interactions are presented in figure 3.23. A) corresponds to the formation of a diffuse ion layer beneath the sulfobetaine head group as with the proposed models for NaCl and $CaCl_2$. B) shows partial penetration of the perchlorate anion into the head group region of the monolayer, driven primarily through the interaction between the negatively charged oxygen moiety on the perchlorate anion and the positively charged ammonium group. C) represents the inclusion of the entire perchlorate anion into the head group region of the monolayer, again driven through the electrostatic interaction of oppositely charged groups.

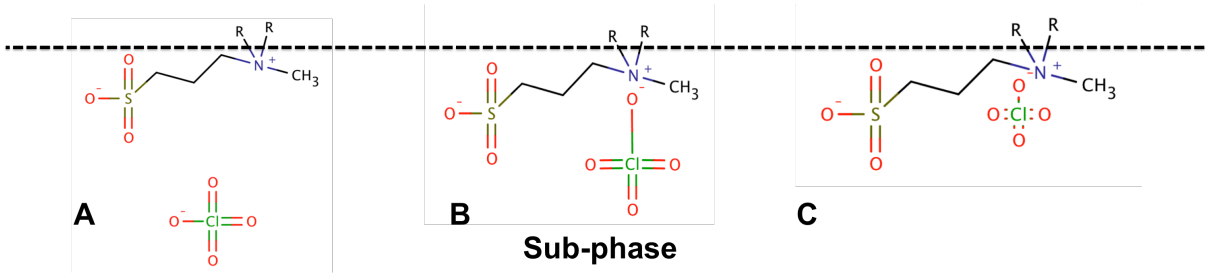

Fig 3.23- Possible modes of interactions for the perchlorate anion with the sulfobetaine head group. A) the formation of a diffuse ion layer beneath the surfactant head group. B) partial penetration of the perchlorate anion into the head group and C) full penetration of the perchlorate anion into the head group.

As with the data shown for the single tailed species, x-ray reflectometry is likely to be most sensitive to the interaction of large ions with the surfactant head group. Given that the anion contains a chlorine atom, which will scatter x-rays much more than neutrons, the x-ray data has been used to rationalise the proposed modes of interaction presented in figure 3.23. Figure 3.24 shows raw x-ray reflectometry data at 35 mNm^{-1} along with models generated from the suggested modes of interaction shown in figure 3.23.

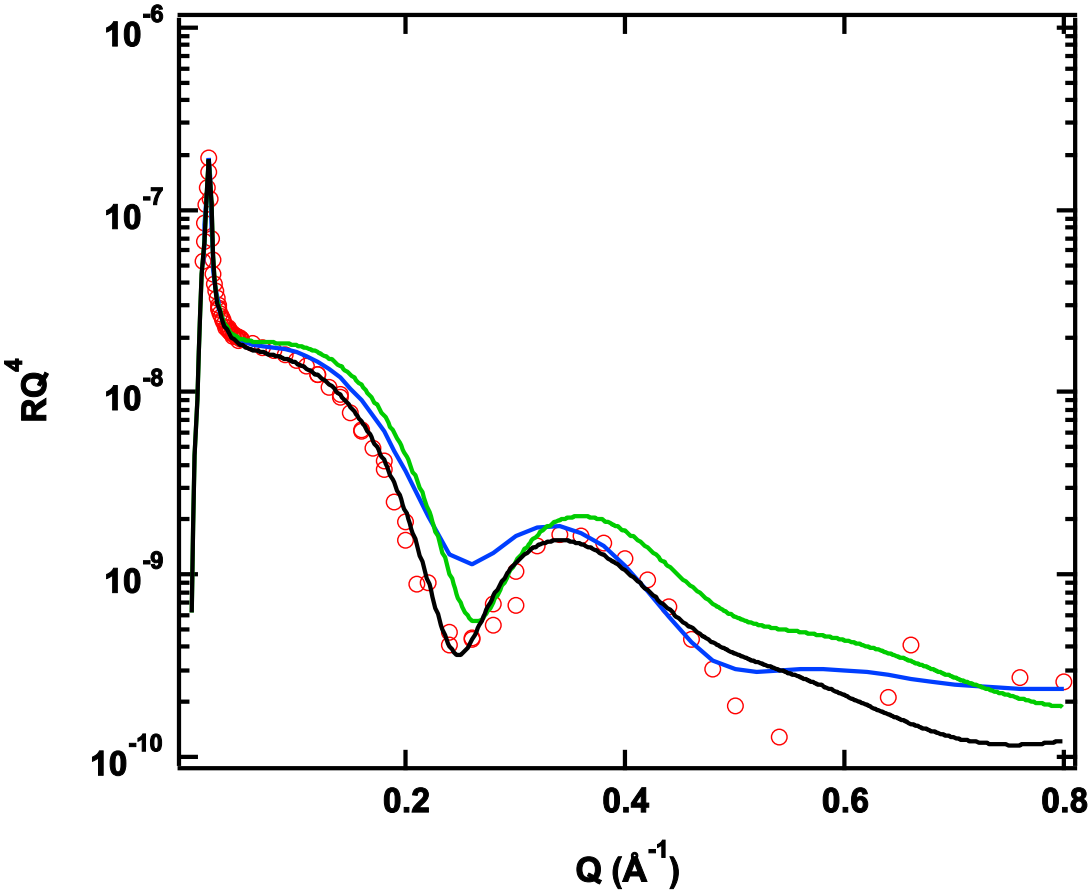

Fig 3.24- Models generated from modes of interaction presented in figure 3.25. A (blue)- diffuse ion layer with no ion interaction. B (green)- partial incorporation of perchlorate anion into head group region. C (black)- entire inclusion of perchlorate anion into head group region of surfactant.

The structural parameters used for each model presented in figure 3.24 are shown in table 3.12. Model A) was generated using the same structural parameters as for the surfactant on a pure water sub-phase. Allowing for a small increase in the thickness of the head group and accounting for the partial incorporation of the perchlorate anion generated model B. This was calculated by increasing the scattering length density from 14.4 to 15.7 x 10^{-6} $Å^{-2}$. An increase in scattering length density of this kind accounts for the incorporation of the negatively charged oxygen moiety on the perchlorate anion into the head group region of the surfactant. Increasing the volume and scattering length density of the head group by one oxygen atom generated this model (volume of oxygen atom was calculated at 0.9 $Å^3$, whilst a scattering length for oxygen of

2.21 $x10^{-5}$ $Å^{-1}$ was used)[21 22]. Model C) was generated by a larger increase in head group thickness compared to model B. The scattering length density of the head group was also increased from 14.4 to 29.1 x 10^{-6} $Å^{-2}$. This increase in scattering length density accounts for the presence of the entire perchlorate anion penetrating into the head group region of the surfactant and was based on a scattering length of Cl and O of 4.79 $x10^{-5}$ and 2.21 $x10^{-5}$ $Å^{-1}$ respectively[22]. The volume of the head group was also increased to account for the volume of the perchlorate anion, which is 22.1 Å[321].

	Scattering Length Density (10^{-6} Å^{-2})			Layer and sub-phase	Model: Surface pressure /mN m^{-1} 35	
	A	B	C		t/Å	σ /Å
Lipid Tail	10.5	10.5	10.5	A B C	18.1 17.8 17.8	5.9
Lipid Head	14.4	15.7	29.1	A B C	4.5 5.1 6.1	2.9
Water	9.45					2.3

Table 3.12- Structural parameters used to generate models A, B and C presented in figures 3.25 and 3.26 for SB3-18-2 at 35 mNm^{-1} on a $NaClO_4$ sub-phase.

It is clear that the best fit for the data is model C that allows for the incorporation of the entire perchlorate anion. An increase in the scattering length density from 14.4 to 29.1 x 10^{-6} $Å^{-2}$ suggests a 1:1 binding mechanism between the anion and the head group of the surfactant, and most likely proceeds through the negatively charged perchlorate and the positively charged ammonium group of the surfactant head. Figure 3.25 shows the co-refined reflectometry data for the monolayer on $NaClO_4$ at 6 and 35 mNm^{-1}. A scattering length density profile for the same system at 35 mNm^{-1} is also shown. Table 3.13 shows the structural parameters used to model the data. The neutron scattering length density of the head group has also been increased to account for the incorporation of the perchlorate anion into the head group region of the surfactant. This has been calculated in the same way as described previously for the x-ray scattering length density.

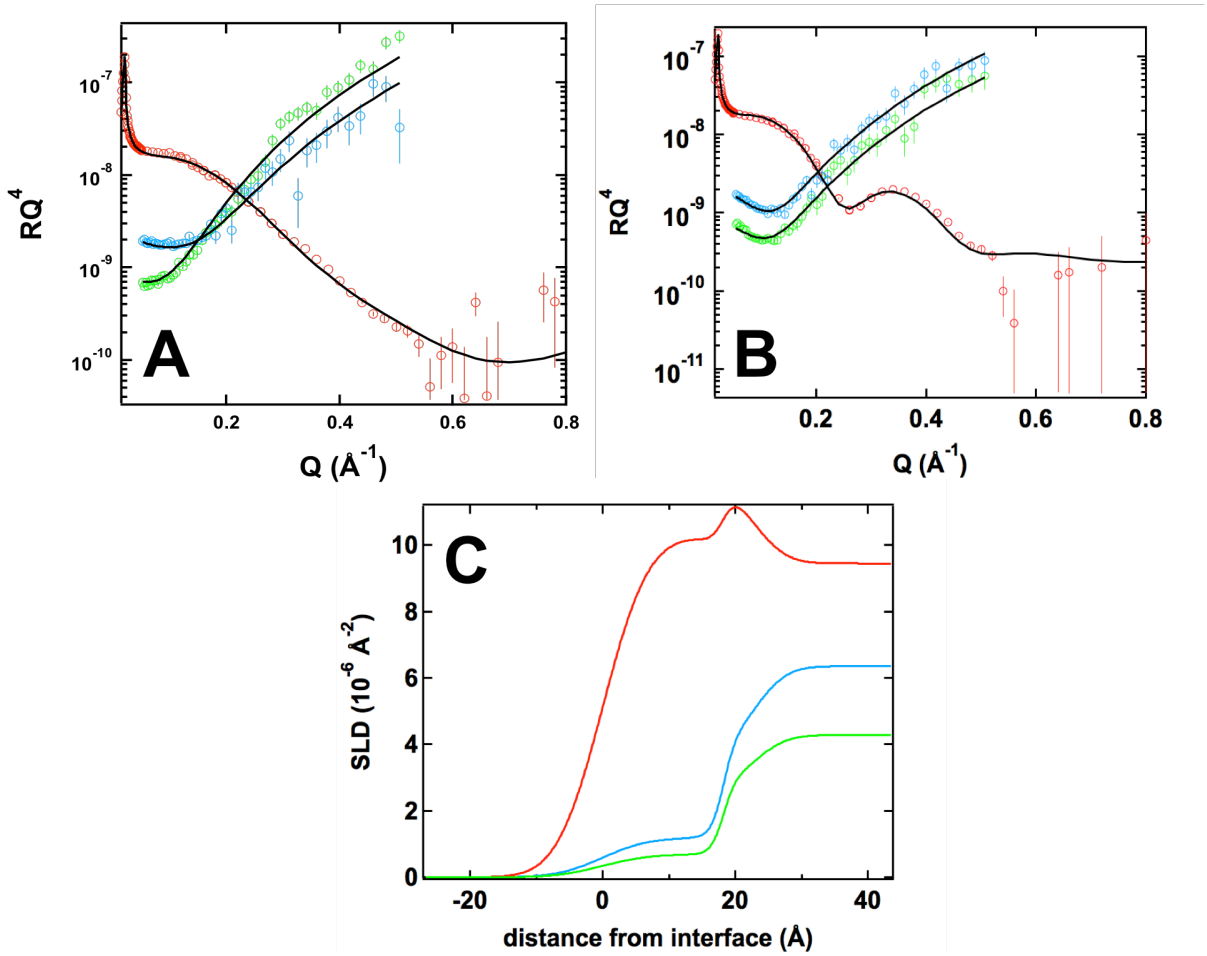

Fig 3.25- Co-refined XRR and NR data for SB3-18-2 on $NaClO_4$ at A) 6 and B) 35 $^{-1}$. C) shows an example scattering length density profile for the relevant model at 35 mNm^{-1}. X-ray data is shown in red, D_2O contrast shown in blue and 70 % D_2O contrast is shown in green.X^2 values are 2.3, and 1.9 x 10^{-17} for 6 and 35 mNm^{-1} respectively.

	Scattering Length Density (10^{-6} Å^{-2})			Model: Surface pressure /mN m^{-1}			
				6		35	
	D_2O	70 % D_2O	x-ray	t/Å	σ /Å	t/Å	σ /Å
Lipid Tail	-0.46		10.5	6.8 ±0.4	4.9 ±0.3	17.8 ±0.3	5.9 ±0.5
Lipid Head	2.8		29.1	5.6 ±0.3	3.0 ±0.5	6.8 ±0.4	2.8 ±0.3
Water	6.35	4.28	9.45		3.0 ±0.4		2.6 ±0.3

Table 3.13- Summary of fitting parameters used to model the SB3-18-2 monolayer on a $NaClO_4$ sub-phases at surface pressures of 6 and 35 mNm^{-1}.

3.6 Concluding Remarks

Langmuir trough measurements, BAM and co-refined XRR/NR have shown that single tailed sulfobetaine surfactants remain in one phase throughout lateral compression, whilst double tailed species undergo a two-dimensional phase transition when compressed. This has been rationalised by an increase in Van der Waals interactions for the double tailed species owing to the addition of the second hydrocarbon chain.

This has also been shown by marked differences in chain tilt relative to the surface normal.

It is clear that the presence of salt has little affect on the single tailed sulfobetaine surfactant, whilst only the perchlorate anion affects the structure and phase behaviour of the double tailed species. The key question of the affect of head group charge reversal on the interaction of salt has been probed showing that minimal salt interaction occurs. It does suggest however that the surfactant head group may have a higher affinity for negatively charged ions. This is in contrast to phospholipids where they are reported to have a greater affinity for cations. The presence of the negatively charged perchlorate anion stabilises the LC phase over the LE phase for sulfobetaine surfactants. This is in contrast to double tailed phospholipids where the presence of cations has this effect.

Sulfobetaines are regularly used in mild formulations such as baby shampoo. This study has highlighted some aspects of their fundamental physical chemistry. Such little interaction with salt may be of advantage in the formulation industry where salt is commonly added to commercial products. These surfactants could be added to stabilise commercial formulations without the worry of salt inhibiting their performance. Sulfobetaines have also shown promise as biocompatible coatings, however little was known with regard to the mechanism of such biocompatibility. Given that salt interactions play a key role in protein adsorption at interfaces, their lack of interaction with salt may play a large role in inhibiting biofouling. Finally sulfobetaines have been reportedly used for temperature controlled drug release. The knowledge gained from this work in terms of the phase behaviour of these species is particularly relevant here. Also the development of a novel double tailed species with defined phase behaviour may prompt their further use to this effect. For a review of possible future work for these sulfobetaine systems the reader is directed to chapter 6 of this thesis.

3.7 References

1. Guangmiao Q, Cheng J, Wei J, et al. Synthesis, characterization and surface properties of series sulfobetaine surfactants. Journal of Surfactants and Detergents 2011;**14**(1):31-35.
2. Reich C. *Surfactants in Cosmetics*. 2 ed. New York: Marcel Dekker, 1997.
3. Lowe AB, Vamvakaki M, Wassal MA, et al. Well-defined sulfobetaine-based statistical copolymers as potential antibioadherent coatings. Journal of Biomedical Materials Research 2000;**52**(1):88-94.
4. Yuan Y, Ai F, Zang X, et al. Polyurethane vascular catheter surface grafted with zwitterionic sulfobetaine monomer activated ozone. Colloids and Surfaces B: Biointerfaces 2004;**35**(1):1-5.
5. Gomez-Serranillos IR, Minones J, Dynarowicz-Latka P, et al. Study of pi-A isotherms of miltefosine monolayers spread at the air/water interface. Physical Chemistry Chemical Physics 2004;**6**:1580-86.
6. Davies; JT, Rideal EK. *Interfacial Phenomena*. New York: Reinhold, 1963.
7. Osak A, Dynarowicz-Latka P, Conde O, et al. Edelfosine- A new antineoplastic drug based on a phospholipid like structure: The Langmuir monolayer study. Colloids and Surfaces A: Physiochemical Engineering Aspects 2008;**319**(2008):71-76.
8. Flasinski M, Broniatowski M, Wydro P, et al. Comparative characteristics of membrane-active single-chained ether phospholipids: PAF and Lyso-PAF in Langmuir monolayers. Journal of Physical Chemistry B 2012;**116**:3155-63.
9. Flasinski M, Wydro P, Broniatowski M. Lyso-phosphatidylcholines in Langmuir monolayers- Influence of chain length on physiochemical characteristics of single-chained lipids. Journal of colloid and interface science 2014(418):20-30.
10. Mohwald H. *Handbook for Biological Physics*: Elsevier Science B.V, 1995.
11. Ma G, Allen HC. Condensing effect of palmitic acid on DPPC in mixed Langmuir monolayers. Langmuir 2007;**23**:589-97.
12. Yaseen M, Lu JR, Webster JRP, et al. Adsorption of single chain Zwitterionic phosphocholine surfactants: Effects of length of alkyl chain and head group linker. Biophysical Chemistry 2005;**117**(3):263-73.
13. Li ZX, Dong CC, Wang JB, et al. Unusual surface structures in layers of cationic gemini surfactants adsorbed at the air/water interface. Langmuir 2002;**18**:6614-22.
14. Kewalramani K, Hlaing H, Ocko BM, et al. Effects of divalent cations on phase behaviour and structure of a zwitterionic phospholipid (DMPC) monolayer at the air-water interface. The Journal of Physical Chemistry Letters 2010;**1**:489-95.
15. Petelska AD, Figaszewski Z. The equilibria of lipid-K+ ions in monolayers at the air-water interface. Journal of Membrane Biology 2011;**244**:61-66.
16. Chapman D, Peel WE, Kingston B, et al. Lipid phase transitions in model biomembranes. The effect of ions on phosphatidylcholine bilayers. Biochimica et Biophysica Acta 1977;**464**:260-75.

17. Seelig J. Interaction of phospholipids with calcium ions. On the role of the head groups. Journal of Cell Biology International Reports 1990;**14**(129):353-59.
18. Lu JR, Simister EA, Thomas RK. Structure of an octadecyltrimethylammonium bromide layer at the air/water interface determined by neutron reflection: Systematic errors in reflectivity measurements. The journal of physical chemistry 1993;**97**:6024-33.
19. Holdaway JA. A study of the structure and formation of biocompatible mesostructured polymer-surfactant hydrogel films. University of Bath, 2014.
20. Hardy NJ, Richardson TH, Grunfeld F. Minimising monolayer collapse on Langmuir troughs. Colloids and Surfaces A: Physiochemical Engineering Aspects 2006;**284-285**:202-06.
21. Shannon RD. Revised effective ionic radii and systematic studies of interatomic distances in halides and chalcogenides. Acta Crystallographica 1976;**32**(5):751-67.
22. Chantler CT, Olsen K, Dragoset RA, et al. Detailed tabulation of atomic form factors, photoelectric absorption and scattering cross section, and mass attenuation coefficients for z=1-92 from E=1-10 eV to 0.4-1.0 MeV. Journal of phycisal and chemical reference data 1995;**24**:71-643.
23. Dahmen-Levison;, Brezesinski G, Mohwald H. Monolayer structures of triple-chain phosphatidylcholines as substrates for phospholipases. Colloids and Surfaces A: Physiochemical Engineering Aspects 2000;**17**:97-103.
24. Brezesinski G, Dietrich A, Struth B, et al. Influence of ether linkages on the structure of double-chain phospholipid monolayers. Chemistry and Physics of Lipids 1995;**76**:145-57.
25. Duncan SL, Larson RG. Comparing experimental and simulated pressure-area isotherms for DPPC. Biophysocal Journal 2008;**94**:2965-86.
26. Espinosa G, Montero-Lopez I, Monroy F, et al. Shear rheology of lipid monolayers and insights on membrane fluidity. Proceedings of the National Academy of Sciences 2010;**108**(15):6008-13.
27. Aroti AL, E; Maltseva, E; Brezesinski, G. Effects of hofmeister anions on DPPC langmuir monolayers at the air-water interface. Journal of Physical Chemistry B 2004;**108**:15238-45.
28. Henon SM, J. Microscope at the Brewster angle: Direct observation of first order transitions in Langmuir monolayers. Review of Scientific Instruments 1991;**64**(4):936-39.
29. Honig D, Mobius D. Brewster Angle Microscopy of LB films on solid substrates. Chemical Physics Letters 1991;**195**:50-52.
30. Honig DM, D. Direct visualisation of monolayers at the air-water interface by brewster angle microscopy. Journal of Physical Chemistry 1991;**95**(12):4590-92.
31. Kaercher T, Honig D, Mobius D. Brewster angle microscopy: A news method for visualising the spreading of Meibomian lipids. International Opthamology 1993;**17**:341-48.

32. Telesford DM. Langmuir trough and Brewster angle microscopy study of model lung surfactant monolayers at the air/aqueous interface. Ohio State University, 2012.
33. Mohwald H. Surfactant layers at water surfaces. Reports on Progress in Physics 1993;**56**:653-85.
34. Albrecht O, Gruler H, Sackmann E. Polymorphism of phospholipid monolayers. Le Journal de Physique 1978;**39**:301-13.
35. Rettig W, Koth C, Dorfler HD. Kompressionsverhalten und Gleichgewichtsspreitungsdriicke bin irer monomolekularer Dimyristoylkephalin/Dilauroylkephalin-Mischungen Colloid and Polymer Science 1984;**262**:747-53.
36. Rettig W, Dorfler HD, Koth C. Entmischungserscheinungen in binären Monoschichten des Systems Dimyristoylkephalin/Dipalmitoyl-N-methylkephalin, untersucht mittels verschiedener Spreitungs- und Oberflächentechniken. Colloid and Polymer Science 1985;**263**:647-53.
37. Barker RD. al-PC SAM approach to supported bilayers: Developing a novel model membrane system. University of Bath, 2012.
38. Tveten EG. X-ray and neutron reflectivity studies of nanodiscs below the air-water interface. University of Copenhagen, 2011.
39. Vaknin D, Kjaer K, Als-Nielsen J, et al. Structural properties of phosphatidylcholine in a monolayer at the air/water interface. Biophysical Journal 1991;**59**(1325-1332).
40. Bell GM, Combs LL, Dunne LJ. Theory of Cooperative Phenomena in Lipid Systems. Chemical Reviews 1981;**81**:15-48.

Chapter 4- Characterising protein interactions with functionalized phospholipid monolayers

This chapter will focus on the protein alignment section of this thesis. As previously discussed in the introduction, this part of the work aims to first assess the interaction of soluble proteins with a functionalized lipid monolayer. This is in an attempt to investigate the relationship between the concentration of the His-tag chelating lipid, DOGS-NTA-Ni, at the interface and protein interaction.

The approach taken here was to use the soluble protein, penicillin binding protein 3, as the protein is found within bacterial cells where it is responsible for cell wall synthesis. The protein is therefore biologically important[1-4]. As a proof of concept to ensure that the his-tagged protein would bind to a lipid interface the protein interaction with lipid vesicles was probed through the use of DLS. Next monolayers containing DOGS-NTA-Ni, were investigated at the air-water interface using BAM. Attempts were then made to transfer and characterize this system at the solid-liquid interface. This was achieved through the use of QCM and neutron reflection.

4.1 Characteising protein interactions with functionalized phospholipid vesicles

In order to understand the interaction between proteins and phospholipid membranes containing the his-tag chelating lipid, DOGS-NTA-Ni, protein interactions on unilamellar phospholipid vesicles were first probed. Dynamic light scattering was utilized to assess protein interaction. Vesicle compositions of 1, 5 and 10 mol % DOGS:DMPC were chosen as model systems due to their ease of preparation and, the large presence of DMPC based vesicles in the literature[5-8].

4.1.1 Vesicle characterization

Before the addition of protein to the vesicle samples, the structure of the vesicles alone was analysed by means of SAXS and DLS. Figure 4.1

shows the DLS results for DMPC only, 1, 5 and 10 mol % DOGS:DMPC vesicles.

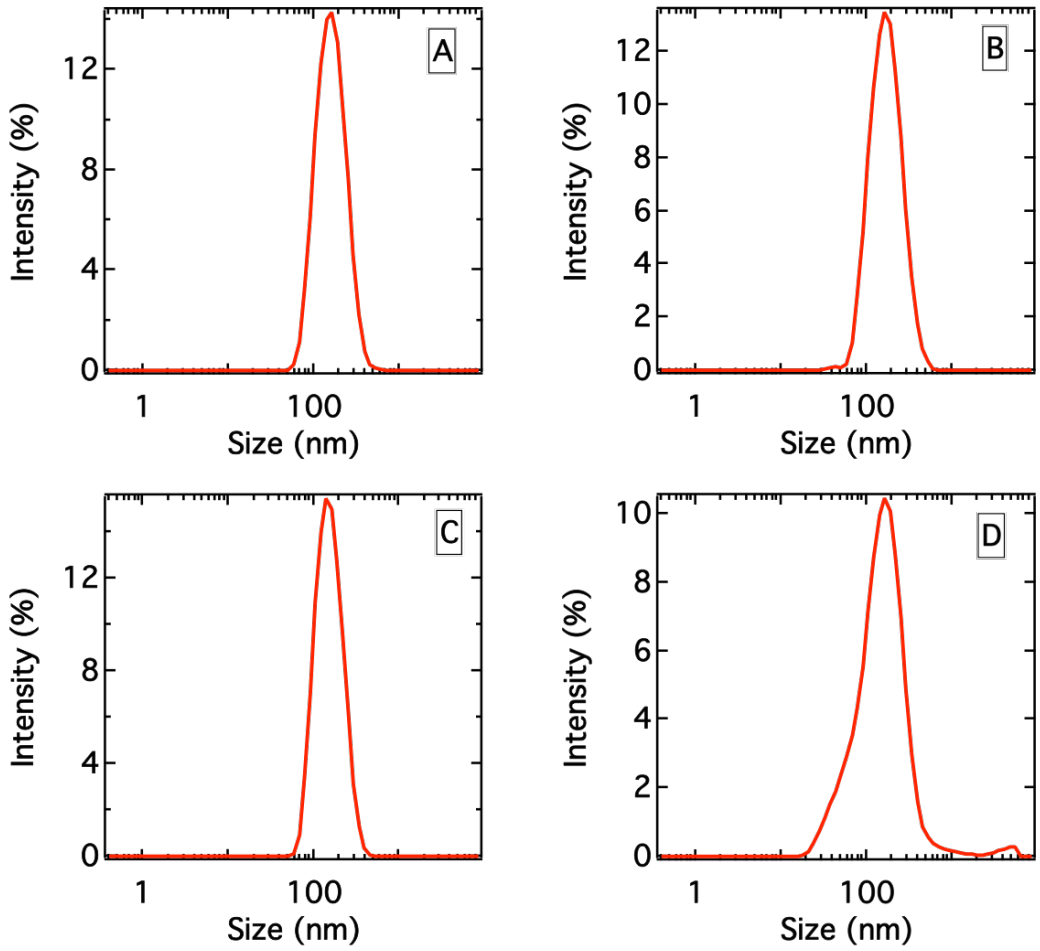

Fig 4.1 DLS data for DMPC only (d), 1 (a), 5 (b) and 10 (c) mol % DOGS:DMPC vesicles (data shown is an average of three repeats).

Extrusion of DMPC only, 1 5 and 10 mol % DOGS hydrated lipid solutions yield vesicles that are reproducible in size. Diameters determined from DLS are 164 ± 23 nm. Plots A-C in figure 4.1 suggest that the polydispersity of the vesicles containing DOGS is less than the pure DMPC vesicles. This can be rationalized by considering the phase transition of the lipids. DMPC has a phase transition of 24 °C [9], a value at or very close to room temperature. It is likely therefore that at any one point during laboratory measurements the equilibrium point of the phase of the entire vesicle will be changing due to small changes in ambient temperature. This will ultimately lead to larger fluctuations in vesicle size[10] [11]. The main phase transition for DOGS-NTA-Ni has not been reported,

however the tail group of this lipid is structurally analogous to DOPC. The main phase transition of DOPC is -16.5 °C [12] and hence the lipid will remain in a fluid like state at ambient temperatures. Altering the phase transition of the constituent lipids in multi-component systems in this way has been shown to ultimately change the phase behavior of the entire vesicular structure, and in this case, leads to a more stable- less polydisperse system[13 14].

To confirm that the vesicles probed by DLS were unilamellar in nature, SAXS experiments were performed. Figure 4.2 shows SAXS data, in the form of a Porod plot, for DMPC only and 1 mol % DOGS vesicles.

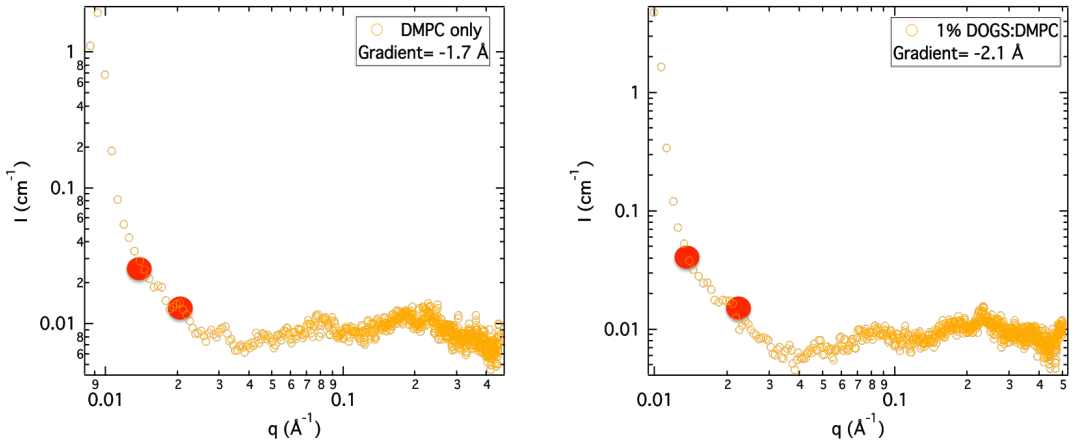

Fig 4.2- SAXS data in the form of a Porod plot for DMPC only and 1 mol % DOGS:DMPC vesicles. Red markers highlight the point at which the gradient was calculated.

Calculating the gradient between approximately 0.015 and 0.025 Å^{-1} yields gradients of -1.7 Å for the DMPC only vesicles and -2.1 Å for the 1 mol % DOGS:DMPC vesicles. This is suggestive of vesicular structures containing two-dimensional planar bilayers[5 15 16]. Furthermore there is no diffraction peak observed at 0.1 Å^{-1}, which would be expected for a multi-lamellar system[17].

4.1.2 Characterisation of PBP3 binding with DLS

Before proceeding to protein binding characterization the bare protein was measured by DLS giving a mean hydrodynamic diameter of 7.59 nm. This figure agrees well with published diffraction data for the crystal structure of the protein[18].

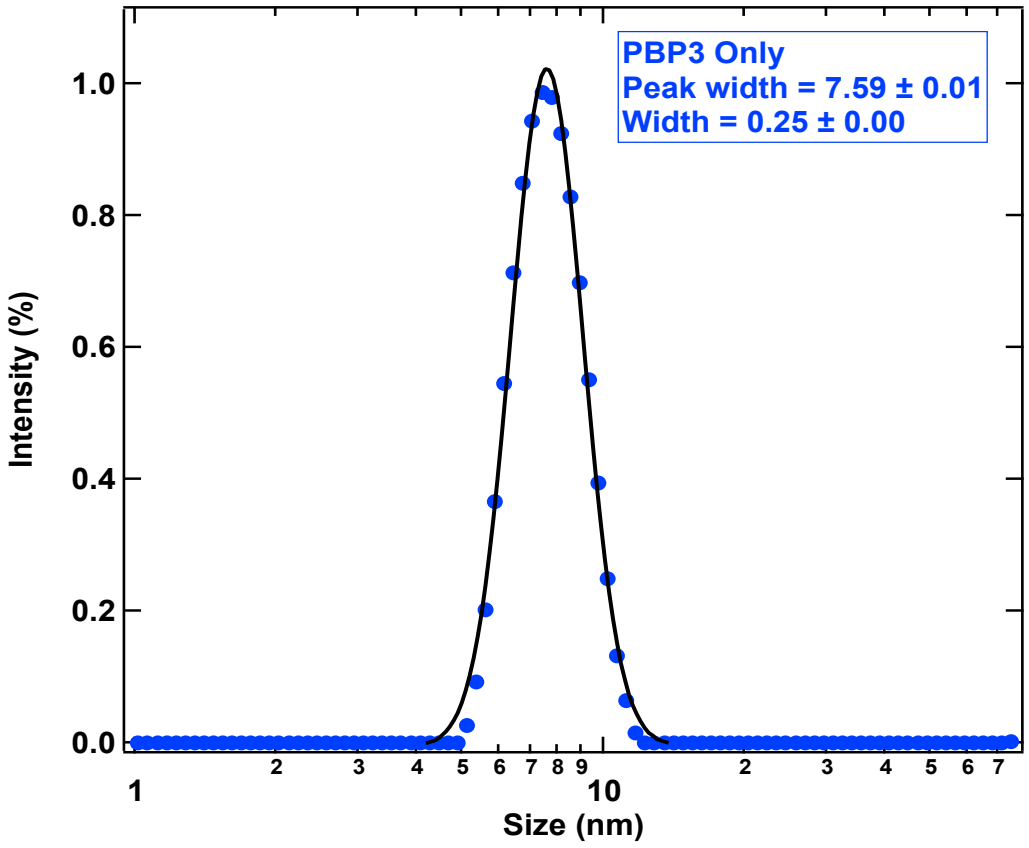

Fig 4.3- DLS results for the hydrodynamic diameter of PBP3 (data shown is an average of 3 repeats).

Upon addition of PBP3 to vesicle solutions containing 1, 5 and 10 mol % DOGS:DOPC the hydrodynamic diameter of the vesicles increased. This is shown in figure 4.4 by a shift in the size (diameter) to the right (greater diameter). The average increase in size is presented in figure 4.5.

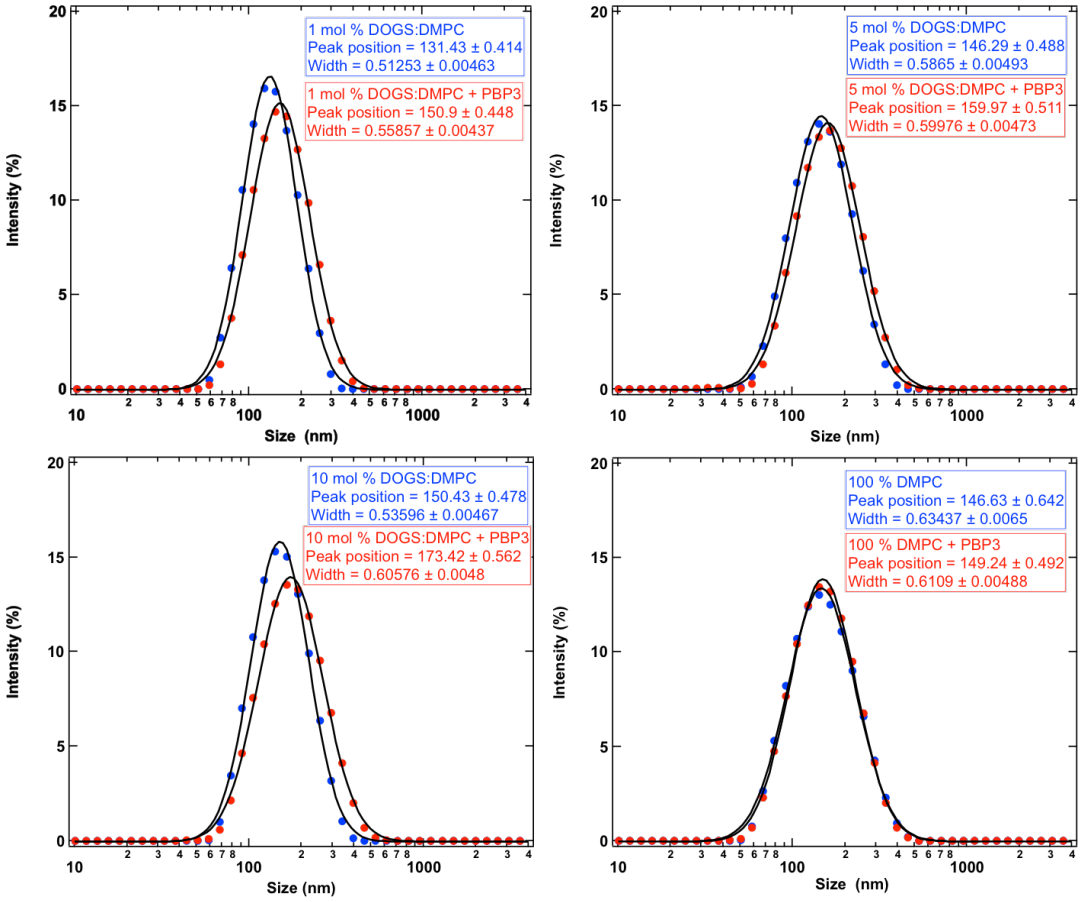

Fig 4.4- Example DLS plots showing the increase in size (diameter) upon addition of PBP3 to vesicle solutions containing 0, 1, 5 and 10 mol % DOGS:DOPC (data shown is an average of three repeats).

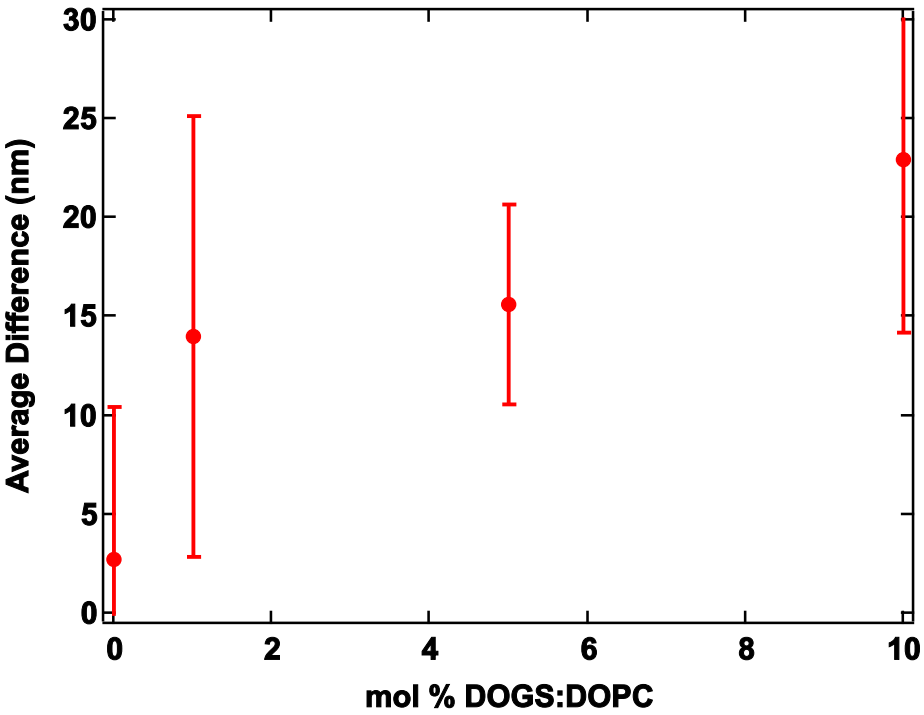

Fig 4.5- Average increase in size upon addition of PBP3 to vesicles containing 0, 1, 5 and 10 mol % DOGS:DOPC (data shown is an average of three repeats).

As the mol % of DOGS within the monolayer is increased it is clear that, upon exposure to protein, the vesicles become larger. The average increase in size (diameter) is largest for 10 mol % DOGS:DOPC and smallest for 0 mol % DOGS:DOPC. The increase in diameter of the 0 mol % DOGS:DOPC vesicle is attributed to small amounts of non-specifically bound protein. This is most likely through electrostatic interactions as the protein has a net positive charge at pH 7.5 (pKa 9.58) and hence electrostatic interactions between the lipid head groups and protein are likely[19]. These results are similar to work demonstrated by Masek *et al* for similar systems using GFP as the model protein[20].

The hydrodynamic diameter of the protein was determined as 7.59 nm. If monolayer coverage of the protein upon the vesicle surface occurred, a theoretical increase in the effective diameter of the vesicle of 15.2 nm would be expected. The average increase in diameter for 1, 5 and 10 mol % DOGS:DOPC vesicles upon protein addition is close to this theoretical

value, being 14, 15.6 and 22.9 nm respectively. One possible explanation for the larger increase in diameter of 22.9 nm for 10 and mol % DOGS:DOPC is due to the formation of a secondary layer of non-specifically bound protein, interacting with an already crowded vesicle surface. These results are consistent with similar systems for protein interactions with vesicles containing DOGS studied by DLS[20 21].

DLS is only able to give information on the increase in size of hydrodynamic diameter. However assuming that the distribution of DOGS-NTA-Ni is even throughout the bilayer leaflet a protein:chelating lipid ratio can be calculated for the protein concentrations used here. These ratios are 1:19, 1:97 and 1:179 for 1, 5 and 10 mol % chelating lipid respectively[19]. This indicates that the protein is unlikely to fill all of the vacant DOGS head groups. The DLS results show a general trend in that as the concentration of chelating lipid increases, so too does the amount of protein at the vesicle interface (increased diameter). The values for 1 and 10 mol % are still within, and extremely close to, the theoretical value for monolayer coverage. Masek *et al* have shown similar results for analogous systems but using GFP[20]. They have shown that the specific binding capacity of vesicles containing protein chelating lipids for GFP is as low as 1:40 protein:chelating lipid. GFP is 2.6 times larger than PBP3 and is therefore expected to saturate the surface at lower protein:chelating ratios[19 20].

4.2 Characterising protein interactions upon functionalized lipid monolayers at the air-water interface

4.2.1 Brewster Angle Microscopy Studies

Having gained an insight into the characteristics of the PBP3-DOGS-NTA-Ni system, it was then appropriate to assess the difference of protein binding at the air-water interface. This study focused on 5, 10 and 20 mol % DOGS:DOPC monolayers formed at the air-water interface.

Higher DOGS concentrations were selected here so that significant binding of protein to the interface could be visualized using BAM.

For two key reasons the bulk-diluting phospholipid was changed from DMPC to DOPC. Firstly DOPC is structurally similar to DOGS-NTA-Ni and hence has a similar phase transition[12]. It was considered desirable to form a monolayer in which both the constituent lipids were in the same phase at room temperature. This was in an attempt to stop the preference of protein interactions with any one specific phase, in a monolayer where lipids may phase separate. Secondly DOPC is unsaturated and therefore allows the monolayer to retain fluidic like properties[22]. Maintaining an overall fluid like nature will ultimately promote the lateral mobility of formed protein-lipid complexes. This in turn will allow for increased protein-protein interaction and may promote the formation of an ordered protein layer[23]. Figure 1.15 of the introduction shows images of proteins aligned in two-dimensions at lipid interfaces. These are important when comparing the images below.

5 mol % DOGS:DOPC

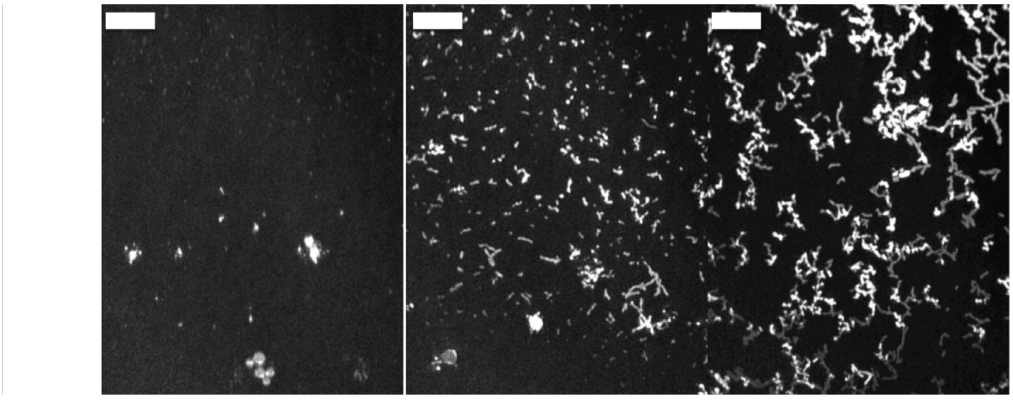

Fig. 4.6- From left to right: BAM pictures for the crystallization of PBP-3 upon a phospholipid monolayer containing 5 mol % DOGS-NTA-Ni at 35, 48 and 74 minutes. The scale bar represents 50 μm.

Figure 4.6 shows protein adsorption monitored by BAM at 35, 48 and 74 minutes. The image at 35 minutes corresponds to the onset of protein adsorption. By 48 minutes the protein layer is beginning to grow which

will be facilitated by the lateral mobility of the protein at the interface and, the subsequent protein-protein interactions that this will induce[24]. At 74 minutes the protein is beginning to form a homogenized layer of protein upon the lipid monolayer. These images are reminiscent of the BAM images by Courty *et al*[25] shown in figure 1.12C of chapter 1. Here it was shown that the protein, HuPr, could form crystalline layers with a high degree of cross-linking upon DOGS-NTA-Ni monolayers. It is likely that initial protein adsorption is in the form of two-dimensional patches. As more protein is attracted to the interface, the protein-protein interactions increase and these patches begin to converge and cross-link[25-27].

10 mol % DOGS:DOPC

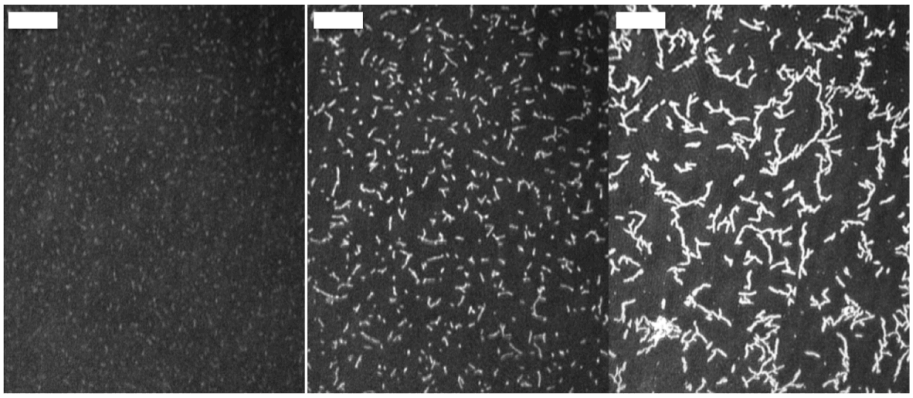

Fig 4.7- From left to right: BAM pictures for the aggregation of PBP-3 upon a phospholipid monolayer containing 10 mol % DOGS-NTA-Ni at 6, 15 and 42 minutes. The scale bar represents 50 μm.

Figure 4.7 represents PBP3 interaction with a 10 mol % DOGS:DOPC monolayer at 6, 15 and 42 minutes. Here it is clear that initial protein adsorption is much faster owing to the larger mol % of DOGS within the monolayer. Protein adsorption occurs within 6 minutes of monolayer exposure to the protein. At 6 and 15 minutes there is a high degree of protein adsorbed to the surface of the lipid monolayer. These initial structures are not dissimilar similar to the kinds of structures obtained by Bischler *et al* using low resolution electron microscopy in which they showed the two-dimensional alignment of yeast polymerase upon

monolayers containing DOGS functionalized lipids[27], again supporting the notion of initial protein adsorption being in the form of small crystalline patches. Whilst after 42 minutes these crystalline patches start to coalesce, again similar to that found by Courty *et al*[25]. However BAM is unable to distinguish between crystalline and aggregate phases.

20 mol % DOGS:DOPC

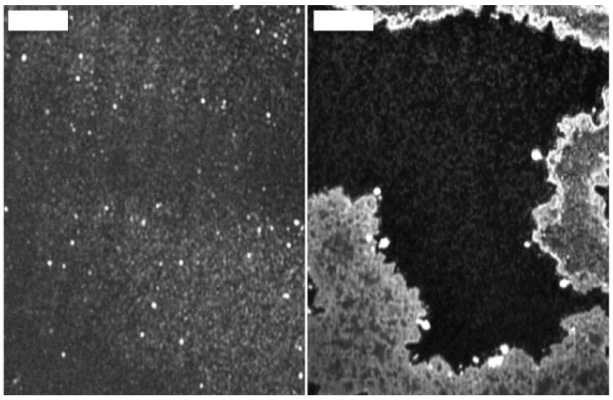

Fig 4.8- From left to right: BAM pictures for the adsorption of PBP-3 upon a phospholipid monolayer containing 20 mol % DOGS-NTA-Ni at 30 and 55 minutes. The scale bar represents 50 μm.

Figure 4.8 shows protein adsorption on a 20 mol % DOGS:DOPC monolayer at 30 and 55 minutes. Initial protein adsorption is on a similar time scale to the 10 mol % DOGS:DOPC monolayer, with the monolayer being heavily saturated by protein after 30 minutes. However there is a clear difference between this monolayer and the 5 and 10 mol % DOGS monolayer. After 55 minutes it is clear that there is a large degree of protein aggregate at the surface. This is due to the fact that there are now large numbers of protein binding sites within the monolayer.

Characterising the interaction of PBP3 with DOGS:DOPC monolayers at the air-water interface suggests that upon increasing the number of protein binding sites within the monolayer, the degree of secondary, non-specific protein adsorption also increases. A large number of protein molecules are initially attracted to the interface through a specific mechanism. The larger the number of initial protein molecules that form complexes with the functionalized head groups of the monolayer, the

more protein there is for subsequent secondary, or non-specific, protein adsorption.

4.3 Protein interactions at the solid-liquid interface

The system described previously was then transferred to the solid-liquid interface in an attempt to investigate whether or not the relationship between ratios of lipids (chelating and bulk) and protein interaction were consistent. Being able to two-dimensionally crystallise proteins, or form ordered arrays of protein, at the solid-liquid interface could provide an additional variable in protein crystallization trials which currently do not consider the influence of the substrate. Seeding of crystallization with micro crystals is now relatively common practice and so the ability to transfer this to the interface may be helpful in nucleating bulk crystal growth. Crystallisation upon solid-supported lipid monolayers may also offer solutions for proteins that have solubility issues (such as membrane proteins) as the lipid environment provides a more “comfortable” interface.

Protein interaction at the solid-liquid interface was measured using QCM and neutron reflectometry. QCM was able to assess nanogram addition of the protein to the surface, whilst also ensure the formation of stable lipid monolayers. Neutron reflectometry was then used to assess the thickness of the formed protein layer and the volume fraction at the interface. These two techniques combined provided a powerful combination for characterization of the formed protein layer.
The chosen lipids were the same as with the air-water interface studies for reasons discussed earlier.

4.3.1 Quartz Crystal Microbalance Studies

Formation of lipid monolayers

Before the characterization of adsorbed protein layers the formation of lipid monolayers was assessed. Monolayer adsorption onto a

hydrophobic supporting layer was measured. For details of this preparation see the materials and methods section of this thesis. This was completed for the control lipid monolayer (100 mol % DOPC) and 5, 10 and 20 mol % DOGS monolayers. Figure 4.9 shows the frequency decrease with respect to time from the point of small unilamellar vesicle injection.

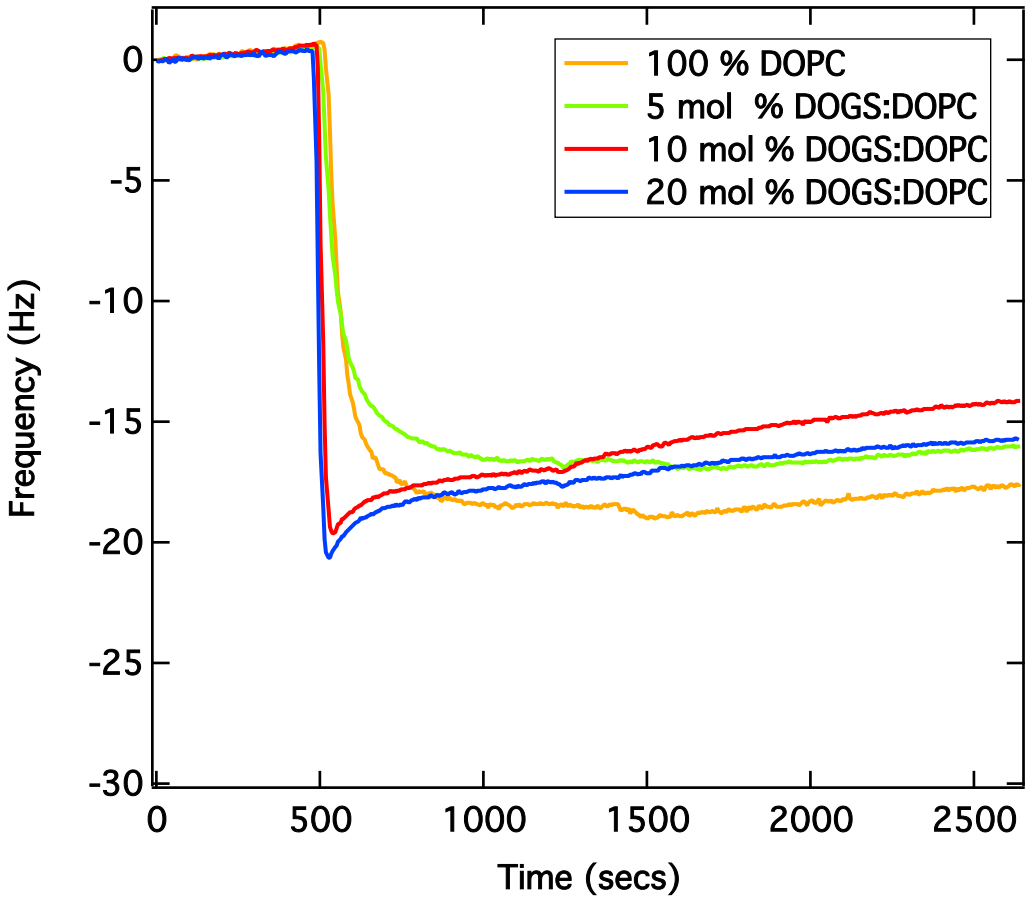

Fig 4.9- Frequency vs time plot for a 100 mol % DOPC monolayer and 5, 10 and 20 mol % DOGS monolayer formation.

The characteristics of monolayer formation assessed with QCM are well established. It is generally agreed that the formation of a monolayer can be observed with a frequency decrease that lies in between -15 to -20 Hz[28] [29] [30]. Figure 4.8 shows a decrease in frequency for all of the monolayers here of -18 to -14 Hz and lies within the frequency reduction regime for a lipid monolayer.

Another way to ensure lipid monolayer formation is to track the change in dissipation after the injection of the lipid vesicle solution. Figure 4.10 shows the change in dissipation with time post vesicle injection for the four monolayers formed in this study.

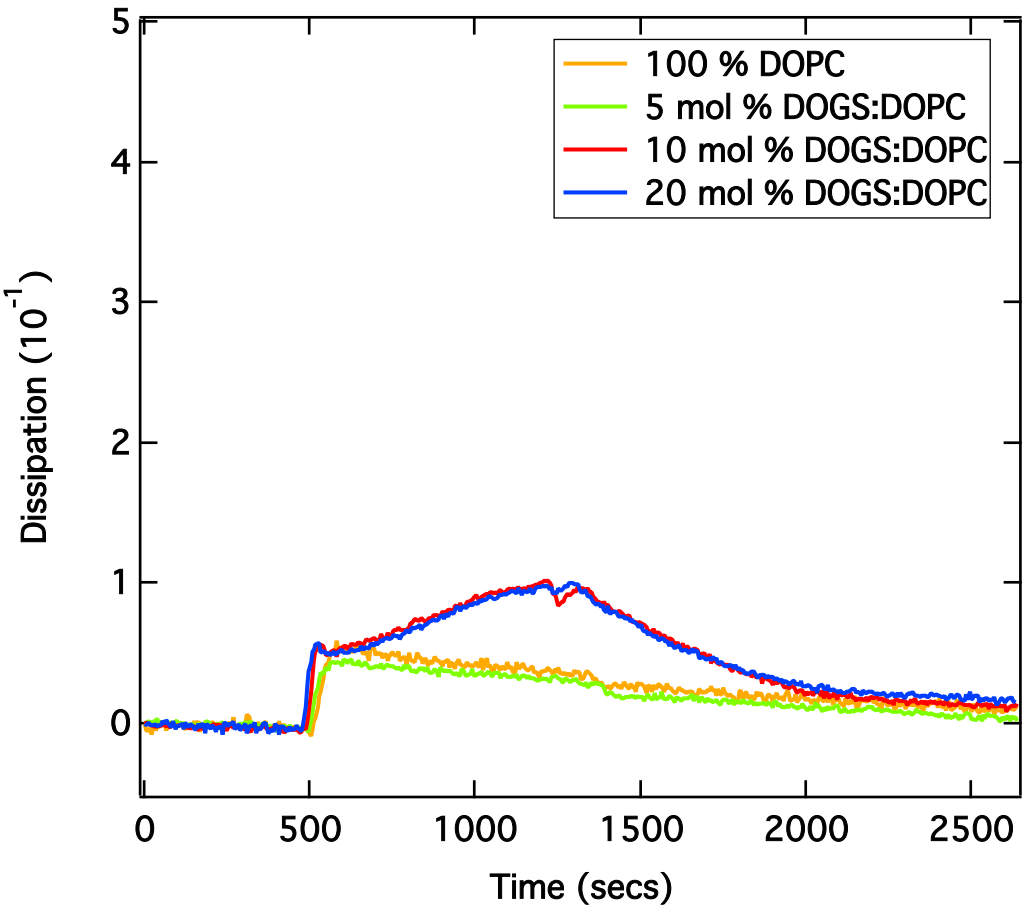

Fig 4.10- Dissipation-time plots after vesicle injection for 100 mol % DOPC and 5, 10 and 20 mol % DOGS monolayers.

Figure 4.9 and figure 4.10 suggest that the adsorption of the vesicles follows simple first order kinetics. This is rationalized by frequency decreases within the monolayer regime. It is also known that vesicle adsorption is driven by the hydrophobic effect and/or Van der Waals interaction between lipid tails and the hydrophobic interface. The dissipation-time plot (D-f plot) in figure 4.10 supports this notion[30]. The initial sharp rise in dissipation upon vesicle injection is due to the

adsorption of intact vesicles on the surface. The intact vesicles will contain a relatively large quantity of water and not form a rigid film. As these vesicles start to rupture water will be expelled from the system, causing the formation of a rigid monolayer. This is shown by a decrease in dissipation with time[31].

Characterisation of protein adsorption

Once lipid monolayers had been formed and characterised the protein, penicillin binding protein 3, was injected and the concentration within the QCM cell increased from 5-25 μg ml^{-1} in increments of 5 μg ml^{-1}. The raw data in the from of a frequency-time plot can be seen in figure 4.11.

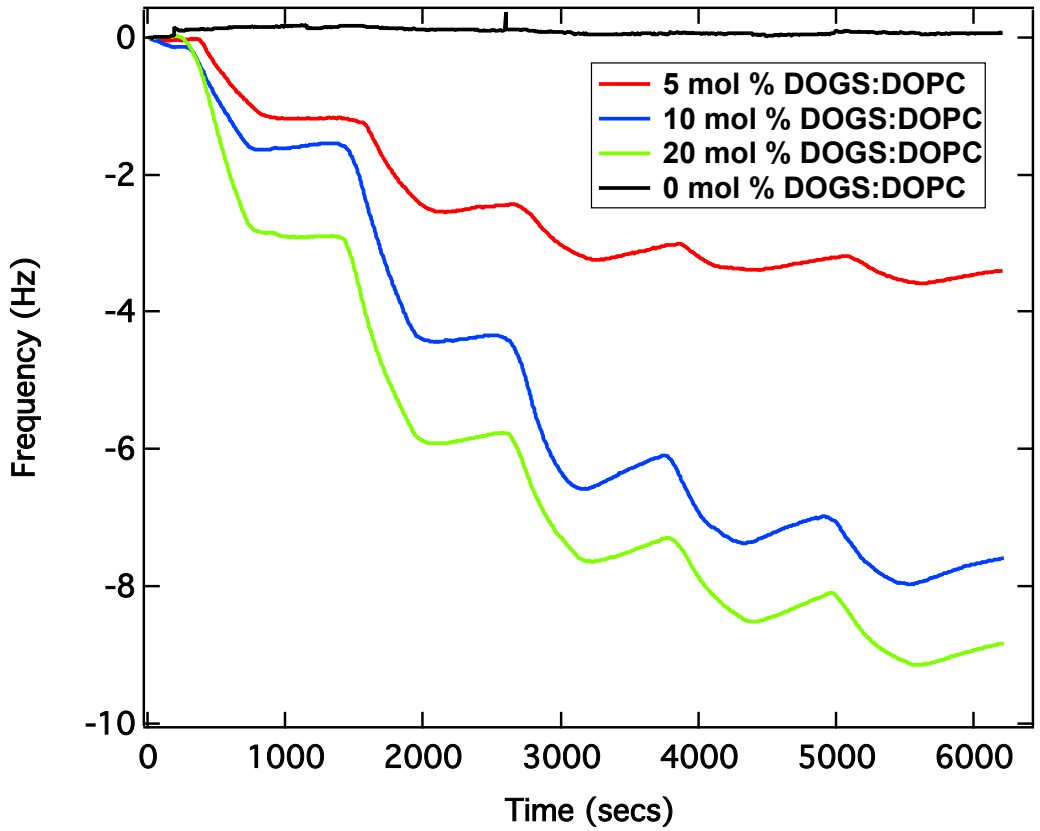

Fig 4.11- Frequency-time plot for the addition of 5-25 μg ml^{-1} (in increments of 5 μg ml^{-1}) of penicillin binding protein 3 to 0, 5, 10 and 20 mol % DOGS:DOPC lipid monolayers.

There is limited adsorption of protein onto the control lipid monolayer containing no DOGS. More generally it is evident that as the concentration of protein within the system is increased, so too does the adsorption of protein to the monolayer surface. This is also true for the concentration of DOGS within the monolayer, which also shows a positive correlation between the mole percent of DOGS and the subsequent mass of adsorbed protein.

As with the adsorption of lipid vesicles it is also important to note the change in dissipation with protein adsorption. A dissipation-time plot for the above data is shown in figure 4.12.

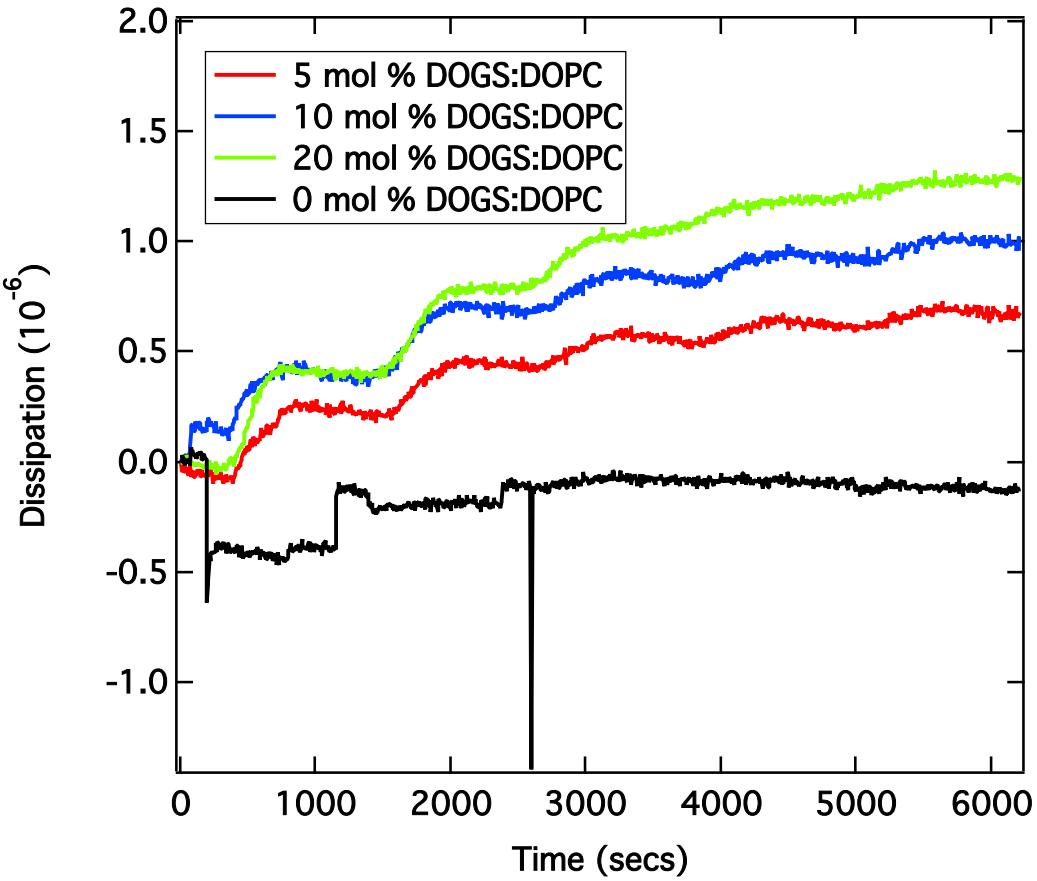

Fig 4.12- Dissipation-time plot for the addition of 5-25 μg ml^{-1} (in increments of 5 μg ml^{-1}) of penicillin binding protein 3 to 0, 5, 10 and 20 mol % DOGS:DOPC lipid monolayers.

The change in dissipation upon protein adsorption to the monolayer headgroups is minimal at all protein concentrations assessed in this study. Even at the highest protein concentration of 25 μg ml^{-1} the change in dissipation does not exceed 1.5 x 10^{-6}. This is indicative of a relatively tightly bound protein layer in which the protein molecules themselves are oscillating in a similar manner to the lipid monolayer. It is noticeable however that as in the concentration of protein at the interface is increased (either through increasing DOGS concentration or protein concentration) the dissipation rises by small amounts. This shows that although the protein is still a relatively rigid layer, and well coupled to the monolayer, it is increasing in visco-elasticity[32]. It is generally agreed that in such circumstances, and when the dissipation for a given layer does not exceed 2 x 10^{-6}, that the Saurbrey model is valid[32-35]. This model can be used to estimate the mass of adsorbed protein on the surface of the lipid monolayer. The Saurbrey model correlates the change in frequency (Hz) to the adsorbed mass of a given layer (g)[36 37]. The Saurbrey model has been described in the principles of analysis section of this thesis (section 2.9). For reference the equation is shown in equation 2.1,

$$\Delta m = -C\frac{1}{n}\Delta f \qquad \text{(Equation 4.1)}$$

where Δm is the change in mass, Δf the change in frequency, C is a constant of 17.7 ng cm^{-2} s^{-1} and n is the overtone used.

An adsorption isotherm based on the frequency-time plot shown in figure 4.11 is presented in figure 4.13.

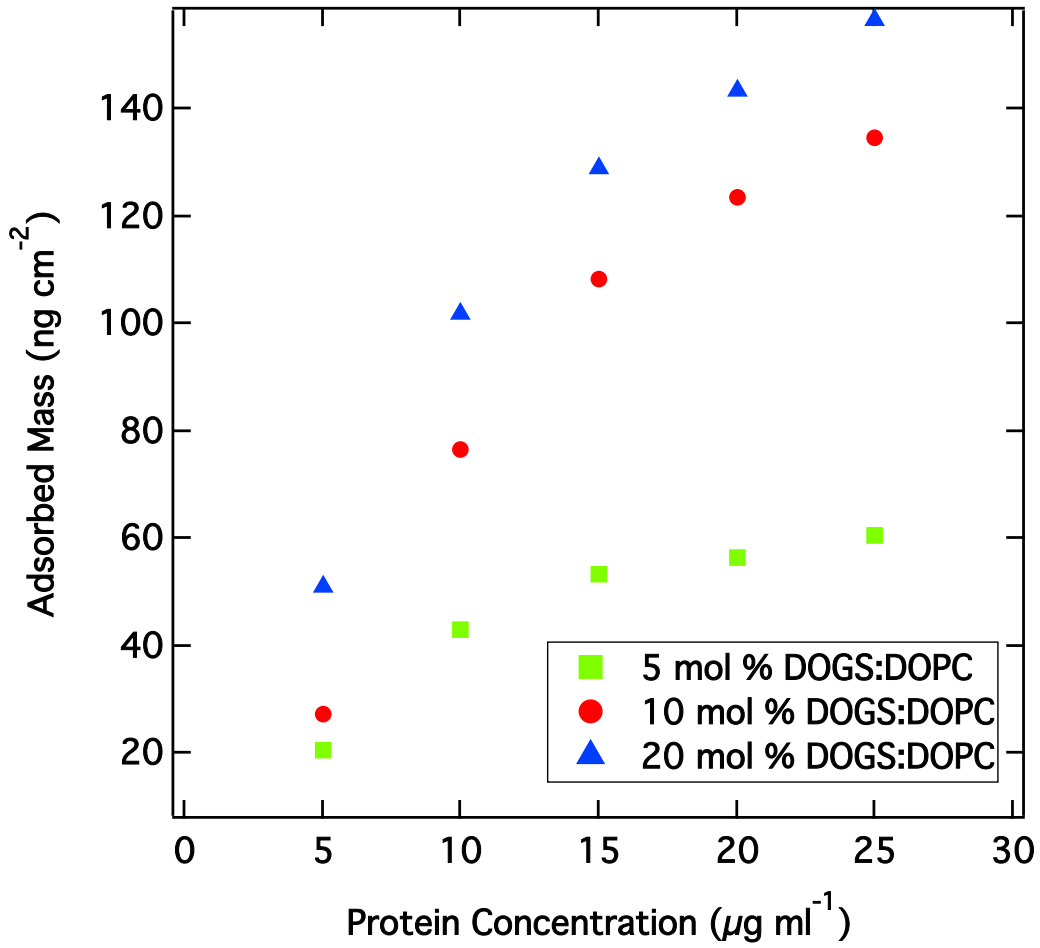

Fig 4.13- Adsorption isotherm based on the Saurbrey model for the addition of 5-25 μg ml^{-1} (in increments of 5 μg ml^{-1}) of penicillin binding protein 3 to 0, 5, 10 and 20 mol % DOGS:DOPC lipid monolayers.

The adsorption isotherm in figure 4.13 shows that as the concentration and mol % of DOGS within the monolayer increases so too does the mass, or concentration of protein, at the interface. It appears that for the 5 mol % DOGS:DOPC monolayer the system is beginning to reach maximum surface coverage of protein at around 50 ng cm^{-2} and a protein concentration of 25 μg ml^{-1}. This is seen by the onset of a plateau in adsorbed mass at higher protein concentrations. From analysis of the QCM data it is evident that there will be around 1.2 x 10^{12} DOGS headgroups in 1 cm^2 of the lipid monolayer. This is compared to 5.9 x 10^{11} protein molecules. Although it is clear that there are less protein molecules on the surface compared with the number of available binding

sites, the protein concentration of protein at the interface is beginning to plateau at 25 μg ml^{-1} of protein and 5 mol % DOGS.

The monolayers containing 10 and 20 mol % DOGS do not show any plateau feature, giving maximum adsorbed mass values at around 130 and 150 ng cm^{-2} respectively. At 10 mol % DOGS there will be approximately 2 x 10^{12} DOGS head groups present in 1 cm^2 at the interface. From the isotherm data in figure 2.13 the number of protein molecules at the interface is 1.33 x 10^{12} cm^{-2}, again a value less than the number of available DOGS head groups. The situation is the same for 20 mol %, where 4.5 x 10^{12} cm^{-2} head groups are available for protein binding but only 1.54 x 10^{12} cm^{-2} protein molecules are found at the interface. It is clear that the higher the concentration of DOGS within the monolayer the more protein there is present at the interface. It is interesting that the 5 mol % DOGS monolayer begins to plateau at 25μgml^{-1} of protein yet there is no plateau for 10 and 20 mol % DOGS at the equivalent protein concentration. A steric argument cannot be made here as if there was some maximum surface concentration of protein that inhibited the subsequent adsorption of protein to the interface, it should be insensitive to the mol % of DOGS within the monolayer. Therefore to gain insight into the kinetics of protein adsorption it is possible to analyze D-f plots.

As discussed previously analysis of the dissipation throughout protein adsorption can give information on the process of adsorption at an interface. It has been shown that changes in dissipation can be linked to the variation in structure[38 39] and/or kinetics[40] of protein adsorption at an interface. Of particular interest are so called D-f plots. These are plots which track the change in dissipation per unit of frequency and are useful in highlighting changes in dissipation as the mass load of the crystal is increased[34 41].
Figure 4.14 shows D-f plots at a fixed protein concentration of 15 μg ml^{-1} for 5, 10 and 20 mol % DOGS:DOPC monolayers.

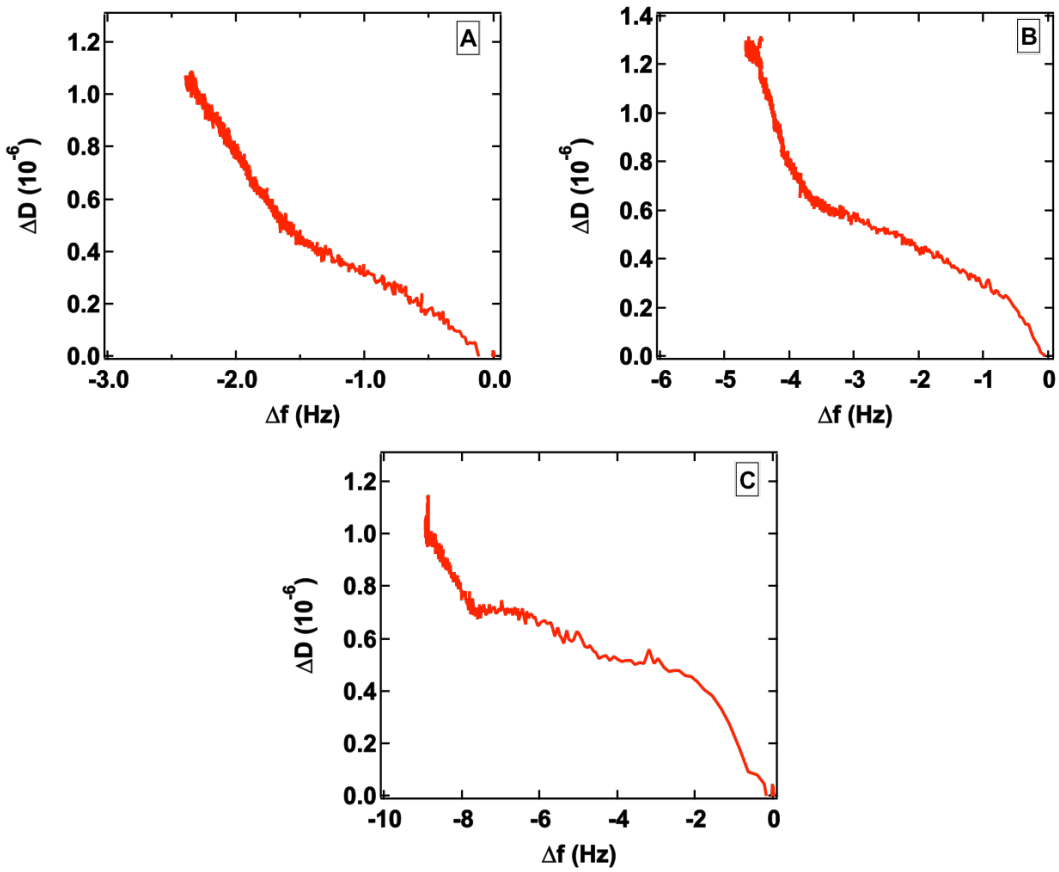

Fig 4.14- D-f plots for a fixed protein concentration of 15 μg ml^{-1} on A) 5 mol % DOGS:DOPC, B) 10 mol % DOGS:DOPC and C) 20 mol % DOGS:DOPC

For all three DOGS concentrations there is an initial sharp rise in dissipation with respect to frequency as f decreases from 0. This corresponds to protein injection and the rapid adsorption of specifically bound protein to the monolayer. This then begins to level off. There is then a second sharp rise in dissipation in which the visco-elastic properties of the layer change substantially and at a more rapid rate. The possibility of a structural change within the monolayer is unlikely, given that the protein cannot cross-link with itself or cannot rearrange on the surface as it is specifically oriented via the histidine chelating DOGS head group. Although the possibility of some forms of two-dimensional crystalline phase formation cannot be ruled out. However it is more likely that this sharp rise in dissipation corresponds to a second adsorption event in which non-specifically bound protein begins to adsorb to the pre-

formed protein layer. It would be expected that this secondary, non-specifically bound protein layer would lead to a rise in dissipation as the interaction is non-specific and is essentially a protein aggregate layer. It is therefore likely to contain more water than the first protein layer and have a higher visco-elasticity, leading to the sharp rise in dissipation. This has been observed previously for the adsorption of HSA at the interface where an initial rigid protein layer was observed followed by a sharp rise in dissipation due to a secondary less rigid protein layer[42]. This phenomenon has also been observed for a pre-oriented peptide layer where anti-body binding (a large immunoglobulin protein) was assessed through use of the QCM-D technique. D-f plots showed that smaller rises in dissipation corresponded to specific peptide-antibody interactions, whilst non-specific protein interactions gave rise to sharper rises (larger gradients) in dissipation per unit of frequency[43]. This phenomenon is clearly observed here over the "two-gradient regime" of protein adsorption, in which an initial small rise in dissipation is observed, followed by a steeper gradient increase in dissipation, as more visco-elastic-non specifically bound protein adsorbs to the interface.

There is practically no interaction between the protein and the monolayer containing no chelating lipid. Therefore any protein bound to the DOGS containing monolayer must be either at the DOGS head group or subsequent non-specifically bound protein. QCM is able to give insight into the mass and kinetics of protein adsorption. However this technique is unable to provide any real insight into the structure of the formed protein layer(s). Neutron reflectometry was therefore conducted to make attempts to couple observations from the QCM with structural information.

4.3.2 Neutron Reflectometry

Neutron reflectometry was performed under similar conditions to the QCM study. Due to time constraints associated with beam time, protein concentrations of 5, 10 and 25 μg ml^{-1} were investigated on monolayers containing 10 and 20 mol % DOGS. The experimental set-up can be seen in the materials and methods section of this thesis.

The experiment proceeded through the use of 4 neutron reflectometry cells. This corresponded to 4 lipid monolayers in total (and thus 4 hydrophobic OTS layers). Two of these contained 10 mol % DOGS leaving two containing 20 mol % DOGS. This was to enable the characterization of the adsorbed protein layer in two differing contrasting solvents, H_2O and D_2O. Three of the hydrophobic OTS layers and the 4 lipid monolayers were characterized in 3 contrasting solvents, H_2O, 4MW and D_2O. The one remaining OTS layer was characterized only in D_2O to check for consistency. This was due to a lack of experimental time at the neutron source. The OTS monolayers and lipid monolayers were analysed in three contrasting solvents to enable a rigorous model to be obtained for the supporting layers before protein injection.

Pre-characterisation of OTS layer and lipid moonolayers

Figure 4.15 shows neutron reflectometry data for the four hydrophobic OTS layers along with the four lipid monolayers used for this experiment. The figure also includes examples of scattering length density profiles shown in one contrast for the OTS layer and the subsequent profile after lipid vesicle injection. D_2O was chosen here as it provides the best contrast between the hydrogenated layers and the deuterated solvent.

Table 4.1a shows the parameters used to model the data and table 4.1b shows the scattering length density values used for each layer in the model. Scattering length densities were calculated as follows. SiO_2 was calculated assuming a volume of 47 Å^3 [44], OTS calculated for an assumed volume of 542 Å^3 [45], the lipid tails with an assumed volume of 985 Å^3 [46] and the phosphocholine head group SLD calculated with an assumed volume of 268 Å^3 [44]. The scattering length density of the DOGS-NTA-Ni head group was calculated with an assumed volume of 225 Å^3 [47]. The SLD of the DOGS-NTA-Ni:DOPC monolayer head groups was calculated by the ratio of volume fraction of DOGS:DOPC within the head group region. Although in practice, given the small amounts of DOGS within the monolayer, this represents tiny changes in SLD. For values of the scattering lengths used to calculate these parameters see table 2.1 in the principles of analysis section. All neutron reflectomerty data was co-refined together to constrain the model as much as possible.

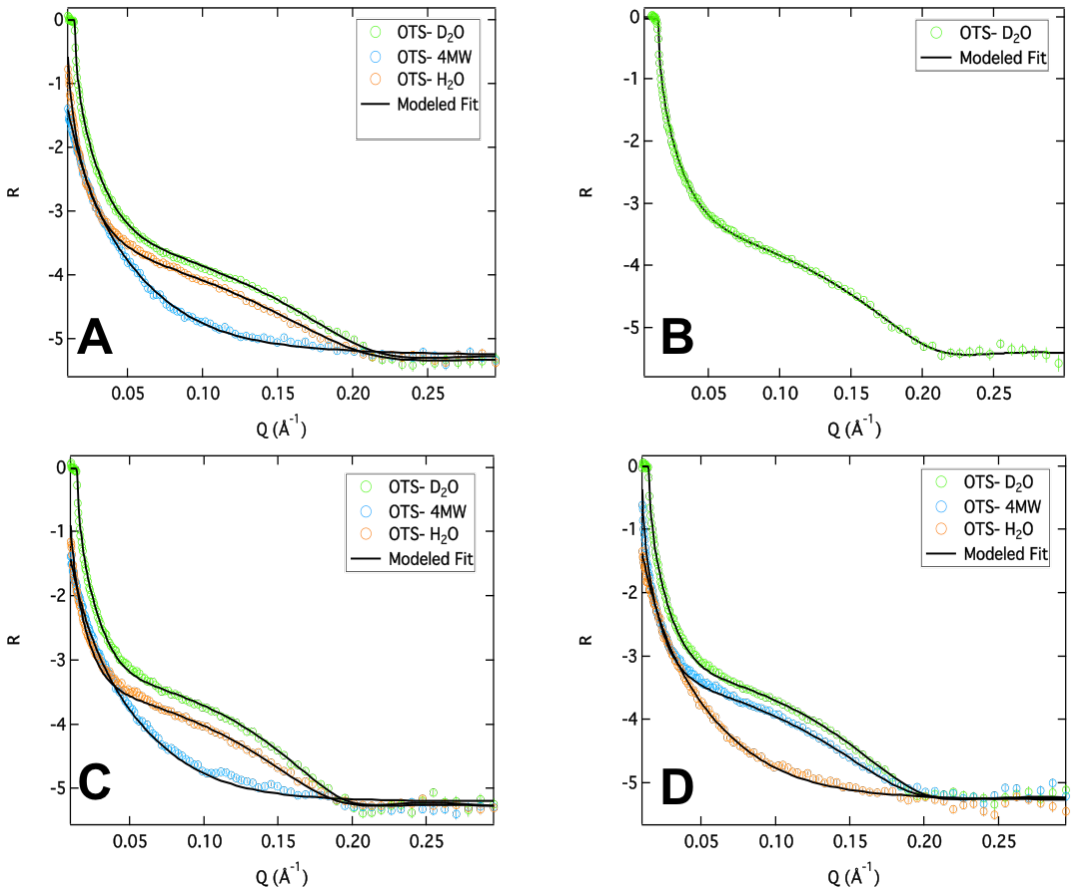

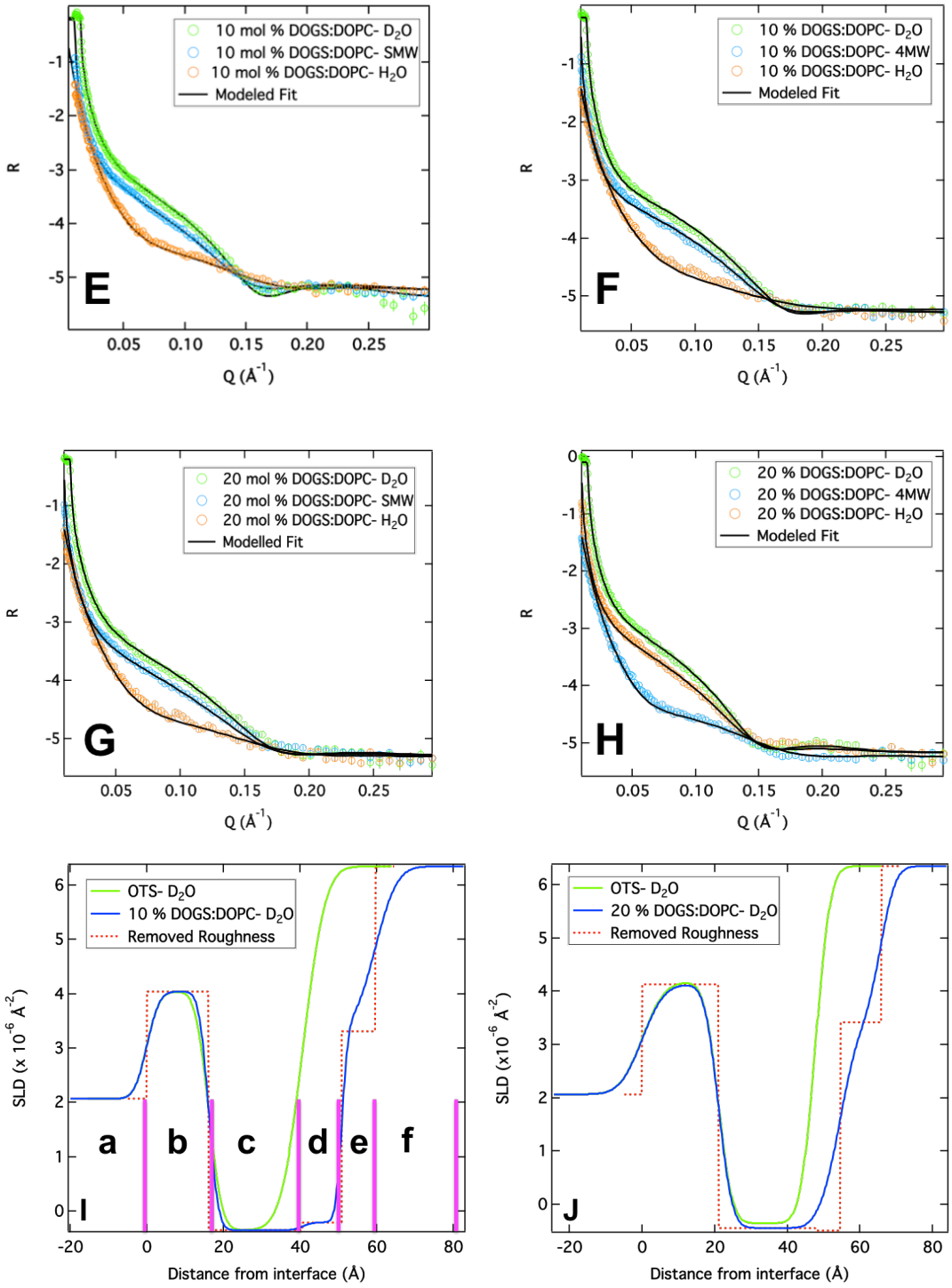

Fig 4.15- A-D: Neutron reflectometry profiles in D_2O, 4MW (water contrast matched to and SLD of 4 x 10^{-6} $Å^{-2}$) and H_2O for the four hydrophobic OTS layers measured. E and F: Neutron reflectometry profiles for 10 mol % DOGS:DOPC monolayers in D_2O, 4MW and H_2O. G and H: Neutron reflectometry profiles for 20 mol % DOGS:DOPC monolayers in D_2O, 4MW and H_2O. I and J: Example scattering length

density profiles for OTS, 10 and 20 mol % DOGS in D_2O; the dashed red line corresponds to the theoretical SLD profile where the roughness parameter has been removed. Pink lines correspond to layers of the model. a= Si, b= SiO_2, c= OTS, d= lipid tails, e= lipid heads, f= solvent.

Layer	Thickness (Å)	% Hydration	Roughness (Å)
Si (a)	INF	-	4.6 ± 1.0
SiO_2 (b)	19.2 ± 3	22 ± 2	3.6 ± 1
OTS (c)	26 ± 1	0	3.3 ± 0.7
Lipid Tails (d)	6.5 ± 2.7	12.5 ± 3	2 ± 0.4
Lipid Heads (e)	9.4 ± 1.6	52.1 ± 12.1	3.1 ± 1.2
Solvent (f)	-	-	4.6 ± 0.8

Table 4.1a- Table to show structural parameters used to model the neutron reflectometry data presented in figure 4.15. The letters in parenthesis correspond to labels in this figure.

Layer	SLD (x 10^{-6} $Å^{-2}$)
Si	2.07
SiO_2	3.47
OTS	-0.35
DOPC Tails	-0.21
DOPC Head group	1.8
DOGS Head group	1.43
H_2O	-0.56
D_2O	6.35
4MW	4

Table 4.1b- Table to show summary of scattering length densities used to model the neutron reflectometry data in figure 4.15.

The modeled SiO_2 layers are found to be 19.2 (± 3) Å in thickness with a hydration (by volume) of 22 (± 2) %. This is in good agreement with values found in the literature where values range from 14-22 Å in thickness and 10 -30 % hydration[48 49]. Although the model proposed here implies that the water is uniformly distributed throughout this layer, it is most likely distributed toward the bulk solvent side of the layer, thus contributing to the modeled roughness of the layer[45 50]. The hydrophobic OTS layer was found to have a thickness of 26 ± 1 Å. This value is in good agreement with the literature where typical OTS layers range from 24 Å to 28 Å in thickness[44 45 48 51]. Thickness values on this scale correspond to an OTS layer with a fully extended chain that forms perpendicular to the interface[45]. An OTS layer of this thickness has been shown to comprise of two distinct interfacial regions. One in which the OTS tails form a crystalline-like phase, where the tails are all aligned perpendicular to the interface and, another in which they are much more liquid like with a high degree of disorder[44]. This is likely to be the case for the OTS layers observed here however there is insufficient contrast between the SLD values of the crystalline and liquid phases to structurally determine their scattering contributions (crystalline= -0.44 and liquid= -0.31 x $^{-6}$ Å^{-2})[50]. It is possible to calculate the area per molecule of OTS (assuming a uniform layer) at the interface by taking the scattering length of the molecule and dividing it by the product of the layer thickness and the modeled SLD. For the layers investigated here this yields a value of 21 Å^2 molecule^{-1} ± 1. Scattering studies have revealed that the cross-sectional area of hydrocarbon chains with a similar chain length are 19-21 Å^2 [52 53]. This along with the lack of hydration found within the layer is indicative of a densely packed OTS layer[50 54-56].

The values for the thickness of the DOPC:DOGS monolayers were found to be 15.9 ± 3 Å. These values are in broad agreement with those found in the literature for other similarly studied systems[46 57 58]. It has been reported that a DOPC bilayer measured by neutron reflectivity is 39 Å in thickness. Taking half of this to be the contribution of a monolayer leaflet, this would yield a value of 18 Å for a DOPC monolayer. The values obtained here are slightly smaller than those found in a bilayer as there is

less water in the system and the interaction between phospholipid tails and hydrophobic layer is driven by Van der Waals interactions, whilst the formation of the layer is driven by hydrophobic effect. Vesicle adsorption has been demonstrated to yield surface coverages for phospholipid bilayers in excess of 80 %[59-61]. The surface coverage for the lipids in this study was found to be 0.875 ± 0.03 (> 80 % coverage), values which agree with the reported literature coverage. Assuming a uniform layer this corresponds to an APM value of 92.9 ± 18.2 $Å^2$ $molecule^{-1}$. The value obtained here is in good agreement with neutron reflectometry performed on solid supported DOPC bilayers, which reported an APM of 90 $Å^2$ $molecule^{-1}$ [46]. Corresponding literature values for similar phosphatidylcholine based phospholids show typical APM values at 60.5 $Å^2$ $molecule^{-1}$ for DMPC[44] and 65 $Å^2$ $molecule^{-1}$ for DPPC[59]. These values are much lower than the values reported here as the monolayers used in this study are composed largely of the fluidic DOPC lipid. DOPC has a phase transition temperature of -16.5 °C[12] compared with that of DPPC in which the phase transition occurs at 41.3 °C[62]. The APM of DOPC is therefore expected to be far higher at room temperature than other such phospholipids.

Characterisation of protein adsorption using neutron reflectometry

Protein adsorption was characterized in two contrasting solvents, D_2O and H_2O. Due to time constraints associated with beam time the SMW or 4MW contrast was not achievable.

Figure 4.16 shows the neutron reflectometry results obtained for a 10 and 20 mol % DOGS monolayer at three concentrations of protein (5, 10 and 25 μg ml^{-1}) in D_2O and H_2O. Also shown are example scattering length density profiles for a constant protein concentration of 10 μg ml^{-1} on 10 and 20 mol % DOGS:DOPC monolayers in H_2O and D_2O. Table 4.2 shows the fitting parameters used to model the neutron reflectometry data. The table does not show the results for the underlying lipid and OTS

layers as exactly the same parameters were used as shown in table 4.1a. The only modification was for the addition of the protein layer. A scattering length density of 1.85 x 10^{-6} $Å^{-2}$ was used for the protein layer and was calculated using the primary amino acid sequence of the protein[18] and the biomolecular scattering length density calculator[63].

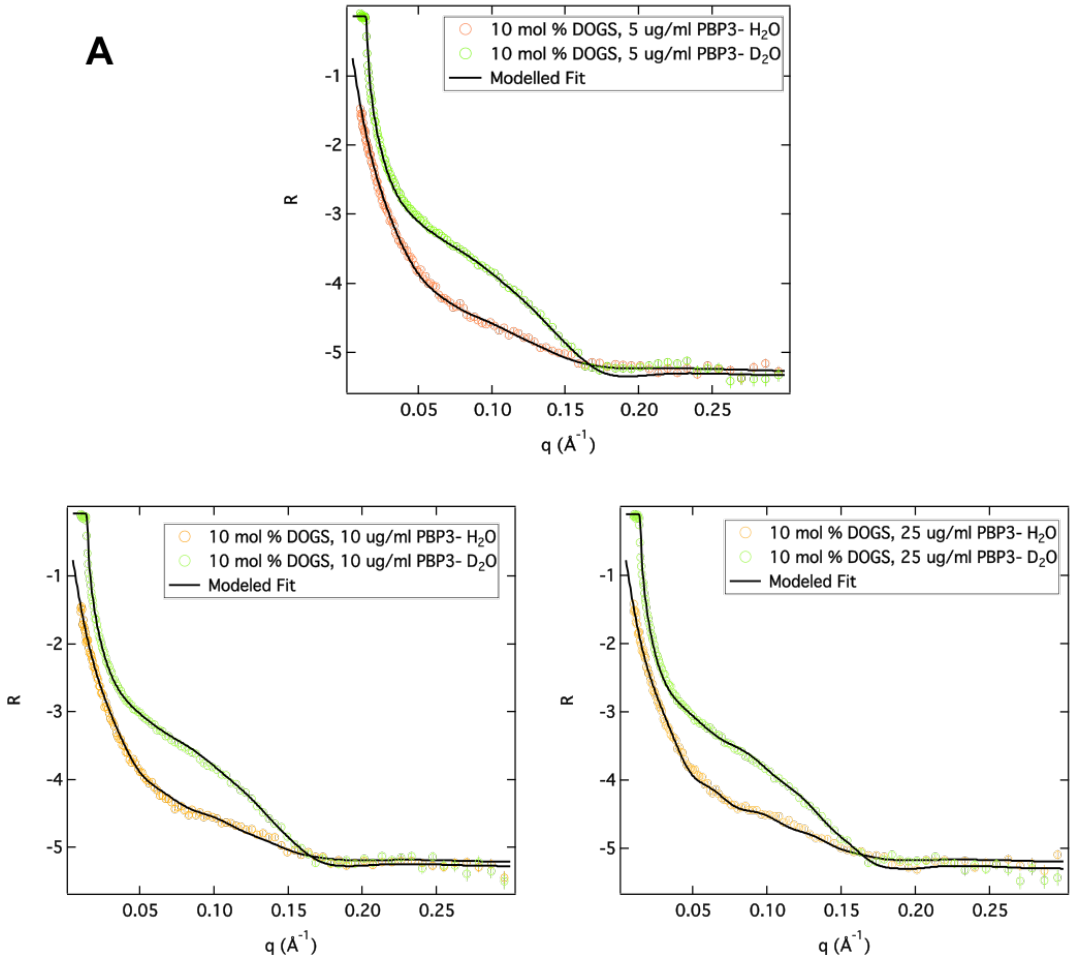

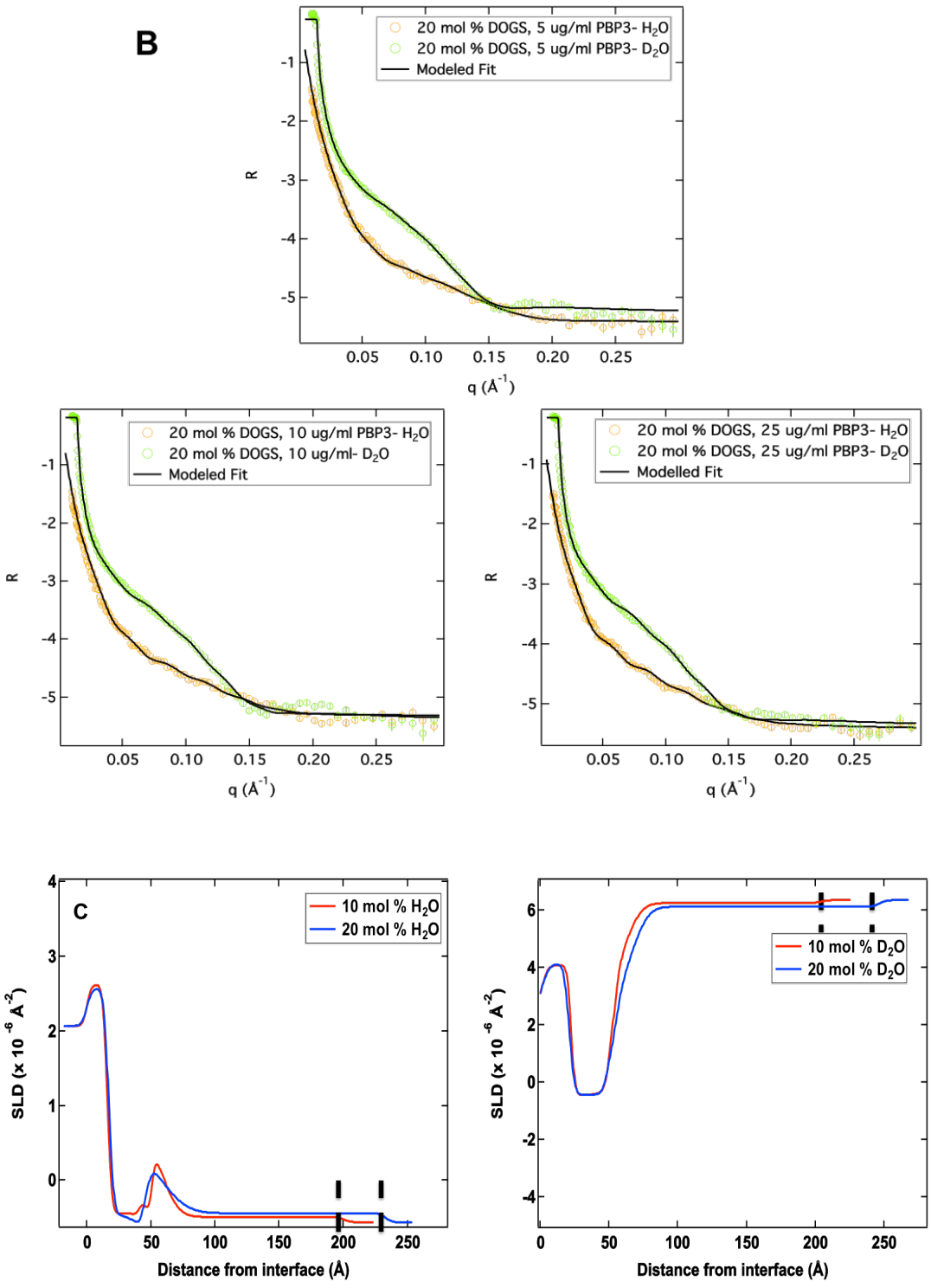
B
20 mol % DOGS, 5 ug/ml PBP3- H2O
20 mol % DOGS, 5 ug/ml PBP3- D2O
Modeled Fit
R
q (Å-1)
20 mol % DOGS, 10 ug/ml PBP3- H2O
20 mol % DOGS, 10 ug/ml- D2O
Modeled Fit
20 mol % DOGS, 25 ug/ml PBP3- H2O
20 mol % DOGS, 25 ug/ml PBP3- D2O
Modelled Fit
C
10 mol % H2O
20 mol % H2O
SLD (x 10-6 Å-2)
Distance from interface (Å)
10 mol % D2O
20 mol % D2O

Fig 4.16- Neutron reflectometry profiles for 5, 10 and 25 μg ml^{-1} PBP3 solutions on A) 10 and B) 20 mol % DOGS:DOPC lipid monolayers. C shows example scattering length density profiles for a constant protein concentration of 10 μg ml^{-1} on these lipid monolayers.

10 mol % DOGS:DOPC				
Protein Concentration (μg ml^{-1})	Thickness (Å)	Roughness (Å)	Volume fraction of protein at interface	Concentration of protein at interface (ng cm^{-2})
5	142.3 ± 1	11 ± 3	0.01	19.3 ± 4.5
10	142 ± 1	9.8 ± 0.4	0.026	49.8 ± 10.3
25	143.2 ± 2.1	8.5 ± 3.5	0.06	109.2 ± 9.8
20 mol % DOGS:DOPC				
5	173 ± 4	9.8 ± 3.3	0.02	46.7 ± 1
10	178.5 ± 3.5	13.2 ± 4.7	0.051	121.6 ± 1
25	173 ± 2	17.6 ± 10.5	0.063	146 ± 10.6

Table 4.2- Summary of fitting parameters used to model protein adsorption at the interface on 10 and 20 mol % DOGS:DOPC monolayers at 5, 10 and 25 μg ml^{-1} of PBP3.

From the information presented in table 4.2 it is possible to calculate the area per molecule of the protein within the protein layer (A) at the interface by,

$$A = \frac{V_p}{\phi_p \tau} \qquad \text{(equation 2.2),}$$

where V_p is the volume of the protein of interest, Φ_p is the volume fraction of protein at the interface and τ is the thickness of the protein layer[64]. The number of moles per unit area can then be calculated and hence the concentration of protein at the interface in ng cm^{-2}. The volume of the protein from the literature is 75058 Å^3 [18 63].

Using this volume, the neutron reflectometry data can therefore be used to determine an adsorption isotherm, which is presented in figure 4.17.

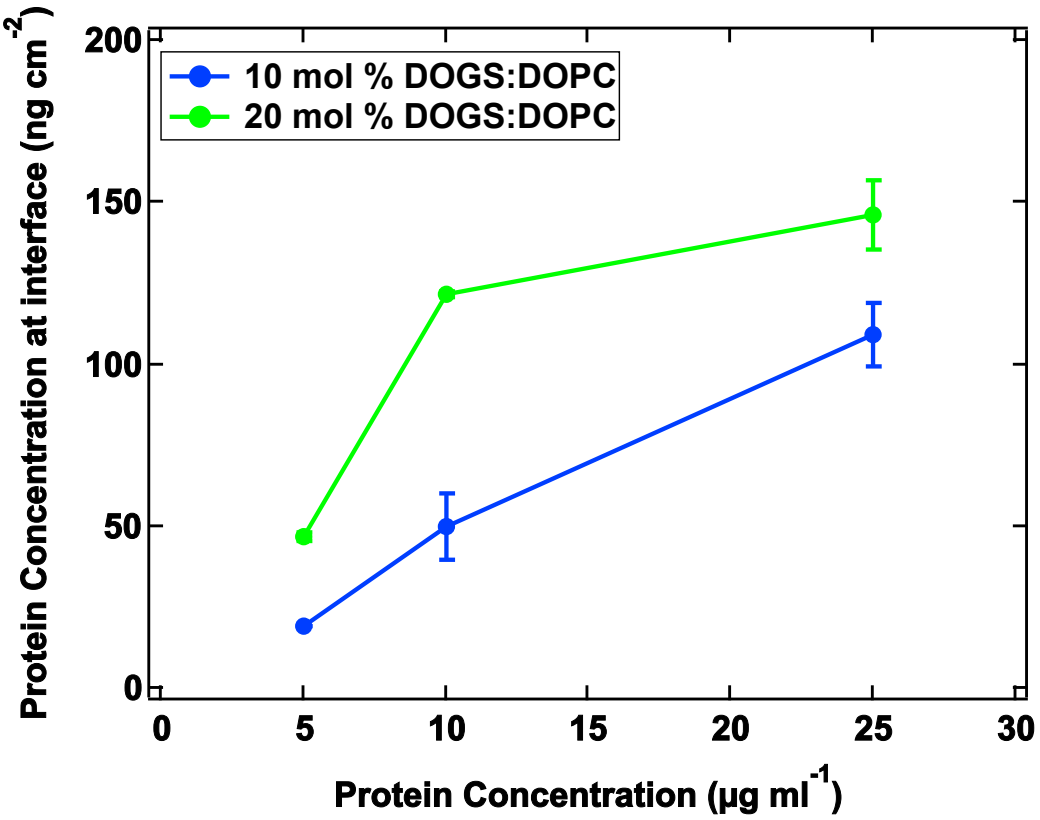

Fig 4.17- Adsorption isotherm for 5, 10 and 25 µg ml^{-1} on 10 and 20 mol % DOGS:DOPC monolayers derived from neutron reflectometry data.

The trend in protein adsorption with increasing DOGS concentration and protein concentration supports the QCM adsorption isotherm presented in figure 4.13. The discrepancy between these data sets is plotted in figure 4.18.

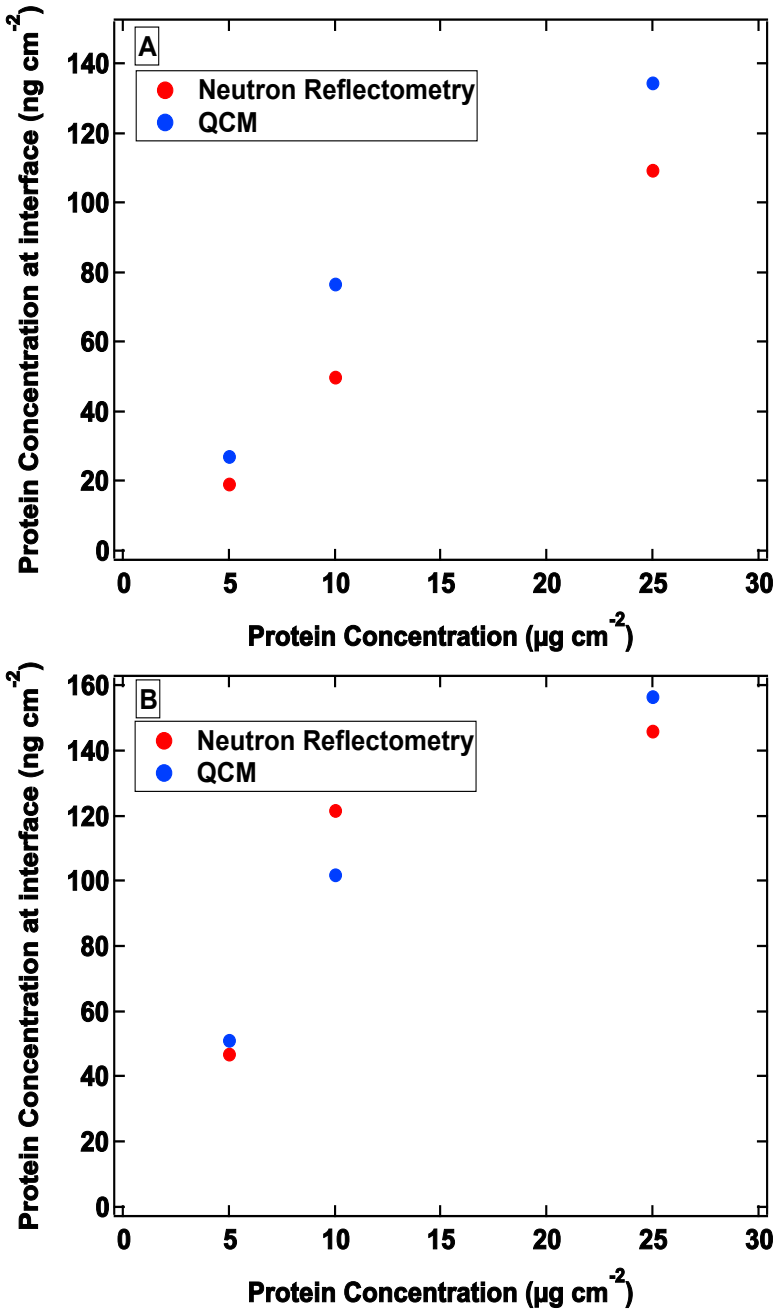

Fig 4.18- Adsorption isotherms derived from neutron reflectometry and QCM measurements at 5, 10 and 25 µg ml^{-1} protein solutions for A) 10 mol % DOGS:DOPC and B) 20 mol % DOGS:DOPC monolayers.

The QCM and neutron data are broadly consistent with each other and agree to within 15.8 ± 9.5 ng cm^{-2}. This is an appropriate agreement given the relatively large surface concentration of protein and the inherent differences between the two techniques. Others have attributed

discrepancies in results between the two techniques to large differences between the geometry of the sample cells[65].

The thickness of the protein layer is presented in table 4.2. Figure 4.20 shows example scattering length density profiles for a constant protein concentration of 10 μg ml^{-1} on 10 and 20 mol % DOGS:DOPC monolayers in H_2O and D_2O. These have been shown to highlight the apparent increase in protein layer thickness on increasing the mol % of DOGS within the monolayer. The increase in protein layer thickness has been shown by the addition of two black dashed lines. A constant thickness in protein layer was found regardless of protein concentration of 143 ± 1 Å and 175 ± 3 Å for 10 and 20 mol % DOGS:DOPC respectively. The thickness of these layers is reasonable and similar values have been reported for DOGS:SOPC monolayers at the air-water interface deduced by XRR[66], probing the interaction of a similarly sized protein[67]. The unit cell parameters of penicillin binding protein 3 are 69 x 83 x 89 Å[18]. We would therefore expect that a complete monolayer of protein would have an average thickness of around 80 Å. The thicknesses observed therefore correspond to approximately 2 layers of protein. A ribbon diagram of the protein is shown in figure 4.19.

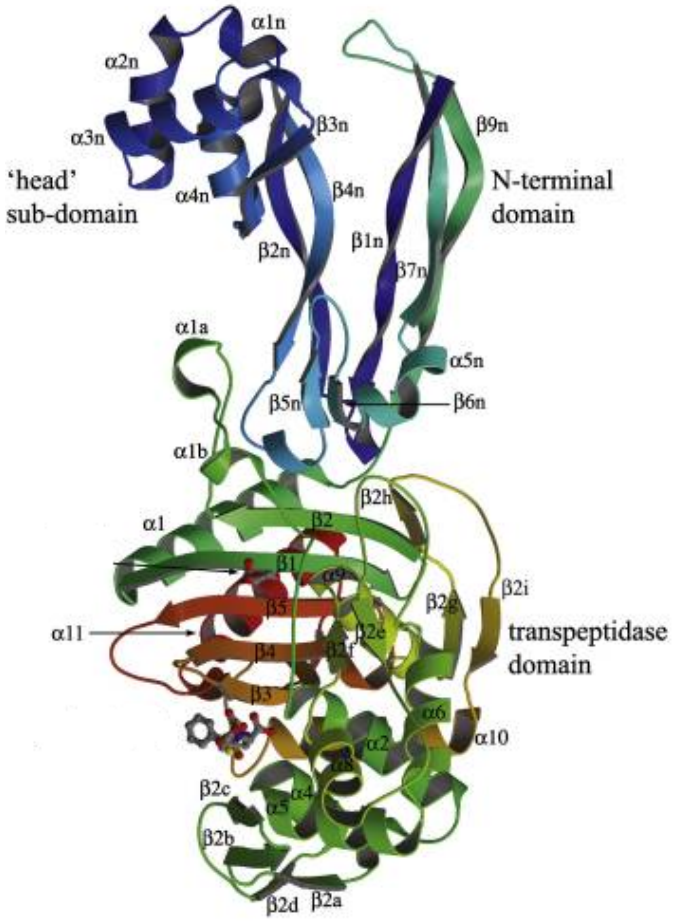

Fig 4.19- Ribbon diagram of PBP3. Image re-produced with permission from reference[18].

The protein used in this study contained a hexahistidine tag attached to its N-terminus. The two layers observed for both 10 and 20 mol % DOGS:DOPC monolayers may be defined by a distinct mechanism of interaction. The first layer is assumed to be a pre-oriented specifically bound layer, interacting with the DOGS head group within the monolayer via its N-terminus. Whilst the second layer will correspond to a non-specifically bound, protein aggregate layer. The fact that the observed layer thickness is larger for the 20 mol % DOGS monolayer can be rationalized by the fact that upon non-specific adsorption, there is more protein present at the interface, which will ultimately lead to the growth of a larger secondary protein layer.

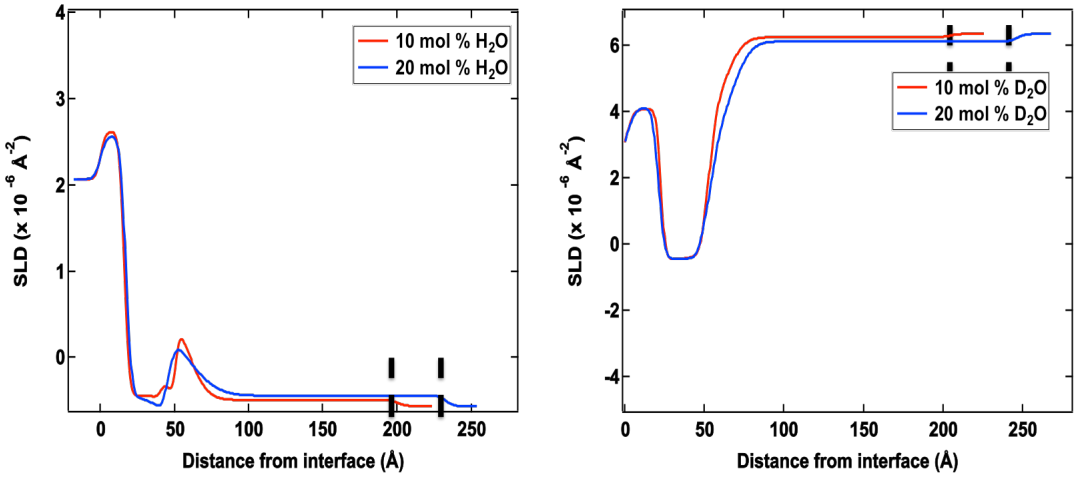

Fig 4.20- Scattering length density profiles for 10 μg ml^{-1} protein solution on 10 and 20 mol % DOGS:DOPC monolayers in H_2O and D_2O.

4.4 Concluding Remarks

The interaction of PBP3 with vesicles containing DOGS-NTA-Ni proceeds via monolayer coverage for 1 and 5 mol % chelating lipid. This has been shown by increases in the hydrodynamic diameter of approximately twice the hydrodynamic diameter of the protein. When there is 5 mol % chelating lipid in the system the apparent increase in diameter of the vesicles upon protein injection increases to 22.9 nm. This is due to the adsorption of non-specifically bound protein to an already formed monolayer of specifically bound protein.

The interaction of the protein with monolayers composed of 5, 10 and 20 mol % DOGS:DOPC at the air-water interface was assessed by BAM. Here it was qualitatively shown that as the concentration of DOGS within the monolayer was increased so too was the amount of protein adsorbed. For 5 and 10 mol % DOGS:DOPC monolayers it was shown that initial protein binding, and subsequent lateral organization, is likely to proceed via the formation of small patches which then coalesce with time. The 20

mol % DOGS:DOPC monolayer seemed to show the presence of a large amount of protein aggregate at the interface.

QCM was utilized to assess the mass of protein adsorbing at the interface. When either the protein concentration or the DOGS concentration is increased so too does the mass of protein at the interface. Given that the protein is highly unlikely to change its conformation or cross-link with itself, this implies that the later stages of adsorption are more visco-elastic in structure. This must be due to the adsorption of non-specifically bound protein to an already formed protein monolayer.

Neutron reflectometry agrees with the results obtained by QCM when the volume fraction, and hence the mass of protein, is calculated at the interface. The thickness of the protein layer is consistent with a layer that is roughly two protein molecules in thickness. More importantly the best fits are obtained for an increasing thickness on going from 10 to 20 mol % DOGS within the monolayer. This implies that the more specific protein adsorption that occurs in the first stage of protein adsorption, the more “vacant” protein molecules there are for the subsequent interaction of non-specifically bound protein.

It is clear that there are marked differences between the adsorption of protein to a vesicular interface as opposed to a planar monolayer. Vesicles show less of a propensity towards the binding of non-specifically bound protein, especially at reduced DOGS concentrations. Protein at 1 and 5 mol % DOGS suggests monolayer coverage of the protein. The comparable formulations for the planar lipid monolayer show that protein aggregation occurs regardless of DOGS concentration. To the authors knowledge there are no systematic studies, which specifically compare these two systems with any one protein. There have been numerous studies comparing the interactions of proteins on vesicles[20 21] and planar lipid layers at the air-water interface.[23 68-70]. The reason for the lack of non-specific protein adsorption, or monolayer only formation, for the

vesicle system here may be down to a few key reasons. Firstly the effect of curvature may play a role in the adsorption of protein. The relatively small vesicles studied here will have a much larger curvature in comparison to the planar lipid monolayer (effective curvature of zero). It has been shown that increasing the curvature of a system can reduce the amount of adsorbed protein at the interface, especially where larger proteins are concerned[71 72]. The much larger curvature of the lipid vesicles may suppress protein interaction and adsorption at the interface compared to the planar monolayer with zero curvature. It has also been shown that sufficient coverage of proteins on a vesicle surface can itself induce a greater curvature[73]. This increase in curvature may ultimately lead to the suppression of subsequent non-specific protein binding. Secondly the structure of the vesicle is a bilayer and not a monolayer. Assuming the concentration of DOGS throughout the bilayer is even, this reduces the effective number of available binding sites for the protein to half the number in a monolayer. This reduction in available binding sites may reduce the amount of specifically adsorbed protein and hinder the formation of a non-specifically bound protein layer. This is compared to the planar monolayer where all binding sites are potentially available and there is zero curvature. The increase in specific protein interaction then acts as an “anchor” for the adsorption of more non-specifically bound protein.

Having characterized the nature of a soluble his-tagged protein with monolayers containing DOGS-NTA-Ni, the intention was then to see if this system is applicable to a membrane protein. The end goal of this work was to align membrane protein containing nanodiscs at the solid-liquid interface using the specific attachment of DOGS-NTA-Ni. It was therefore vital to understand the relationship between the protein and his-tag within the monolayer. Before proceeding with attempts to align membrane protein containing nanodiscs, it is important to gain knowledge of how empty nanodiscs interact and adsorb at the interface. This along with attempts made to adsorb the protein containing discs will be discussed in the next chapter.

4.5 References

1. Spratt BG. Distinct penicillin binding proteins involved in the division, elongation and shape of Escherichia Coli K12. Proceedings of the National Academy of Sciences 1975;**72**(8):2999-3003.
2. Spratt BG, Pardee AB. Penicillin-binding proteins and cell shape in E. coli. Nature 1975;**254**:516-17.
3. Waxman DJ, Strominger JL. Penicillin-binding proteins and the mechanism of action of beta-lactam antibiotics. Annual Review of Biochemistry 1983;**52**:825-69.
4. Dabernat H, Delmas C, Seguy M, et al. Diversity of B-lactam resistance-conferring amino acid substitutions in penicillin binding protein 3 of haemophilus influenzae. Antimicrobial agents and chemotherapy 2002;**46**(7):2208-18.
5. Kucerka N, Kiselev MA, Balgavy P. Determination of bilayer thickness and lipid surface area in unilamellar dimyristoylphosphatidylcholine vesicles from small-angle neutron scattering curves: a comparison of evaluation methods. European Biophysics Journal with Biophysics Letters 2004;**33**(4):328-34.
6. Maulucci G, Spirito M, Briganti G. Particle size distributions in DMPC vesicle solutions undergoing different sonication times. Biophysical Journal 2005;**88**(5):3543-50.
7. Heyn MP, Cherry RJ, Dencher NA. Lipid-protein interactions in bacteriorhodopsin-dimyristoylphosphatidylcholine vesicles. Biochemistry 1981;**20**(4):840-49.
8. Hunter DG, Frisken BJ. Effect of extrusion pressure and lipid properties on the size and polydispersity of lipid vesicles. Biophysical Journal 1998;**74**(6):2996-3002.
9. Mabrey S, Sturtevant M. Investigation of phase transitions of lipids and lipid mixtures by high sensitivity differential scanning calorimetry. Proceedings of the National Academy of Sciences 1976;**73**(11):3862-66.
10. Needham D, Evans E. Structure and mechanical properties of giant lipid (DMPC) vesicle bilayers from 20 degrees C below to 10 degrees C above the liquid crystal-crystalline phase transition at 24 degrees C. Biochemistry 1988;**27**:8261-69.
11. Watts A, Marsh D, Knowles PF. Characterisation of dimyristoylphosphatidylcholine vesicles and their dimensional changes through the phase transition: Molecular control of membrane morphology. Biochemistry 1978;**17**(9):1792-801.
12. Ulrich A, Sami M, Watts A. Hydration of DOPC bilayers by differential scanning calorimetry. Biochimica et Biophysica Acta 1994;**1191**:225-30.
13. Wolf DE, Dick D. *Current topics in membranes*: Academic press, 1994.
14. Bagatolli L, Sunil Kumar PB. Phase behaviour of multicomponent membranes. Soft Matter 2009;**5**:3234-48.
15. Gallová J, Uhríková D, Hanulová M, et al. Bilayer thickness in unilamellar extruded 1,2-dimyristoleoyl and 1,2-dierucoyl phosphatidylcholine

vesicles: SANS contrast variation study of cholesterol effect. Colloids and Surfaces B: Biointerfaces 2004;**38**(1–2):11-14.
16. Yang P, Lin T, Hu Y, et al. Small-angle x-ray scattering studies of the structure of mixed DPPC/diC7PC micelles in aqueous solutions. Chinese Journal of Physics 2012;**50**(2):349-56.
17. Deme B, Dubois M, Zemb T, et al. Effect of carbohydrates on the swelling of a lyotropic lamellar phase. Journal of Physical Chemistry B 1996;**100**:3828-38.
18. Sainsbury S, Bird L, Rao V, et al. Crystal structures of penicillin binding protein 3 from pseudomonas aeruginosa: Comparison of native and antibiotic-bound forms. Journal of Molecular Biology 2011;**405**(1-3):173-84.
19. Coker H. Characterising the interaction of penicillin binding protein 3 with phospholipid vesicles [Undergraduate thesis]. University of Bath, 2013.
20. Mašek J, Bartheldyová E, Korvasová Z, et al. Immobilization of histidine-tagged proteins on monodisperse metallochelation liposomes: Preparation and study of their structure. Analytical Biochemistry 2011;**408**(1):95-104.
21. Chikh GG, Ming Li W, Schutze-Redelmeier M, et al. Attaching histidine-tagged peptides and proteins to lipid-based carriers through use of metal-ion-chelating lipids. Biochimica et Biophysica Acta 2002;**1567**:204-12.
22. Rinia HA, Krujiff B. Imaging domains in model membranes with atomic force microscopy. FEBS Letters 2001;**504**:194-99.
23. Venien-Bryan C, Lenne P, Zakri C, et al. Characterization of growth of 2D protein crystals on a lipid monolayer by ellipsometry and rigidty measurements coupled to electron microscopy. Biophysical Journal 1998;**74**:2649-57.
24. Dietrich J, Venien-Bryan C. *Strategies for two-dimensional crystallisation of proteins using lipid monolayers*. 1 ed: Imperial College Press, 2005.
25. Courty SL, L; Martel, L; Lenne, P.F; Balavonie, F; Dischert, W; Konovalov, O; Mioskowski, C; Legrand, J; Venien-Bryan, C. Two-dimensional crystallisation of a histidine-tagged protein on monolayers of fluidity-enhanced Ni2+- chelating lipids. Langmuir 2002;**18**(24):9502-12.
26. Al-kurdi.R;, Gulino-Debruc D, Martel L. A soluble VE-cadherin fragment forms 2D arrays of dimers upon binding to a lipid monolayer. Journal of Molecular Biology 2004;**337**(4):881-92.
27. Bischler N, Balavonie F, Milkereit P, et al. Specific interaction and two-dimensional crystallisation of histidine tagged yeast RNA polymerase I on nickel chelating lipids. Biophysical Journal 1998;**74**:1522-32.
28. Ohlsson P-Å, Tjärnhage T, Herbai E, et al. Liposome and proteoliposome fusion onto solid substrates, studied using atomic force microscopy, quartz crystal microbalance and surface plasmon resonance. Biological activities of incorporated components. Bioelectrochemistry and Bioenergetics 1995;**38**(1):137-48.
29. Okahata Y, Ebato H. Application of a quartz-crystal microbalance for detection of phase transitions in liquid crystals and lipid multibilayers. Analytical Chemistry 1989;**61**(19):2185-88.

30. Cho N-J, Frank CW, Kasemo B, et al. Quartz crystal microbalance with dissipation monitoring of supported lipid bilayers on various substrates. Nat Protocols 2010;**5**(6):1096-106.
31. Keller CA, Kasemo B. Surface specific kinetics of lipid vesicle adsorption measured with a quartz crystal microbalance. Biophysical Journal 1998;**75**:1397-402.
32. Vogt BD, Lin EK, Wu W, et al. Effect of film thickness on the validity of the saurbrey equation for hydrated polyelectrolyte films. Journal of Physical Chemistry B 2004:12685-90.
33. Kanazawa K, Cho N-J. Quartz crystal microbalance as a sensor to characterise macromolecular assembly dynamics. Journal of sensors 2009:1-17.
34. Rodahl M, Hook F, Fredriksson C, et al. Simultaneous frequency and dissipation factor QCM measurements of bimolecular adsorption and cell adhesion. Faraday discussions 1997;**107**:229-46.
35. Saurbrey G. Verwendung von schwingsquarzen zur waegun dunner schichten und zur mikrowaegung. Zeitschrift fur physik 1959;**155**:206.
36. Richter R, Mukhopadhyay A, Brisson A. Pathways of lipid vesicle deposition on solid surfaces: A combined QCM-D and AFM study. Biophysical Journal 2003;**85**:3035-47.
37. Richter R, Brisson A. Following the formation of supported lipid bilayers on mica: A study combining AFM, QCM-D and ellipsometry. Biophysical Journal 2005;**88**(3422-3433).
38. Hook F, Kasemo B, Nylander T, et al. Variations in coupled water, viscoelastic properties and film thickness of a Mefp-1 protein film during adsorption and cross-linking: A quartz crystal microbalance with dissipation monitoring, ellipsometry and surface plasmon resonance study. Analytical Chemistry 2001;**73**:5796-804.
39. Reimhult E, Larsson C, Kasemo B, et al. Simultaneous surface plasmon resonance and quartz crystal microbalance with dissipation monitoring measurements of biomolecular adsorption events involving structural transformations and variations in coupled water. Analytical Chemistry 2004;**76**:7211-20.
40. Hook F, Voros J, Rodahl M, et al. A comparative study of protein adsorption on titanium oxide surfaces using in-situ ellipsometry, optical waveguide light mode spectroscopy and quartz crystal microbalance/dissipation. Colloids and Surface B: Biointerfaces 2002;**24**:155-70.
41. Rodahl M, Hook F, Krozer A, et al. Quartz crystal microbalance setup for frequency and Q-factor measurements in gaseous and liquid environments. Review of scientific instruments 1995;**66**(7):3924-30.
42. Hook F, Rodahl M, Brzezinski P, et al. Energy dissipation kinetics for protein antibody-antigen adsorption under shear oscillation on a quartz crystal microbalance. Langmuir 1998;**14**:729-34.
43. Ayela C, Roquet F, Valera L, et al. Antibody-antigenic peptide interactions monitored by SPR and QCM-D: A model for SPR detection of IA-2 autoantibodies in human serum. Biosensors and bioelectronics 2007;**22**:3113-19.

44. Hollinsead CM, Hanna M, Barlow DJ, et al. Neutron reflection from a dimyristoylphosphatidylcholine monolayer adsorbed on a hydrophobised silicon support. Biochimica et Biophysica Acta 2001;**1511**:49-59.
45. Fragneto G, Thomas RK, Rennie AR, et al. Neutron reflection study of bovine B-casein adsorbed on OTS self-assembled monolayers. Science 1995;**267**:657-60.
46. Wacklin HP, Tiberg F, Thomas RK. Formation of supported phospholipid bilayers via co-adsorption with B-D-dodecyl maltoside. Biochimica et Biophysica Acta 2005;**1668**:17-24.
47. Slater JC. Atomic radii in crystals. Journal of chemical physics 1964;**41**(10):3199-205.
48. Fragneto G, Li XZ, Thomas RK, et al. A neutron reflectivity study of the adsorption of aerosol-OT on self-assembled monolayers on silicon. Journal of colloid and interface science 1996;**178**:531-37.
49. Dura JA, Richter CF, Majkrzak CF, et al. Neutron reflectometry, x-ray reflectometry and spectroscopic ellipsometric characterisation of thin SiO2 on Si. Applied physics letters 1998;**73**:2131.
50. Fragneto G, Lu JR, McDermott DC, et al. Structure of monolayers adsorbed on self-assembled monolayers on silicon: A neutron reflectivity study. Langmuir 1996;**12**:477-86.
51. Hines JD, Fragneto G, Thomas RK, et al. Neutron reflection from mixtures of sodium dodecyl sulfate and dodecyl betaine adsorbed at the hydrophobic solid/aqueous interface. Journal of colloid and interface science 1997;**189**:259-67.
52. Rand RP, Chapman DL, Larsson K. Titled hydrocarbon chains of dipalmitoyl lecithin become perpendicular to the bilayer before melting. Biophysical Journal 1975;**15**:1117-25.
53. Vankin D. Structure-function relations in self-assembled C18- and C20-sphingosines monolayers at gas/water interfaces. Journal of the American Chemical Society 2003;**125**:1313-18.
54. DePalma V, Tillman N. Friction and wear of self-assembled trichlorosilane monolayer films on silicon. Langmuir 1989;**5**:868-72.
55. Opila RL, Legrange JD, Markham JL, et al. Effects of surface hydration on the deposition of silane monolayers on silica optical fiber. Journal of adhesion science and technology 1997;**11**(1):1-10.
56. Wasserman SR, Whitesides GM, Tidswell IM, et al. The structure of self-assembled alkylsiloxanes on silicon: A comparison of results from ellipsometry and low-angle x-ray reflectivity. Jorunal of the ameican chemical society 1989;**11**:5852-61.
57. Vaknin D, Kjaer K, Als-Nielsen J, et al. Structural properties of phosphatidylcholine in a monolayer at the air/water interface. Biophysical Journal 1991;**59**(1325-1332).
58. Miller CE, Majewski J, Gog T, et al. Characterisation of thin films at the solid-liquid interface by x-ray reflectivity. Physical Review Letters 2005;**97**:238104-1-04-4.
59. Koenig BW, Krueger S, Orts WJ, et al. Neutron reflectivity and atomic force microscopy studies of a lipid bilayer in water adsrobed to the surface of a silicon single crystal. Langmuir 1996;**12**:1343-50.

60. Csucs G, Ramsden JJ. Interaction of phospholipid vesicles with smooth metal-oxide surfaces. Biochimica et Biophysica Acta 1998;**1369**:61-70.
61. Johnson SJ, Bayerl TM, McDermott DC, et al. Structure of an adsorbed dimyristoylphosphatidylcholine bilayer measured with specular reflection of neutrons. Biophysical Journal 1991;**59**(2):289-94.
62. Biltonen R, Lichtenberg D. The use of differential scanning calorimetry as a tool to characterise liposome preparations. Chemical Physics of lipids 1993;**64**:129-42.
63. Myatt D, Clifton LA. http://psldc.isis.rl.ac.uk/Psldc/. Secondary http://psldc.isis.rl.ac.uk/Psldc/ 2014.
64. Zhao X, Pan F, Lu JR. Interfacial assembly of proteins and peptides: recent examples studies by neutron reflection Journal of the royal society interface 2009;**6**:S659-S70.
65. Cheng G, Liu Z, Murton JK, et al. Neutron Reflectometry and QCM-D Study of the Interaction of Cellulases with Films of Amorphous Cellulose. Biomacromolecules 2011;**12**(6):2216-24.
66. Kroner A, Abuillan W, Deichmann C, et al. Quantitative determination of lateral concentration depth profile of histidine tagged recombinant proteins probed by grazing incidence x-ray fluorescence. The journal of physical chemistry B 2013;**117**:5002-08.
67. Ciatto C, Bahna F, Zampieri N, et al. T-cadherin structures reveal a novel adhesive binding mechanism. Nature Structural and Molecular Biology 2010;**17**(3):339-47.
68. Clifton LA, Green RJ, Hughes AV, et al. Interfacial structure of wild-type and mutant forms of puroindoline-b bound to DPPG monolayers. Journal of Physical Chemistry B 2008;**112**:15907-13.
69. Clifton LA, Skoda MWA, Daulton EL, et al. Asymmetric phospholipid: lipopolysaccharide bilayers; a Gram negative bacterial outer membrane mimic. Interface 2013;**10**.
70. Blankenburg R, Meller P, Ringsdorf H, et al. Interaction between biotin lipids and streptavidin in monolayers: Formation of oriented two-dimensional protein domains induced by surface recognition. Biochemistry 1989;**28**:8214-21.
71. Cedervall T, Lynch I, Lindmann S, et al. Understanding the nanoparticle-protein corona using methods to quantify exchange rates and affinities of proteins for nanoparticles. Proceedings of the National Academy of Sciences 2007;**104**(7):2050-55.
72. Lynch I, Dawson KA. Protein-nanoparticle interactions. Nanotoday 2008;**3**(1-2):40-47.
73. Callan-Jones A, Bassereau P. Curvature-driven membrane lipid and protein distribution. Current opinion in solid state and materials science 2013;**17**:143-50.

Chapter 5.0 Nanodisc interactions with phospholipid monolayers

This chapter will continue with the theme of protein alignment at lipid interfaces. The aim of this chapter was to consider novel ways of aligning membrane proteins at the interface. The approach was to use nanodisc systems in order to develop a system that is capable of delivering membrane proteins to an interface for further structural study through reflectometry and grazing incidence diffraction techniques.

Experiments began by attempting to adsorb empty SMA-nanodiscs upon lipid monolayers at the air-water interface. This was completed using the Langmuir trough and neutron reflectometry. Using the Langmuir trough enabled real time monitoring of the surface pressure as the nanodiscs adsorbed, whilst neutron reflectometry was able to characterize the structures formed at the interface.

The second half of this chapter is devoted to transferring this system to the solid-liquid interface. Here analogous lipid monolayers were chosen and adsorbed onto hydrophobic self-assembled monolayers using the same techniques as those in the previous chapter for the soluble protein alignment studies. Neutron reflectometry provided characterization of the interfacial structure after nanodisc adsorption.

The final section of this chapter gives a brief summary of attempts made to align nanodiscs containing the membrane protein ZipA on a funtionalised lipid monolayer at the solid-liquid interface.

5.1 Nanodisc adsorption at the air-water interface

As a proof of concept and to ensure that nanodiscs would adsorb to a lipid monolayer the experiment was first conducted at the air-water

interface. Here an h-POPC monolayer was used to assess the interaction of deuterated DMPC nanodiscs. This approach was found to work for protein-stabilised nanodiscs as discussed in the introduction (section 1.4.4)[1 2].

5.1.1 Trough measurments

Figure 5.1 shows surface pressure-time plots for a POPC monolayer underneath which a DMPC nanodisc solution has been injected. The nanodiscs were injected underneath the lipid monolayer at a surface pressure of 15 mNm^{-1}, which corresponds to the monolayer in the liquid expanded phase[3].

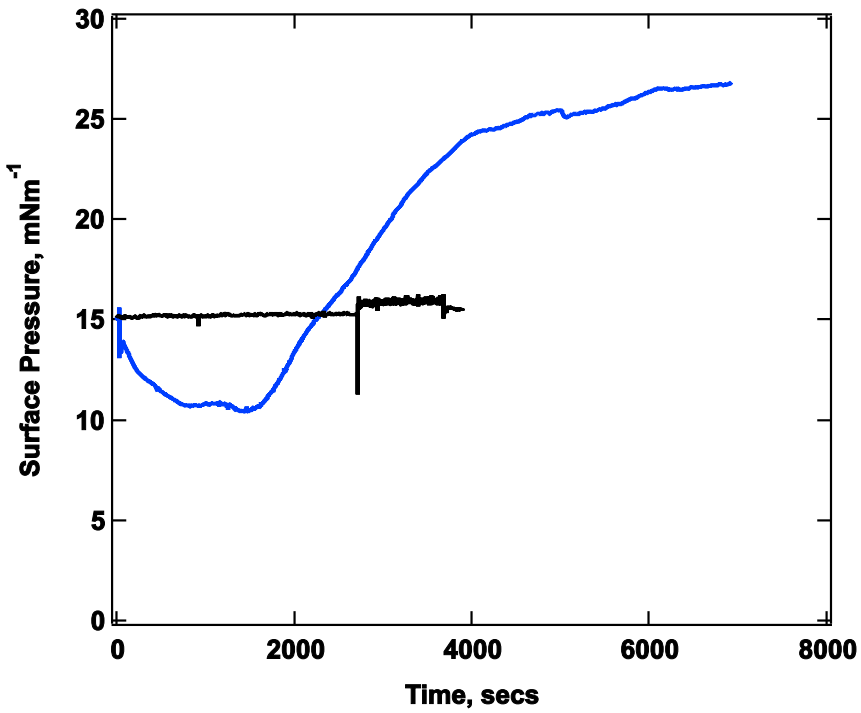

Fig 5.1- Surface pressure-time plot for the injection of nanodiscs underneath a POPC monolayer at the air-water interface. The black line shows the surface pressure evolution of a pure POPC monolayer and the blue line shows the surface pressure evolution when nanodiscs are injected.

It is clear that when nanodiscs are present in the sub-phase there is a large increase in surface pressure from 15 to around 25 mNm^{-1}. This is most likely due to lipid exchange between the nanodiscs and the POPC monolayer.

5.1.2 Pre-characterisation of the lipid monolayer

The POPC monolayer was first measured before nanodisc adsorption. Figure 5.2 shows neutron reflectometry for an h-POPC monolayer spread on the surface of water at a surface pressure of 15 mNm^{-1} along with a scattering length density profile. The monolayer was characterized in two contrasting solvents, D_2O and ACMW. Table 5.0a shows the values used to model the data. The scattering length density of the PC headgroup has been calculated with an assumed volume of 268 $Å^3$ [4] and the POPC tail group has been calculated with an assumed volume of 934 $Å^3$ [3]. The scattering length density values used to model the data are also shown in table 5.0b.

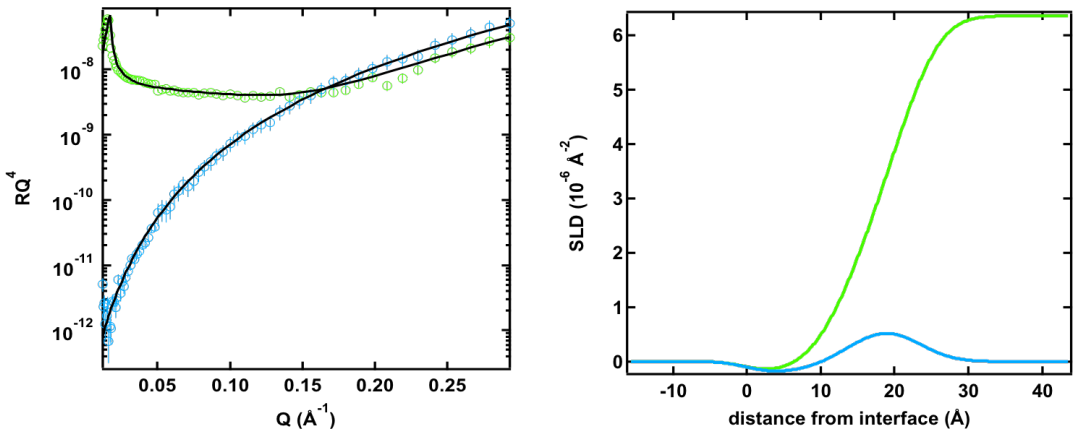

Fig 5.2- Neutron reflectometry data and scattering length density profile for a h-POPC monolayer at the air-water interface. D_2O contrast is shown in green and ACMW contrast is shown in blue. The black line represents the modeled fit.

Layer	Thickness (Å)	% Hydration	Roughness (Å)
Lipid Tail	16.3 ± 1	0	2.4 ± 1
Lipid Head	9.6 ± 1	52 ± 5	4.1 ± 2

Table 5.0a- Summary of parameters used to model the data in figure 5.2.

Layer	SLD (x10^{-6} Å^{-2})
Lipid Tails	-0.21
Lipid Heads	1.8
ACMW	0
D_2O	6.35

Table 5.0b- Scattering length density values used to model the data in figure 5.2.

The value modeled for the thickness of the POPC tail and head groups is in good agreement with the literature where values for the tail groups are often reported between 16-20 Å [3] and the head groups between 5-10 Å [3] [5] in thickness.

5.1.3 Characterising nanodisc adsorption

A h-POPC monolayer was spread to a surface pressure of 15 mNm^{-1} over a sub-phase containing nanodiscs in which the phospholipid tails were deuterated. The approach was different here, as compared to the trough studies, due to the small volumes of nanodiscs available and the fact that it was only possible to use a very small trough. The nanodiscs could therefore not be injected underneath a pre-formed lipid monolayer. The system was allowed to equilibrate for around 30 minutes before reflectometry data was acquired. Measurements were made in D_2O and ACMW.

Figure 5.3 shows raw reflectometry data for the bare h-POPC monolayer and the monolayer with nanodiscs adsorbed to the surface. This is shown to highlight the difference in reflectivity upon nanodisc adsorption to the

lipid interface. Only the D_2O contrast is shown here, however the model will be considered later in this section, where both D_2O and ACMW contrasts are shown. From this plot it is clear that a fringe minimum occurs at ca. Q=0.15 $Å^{-1}$.

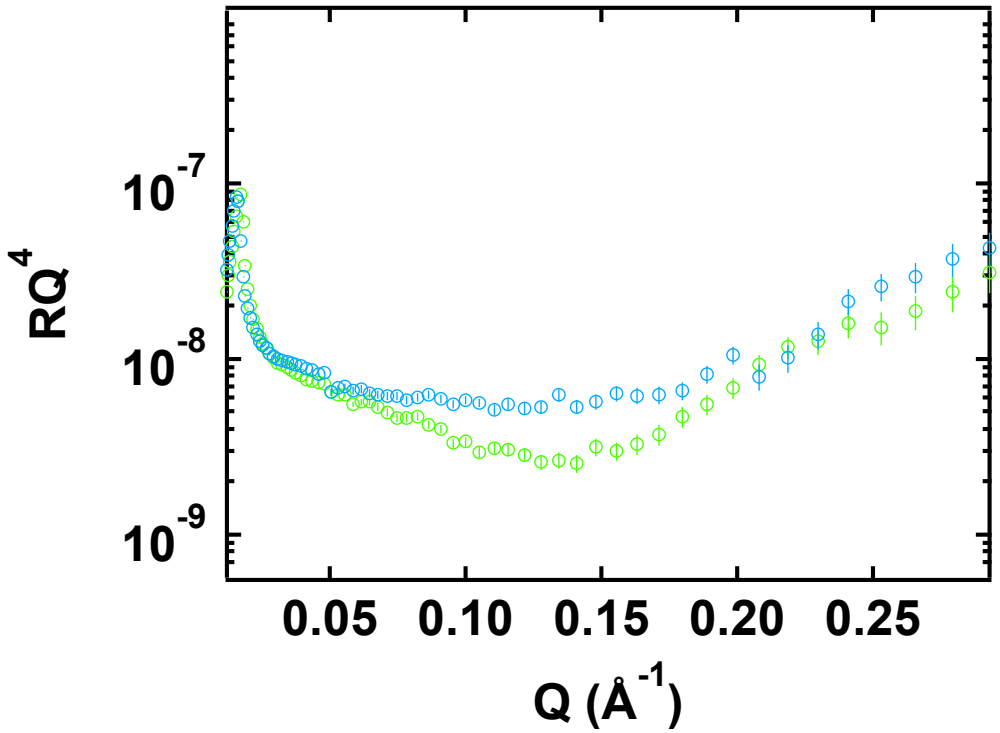

Fig 5.3- Change in reflectivity upon the adsorption of nanodiscs to a POPC monolayer. The data for the bare POPC monolayer is shown in blue and the data for nanodisc adsorption is shown in green.

Before discussing the model used for nanodisc adsorption, it is important to consider the scattering length density of a nanodisc layer.

The SLD of a nanodisc layer has been calculated from structural parameters found from SANS studies[6]. The model used to obtain structural parameters of the SMA-nanodiscs has been presented in section 1.3.3 of the introduction. From this model the volume fraction of lipids (DMPC) and polymer (SMA) was calculated. The SLD of an adsorbed nanodisc layer can be calculated using the following equation,

$$\rho_{nanodisc} = \rho_{SMA} \cdot \chi_{SMA} + \rho_{lipid} \cdot \chi_{lipid}$$ (equation 5.0),

where ρ_{SMA} and ρ_{lipid} are the scattering length densities of the polymer and lipid, whilst χ_{SMA} and χ_{lipid} are the volume fraction of polymer and lipid in one nanodisc. These values are presented in table 5.1. The SLD of d-DMPC has been calculated assuming a molecular volume of 1101 Å^3 [7], whilst the SLD of the polymer has been used from the work by Jamshad *et al*[6]. This method has also been used in the literature to calculate the SLD of MSP-nanodiscs[1 2].

Component	Volume fraction	Scattering length density (x10^{-6} Å^{-2})
d-DMPC	0.53	5.92
Polymer	0.47	1.89
Nanodisc	1	4.02

Table 5.1- Calculated scattering length density for a nanodisc layer adsorbed at the interface.

Figure 5.4 shows reflectometry data for d-DMPC nanodiscs adsorbed to an h-POPC monolayer. A scattering length density profile is also shown and compared to the SLD profile of the POPC monolayer without nanodiscs present (for clarity only the D_2O contrast is shown here). Table 5.2 shows parameters used to generate the model fit.

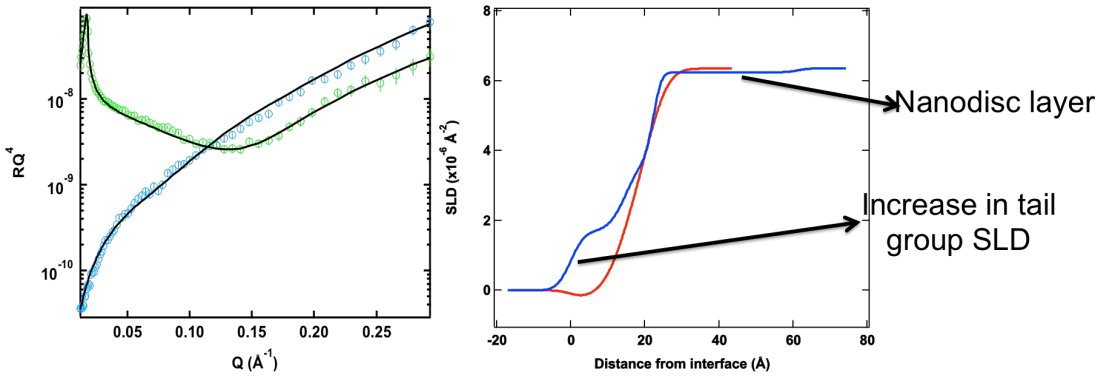

Fig 5.4- Neutron reflectometry profile and scattering length density profile for a POPC monolayer with adsorbed d-DMPC nanodiscs. D_2O contrast is shown in green, ACMW contrast is shown in blue.

Layer	Thickness (Å)	SLD (x 10^{-6} Å^{-2})	Volume fraction at interface	Roughness (Å)
Lipid Tails	16.3 ± 1	1.7	-	2.4 ± 1
Lipid Heads	9.6 ± 1	1.8	-	4.1 ± 1
Nanodiscs	39 ± 3	4.02	0.04 ± 0.01	3 ± 2

Table 5.2- Parameters used to model the reflectometry data presented in figure 5.4.

There are two distinct changes that occur when the nanodiscs are present in the system. The first is an apparent increase in the total thickness of the interfacial layer, and a simultaneous change in the POPC monolayer structure at the air-water interface. These results confirm the formation of a nanodisc film below the air-water interface, adsorbed onto the POPC monolayer. The observed increase in thickness of 39 Å is in excellent agreement with the thickness of lipid bilayers characterised through diffraction experiments (40 Å) and also agrees with the thickness values found for adsorbing MSP-nanodiscs (39 Å) [127]. This implies that the nanodiscs are aligned with their lipid bilayer parallel to the interface. The second distinct change is that the h-POPC monolayer is enriched with deuterated phospholipids as a result of lipid exchange from the

nanodisc layer. This is shown by an increase in surface pressure as shown by the surface pressure-time plot shown in figure 5.1, and an observed increase in scattering length density of the POPC monolayer tail group region due to the presence of deuterated DMPC tails. The scattering length density modeled for the tail group of the lipid monolayer can be used to calculate the volume fraction of d-DMPC that has exchanged from the nanodiscs into the monolayer. The scattering length density of the monolayer will now be given by,

$$\rho_{nanodisc\ layer} = (\rho_{h-POPC} \cdot \chi_{h-POPC}) + (\rho_{d-DMPC} \cdot \chi_{d-DMPC}) + (\rho_{SMA} \cdot \chi_{SMA})$$

(equation 5.1).

Therefore the observed increase in scattering length density of the monolayer tail group corresponds to a volume fraction of 0.66 POPC and 0.34 d-DMPC within the monolayer.

It is well known that dynamic exchange can occur between polymer micelles[8-10]. This has also been shown for DMPC unilamellar vesicles where time-resolved SANS (TR-SANS) has shown exchange of lipid between vesicles in solution[11]. This phenomenon has recently been extended to MSP-nanodiscs where it was shown that rapid exchange of lipids between nanodiscs occurs. This exchange is mediated by monomeric diffusion of lipid in an aqueous medium and not through collisions between nanodiscs. These dynamic properties of lipid exchange between discs are thought to be a consequence of their entropically unstable state. They are considered entropically unstable as the tight packing of lipids within the disc lowers the entropy of the system. This therefore means that they undergo a rapid, enthalpically unfavourable but entropically favourable lipid exchange process[12]. This is coupled with the fact that there is an entropic gain when two lipids mix within a monolayer at the air-water interface and within the discs[2]. The discs adsorbed at the interface in these experiments are adsorbed upon a hydrogenated lipid monolayer. Given that lipid exchange happens so

rapidly in an aqueous medium, it is reasonable to expect that it may be even more prevalent at the interface of a lipid monolayer. The phenomenon of lipid exchange from the discs and the orientation of nanodisc alignment agree with results found by Wadsater *et al* for MSP-nanodiscs[2].

5.1.4 The effect of lipid interface

Another interesting aspect is the role of the polymer charge on the adsorption at a lipid monolayer. To assess this a cationic dioctadecyldimethylammonium bromide (DODAB) monolayer was also investigated. This presents a positively charged interface to the negatively charged polymer in the nanodiscs in the sub-phase.

5.1.5 Trough Studies

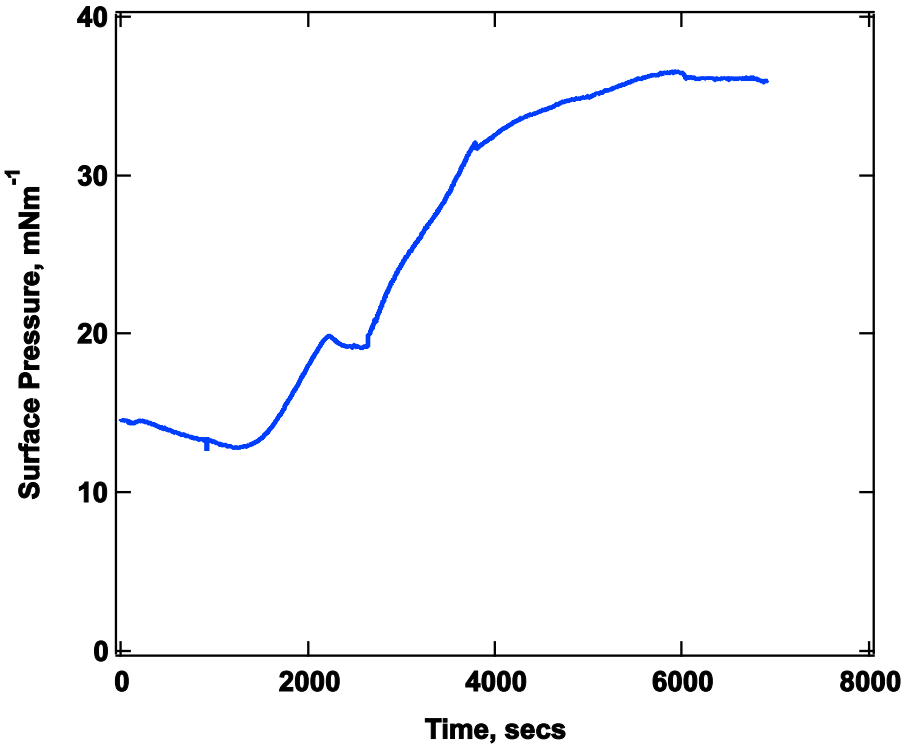

Fig 5.5-Evolution of surface pressure with time after injection of nanodiscs underneath a DODAB monolayer at 15 mNm^{-1}.

Figure 5.5 shows the evolution of the surface pressure when nanodiscs are injected beneath a DODAB film at a surface pressure of 15 mNm^{-1}. As with the discs on the POPC monolayer there is a large increase in surface pressure upon nanodisc injection from 15 to 35 mNm^{-1}

5.1.6 Pre-characterisation of the lipid monolayer

As above the DODAB monolayer was first pre-characterised before nanodisc adsorption. Figure 5.6 shows neutron reflectometry data in D_2O and ACMW along with the scattering length density profile for a DODAB monolayer with and without nanodiscs present (again for clarity only D_2O profile shown). Table 5.3 shows the parameters used to model this data. Generally due to the simplicity of the DODAB head group as compared with the phosphocholine head group, it is difficult to differentiate between the headgroup and tail group layers and the surfactant can be modelled as a single layer at the interface[2 13]. This approach was taken here and the scattering length densities were calculated as follows. DODAB was calculated with an assumed volume of 1174 $Å^3$ [13] and the nanodisc SLD was calculated as for the study on the POPC monolayer.

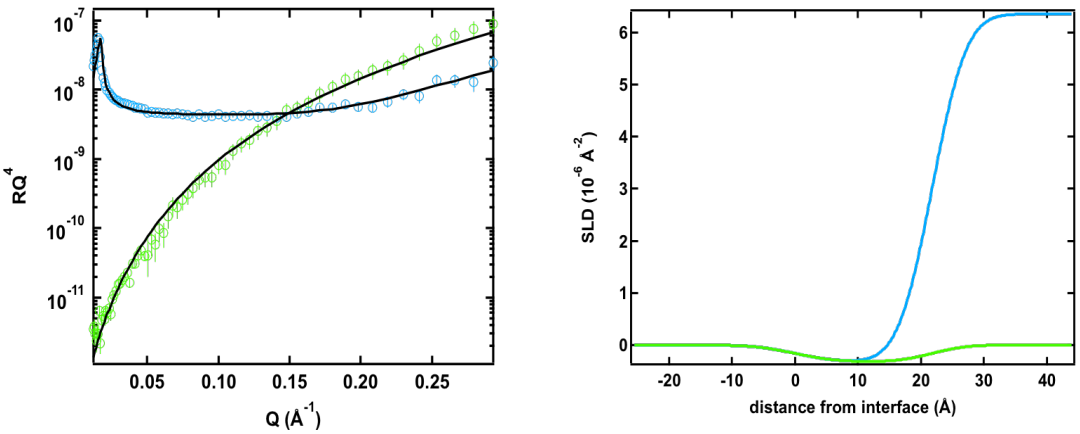

Fig 5.6- Neutron reflectometry data and scattering length density profile for a h-DODAB monolayer at the air-water interface. D_2O contrast is shown in blue and ACMW contrast is shown in green. The black line represents the modeled fit.

Layer	Thickness (Å)	SLD (x 10^{-6} Å^{-2})	% Hydration	Roughness (Å)
DODAB	21.8 ± 2	-0.32	10 ± 3	4.3 ± 1

Table 5.3- Summary of parameters used to fit the data in figure 5.6.

A modeled thickness of 21.8 Å for the DODAB monolayer is in good agreement with neutron reflectometry studies which have reported a thickness of 22 Å [13] and ellipsometric studies which have reported a thickness of 21 Å [14].

The monolayer was subsequently characterized in the presence of d-DMPC nanodiscs. Figure 5.7 shows reflectometry data and an SLD profile showing the adsorption of a nanodisc layer. Table 5.4 shows the parameters used to model this data.

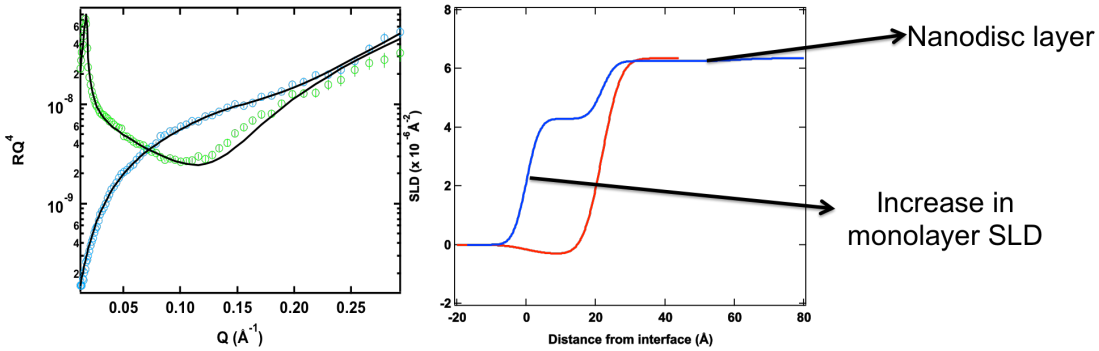

Fig 5.7-Neutron reflectometry data and scattering length density profile (ACMW contrast) for a d-DMPC nanodisc adsorption onto a DODAB monolayer. D_2O contrast is shown in green and ACMW in blue. The black line corresponds to the model fit.

Layer	Thickness (Å)	SLD (x 10^{-6} Å^{-2})	Volume fraction at interface	Roughness (Å)
DODAB monolayer	21.8 ± 2	3.9 ± 0.3	-	4.3 ± 2
Nanodiscs	39 ± 3	4.02	0.04	2.8 ± 1

Table 5.4- Summary of parameters used to fit the data shown in figure 5.7.

As with the nanodiscs on POPC there is a modeled increase in the scattering length density of the lipid monolayer as a result of enrichment with deuterated phospholipids from the nanodisc. There is also now an energetic component involved in the exchange of lipids from the nanodisc to the lipid monolayer, with the electrostatic repulsion within the cationic film being reduced by the incorporation of zwitterionic DMPC. The incorporation of lipids within the DODAB film is even more prevalent when compared to the POPC monolayer. This is further supported by the evolution in surface pressure with time upon nanodisc injection where a larger increase of up to 35 mNm^{-1} is observed for the DODAB monolayer. This is in contrast with the smaller increase for nanodisc injection on a

POPC film of up to 25 mNm^{-1}. The scattering length density of the layer can thus be described as,

$$\rho_{nanodisc\ layer} = (\rho_{h-DODAB} \cdot \chi_{h-DODAB}) + (\rho_{d-DMPC} \cdot \chi_{d-DMPC}) + (\rho_{SMA} \cdot \chi_{SMA})$$

(equation 5.2),

and corresponds to a volume fraction of 0.74 d-DMPC and 0.26 h-DODAB. This is clearly an extremely large magnitude of lipid exchange driven by the entropic gain of expulsion of lipids from the disc, the entropic gain of mixing within the monolayer and the energetic gain of dampening electrostatic repulsions within the DODAB monolayer. Figure 5.8 shows a schematic summary of nanodisc alignment on lipid monolayers at the air-water interface.

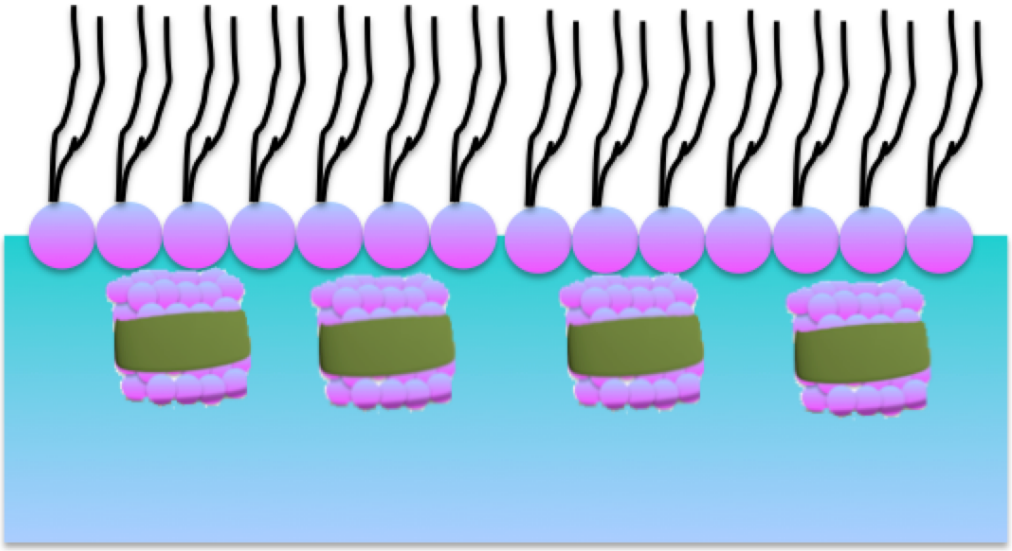

Fig 5.8- Schematic representation of nanodisc adsorption at the air-water interface.

5.1.7 The effect of nanodisc composition

The effect of adding 25 % DMPG (a negatively charged phospholipid) into the nanodiscs was also assessed. The POPC monolayer was spread on a solution of nanodiscs containing 25 vol % of DMPG:DMPC to a surface pressure of 15 mNm^{-1}. Figure 5.9 shows the reflectometry data for nanodisc adsorption and the corresponding scattering length density profile. Table 5.5 shows the parameters used to model this data. The scattering length density of the nanodiscs was calculated as with the 100 % DMPC discs but taking into account a 25 vol % of the lipids for DMPG. The scattering length density of DMPG was calculated assuming a volume of 1025 $Å^3$ [15]. However given the similarities between lipid structure this equates to only very small changes in the nanodisc SLD.

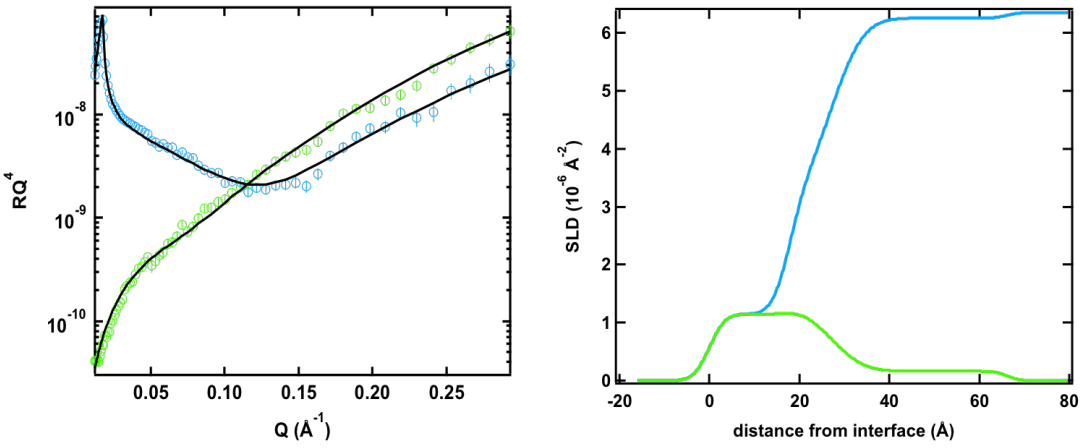

Fig 5.9-Neutron reflectometry data and scattering length density profile (D_2O contrast) for a 25 vol % d-DMPG nanodisc adsorption on a POPC monolayer. D_2O contrast is shown in blue and ACMW in green. The black line corresponds to the model fit.

Layer	Thickness (Å)	SLD (x 10^{-6} $Å^{-2}$)	Volume fraction at interface	Roughness (Å)
Lipid Tails	17.6 ± 1	1.2 ± 0.2	-	2.7 ± 1
Lipid Heads	9.5 ± 1	1.8	-	3.0 ± 2
Nanodiscs	39 ± 3	4.02	0.04 ± 0.01	5.6 ± 2

Table 5.5- Summary of parameters used to fit the data shown in figure 5.9.

The common features shown upon nanodisc adsorption are once again featured in the data presented above. This is a modeled increase in the SLD of the lipid monolayer suggestive of the monolayer becoming enriched in phospholipids as a result of exchange from the nanodiscs. It is interesting to note here that when 25 % DMPG is present within the nanodisc, lipid exchange to the monlayer is reduced. The change in scattering length density of the lipid tail region for the 25 % DMPG system is -0.21 to 1.2 x 10^{-6} $Å^{-2}$, as opposed to -0.21 to 1.7 x 10^{-6} $Å^{-2}$ for the pure DMPC nanodiscs. This may be due to the fact that the presence of a different kind of lipid within the nanodisc provides a slight entropic stabilization for the system, reducing the need for lipid exchange[2]. However it is not possible to accurately determine the volume fraction of each lipid within the monolayer as there is now more than two components within the monolayer, unless more contrasts are measured. The modeled increase in the thickness of the interfacial layer is 39 Å, which is suggestive of the nanodiscs adsorbing with their bilayer perpendicular to the interface as seen above for the DMPC nanodiscs.

5.1.8 Probing alternative models for the adsorption of nanodiscs

To validate the model described above for the description of the observed reflectivity for these systems, we have calculated the reflectivity for alternative models, and the results are summarized in figure 5.10. The

alternative models consist of the nanodisc adsorbing but without any lipid exchange (model 1), no nanodisc adsorption but with lipid exchange from nanodiscs in the bulk solution (model 2), nanodisc alignment with their long axis perpendicular to the lipid interface (model 3), nanodisc alignment with a tilted conformation relative to the surface normal (model 4) and a random orientation in which there is a mixture of both tilted and parallel alignment (model 5). For clarity only the D_2O contrast is shown in these proposed alternative models. Analysis of the potential models shown in figure 5.10 shows that the best fit is obtained for a single nanodisc layer adsorbed at the lipid interface with its long axis parallel to the lipid surface.

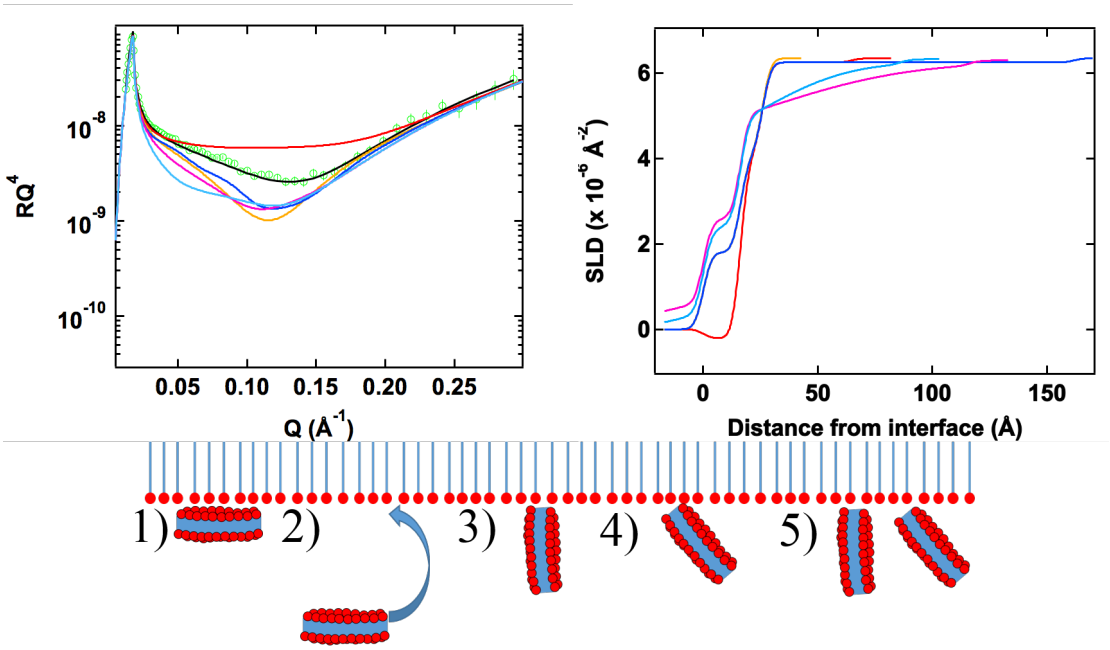

Fig 5.10- Experimentally observed neutron reflectometry data for d-DMPC nanodiscs adsorbed to a POPC monolayer (green circles) and the calculated reflectivity for nanodisc adsorption with no exchange (model 1, red line), no disc adsorption but lipid exchange from discs in solution (model 2, orange line), nanodisc adsorption with their long axis perpendicular to the lipid interface (model 3, dark blue line), a tilted nanodisc conformation relative to the surface normal (model 4, magenta line) and a random orientation of nanodisc adsorption consisting of both tilted and parallel alignment (model 5, light blue line). The modeled fit proposed previously is shown in black.

5.2 Aligning Nanodiscs at the solid-liquid interface

Attempts were then made to transfer the system described at the air-water interface to the solid-liquid interface.

5.2.1 Adsorption on bare silica substrate

Initially the nanodiscs were injected over a bare SiO_2 layer to see whether or not they would adsorb directly at this interface.

Figure 5.11 shows the neutron reflectometry profiles and scattering length density profiles for the silicon interface before and after nanodisc injection. Table 5.6 shows the parameters used to model the data. The bare silicon interface was first characterised in D_2O and H_2O and after nanodisc injection the system was characterised in 4MW to highlight any material that may have adsorbed to the interface. Due to a lack of time at the neutron source this was the only contrast completed for this interface.

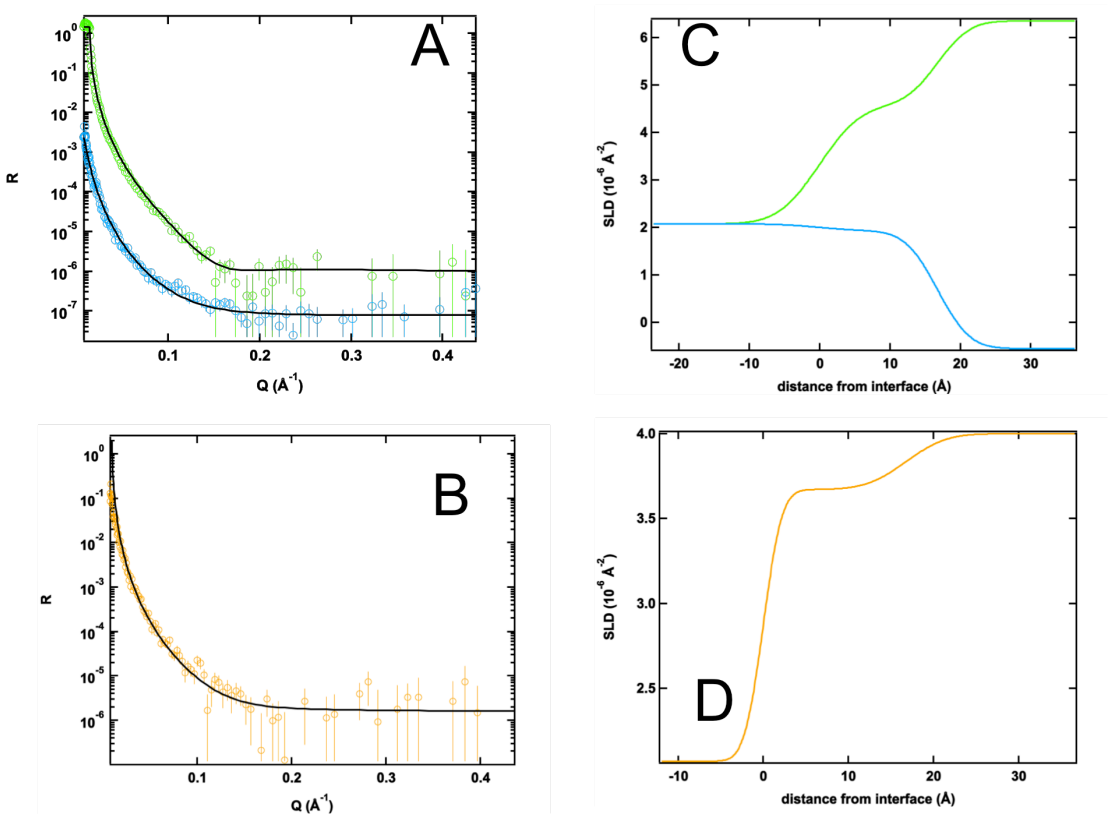

Fig 5.11- Neutron reflectometry data showing A) silicon interface before nanodisc injection in D_2O (green) and H_2O (blue), B) silicon interface after nanodisc injection in 4MW, C and D) corresponding SLD profiles for A and B respectively, same colours for solvent contrast apply.

Layer	SLD (x 10^{-6} Å^{-2})	Thickness (Å)	% Hydration	Roughness (Å)
Si	2.07	INF	-	2.3 ± 3
SiO_2	3.47	16 ± 2	38 ± 6	4.6 ± 3

Table 5.6- Structural parameters used to model reflectometry data presented in figure 5.11.

The thickness of the interfacial layer between silicon and the solvent does not change upon nanodisc injection and retains a thickness of 16 ± 2 Å. This is indicative of no nanodisc adsorption at the interface and is most likely due to electrostatic repulsion between the negatively charged

nanodiscs and the surface excess of negatively charged SiO^- groups at the silica interface at pH > 7[16]. Although this cannot be explicitly shown due to the lack of contrast experiments completed for this system. It is interesting to note that this behavior is in contrast to that seen for the MSP-nanodiscs, which have been shown to adsorb to the silicon-water interface with their bilayers parallel to the silicon plane[1]. Here large fringe minima were observed upon nanodisc adsorption. Given that no such minima were observed here, adsorption onto a bare silica substrate was not pursued further. Here the protein belt, in contrast to the polymer belt, has no net charge. It is therefore likely that increasing the charge of the surrounding belt induces electrostatic repulsion between the belt and the surface and inhibits the adsorption of the nanodsics.

5.2.2 Nanodisc adsorption on a solid supported zwitterionic lipid monolayer

Adsorption of discs on a zwitterionic lipid monolayer was then investigated in an attempt to understand the kind of electrostatic interactions seen for the air-water interface. As with the protein adsorption studies in chapter 4, nanodisc adsorption was also investigated on a zwitterionic DOPC monolayer.

5.2.3 Pre-characterisation of OTS and DOPC monolayer

The surface was characterised before and after the deposition of the DOPC vesicle solution. This yielded information for the hydrophobic OTS layer and the subsequently adsorbed DOPC monolayer. Figure 5.12 shows neutron reflectomerty data for the bare OTS layer and the formed DOPC monolayer along with the scattering length density profile, which has been labeled, to highlight individual regions of the model. Table 5.7 shows parameters used to generate this model. To save time at the neutron source the OTS layer was only characterised in D_2O and 4MW,

as these will yield the best information due to the fact that the OTS is hydrogenated. The DOPC monolayer was characterised in D_2O, 4MW and H_2O. The scattering length densities of constituent layers have been calculated as follows. SiO_2 has been calculated assuming a molecular volume of 47 $Å^3$ [4], OTS with an assumed volume of 542 $Å^3$ [17], the lipid tails with an assumed volume of 985 $Å^3$ [18] and the PC lipid head group with an assumed volume of 268 $Å^3$ [4]. These values can be found in table 4.1b in chapter 4.

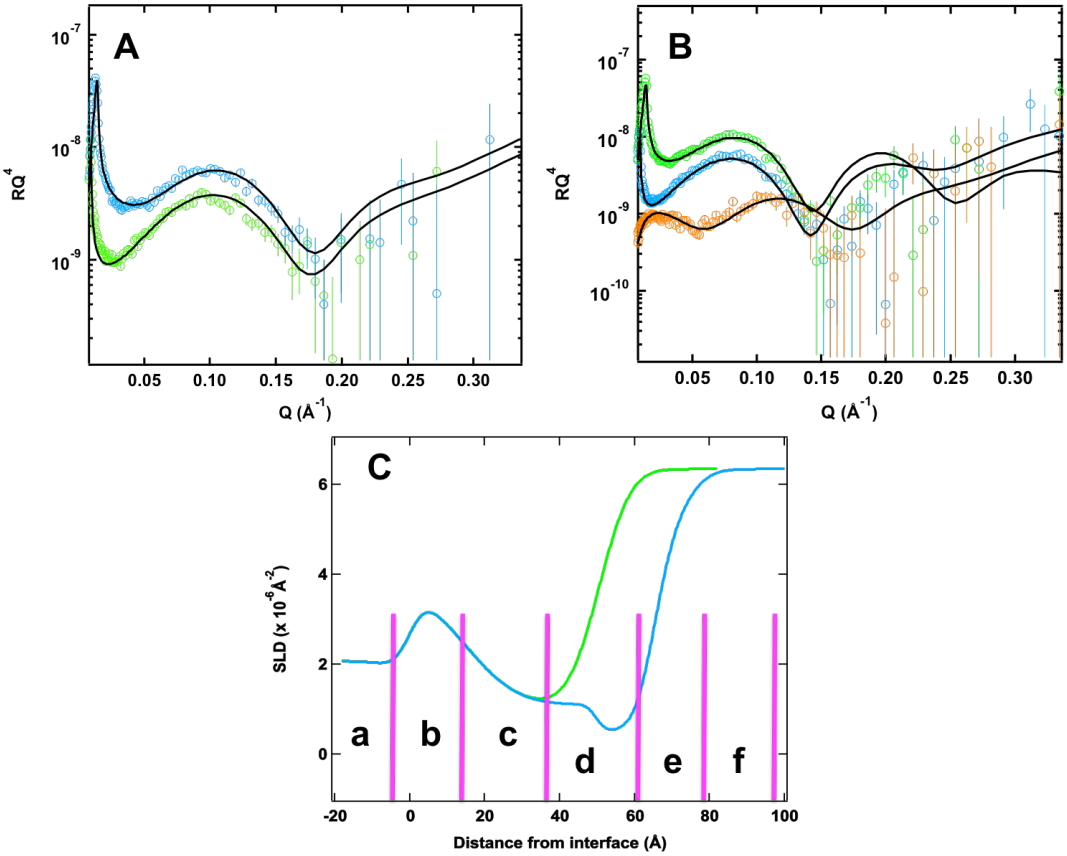

Fig 5.12- A and B) neutron refelctometry profiles for the hydrophobic OTS monolayer and the formed DOPC monolayer respectively. D_2O data is shown in blue, 4MW in green and H_2O in orange. C) scattering length density profile for the formation of the DOPC lipid monolayer in D_2O contrast. a=silicon substrate, b=SiO_2, c=OTS, d=lipid tails, e=lipid headgroups and f=solvent.

Layer	Thickness (Å)	% Hydration	Roughness (Å)
Si (a)	INF	-	2.8 ± 1
SiO_2 (b)	14.7 ± 2	20 ± 4	3.2 ± 1
OTS (c)	35.7 ± 4	20 ± 2	10.5 ± 2
Lipid Tails (d)	14.5 ± 1	10 ± 1	3 ± 1
Lipid Heads (e)	4.5 ± 1	46 ± 6	3.1 ± 1
Solvent (f)	INF	-	2.6 ± 1

Table 5.7- Parameters used to model neutron reflectometry data presented in figure 5.12. The letters in parenthesis correspond to layers shown on the SLD profile.

The modeled SiO_2 thickness and hydration are comparable to those found in the literature as discussed in chapter 4[19 20]. The thickness of the SiO_2 layer modeled here is slightly less than those found for chapter 4. This is due to variation between differing blocks used on different experiments.

The OTS layer found here is markedly different to that of the OTS layers presented in chapter 4. The thickness of 35 Å and high volume fraction of water at 20 % is indicative of a uniform layer of water present throughout the OTS layer. This is further supported by the higher modeled roughness. Here the surfactant has adsorbed in islands upon the silicon substrate with the “empty” space filled with water[21]. This has been demonstrated by AFM studies of OTS adsorption on mica[22]. In such circumstances it is therefore difficult to assess the APM value of the OTS monolayer. The OTS layer here is therefore rougher with a lower coverage at around 80 %. Although this coverage value is not as high as the values found in chapter 4 it is still possible to deposit a lipid monolayer upon this surface. Despite poor coverage the 18 carbon long tail group of the OTS monolayer still has a significant level of Van der

Waals attractive forces that allow it to create a densely packed and hydrophobic interface.

The value found for the thickness of the DOPC layer was 19 Å ± 1. This is in good agreement with the literature and the theoretical thickness of a DOPC monolayer of 18 Å[18 23-25]. This corresponds to an APM for the DOPC monolayer of 87.6 $Å^2$ mol^{-1}. This is in good agreement with literature values for DOPC monolayers which are reported at around 90 $Å^2$ mol^{-1} [23].

5.2.4 Characterising nanodisc adsorption

Having characterised the OTS and DOPC monolayer, nanodisc adsorption was studied. The first nanodisc system studied consisted of 100 % d-DMPC lipids and the protonated SMA polymer. The modeled values for the supporting layers are not reported here as they are the same as the values reported in table 5.7. The scattering length density of the nanodisc layer is also the same as used at the air-water interface.

Figure 5.13 shows raw reflectometry data for the nanodisc adsorbing to the DOPC monolayer compared to the reflectometry profile of the bare DOPC monolayer. Only the H_2O contrast is shown here.

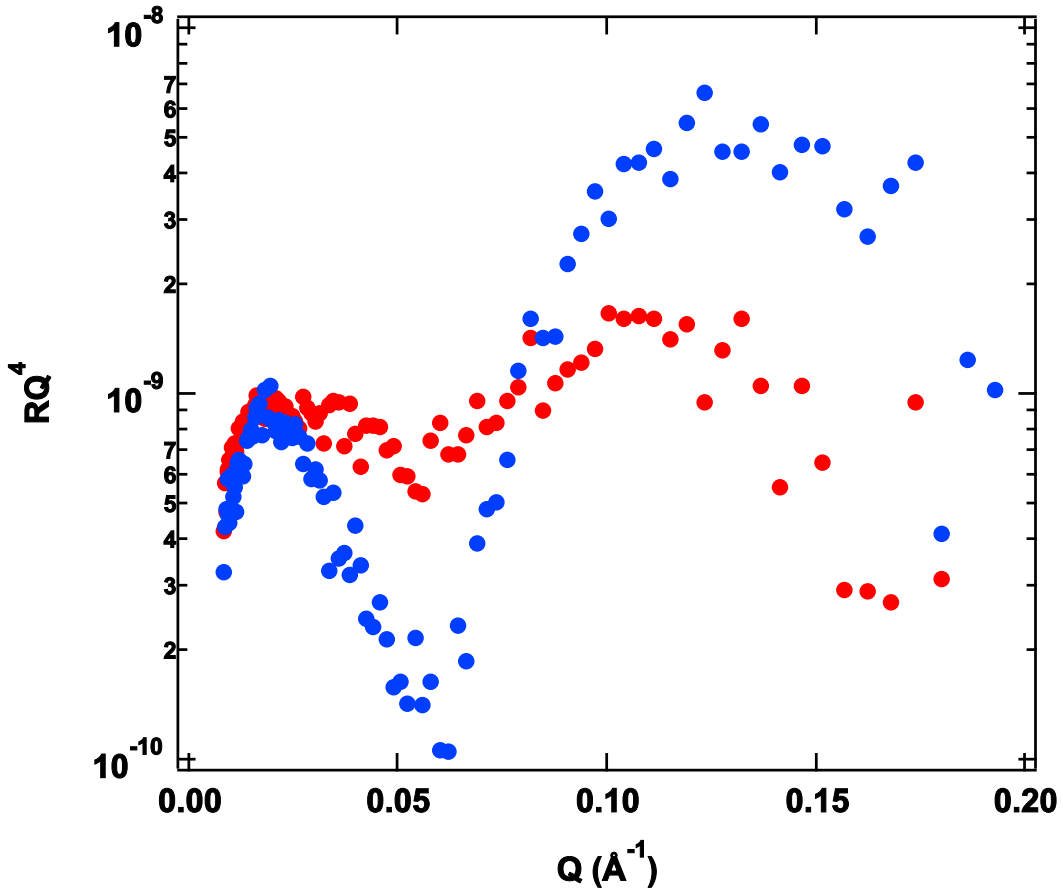

Fig 5.13- Raw reflectometry data for nanodisc adsorption to a DOPC monolayer in H_2O contrast. The red data corresponds to the bare DOPC monolayer and the blue data corresponds to the DOPC monolayer after nanodisc injection.

Of particular note here is the large fringe observed in the data. This is clear evidence of a significant change in the presence of nanodiscs and is most visible in H_2O because this has the greatest contrast with the deuterated lipids within the disc. It has been shown that for MSP-nanodiscs composed of DMPC adsorbed on a solid silicon substrate, the thickness of the nanodisc layer is equivalent to the thickness of a DMPC bilayer[1]. This has also been shown with the systems studied here at the air-water interface. Figure 5.14 shows a model calculated for the scattering length density of the nanodisc layer taken from table 5.1 and a thickness of a DMPC bilayer of 40 Å. This model has used thickness values taken from the pre-characterisation of the underlying layers which was presented in table 5.7.

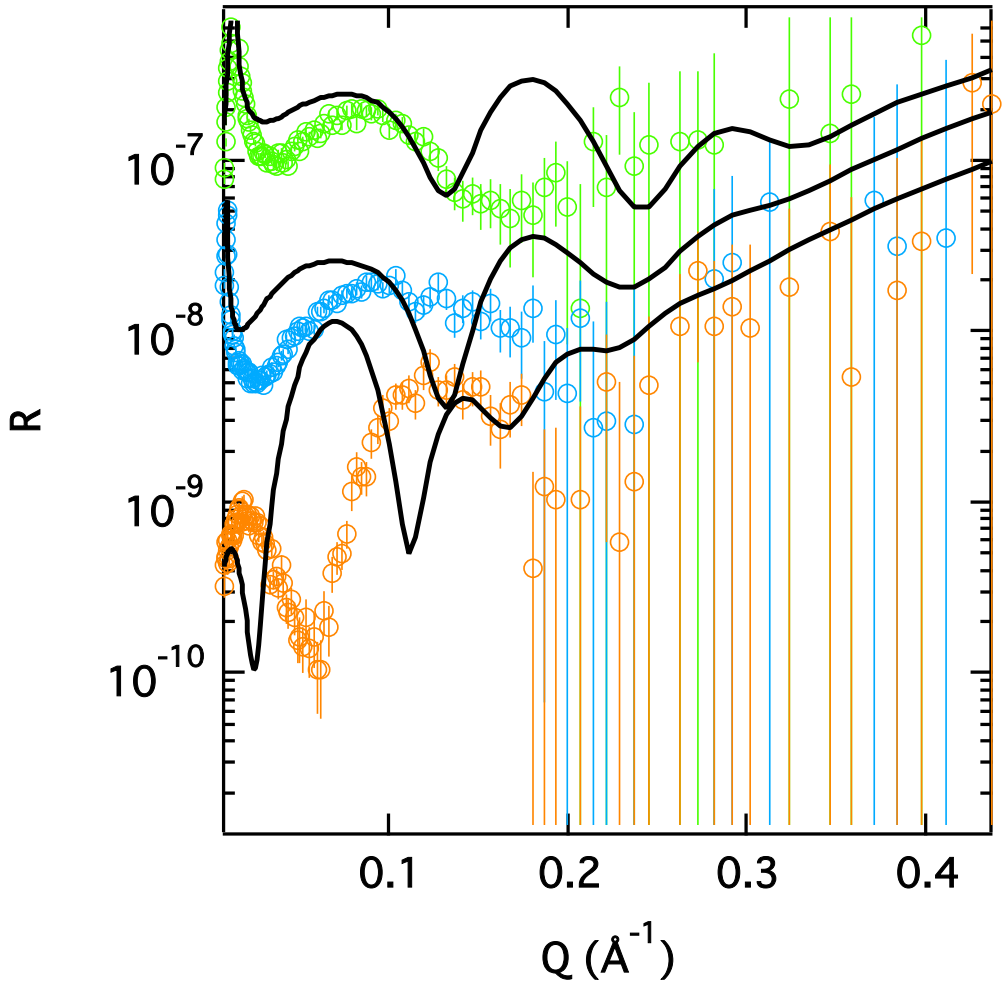

Fig 5.14- Calculated reflectivity for a 100% d-DMPC nanodisc adsorbed on a hydrogenated DOPC monolayer.

It is clear that this does not provide a good fit for the experimentally observed nanodisc adsorption data. However as with the studies at the air-water interface it is likely that lipids are exchanging from the nanodiscs into the supporting lipid monolayer.

Figure 5.15 shows modeled reflectometry data, along with a scattering length density profile, which accounts for the exchange of deuterated lipids from the nanodiscs into the supporting lipid monolayer. The values for the supporting layer are not presented here, as they are identical to those presented in table 5.7. The values used to model the disc and DOPC monlayer are shown in table 5.8.

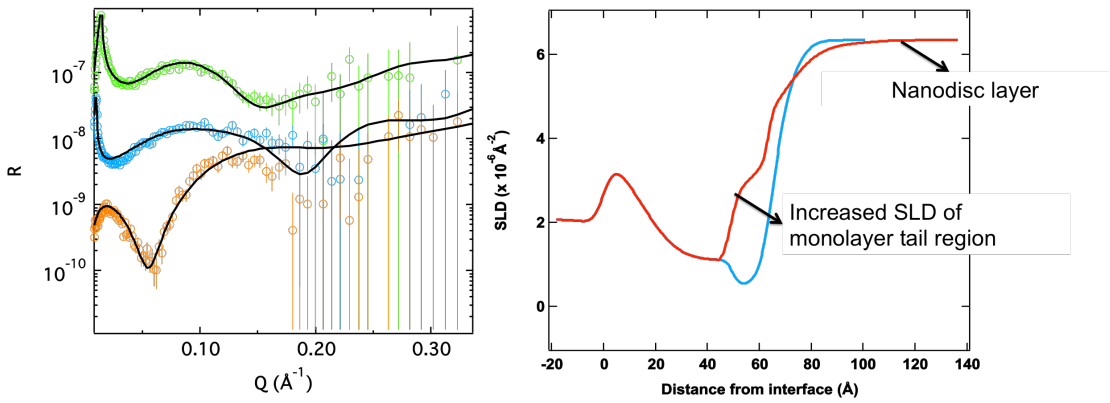

Fig 5.15- Co-refined neutron reflectometry data for a nanodisc adsorbed on a DOPC monolayer. D_2O contrast is shown in green, 4MW in blue and H_2O in orange. The black line corresponds to the model fit (left). Scattering length density profile highlighting the increase in scattering length density of the hydrogenated DOPC monolayer owing to the exchange of deuterated DMPC lipids from the nanodiscs. The original monolayer data is shown in blue, whilst the data for adsorbed nanodiscs is shown in red (right).

Layer	Thickness (Å)	SLD (x 10^{-6} Å^{-2})	Roughness (Å)	Volume fraction at interface
Lipid Tails	14.5 ± 1	2.7 ± 0.2	3.0 ± 1	-
Lipid Head group	4.5 ± 1	1.2	3.1 ± 1	-
Nanodiscs	39 ± 3	4.02 ± 0.2	11.9 ± 3	0.05 ± 0.01

Table 5.8- Summary of parameters used to model the reflectometry data presented in figure 5.15.

It is now possible to model a nanodisc layer with a thickness of 39 Å, which is in good agreement with the thickness found for DMPC lipid bilayers (40 Å) and also agrees with the thickness values found for adsorbing MSP-nanodiscs at the solid-liquid interface (39 Å) [127]. This corresponds to nanodiscs adsorbing with their bilayer parallel to the

supporting lipid monolayer. The exchange of d-DMPC into the h-DOPC monolayer is also taken into account and can be modelled by,

$$\rho_{monolayer} = (\rho_{h-DOPC} \cdot \chi_{h-DOPC}) + (\rho_{d-DMPC} \cdot \chi_{d-DMPC}) \quad \text{(equation 5.3)}.$$

Assuming that the volume fraction of polymer within the nanodiscs does not change (this is supported by TR-SANS studies of MSP-nanodiscs[12]), it is possible to calculate the volume fraction of d-DMPC within the supporting monolayer as a result of exchange from the discs. The increase in scattering length density of the tail region of the DOPC monolayer from -0.21 to 2.7 x 10^{-6} $Å^{-2}$ corresponds to a volume fraction of 0.49 and 0.51 of h-DOPC and d-DMPC respectively.

5.2.5 Probing alternative models for the adsorption of nanodiscs

To show that the model described above is unique the reflectivity can be calculated for alternative modes of nanodisc adsorption. These are summarized in figure 5.16. The alternative models consist of nanodiscs adsorbing but with no lipid exchange between the discs and the solid supporting monolayer (model 1), no nanodisc adsorption but with lipid exchange from nanodiscs in the bulk solution (model 2), nanodisc alignment with their long axis perpendicular to the interface (model 3), nanodisc alignment with a tilted conformation relative to the surface normal (model 4) and a random orientation in which there is a mixture of both tilted and parallel alignment (model 5). As with the alternative models presented in figure 5.10 for nanodisc alignment at the air-water interface, only the H_2O contrast data is shown, as it is contains the best isotopic contrast between the deuterated lipids within the nanodiscs.

Analysis of the potential models shown in figure 5.16 shows that the best fit is obtained for a single nanodisc layer adsorbed at the lipid interface with its long axis parallel to the lipid surface.

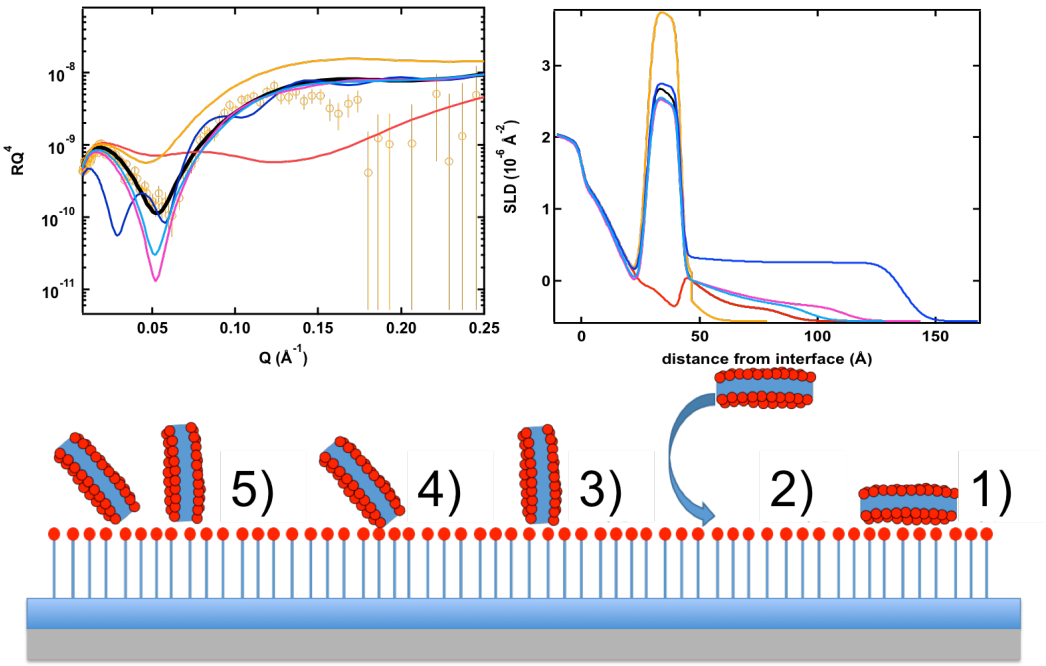

Fig 5.16- Experimentally observed neutron reflectometry data for d-DMPC nanodiscs adsorbed to a DOPC monolayer (orange circles) and the calculated reflectivity for nanodisc adsorption with no exchange (model 1, red line), no disc adsorption but lipid exchange from discs in solution (model 2, orange line), nanodisc adsorption with their long axis perpendicular to the lipid interface (model 3, dark blue line), a tilted nanodisc conformation relative to the surface normal (model 4, magenta line) and a random orientation of nanodisc adsorption consisting of both tilted and parallel alignment (model 5, light blue line). The modeled fit proposed previously is shown in black.

It is clear that when the reflectivity from a random or perpendicular orientation is calculated and compared to the experimental reflectivity data, the fit does not match. This supports the notion that the nanodiscs are aligning with their bilayer parallel to the lipid interface.

5.2.6 The effect of lipid interface

In section 5.1 it was shown that nanodisc adsorption is mediated by electrostatic interactions between the interface and the charged nanodisc. Thus in order to understand whether these effects are maintained at the solid-liquid interface, the lipid monolayer was changed to the cationic

monolayer, DODAB. Characterization through neutron reflectometry proceeded in the same manner as for the discs on the DOPC monolayer.

Figure 5.17 shows neutron reflectometry profiles for the bare OTS layer and the formed DODAB monolayer, along with the associated SLD profiles. The SLD profile has been labeled to highlight individual regions of the model. For clarity only one contrast is shown (D_2O as this has the highest contrast between the hydrogenated OTS and lipid monolayer). As with the previously discussed characterisation of the OTS and lipid monolayer, only D_2O and 4MW contrasts were measured to save time at the neutron source. Table 5.9a shows the parameters used to model the data, whilst table 5.9b shows the scattering length densities. The scattering length densities for SiO_2, OTS and DODAB were calculated as with previous sections.

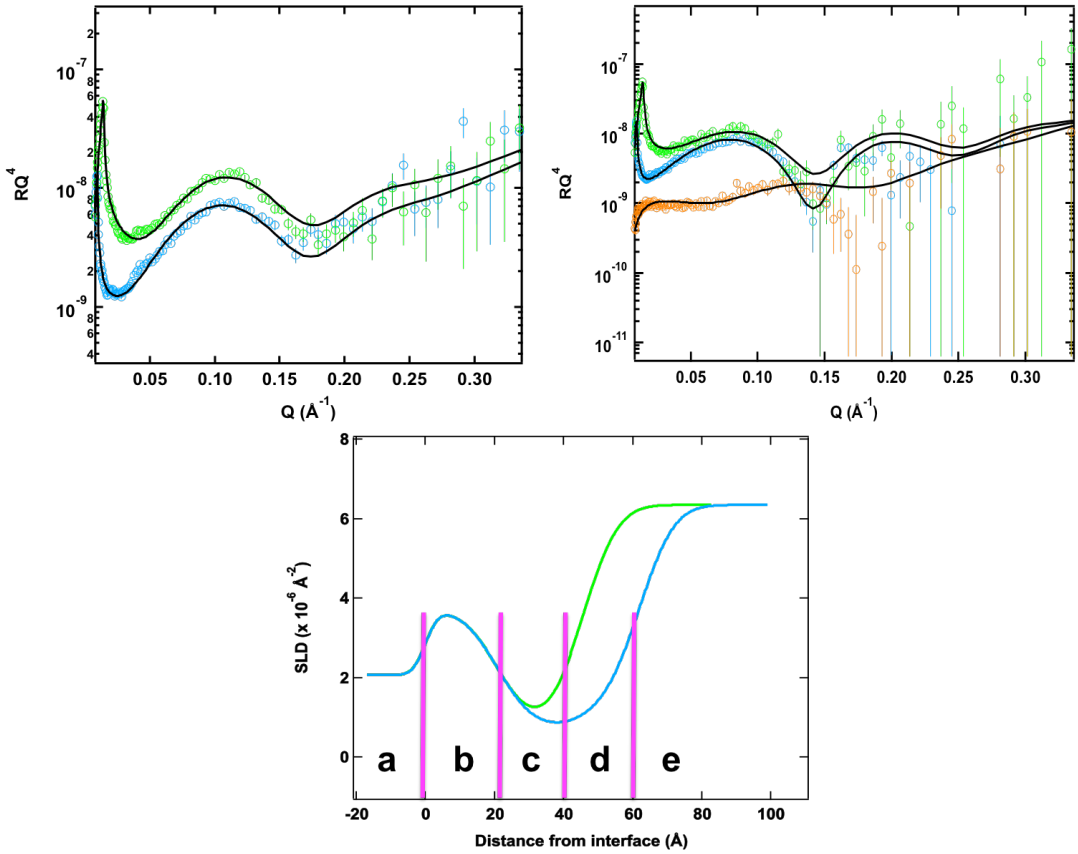

Fig 5.17- A and B) neutron refelctometry profiles for the hydrophobic OTS monolayer and the formed DODAB monolayer respectively. D_2O data is shown in green, 4MW in blue and H_2O in orange. C) scattering length density profile for the formation of the DODAB lipid monolayer in D_2O

contrast. a=silicon substrate, b=SiO_2, c=OTS, d=lipid monolayer, e=solvent.

Layer	Thickness (Å)	% Hydration	Roughness (Å)
Si (a)	INF	-	4.9 (±2)
SiO_2 (b)	20.8 (±1)	8 (±2)	3.0 (±1)
OTS (c)	24.8 (±1)	17 (±2)	8 .0(±1)
DODAB Monolayer (d)	16.3 (±1)	20 (±4)	6 (±1)
Solvent (e)	INF	-	3.7 (±2)

Table 5.9a- Parameters used to model neutron reflectometry data presented in figure 5.17. The letters in parenthesis correspond to the layers on the SLD profile.

Layer	SLD (x 10^{-6} $Å^{-2}$)
Si	2.07
SiO_2	3.47
OTS	-0.35
DODAB Monolayer	-0.32

Table 5.9b- List of scattering length densities used to model the data in figure 5.17.

The SiO_2 layer is in good agreement with thickness and hydration values reported in the literature as described previously[18 20 21]. The thickness of the hydrophobic OTS layer was modeled with a thickness of 24.8 (±1) Å. This is in good agreement with the literature where thickness values are reported at 24-28 Å. The thickness reported here corresponds to an OTS layer with an APM of 26.4 (±2) $Å^2$ mol^{-1}. Scattering studies have revealed that the cross-sectional area of hydrocarbon chains with a similar chain length are 19-21 $Å^2$ [2 24 26]. This is therefore indicative of a densely packed OTS layer with a small amount of hydration.

The DODAB layer was modelled with a thickness of 16.3 (±1) Å. This yields an APM value of 55.7 (±3) $Å^2$ mol^{-1}. These values are in good agreement with the literature where thickness values for DODAB monolayers are reported at 17-20 Å[13], whilst APM values are reported at 50-60 $Å^2$ mol^{-1} [27 28].

5.2.7 Characterising nanodisc adsorption

Once the characterisation of the OTS and DODAB monolayer was complete the nanodiscs were injected into the sample cell. As with the previously discussed system deuterated DMPC nanodiscs were used and measured in D_2O, 4MW and H_2O. Figure 5.18 shows the raw neutron reflectometry profiles in these three contrasts.

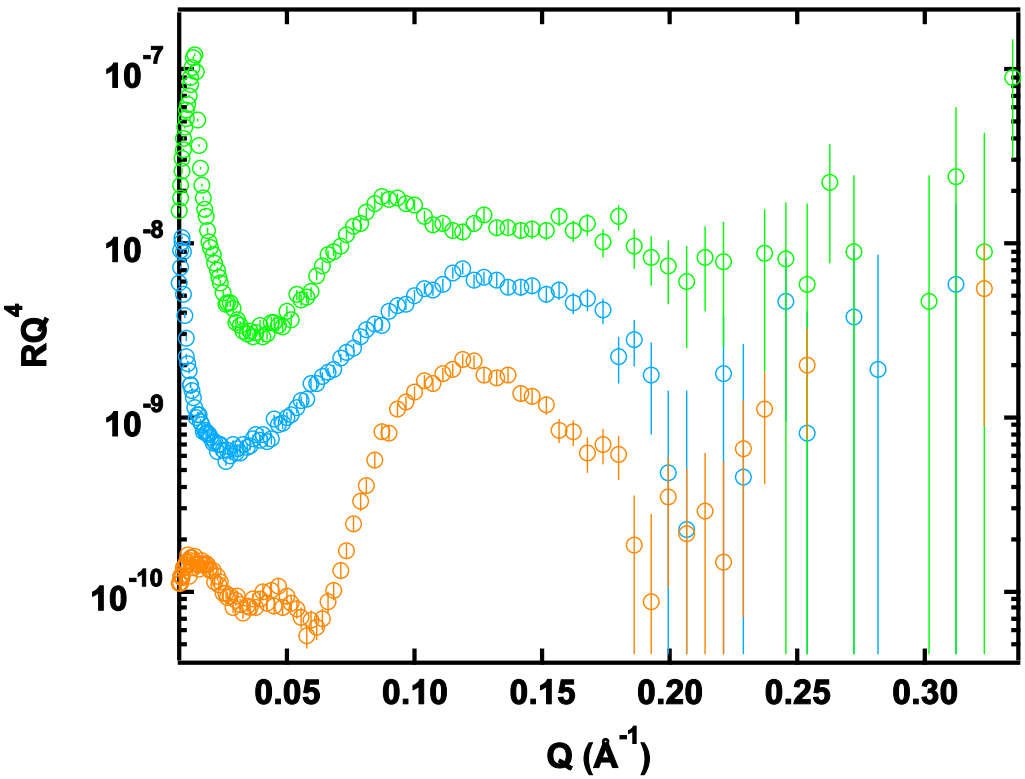

Fig 5.18- Raw neutron reflectometry data for 100 % d-DMPC nanodisc adsorption onto a DODAB lipid monolayer. D_2O contrast is shown in green, 4MW in blue and H_2O in orange.

From initial inspection of the raw data it is clear that there is a difference in the scattering data as compared to the DODAB layer with no discs (figure 5.17) or the equivalent nanodiscs on a DOPC monolayer (figure 5.15). Given that both lipid monolayers have similar thickness values it is reasonable to assume that the orientation of nanodisc adsorption may be different on a charged lipid monolayer. Figure 5.19 shows the modeled reflectometry data along with scattering length density profiles showing nanodisc adsorption. Table 5.10 shows the parameters used to model the data. The scattering length density of the lipid monolayer has been modified to account for lipid exchange as with the nanodisc system discussed in the previous section. The theoretical scattering length density of the nanodisc layer was calculated as reported in table 5.1.

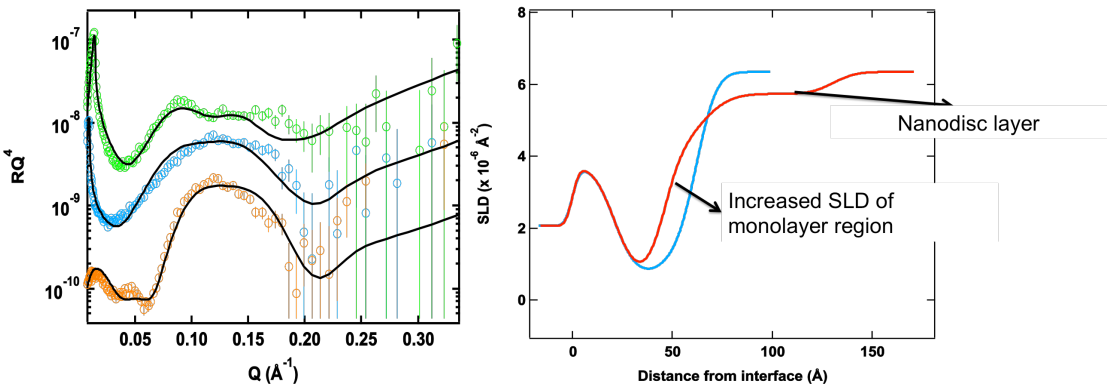

Fig 5.19- Co-refined neutron reflectometry data for a nanodisc adsorbed on a DODAB monolayer. D_2O contrast is shown in green, 4MW in blue and H_2O in orange. The black line corresponds to the model fit (left). Scattering length density profile highlighting the increase in scattering length density of the hydrogenated DODAB monolayer owing to the exchange of deuterated DMPC lipids from the nanodiscs. The original monolayer data is shown in blue, whilst the data for adsorbed nanodiscs is shown in red (right).

Layer	Thickness (Å)	SLD (x 10^{-6} $Å^{-2}$)	Roughness (Å)	Volume fraction at interface
DODAB Monolayer	16.3 (± 1)	3.4 ± 0.2	6.0 (±1)	-
Nanodiscs	83 (±5)	4 ± 0.2	12 (±3)	0.17 (±0.02)

Table 5.10- Summary of parameters used to model the reflectometry data presented in figure 5.19.

The modeled thickness of the nanodisc layer is now found at 83 (±5) Å. This is considerably thicker than the theoretical thickness of a DMPC or a DODAB bilayer and suggests that, at a positively charged interface, the nanodisc adopts a tilted conformation. If the nanodisc adsorbed with its bilayer perpendicular to the interface, it would have a theoretical thickness of 106 Å[6]. Therefore through the use of a simple geometrical argument, as outlined for surfactant monolayers in section 3.2.2, it is possible to estimate the nanodisc tilt perpendicular to the interface. This has been calculated at 31.8 ° relative to the surface normal. A large electrostatic component of nanodisc adsorption was suggested to occur for the negatively charged SiO_2 interface where no nanodisc adsorption occurred due to repulsion between the negatively charged polymer and surface. With a cationic lipid surface there is now a more favorable electrostatic interaction between the negatively charged polymer belt and DODAB headgroups. This leads to nanodisc adsorption in an end-on orientation, heavily influenced by the polymer belt interaction with the lipid head groups.

The amount of lipid exchange from the nanodiscs to the DODAB layer can also be calculated using the same methodology as in section 5.1.3. A modeled scattering length density of 3.4 x 10^{-6} $Å^{-2}$ indicates that the volume fraction of DODAB and d-DMPC within the monolayer is 0.35 and 0.65 respectively.

5.2.8 Probing alternative models for the adsorption of nanodiscs

As with the nanodiscs adsorbed upon a solid supported DOPC monolayer it is also possible to calculate the reflectivity from alternative models and compare these to the experimental reflectivity data. Figure 5.20 shows alternative models calculated for nanodisc adsorption but with no lipid exchange (model 1), no nanodisc adsorption but with lipid exchange from nanodiscs in the bulk solution (model 2), nanodisc alignment with their bilayer parallel to the interface (model 3) and a random orientation of nanodiscs in which there are both parallel and perpendicular modes of adsorption. From analysis of figure 5.20 it is clear that the bset fit is found for the nanodiscs aligned upon the DODAB monolayer with a tilted conformation.

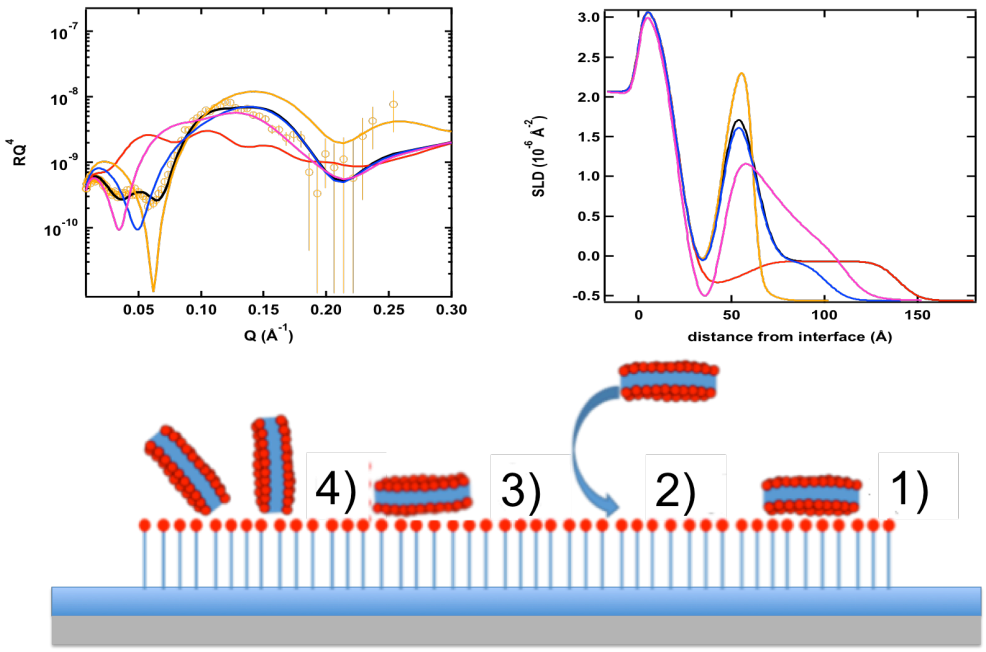

Fig 5.20- Alternative models considered for the adsorption of DMPC nanodiscs onto a solid supported DODAB monolayer. Nanodisc adsorption but with no lipid exchange (model 1, red line), no nanodisc adsorption but with lipid exchange from nanodiscs in the bulk solution (model 2, orange line), nanodisc alignment with the bilayer parallel to the interface (model 3, dark blue line) and radom mode of nanodisc adsorption consisting of both parallel and perpendicular alignment (model 4, magenta line). The experimentally observed data is shown in orange circles and the best fit is shown with a black line.

It is clear that the magnitude of lipid exchange is greater for the nanodiscs upon a positively charged lipid monolayer. This is reasonable as, once again; there is now an electrostatic component involved with lipid exchange between the nanodisc and the lipid monolayer. Lipids within the DODAB monolayer have an associated electrostatic repulsion. It is therefore energetically favorable for the lipids to exchange with a neutral PC lipid from the nanodisc to dampen electrostatic repulsions

within the monolayer. This is also coupled with an entropic gain within the system due to the mixing of lipids[2]. There is also a favorable interaction between the positively charged DODAB head groups and the negatively charged polymer belt, which is also likely to increase the magnitude of lipid exchange between the disc and supporting monolayer. Nanodisc alignment for disc adsorption on a DOPC and DODAB monolayer at the solid-liquid interface is shown schematically in figure 5.21.

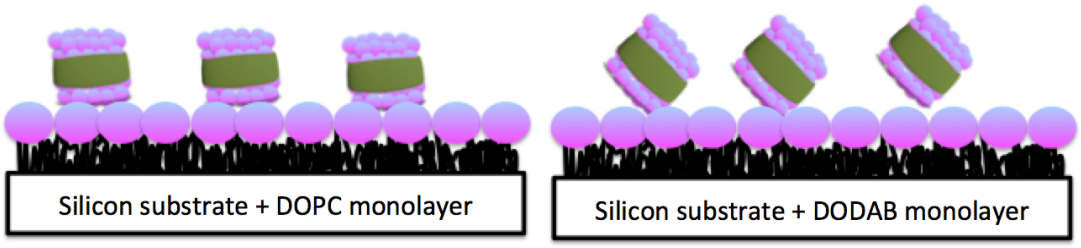

Fig 5.21- Schematic representation of nanodisc adsorption at the solid-liquid interface on a zwitterionic DOPC and cationic DODAB monolayer.

5.3 Attempts made to adsorb nanodiscs with an encapsulated membrane protein

The last section of this chapter highlights attempts made to adsorb nanodiscs containing the membrane protein ZipA to a lipid interface. The design of this experiment can be found in section 1.4 of the introduction, but the reader is reminded that the approach here is a marriage of the techniques presented in chapters 4 and 5. The idea was to adsorb a membrane protein encapsulated within a nanodisc and to use a His-tag on the outer membrane region of the protein to specifically adsorb the disc to the interface.

Experiments were conducted on D17 at the ILL reactor source in Grenoble and INTER at the ISIS spallation source in Oxford. Nanodiscs containing ZipA were injected onto DOPC lipid monolayers containing 0 mol % and 20 mol % DOGS within a bulk DOPC monolayer.

5.3.1 Pre-characterisation of OTS and lipid monolayers

As with experiments already presented above, before the nanodiscs were injected, the OTS and lipid monolayers were characterized in D_2O, H_2O and either SMW (0.38:0.62 D_2O:H_2O) or 4MW (0.66:0.34 D_2O:H_2O). Figure 5.22 shows reflectometry data for the underlying OTS, 100 mol % DOPC monolayer and the 20 %:80 % DOGS:DOPC monolayer. Again for clarity, only the SLD profile for the D_2O contrast is shown in this figure. The parameters used to model the data are shown in table 5.11a. The scattering length densities have been calculated as those in table 2.1b, chapter 4 and are shown here again in table 5.10b.

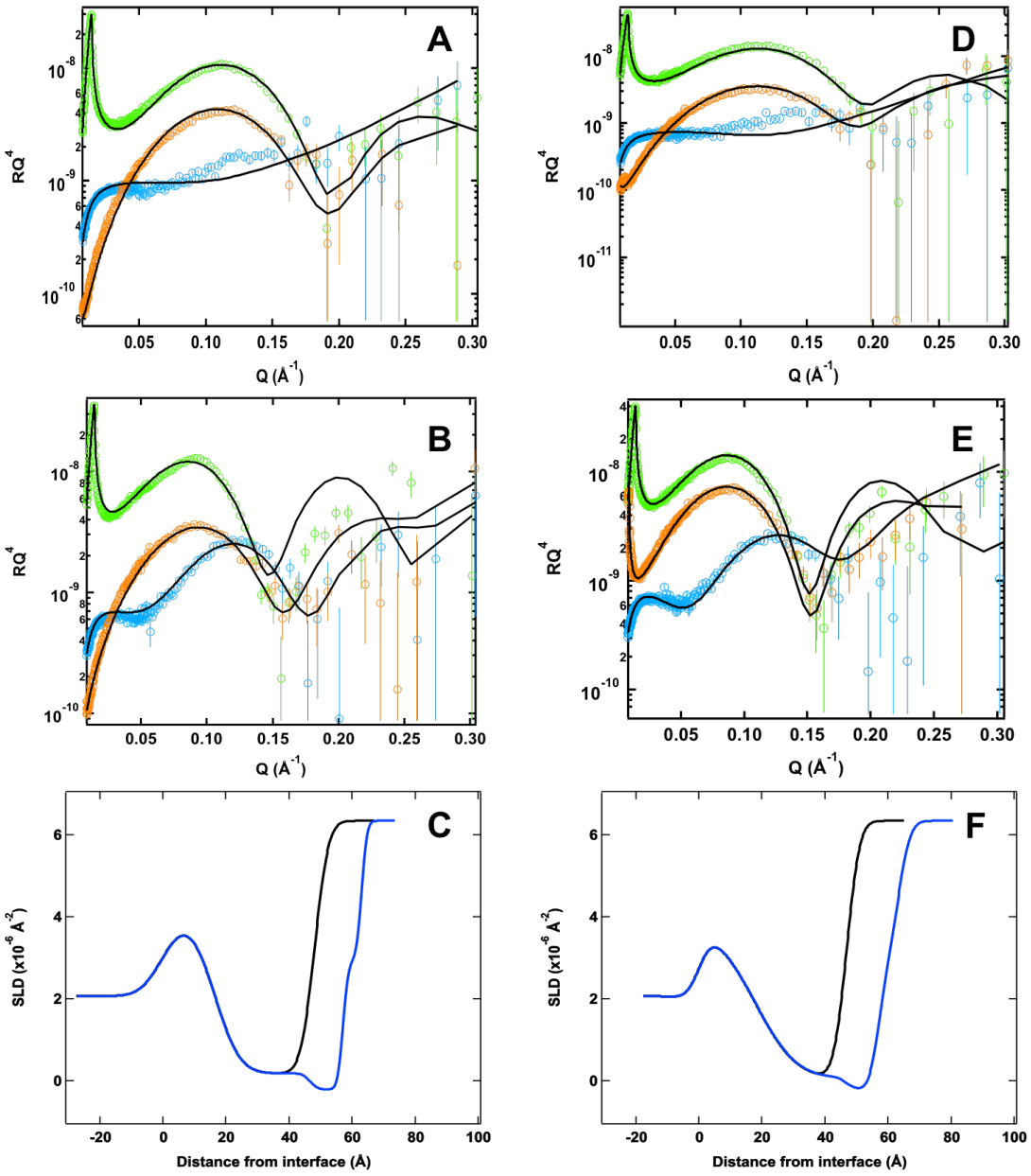

Fig 5.22- A-C) neutron reflectometry profiles for OTS (A) and DOPC monolayer (B) along with the corresponding scattering length density profile(C). D-E) neutron reflectometry profile for OTS (D), 20 mol % DOGS monolayer (E) and the corresponding scattering length density profile(F). D_2O contrast is shown in green, H_2O in blue and either SMW or 4MW in orange.

Layer	Thickness (Å)	% Hydration	Roughness (Å)
Si	INF	-	3.2 ± 1.0
SiO_2	17.8 ± 2	19 ± 10	3.2 ± 2
OTS	29 ± 1	7 ± 2	6.3 ± 4
Lipid Tails	10.5 ± 1	0	2.3 ± 0.3
Lipid Heads	6.3 ± 1	25 ± 2	2.5 ± 1.2
Solvent	-	-	3.0 ± 0.8

Table 5.11a- Summary of parameters used to model the data presented in figure 5.22.

Layer	SLD (x 10^{-6} $Å^{-2}$)
Si	2.07
SiO_2	3.47
OTS	-0.35
DOPC and DOGS Tails	-0.21
DOPC Head group	1.8
DOGS Head group	1.43

Table 5.11b- Table to show summary of scattering length densities used to model the neutron reflectometry data in figure 5.22.

The modeled SiO_2 layers are 17.8 ± 2 Å, with a percentage hydration of 19 %. This is in good agreement with the literature where values are reported between 14-22 Å in thickness and 10-30 % hydration[19 20]. The modeled thickness of the OTS layer is 29 ± 1 Å. This is in good agreement with the literature where values of 28 Å thick have been reported[25 29]. The thickness value modeled here corresponds to an APM value of 21.5 $Å^2$ mol^{-1} and is in good agreement with values found for the cross sectional area of hydrocarbon chains of the same thickness at 19-21 $Å^2$ [24 26]. This therefore corresponds to a densely packed layer of OTS

on the surface with only a small amount of hydration found within the layer[30-32].

Values for the thickness of the DOPC monolayers were modeled at 16.8 ± 1 Å. These values are in broad agreement with those found in the literature for other similarly studied systems[23 25 33]. This leads to an APM value of 75 $Å^2$ mol^{-1} which is in good agreement for phospholipid systems at this interface[18 23 34].

Figure 5.23 shows reflectometry data for the injection of nanodiscs containing the membrane protein ZipA over the 20 mol % DOGS monolayer and the DOPC monolayer. This is also plotted with the data shown in figure 5.23. Only the contrasts in D_2O have been shown, as this is likely to have the greatest contrast between the solvent and any adsorbed membrane protein discs.

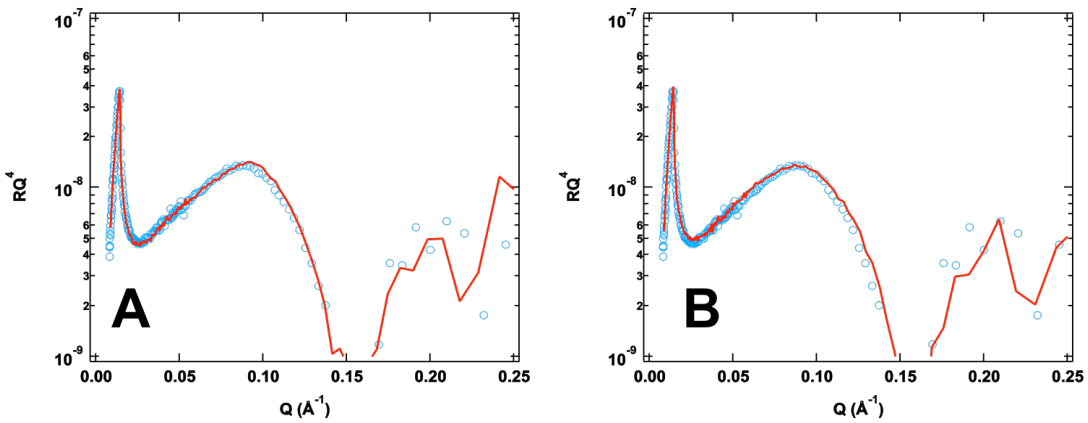

Fig 5.23- Neutron reflectometry profiles for the injection of membrane protein containing nanodiscs on a DOPC monolayer (A) and a 20 mol % DOGS monolayer (B). The blue circles represent the data shown in figure 5.17 without membrane protein present, whilst the red line corresponds to the reflectivity after nanodisc injection.

It is clear that in the presence of the membrane protein there is no change in the reflectometry profiles as compared to the DOPC monolayer alone. If the membrane protein containing nanodiscs were adsorbing to

the interface then a large fringe would be present as was observed with the adsorption of the empty nanodiscs to the lipid interface. Therefore this prompts the question as to why do empty discs adsorb to the interface and not those containing this membrane protein?

The membrane protein within the nanodisc may entropically stabilize the system. This entropic contribution may negate the need for lipids within the nanodisc to undergo such prevalent exchange mechanisms, which seem to play a large role in nanodisc adsorption. Secondly the extra-cellular region of the membrane protein, which sits outside of the nanodiscs and in solution, may cause steric hindrance. This in turn may inhibit interactions between the polymer belt and the surface or interactions between headgroups of the discs and the lipid monolayer. Any significant inhibition of these interactions may lead to a reduced adsorption of nanodiscs. However this is a very surprising result given that disc adsorption was observed for the empty discs. It was anticipated that the presence of the chelating lipid would increase the level of nanodisc adsorption due to the specific interaction between the His tag on the protein and the DOGS groups within the monolayer. This is not the case for this system. Other reasons for the lack of protein containing nanodisc adsorption may be the change in lipid composition. As highlighted in the introduction the lipid composition within these discs is analogous to the host bacteria from which they have been extracted. The protein filled nanodiscs are therefore composed of other lipid constituents such as lipopolysaccharides which may cause steric hindrance and/or dampen electrostatic interactions between the discs and the surface[35].

5.4 Concluding remarks

The interaction of polymer-stabilized nanodiscs with lipid monolayers at the air-water interface was characterized through Langmuir trough studies and neutron reflectometry. It is possible to adsorb nanodiscs on these lipid monolayers at the air-water interface. Upon adsorption a

nanodisc film is formed which corresponds to the discs aligning to the interface with their bilayer parallel to the lipid plane. There is a distinct exchange of lipids across the interface into the lipid monolayer above the nanodisc film. This is shown by a large increase in surface pressure with time and a modeled increase in the scattering length density of the lipid monolayer. This shows that the lipid monolayer is becoming enriched with deuterated phospholipids from the nanodiscs. Such lipid exchange is driven by an entropic gain for both the nanodisc and the monolayer and, in the case of a cationic monolayer, is driven by an energetic gain through the reduction of electrostatic repulsion at the interface.

At the solid-liquid interface it is clear that nanodisc films form on both zwitterionic and cationic lipid monolayers. Analogous concepts apply in terms of the exchange of lipids from the discs into the supporting lipid monolayer. One interesting result is found for the adsorption of nanodiscs upon the DODAB film where a modeled nanodisc tilt is observed. This implies that the adsorbed nanodisc lies in an “end-on” manner at this interface and not parallel to the lipid plane. This may be a difference in charge density between these two interfaces meaning that the charged polymer head group interaction becomes more apparent at the solid-liquid interface. It could also be the fact that the DODAB monolayer at the solid-liquid interface is slightly rougher than at the air-water interface. Such roughness may induce more interaction between the head group and the charged polymer belt. Either way it is clear that at the solid-liquid interface electrostatic interaction plays a key role in determining nanodisc adsorption. Polymer belt interactions with the solid support play a key role in nanodisc adsorption with a tilted conformation on the DODAB monolayer and, due to electrostatic repulsion, no nanodisc adsorption on the SiO_2 layer.

The last part of this study found that nanodiscs containing the membrane protein ZipA did not adsorb upon a phospholipid monolayer. Various arguments were made as to why this is the case in section 5.3.1. Further

work is needed to test and optimize these conditions to obtain adsorption of the protein filled discs.

It is clear that these systems show great promise in terms of delivering membrane proteins to the interface for further structural analysis using reflectometry and grazing incidence diffraction techniques. Although this particular membrane protein containing nanodisc did not adsorb there are a large number of other systems that can be tried. This will require careful design of future experiments to capitalize on all of the interactions shown here for the empty nanodiscs and a good understanding of the structure of the membrane protein nanodisc system. The work shown here for the empty nanodiscs may also have implications for drug delivery where, if the nanodiscs are to be used to this effect, knowledge of their interaction with phospholipid monolayers (a model for the cellular membrane) will be extremely valuable. Possible future experiments can be found in the concluding chapter of this thesis.

5.5 References

1. Wadsater M, Barker R, Mortensen K, et al. Effect of phospholipid composition and phase on nanodisc films at the solid-liquid interface as studied by neutron reflectivity. Langmuir 2013;**13**(29):2871-80.
2. Wadsater M, Simonsen JB, Lauridsen T, et al. Aligning nanodiscs at the air-water interface, a neutron reflectivity study. Langmuir 2011;**27**(24):15065-73.
3. Akesson A, Lind T, Ehrlich N, et al. Composition and structure of mixed phospholipid supported bilayers formed by POPC and DPPC. Soft Matter 2012;**8**:5658-65.
4. Hollinsead CM, Hanna M, Barlow DJ, et al. Neutron reflection from a dimyristoylphosphatidylcholine monolayer adsorbed on a hydrophobised silicon support. Biochimica et Biophysica Acta 2001;**1511**:49-59.
5. Fenzl W, Sigl L, Richardsen H, et al. The surface-confined structures of dimyristoylphosphatidylcholine bilayers in contact with the vesicle suspension as studied by means of X-ray reflectivity. Colloids and Surfaces A: Physicochemical and Engineering Aspects 1995;**102**(0):247-56.

6. Jamshad M, Grimard V, Idini I, et al. Structural analysis of a nanoparticle containing a lipid bilayer used for detergent free extraction of membrane proteins. Nano Research 2014.
7. Kucerka N, Kiselev MA, Balgavy P. Determination of bilayer thickness and lipid surface area in unilamellar dimyristoylphosphatidylcholine vesicles from small-angle neutron scattering curves: a comparison of evaluation methods. European Biophysics Journal with Biophysics Letters 2004;**33**(4):328-34.
8. Lund R, Willner L, Stellbrink J, et al. Logarithmic chain-exchange kinetics of diblock copolymer micelles. Physical Review Letters 2006;**96**(104):068302.
9. Lund R, Willner L, Richter D, et al. Equilibrium chain exchange kinetics of diblock co-polymer micelles: Tuning and logarithmic relaxation. Macromolecules 2006;**39**(13):4566-75.
10. Willner L, Poppe A, Allgaier J, et al. Time-resolved SANS for the determination of unimer exchange kinetics in block co-polymer micelles. Europhysics Letters 2001;**55**(5):667-73.
11. Nakano M, Fukuda M, Kudo T, et al. Determination of interbilayer and transbilayer lipid transfers by time-resolved small-angle neutron scattering. Phys Rev Lett 2007;**98**(23):238101.
12. Nakano M, Fukuda M, Kudo T, et al. Static and Dynamic Properties of Phospholipid Bilayer Nanodiscs. Journal of the American Chemical Society 2009;**131**(23):8308-12.
13. Dabkowska A, Barlow DJ, Campbell RA, et al. Effect of helper lipids on the interaction of DNA with cationic lipid monolayers studied by specular neutron reflection. Biomacromolecules 2012;**13**(8):2391-401.
14. Kahn JG, Monroy F, Mingotaud C. Adsorption of large inorganic polyanions under a charged Langmuir monolayer: an ellipsometric study. Physical Chemistry Chemical Physics 2003;**5**(2648-2652).
15. Nagle JF, Tristram-Nagle S. Structure of lipid bilayers. Biochimica et Biophysica Acta 2000;**1469**:159-95.
16. Behrens SV, Borkovec M. Electrostatic interaction of colloidal surfaces with variable charge. Jorurnal of physical chemistry B 1999;**103**(15):2918-28.
17. Fragneto G, Thomas RK, Rennie AR, et al. Neutron reflection study of bovine B-casein adsorbed on OTS self-assembled monolayers. Science 1995;**267**:657-60.
18. Wacklin HP, Tiberg F, Fragneto G, et al. Phospholipase A2 hydrolysis of supported phospholipid bilayers: A neutron reflectivity and ellipsometry study. Biochemistry 2005;**44**:2811-21.
19. Fragneto G, Li XZ, Thomas RK, et al. A neutron reflectivity study of the adsorption of aerosol-OT on self-assembled monolayers on silicon. Journal of colloid and interface science 1996;**178**:531-37.
20. Dura JA, Richter CF, Majkrzak CF, et al. Neutron reflectometry, x-ray reflectometry and spectroscopic ellipsometric characterisation of thin SiO2 on Si. Applied physics letters 1998;**73**:2131.

21. Fragneto G, Lu JR, McDermott DC, et al. Structure of monolayers adsorbed on self-assembled monolayers on silicon: A neutron reflectivity study. Langmuir 1996;**12**:477-86.
22. Nakagawa T, Ogawa K. Atomic force microscope images of monolayers from alkyltrichlorosilane on mica surfaces and studies on an anchoring mechanism of alkyltrichlorosilane molecules to the surface. Langmuir 1994;**10**:525-29.
23. Wacklin HP, Tiberg F, Thomas RK. Formation of supported phospholipid bilayers via co-adsorption with B-D-dodecyl maltoside. Biochimica et Biophysica Acta 2005;**1668**:17-24.
24. Vankin D. Structure-function relations in self-assembled C18- and C20-sphingosines monolayers at gas/water interfaces. Journal of the American Chemical Society 2003;**125**:1313-18.
25. Miller CE, Majewski J, Gog T, et al. Characterisation of thin films at the solid-liquid interface by x-ray reflectivity. Physical Review Letters 2005;**97**:238104-1-04-4.
26. Rand RP, Chapman DL, Larsson K. Titled hydrocarbon chains of dipalmitoyl lecithin become perpendicular to the bilayer before melting. Biophysical Journal 1975;**15**:1117-25.
27. Tveten EG. X-ray and neutron reflectivity studies of nanodiscs below the air-water interface. University of Copenhagen, 2011.
28. Cardenas M, Nylander T, Jonsson B, et al. The interaction between DNA and cationic lipid films at the air-water interface. Journal of colloid and interface science 2005;**186**:166-75.
29. Hines JD, Fragneto G, Thomas RK, et al. Neutron reflection from mixtures of sodium dodecyl sulfate and dodecyl betaine adsorbed at the hydrophobic solid/aqueous interface. Journal of colloid and interface science 1997;**189**:259-67.
30. DePalma V, Tillman N. Friction and wear of self-assembled trichlorosilane monolayer films on silicon. Langmuir 1989;**5**:868-72.
31. Opila RL, Legrange JD, Markham JL, et al. Effects of surface hydration on the deposition of silane monolayers on silica optical fiber. Journal of adhesion science and technology 1997;**11**(1):1-10.
32. Wasserman SR, Whitesides GM, Tidswell IM, et al. The structure of self-assembled alkylsiloxanes on silicon: A comparison of results from ellipsometry and low-angle x-ray reflectivity. Jorunal of the ameican chemical society 1989;**11**:5852-61.
33. Vaknin D, Kjaer K, Als-Nielsen J, et al. Structural properties of phosphatidylcholine in a monolayer at the air/water interface. Biophysical Journal 1991;**59**(1325-1332).
34. Koenig BW, Krueger S, Orts WJ, et al. Neutron reflectivity and atomic force microscopy studies of a lipid bilayer in water adsrobed to the surface of a silicon single crystal. Langmuir 1996;**12**:1343-50.
35. Schumann RR, Leong SR, Flaggs GW, et al. Structure and function of lipopolysaccharide binding protein. Science 1990;**249**:1429-31.

Chapter 6- Future Work

Overall work presented in the previous chapters has focused on surface scattering from soft matter at interfaces. Initially x-ray and neutron reflectometry was used to assess the behavior of sulfobetaine Langmuir monolayers and this was supported by data obtained through Langmuir isotherm measurements. Chapters 4.0 and 5.0 discussed the alignment of soluble proteins on functionalized phospholipid monolayers and attempts made to transfer this system to insoluble membrane proteins through the use of nanodiscs.

Although these are two separate bodies of work in their own right, there are distinct areas of overlap that may be pursued in future studies. The projects described here were largely of an exploratory nature and therefore require supporting data from future work to optimize these systems. The characterization of sulfobetaine monolayers has not been reported in the literature, whilst fundamental studies involving protein and polymer-stabilised nanodisc alignment using neutron reflectometry is also entirely novel. The following sections therefore describe future experiments that may be conducted for these systems.

6.1 Sulfobetaine surfactants

Work conducted as part of this thesis has highlighted the importance of Van der Waals interactions in driving the phase transition of a Langmuir monolayer from the liquid expanded phase through to the liquid condensed phase. With just a single tail, and therefore limited Van der Waals interactions, sulfobetaine surfactants remain in one phase throughout lateral compression. Addition of a second hydrocarbon tail promotes increased Van der Waals interactions allowing the surfactant to undergo the first order phase transition into the liquid condensed phase.

The interaction of salt with the surfactant head group has also been probed through Langmuir trough and XRR/NR techniques. This work is suggestive of the formation of a diffuse ion layer beneath the surfactant head group with no significant ion penetration into the head group region. The one case where significant ion penetration was observed was for the di-chain sulfobetaine surfactant upon a 50 mM $NaClO_4$ sub-phase. Here the scattering deviated by a large amount from scattering on pure water or other salt sub-phases (NaCl and $CaCl_2$). The proposed model involves an entire perchlorate anion penetrating into the head group region of the surfactant, giving an increased electron density at the interface. This has also been backed up with Langmuir trough experiments where an increased APM value is observed at a fixed surface pressure and also BAM where a differing nucleation of LC domains is observed on a perchlorate sub-phase.

From a fundamental perspective it would be useful to perform differential scanning calorimetry (DSC) studies of the sulfobetaine surfactants, in particular the double tailed species. This would provide an additional tool in characterizing the phase behavior of these species. Gaining DSC data in the presence and absence of salt ($NaClO_4$) in particular would give more insight into the effects of these salts on phase behavior.

Gaining a deeper understanding of the interaction of salt with the sulfobetaine head group is important for elucidating mechanisms of biocompatibility and utilizing the surfactants to their full potential in industrial formulations. Whilst this has been achieved at the air-water interface it would be interesting to probe these interactions in solution. This could be achieved by forming vesicles of the single and double tailed species through sonication in an aqueous medium. The structure of the vesicles with and without salt could then be probed through DLS and SAXS/SANS. These vesicles may also show promise as drug delivery systems where hydrophobic molecules could be encapsulated within the core of the structure.

From a more applied perspective, one of the key uses of sulfobetaines is for biocompatible films. The inclusion of other molecules within the sulfobetaine monolayer may enhance their biocompatibility. Of particular interest here would be to incorporate varying amounts of phospholipids within the surfactant monolayer and characterize structure using the techniques shown in this thesis. This would also be of interest from a fundamental point of view, as the monolayer would be composed of a mixture of lipids with opposite charge distributions within the head group. This may result in interesting head group conformations at the interface. Sulfobetaines have also been shown to spontaneously form biocompatible films at the air-water interface through the interaction of polymeric materials and co-surfactants[1]. However little is understood with regard to the fundamental polymer surfactant interactions. It would therefore be of interest to probe sulfobetaine-polymer interactions to highlight the mechanistic details of such film formation.

There are a range of novel sulfobetaine structures that could be synthesized. Of particular interest would be the development of highly branched tail groups bound to the sulfobetaine head group as these kinds of compounds have shown great promise as low surface energy materials[2]. Also one other structural analogue is to phenylate the tail group or synthesize a surfactant with an unsaturated tail group. This would be interesting as these kinds of surfactants would enhance the fluidic nature of the film, which has been shown to be of importance for gene/DNA transfection and/or protein alignment at the interface in the case of phospholipids[3 4].

Polymers grafted with sulfobetaine moieties have been shown as promising candidates for gene transfection[5]. It would therefore be of interest to functionalise these monolayers with DOGS containing lipids in an attempt to two-dimensionally align proteins at the air-water and solid-liquid interface. The liquid expanded nature of the single tailed sulfobetaine surfactants may also make them suitable for the formation of nanodiscs. Future experiments may involve attempting to form nanodiscs

with these surfactants or as mixtures with phospholipids. This may impart differing characteristics upon nanodisc behavior.

6.2 Protein interactions with functionalized phospholipid monolayers

It has been demonstrated that it is possible to specifically align the protein, penicillin binding protein 3 upon a vesicle surface, monolayers at the air-water interface and solid-liquid interface. Recruitment of the protein to the lipid interface has been achieved through functionalizing the phospholipid surface with varying molar percentages of the His-tag chelating lipid, DOGS. The work conducted here is suggestive of monolayer coverage for the vesicle system, whilst increasing the molar percentage of DOGS within the vesicle eventually leads to non-specific, multi-layer protein adsorption.

For lipid monolayers at the air-water interface it has been qualitatively shown that as the concentration of the chelating lipid within the monolayer increases so too does the surface concentration of the protein. For monolayers with lower molar fractions of DOGS (5 and 10 mol %) BAM results are suggestive of initial formation of small patches, which coalesce with time. Increasing the molar concentration of the chelating lipid within the monolayer (20 mol %), however appears to form large protein aggregate at the lipid interface.

Combining NR and QCM techniques has been a powerful tool to characterize protein adsorption at the solid-liquid interface. QCM is able to give insight into mechanistic detail of protein adsorption, whilst NR is able to provide the structural characterization of adsorbed layers. QCM is suggestive of two key stages of protein adsorption. The first stage whereby protein is recruited to the membrane via the specific interaction with the His-tag chelating lipid and subsequently through non-specific

adsorption. NR was able to confirm the adsorption of two protein layers by rationalizing structural parameters obtained from the model with the lattice parameters of the protein.

In terms of protein alignment at the interface there are a range of other chelating lipids that could be used to specifically order a protein layer. These include lipids with a copper functionalized head group, also capable of binding His-tags and the streptavidin-biotin system[6 7].

Another interesting study that may result as a product of the work presented here would be to use the two-dimensional alignment of a soluble protein at the solid-liquid interface as a seed for proteins that are tricky to crystallise. This could be completed by forming a two-dimensional array of protein at the lipid interface, and subsequently injecting a protein solution into the sample cell. It would be interesting to see if this would then promote/invoke three-dimensional crystallization. Equally a two-dimensional protein array could also be formed at the air-liquid interface and subsequently dipped by use of the Langmuir-Blodgett technique.

6.3- Nanodisc interactions with lipid monolayers

This work has shown that it is possible to adsorb polymer-stabilised nanodiscs upon lipid monolayers at both the air-water and the solid-liquid interface. At the air-water interface nanodiscs composed of phosphocholine and phosphoglycerol based phospholipids form nanodisc layers that are 39 Å thick, which is in excellent agreement for bilayers composed of these phospholipids. This corresponds to the nanodisc adsorbing to the interface with its bilayer perpendicular to the lipid monolayer.

At the solid-liquid interface the NR data is suggestive of nanodisc interaction being heavily mediated by polymer surface interactions. When

the nanodisc is injected onto an SiO_2 surface, which will be negatively charged due to a surface excess of SiO^- groups, no nanodisc adsorption occurs. Such lack of adsorption is likely to be a result of electrostatic repulsion between the negatively charged polymer belt and the surface. Upon a positively charged DODAB monolayer the modeled data is suggestive of the nanodisc tilting with respect to the surface normal. This is again rationalized by significant interaction between the negatively charged polymer belt and the positively charged lipid head groups.

Once adsorbed the modeled NR data is suggestive of dynamic lipid exchange between the nanodiscs and the lipid monolayer. The data shown in this work is suggestive of the lipid monolayer becoming enriched in phospholipids as a result of exchange from the nanodiscs. This is driven by an entropic gain of the nanodisc system by the release of well-ordered lipid molecules from the disc. When a positively charged monolayer is present lipid exchange is more prevalent due to the energetic component involved in such lipid exchange. The enrichment of the positively charged monolayer with zwitterionic lipids from the nanodiscs will act to dampen electrostatic repulsion within the monolayer.

When a membrane protein is encapsulated within the nanodisc and attempts were made to specifically adsorb these species at the lipid interface, no protein-nanodisc adsorption was observed. This may be due to steric hindrance caused by the presence of the large extracellular region of the membrane protein inhibiting electrostatic interactions between the disc and the surface and specific interactions between the protein his-tag and the DOGS sites within the lipid monolayer.

In terms of alignment at the interface the nanodiscs show promise as systems to find novel ways of studying membrane protein structure. Despite the lack of adsorption shown here there are a number of other membrane protein-nanodisc systmes that could be tried. In particular the membrane protein, PagP,w hich has been successfully incorporated into an SMA-nanodisc[8]. This would be an attractive target for future studies.

The adsorption of nanodiscs may have consequences for biosensing if protein-nanodiscs are ever adsorbed in two-dimensions at the lipid interface.

From a fundamental perspective it would be interesting to conduct kinetic measurements on the nanodiscs. This would involve an analogous experimental set-up as shown in this thesis, however snap shots in the reflectometry would be taken in order to track lipid exchange as a function of time. By using the Arhenius equation it would then be possible to extract thermodynamic properties of lipid exchange at these interfaces. Temperature would also have to be varied in order to extract this information. One interesting point would be to assess if lipid exchange truly was quicker at the interface as opposed to in solution[9].

6.4 Concluding Remarks

Overall this thesis has demonstrated the power of surface scattering techniques to study soft matter at interfaces. For the Langmuir monolayer studies, the combination of x-ray and neutron reflectometry enables the user to pin down a more accurate model to describe the structure of the insoluble film. When coupled with Langmuir trough data the user can objectively constrain the parameters of the modeled fit to realistic and physically relevant parameters.

Neutron reflecometry has also been shown as a powerful technique to assess the interaction of protein at the interface and has been coupled with other surface sensitive techniques, such as QCM, to gain insight into the kinetics of adsorption.

6.5 References

1. Holdaway JA. A study of the structure and formation of biocompatible mesostructured polymer-surfactant hydrogel films. University of Bath, 2014.
2. Alexander S, Smith GN, James C, et al. Low-surface energy surfactants with branched hydrocarbon architectures. Langmuir 2014;**30**(12):3412-21.
3. Ainalem M, Kristen N, Edler KJ, et al. DNA binding to zwitterionic model membranes. Langmuir 2010;**26**(7).
4. Bischler N, Balavonie F, Milkereit P, et al. Specific interaction and two-dimensional crystallisation of histidine tagged yeast RNA polymerase I on nickel chelating lipids. Biophysical Journal 1998;**74**:1522-32.
5. F D, Liu W. Enhanced gene transfection and serum stability of polyplexes by PDMAEMA-polysulfobetaine diblock copolymers. Biomaterials 2011;**32**(2):628-38.
6. Weber PC, Ohlendorf DH, Wendoloski JJ, et al. Structural origing of high-affinity biotin binding to streptavidin. Science 1989;**243**(4887):85-88.
7. Chikh GG, Li WM, Schutze-Redelmeier M-P, et al. Attaching histidine-tagged peptides and proteins to lipid-based carriers through use of metal-ion-chelating lipids. Biochimica et Biophysica Acta (BBA) - Biomembranes 2002;**1567**(0):204-12.
8. Long AR, O'Brien CC, Malhorta K, et al. A detergent-free strategy for the reconstitution of active enzyme complexes from native biological membranes into nanoscale discs. BMC Biotechnology 2013;**13**(41):6750-63.
9. Nakano M, Fukuda M, Kudo T, et al. Static and Dynamic Properties of Phospholipid Bilayer Nanodiscs. Journal of the American Chemical Society 2009;**131**(23):8308-12.

7.0 Appendix

7.1 Sulfobetaine Physical Data

SB3-18-2 (recrystallized from acetone and methanol)

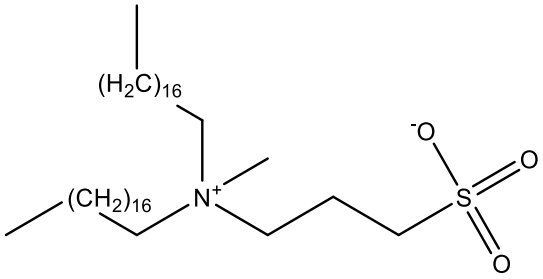

dH (300 MHz, CH_3OD): 0.89 (6H, t, -$(CH_2)_{16}$-$C\underline{H_3}$) 1.26 (64H, m, -$(C\underline{H_2})_{16}$-) 1.69 (4H, m, N^+-$C\underline{H_2}$-$(CH_2)_{16}$-) 2.26 (2H, m, O_3S^--CH_2-$C\underline{H_2}$-) 2.98 (2H, t, O_3S^--$C\underline{H_2}$-) 3.24 (3H, m, N^+-$C\underline{H_3}$) 3.76 (2H, m, SO_3^--CH_2-CH_2-$C\underline{H_2}$-)

3.15 = Methanol, 2.68 = acetone

ν_{max} (film): 2954, 2916, 2872, 2850, 1655, 1483, 1471, 1249, 1204, 1189, 1178, 1038, 717, 608

SB3-20 (recrystallized from acetone and methanol)

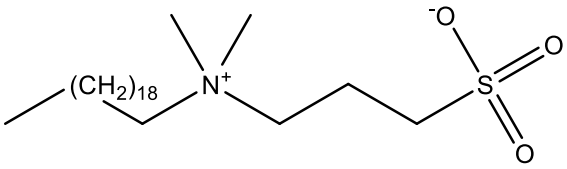

dH (300 MHz, CH_3OD): 0.89 (3H, t, -$(CH_2)_{18}$-$C\underline{H_3}$) 1.29 (36H, m, -$(C\underline{H_2})_{18}$-) 1.78 (2H, m, N^+-CH_2-$(CH_2)_{18}$-) 2.18 (2H, tt, SO_3^--CH_2-$C\underline{H_2}$-) 2.87 (2H, t, SO_3^--$C\underline{H_2}$-) 3.08 (6H, s, N^+-$C\underline{H_3}$) 3.49 (2H, m, SO_3^--CH_2-CH_2-$C\underline{H_2}$-)

3.31 = Methanol

ν_{max} (film): 3039, 2959, 2918, 2851, 1468, 1240, 1227, 1215, 1196, 1183, 1139, 1123, 1039, 1030, 752, 719

SB3-22 (recrystallized from acetone and methanol)

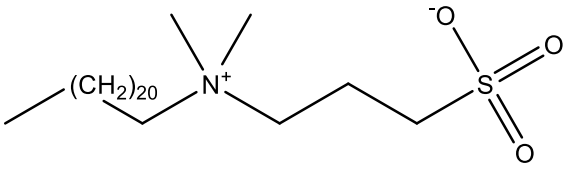

dH (300 MHz, CH_3OD): 0.90 (3H, t, -$(CH_2)_{20}$-CH_3) 1.29 (40H, m, -$(CH_2)_{20}$-) 1.77 (2H, m, N^+-CH_2-$(CH_2)_{20}$-) 2.18 (2H, tt, SO_3^--CH_2-CH_2-) 2.87 (2H, t, SO_3^--CH_2-) 3.08 (6H, s, N^+-CH_3) 3.50 (2H, m, SO_3^--CH_2-CH_2-CH_2-)

3.30 = Methanol

ν_{max} (film): 3039, 2959, 2918, 2851, 1468, 1412, 1317, 1229, 1197, 1182, 1169, 1139, 1123, 1038, 999, 984, 966, 753, 719

SB4-18 (recrystallized from acetone and methanol)

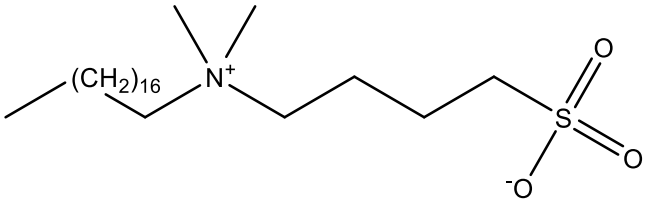

dH (300 MHz, CH_3OD): 0.90 (3H, t, -$(CH_2)_{16}$-CH_3) 1.26 (32H, m, -$(CH_2)_{16}$-)

3.31 = Methanol

ν_{max} (film): 3034, 2917, 2850, 1018, 1491, 1471, 1223, 1200, 1182, 1152, 1063, 1037, 720, 607

^{1}H-NMR Spectra

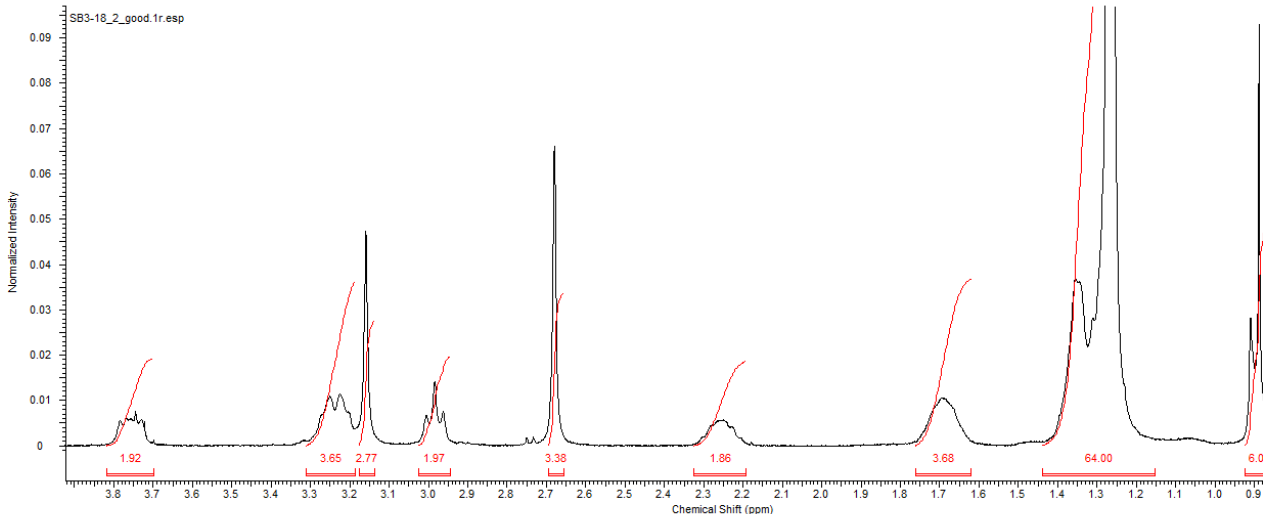

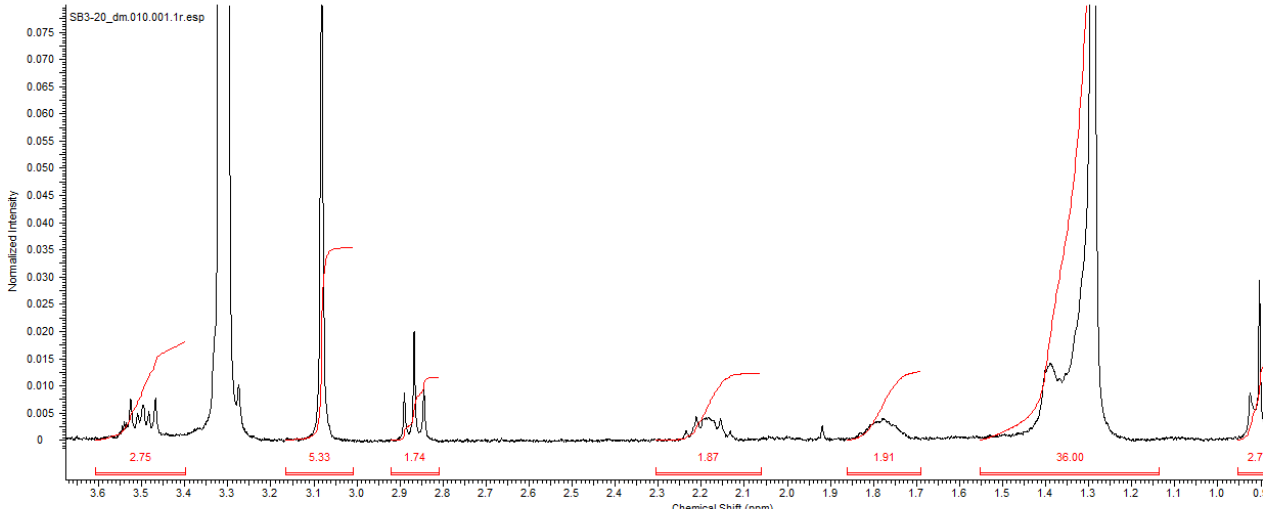

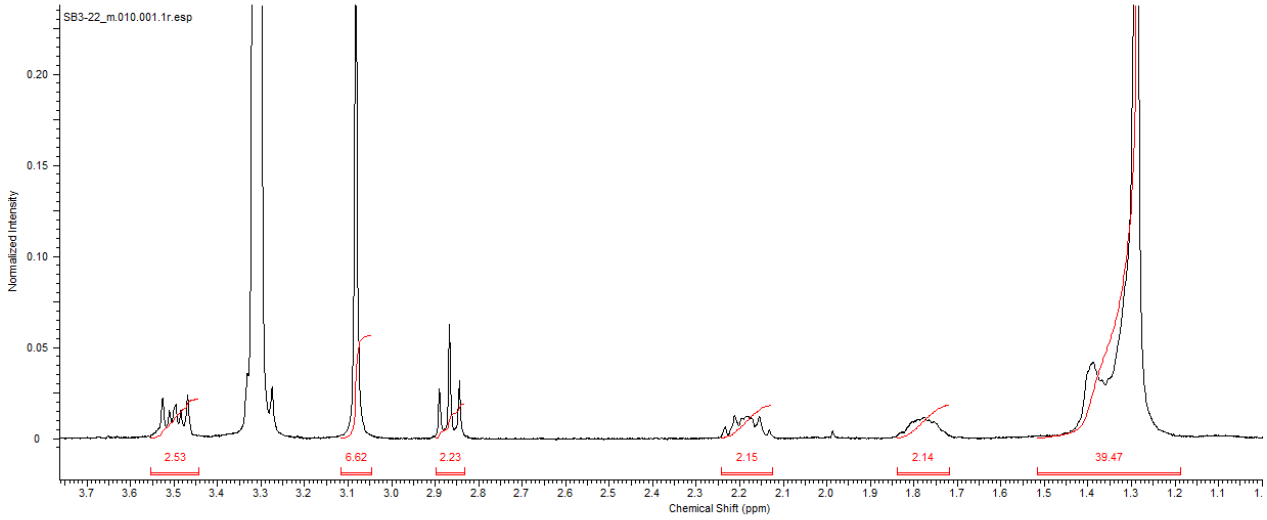
SB3-22_m.010.001.1r.esp
Normalized Intensity
0.20
0.15
0.10
0.05
0
2.53
6.62
2.23
2.15
2.14
39.47
Chemical Shift (ppm)

IR Spectra

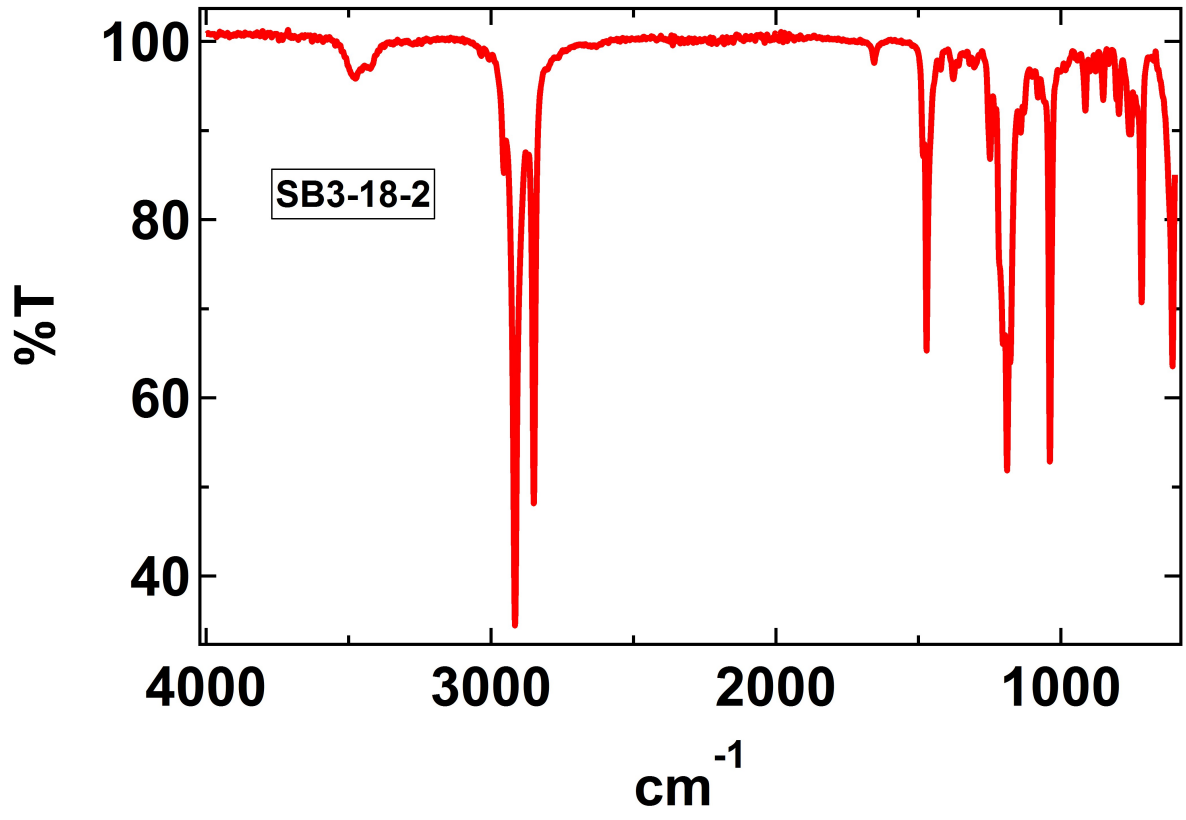
100
80
60
40
%T
SB3-18-2
4000
3000
2000
1000
cm-1

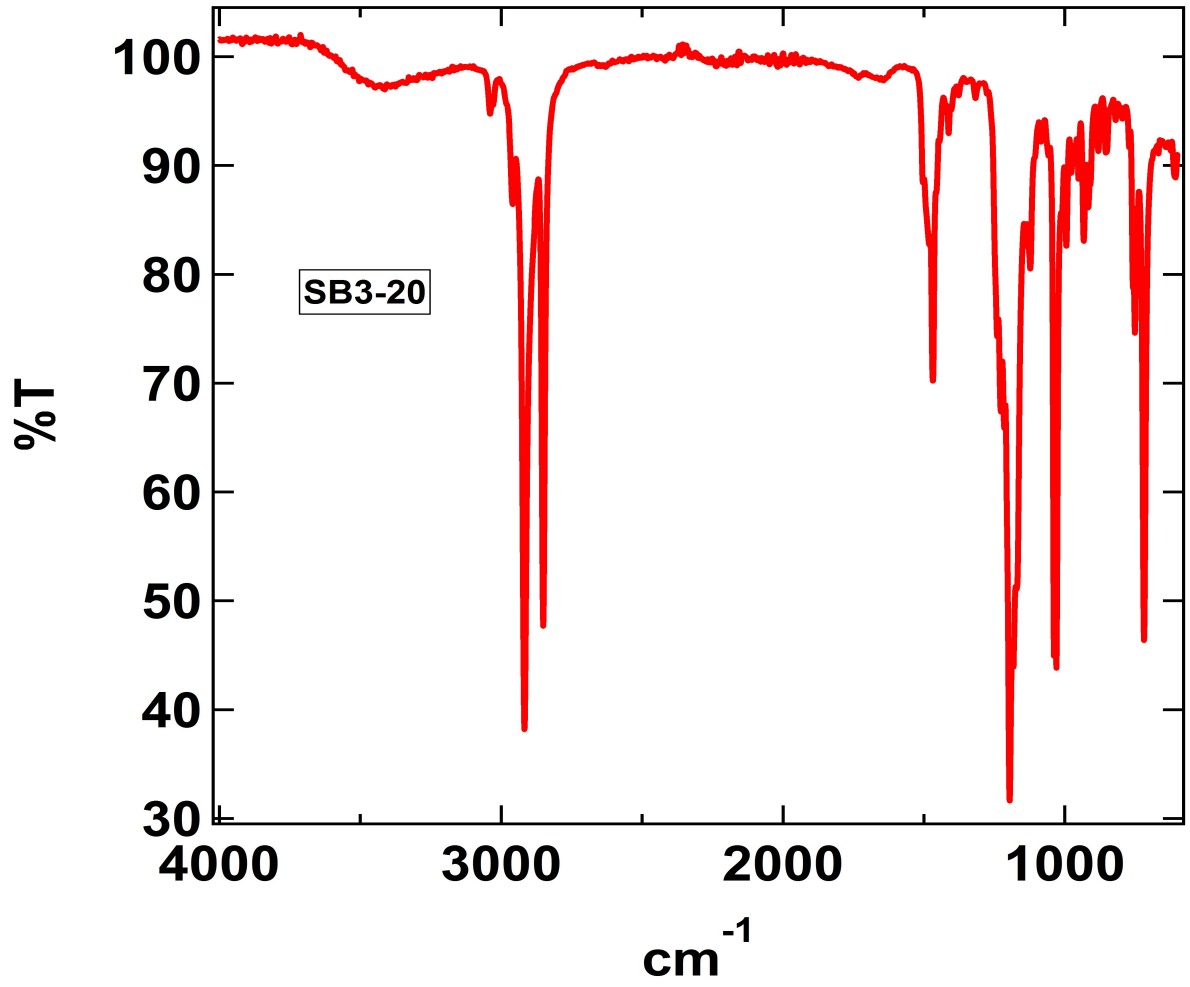
100
90
80
70
60
50
40
30
%T
SB3-20
4000
3000
2000
1000
cm-1

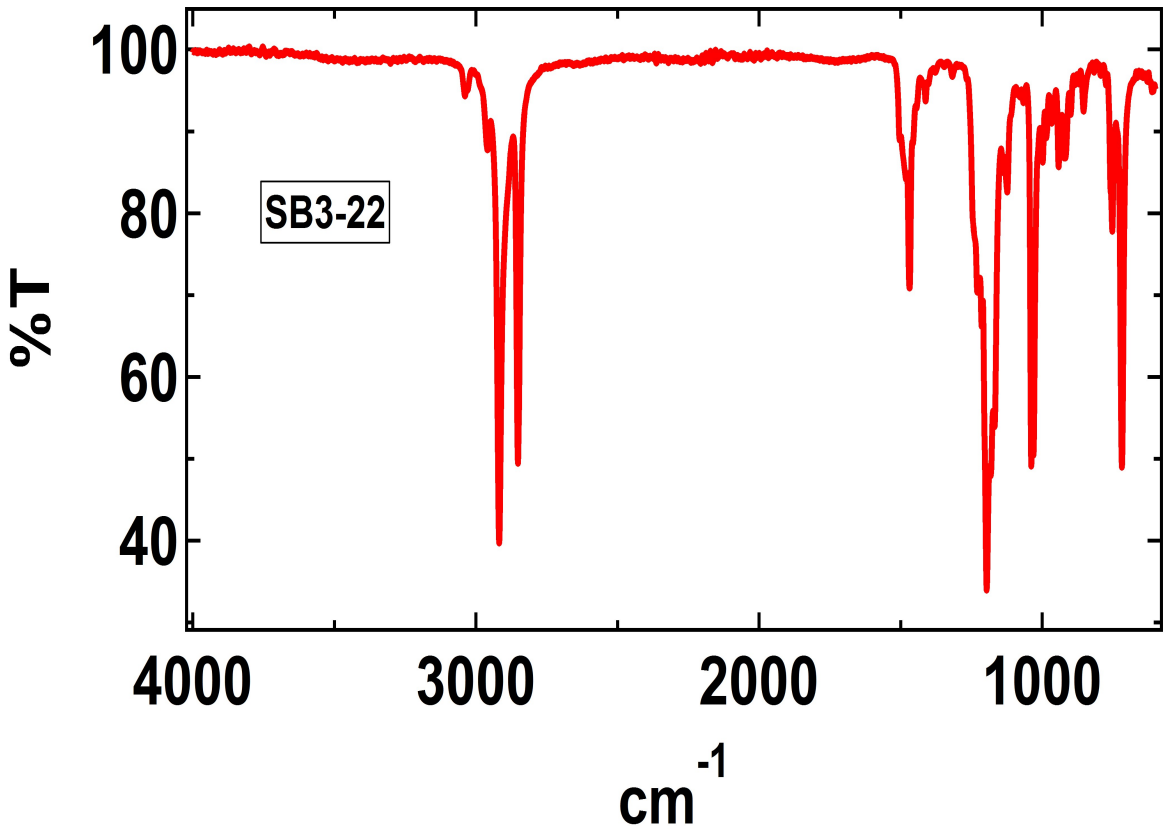

7.2 Confirmation of polymer synthesis for nanodisc experiments

2:1 ratios of styrene:maleic acid with an average molecular weight of 6 kDa have been shown to form 100 % nanodiscs upon addition of the polymer to the relevant phospholipid suspension. In order to prepare “empty” nanodiscs for reflectometry studies, the polymer was first synthesised through the use of RAFT polymerisation. The methodology for polymer preparation can be found in the materials and methods section of this thesis. Briefly the synthesis proceeds via RAFT polymerisation yielding polystyrene-co-maleic anhydride (PSMAnh), followed by the hydrolysis of this polymer to the acidic form, polystyrene-co-maleic acid (PSMA).

GPC was used to confirm the average molecular weight of the polymer (PSMAnh) and the polydispersity index. This is shown in figure 7.0. The retention time of the polymer was compared to a standard consisting of polystyrene at a known molecular weight used to form the calibration

curve (red line, blue dots). The relevant sample peaks are then shown as peaks 1 and 2. The plot shows that the average molecular weight of the synthesised polymer is 6.7 kDa with a polydispersity of 1.14. This highlights that the desired molecular weight of around 6 kDa was obtained with a low polydispersity.

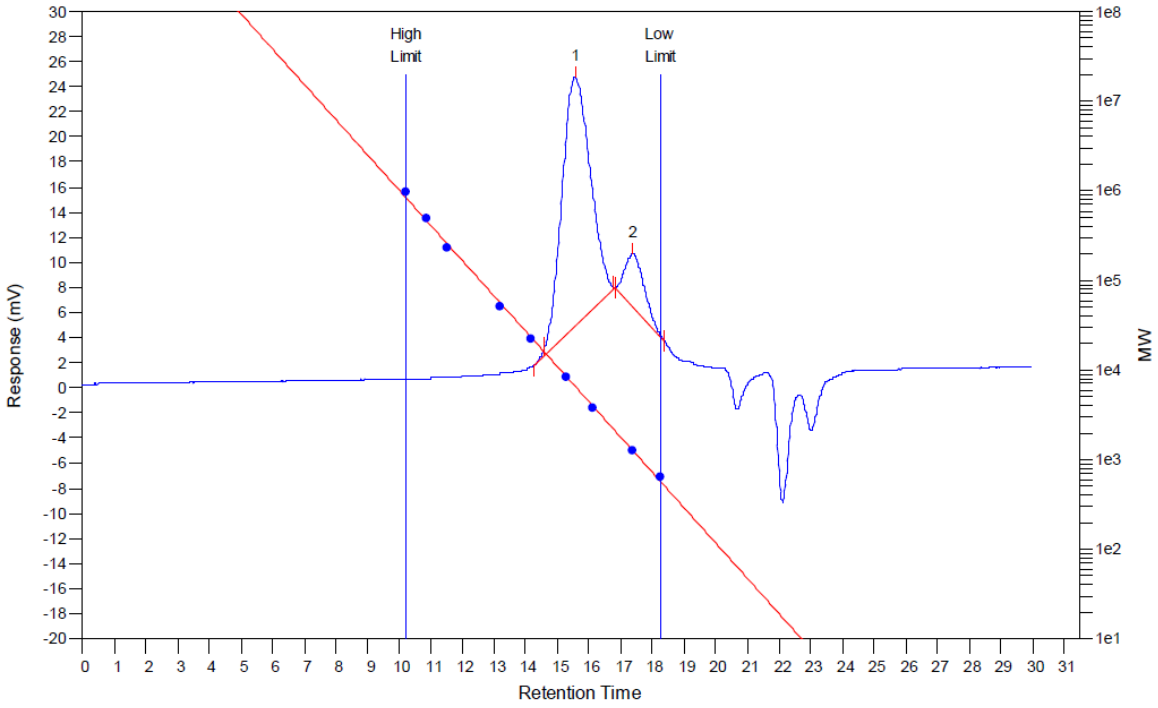

Fig 7.0- GPC plot showing the retention time of PSMAnh compared to the standard of polystyrene at a known molecular weight (red line, blue dots). The sample peaks are designated as 1 and 2.

^{1}H NMR was then used to assess the ratio of styrene to maleic anhydride ratios within the polymer. The NMR spectrum is shown in figure 7.1.

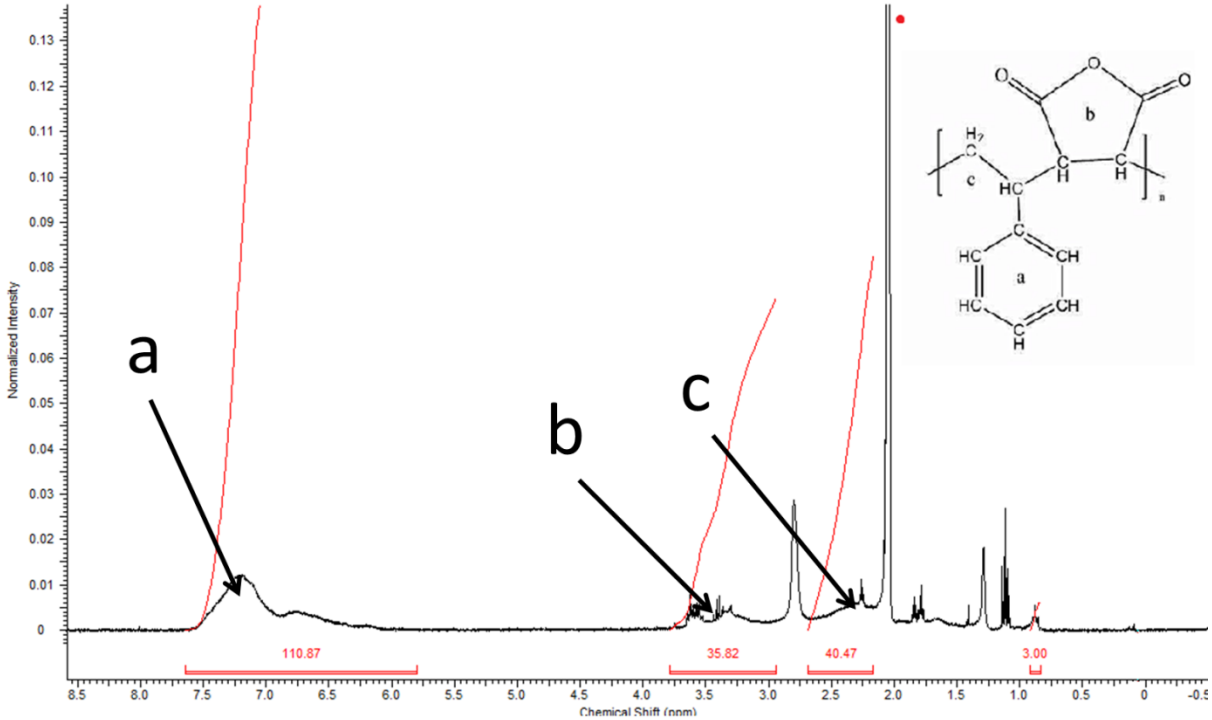

Fig 7.1- ^{1}H NMR spectrum in d-acetone of the 6 kDa polymer. Solvent peak is shown in red.

Figure 7.1 shows three prominent NMR peaks associated with the different parts of the polymer. The peak at 7.25 ppm is responsible for the hydrogen atoms of the aromatic region of the styrene monomers (a). Peaks between 0-4 ppm are designated as the protons in the aliphatic region (b) of the maleic anhydride and the protons in the aliphatic region of the styrene (c). These peaks can be integrated and the ratio of styrene:maleic anhydride units calculated through knowledge of the integration value of 1 styrene proton on the aromatic region of styrene and 1 proton on the maleic anhydride monomer. The ratio of these values then yields the ratio of styrene:maleic anhydride units. When calculated this yields a ratio of 2.2:1 styrene:maleic anhydride. This value is close to the predicted value of 2:1.